The role of materials engineering to mitigate corrosive wear in oil field pumping applications

A Thesis submitted for the degree of Doctor of Philosophy (Ph.D.)

By

Frazer Craig Brownlie

Department of Mechanical and Aerospace Engineering

University of Strathclyde

2017

Dedicated in memory of my Gran.

List of Publications

Journal

Effect of nitriding on the corrosive wear performance of a single and double layer Stellite 6 weld cladding

F. Brownlie, T. Hodgkiess, A. Pearson, A. M. Galloway

(*Wear,* 376-377, pp. 1279-1285, 2017)

Conference

Effect of corrosion on abrasive wear in a range of materials

L. Giourntas, F. Brownlie, G. Karafyllias, T. Hodgkiess, A. M. Galloway

(in conference proceedings, *23rd International conference on Fluid Sealing*, pp. 171–182, 2016)

Corrosive wear behaviour of various stainless steel alloys and a Stellite 6 weld cladding

F. Brownlie, T. Hodgkiess, A. Pearson, A. M. Galloway

(Presented at *Nordtrib 2016*, 14th - 17th June 2016 - Aulanko, Hämeenlinna, Finland)

Acknowledgements

First of all, I would like to thank my supervisors, Dr. Trevor Hodgkiess and Dr. Alexander M. Galloway, for sharing their knowledge and providing me with invaluable support and guidance during my Ph.D. study and writing of my thesis. Without their supervision, the research work reported in this thesis would not have been possible.

I would also like to thank my Weir project champions, Alastair Pearson (Chief Metallurgist, Weir Engineering Services, Glasgow) and Jacob Bayyouk (Senior Engineering Technical Steward, Weir Oil and Gas, Fort Worth, Texas), for their support, encouragement and their industrial advice and feedback.

For technical support, I would like to thank the following people; Mr. James Kelly, for his training and use of the metallographic preparation and examination equipment as well as sharing his vast knowledge and experience in metallurgical examination, Ms. Liza Hall, for her familiarisation and use of the surface profiling equipment, Dr. Fiona Sillars, who assisted me with SEM examinations, Dr. Tiziana Marrocco who aided me with the XRD investigations, Mr. James Gillespie, for his assistance with the hydraulic machine used for my impact test rig, Mr. Fuad Wasame, for waterjet cutting test samples and finally, to Mr. William Downie, for machining and grinding countless test coupons. Without their support, the practical part of my research would not have been possible.

To my laboratory colleagues; Lampros, George, Lloyd, Raphael, Charles, Finlay and Gavin thank you for sharing an unforgettable experience, with many highs and lows. It has been a privilege to work in a team with such hard working, like-minded people.

Lastly, to Fiona, mum and to my family and friends, thank you for your continuous support and encouragement throughout my Ph.D.

Abstract

Hydraulic fracturing is a technique used to stimulate the flow of oil/gas from tight formations of subterranean rock. The pumping equipment used operates under harsh environments; hence, has a short life expectancy. This research focuses on an investigation of corrosive wear issues associated with hydraulic fracturing pump components with a view of finding cost-effective solutions to combat these problems.

A recirculating slurry impingement rig was used to test the materials under corrosive wear conditions. To comprehend the various wear mechanisms occurring during testing a recently-developed, in-house volumetric analysis technique was employed, which combined electrochemical monitoring tests and 3D surface profiling. A novel repetitive impact slurry rig was developed to mimic the repetitive impact metal-metal wear occurring on valves and seats used in the hydraulic fracturing pump.

The enhanced volumetric analysis technique and information from segmented specimens provided a means of unravelling the complex deterioration processes that occur in the different regions of a submerged jet specimen. Post-test examinations of specimens using light-optical and scanning electron microscopy was also undertaken to yield information on mechanisms of degradation.

As hydraulic fracturing equipment is likely to have to operate in a range of water salinities, the effect of salinity on the currently used fluid end (i.e. pump casing) material (UNS G43400) as well as alternative material options was investigated. Increasing salinity from 0.05%NaCl to 10%NaCl was found to have a marginal increase in material loss for the stainless steel alloys, whereas, there was a significant increase for the low alloy steel. Sacrificial anode cathodic protection was also observed to be beneficial in reducing the material loss for the low alloy steel in the corrosive wear conditions.

The effect of nitriding Stellite 6 weld claddings was assessed as a hardfacing and/or repair option for hydraulic fracturing pump components. The nitriding process was found to be detrimental to the corrosion resistance of the Stellite 6 weld claddings; however, the volumetric analysis technique demonstrated that the nitriding process was capable of improving their mechanical erosion resistance.

Additively manufactured alloys were also assessed as alternative materials and/or a repair technique for hydraulic fracturing pump components. The additive manufactured alloys were compared to equivalent alloys which were conventionally manufactured. The additively manufactured alloys were observed to have significantly better corrosion resistance than the wrought alloys in static and flowing conditions. Under solid-liquid erosion-corrosion testing, the additive manufactured alloys and equivalent wrought alloys performed similarly.

A wide range of materials (soft/ductile to hard/brittle) were assessed under repetitive impact with slurry conditions. The results from the novel testing apparatus indicated that there was an optimum material hardness for repetitive impact wear resistance. Hence, suggesting that hardness is required to resist plastic deformation and toughness is required to resist brittle failures.

Table of Contents

Chapter 3: Methodology

Chapter 4: Assessment of fluid end materials and effect of environmental conditions

Chapter 8: General discussion, concluding remarks and recommendations for future work

Appendices

List of Abbreviations

AC	Alternating current
AM	Additive manufacturing
API	American Petroleum Institute
Aux	Auxiliary electrode
C	Corrosion
CAD	Computer aided design
CF	Circularity Factor
CNC	Computer numerical control
CMR	Coating modified resistance
CP	Cathodic protection
DC	Direct current
DIZ	Direct impinged zone
DLC	Diamond-like carbon
E	Erosion
EBAM	Electron beam additive manufacturing
EDM	Electro-discharge machine
EDS	Energy-dispersive X-ray spectroscopy
FCC	Face centred cubic
FEC	Free erosion-corrosion
GTAW	Gas tungsten arc weld
HIPed	Hot isostatic pressed
HVOF	High velocity oxygen fuel
HWTIG	Hot wire tungsten inert gas
ICCP	Impressed current cathodic protection
ISO	International Organisation for Standardisation
LAM	Laser additive manufacturing
LSCM	Laser scanning confocal microscope
MAM	Metal additive manufacturing
MIG	Metal-inert gas
MMA	Manual metal arc
MMC	Metal-matrix composite
Nit.	Nitrided
OA	Outer area

PBF	Powder bed fusion
PC	Personal computer
PF	Powder feed
PIII	Plasma immersion ion implantation
PLC	Public Limited Company
PREN	Pitting resistance equivalent number
PSA	Plasma surface alloyed
PTA	Plasma transferred arc
PVD	Physical vapour deposition
Ref	Reference electrode
S	Synergy
SACP	Sacrificial anode cathodic protection
SAW	Submerged arc weld
SCE	Saturated calomel reference electrode
SEM	Scanning electron microscopy
SLR	Single-lens reflex
TDS	Total Dissolved Salts
TIG	Tungsten inert gas
TML	Total Mass Loss
TVL	Total volume loss
UNS	Unified numbering system
UR	Ultimate resilience
USA	United States of America
UTS	Ultimate tensile strength
VL	Volume loss
WARC	Weir Advanced Research Centre
Work	Working electrode
XRD	X-ray diffraction
ΔC	Enhanced corrosion by erosion
ΔE	Enhanced erosion by corrosion

List of Symbols

°	Degrees
°C	Degrees Celsius
%wt	Weight percentage of content
A	Ampere
A	Area
Ag/AgCl	Silver/silver chloride reference electrode
Al	Aluminium
Al_2O_3	Aluminium oxide
b_a	Tafel constant
C	Carbon
C	Coulombs
Cd	Cadnium
Cl	Chlorine
Co	Cobalt
Cr	Chromium
Cr_2O_3	Chromium oxide
Cu	Copper
e^-	Electron
E	Elastic modulus
E	Potential
E_b	Passive film breakdown potential
E_{corr}	Corrosion potential
E_o	Equilibrium potential
E_{pit}	Pitting potential
E_r	Repassivation potential
Eq.	Equation
F	Faraday's constant
Fe	Iron
$FeCl_2$	Iron chloride
$Fe(OH)_3$	Iron oxide
ft/sec	Feet per second
FTU	Formazin Turbidity Units
g	Gram

gpm	Gallons per minute
gf	Gram-force
hr	Hour
H	Hydrogen
H	Hardness
HB	Brinell hardness
HCl	Hydrochloric acid
H_2O	Water
HRC	Rockwell C hardness
HV	Vickers hardness
Hz	Hertz
i	Current
i_a	Anodic current density
i_{max}	Maximum current density
I_{corr}	Corrosion current density
J	Joule
kgf	Kilogram-force
kg/hr	Kilogram per hour
kN	Kilonewton
K	Kelvin
lbf	Pound-force
lbs/hr	Pounds per hour
L	Litre
m	Mass loss due to corrosion
m	Metre
mg	milligram
mm	Millimetre
mS	MilliSievert
m/s	Metre per second
M	Metal
M	Mole
M	Molar mass
Mn	Manganese
MN	Mega Newton

Mo	Molybdenum
MPa	Mega Pascal
n	Number of electrons
nm	Nanometre
N	Nitrogen
Na	Sodium
NaCl	Sodium chloride
Ni	Nickel
O	Oxygen
OH^-	Hydroxyl ion
pH	Potential of Hydrogen
ppm	Parts per million
psi	Pounds per square inch
P	Perimeter
P	Phosphorus
Pb	Lead
Q	Flow rate
R_a	Arithmetic average of roughness
R_n	Radius of nozzle
s	Seconds
S	Sulphur
Si	Silicon
SiC	Silicon carbide
SiO_2	Silicon oxide
t	Time
Ti	Titanium
v	Poisson's ratio
V	Vanadium
V	Velocity
V	Volt
W	Tungsten
W	Watt
W	Weight loss
W	Wrought

WC	Tungsten carbide
Zn	Zinc
µm	Micrometre

Chapter 1

Introduction

1.1 Introduction

Hydraulic fracturing is a technique used to produce fractures in subterranean rock formations which stimulate the flow of natural gas and/or oil from tight formations. Hydraulic fracturing wells are drilled hundreds to thousands of metres vertically underground and typically extend thousands of metres horizontally. The fractures in the rock (which can extend to several hundreds of metres from the wellbore) are created by pumping large amounts of pressurised fluid into the wellbore and the rock formation. The fluid, used to open and enlarge the fractures, consists of water, proppant and chemicals (acids, gelling agents, inhibitors, etc.). The proppant (sand particles or ceramic balls) is used to hold open the fractures to increase the conductivity of the gas and/or oil [1.1].

Once the injection process is complete, the internal pressure of the rock formation causes the fluid to surface through the wellbore. The returned fluid is often referred to as "flowback" or "produced water" and usually contains the added chemicals plus naturally occurring materials such as brines, hydrocarbons, metals, etc. Traditionally, the flowback water was stored in tanks before off-site treatment, disposal or recycling; however, it is now common for the flowback water to be treated at the hydraulic fracturing site and reused for the injected fluid [1.2].

Typically equipment (such as Figure 1.1) used to pump the hydraulic fracturing fluid into the well is required to withstand high operating fluid pressures (up to 103MPa), high sand loadings (up to 15,900 kg/hr) and have a capacity to pump up to 4320 litres per minute. The hydraulic fracturing fluid composition varies between sites and also during operational stages of the hydraulic fracturing process. The water which is used for the injected fluid varies between sites as local water sources (freshwater or seawater) are used initially with treated flowback water being used in later stages. The chemicals added to the fluid depend upon the rock geology as well as the stage of the hydraulic fracturing process. Amongst the chemicals commonly used are dilute acids (cleans out debris around the rock perforations), gelling agents (assist in keeping the proppant in suspension) and corrosion inhibitors [1.3].

Weir Group PLC is an international engineering company that provides innovative solutions and expert services to the oil and gas, minerals and power industries. Within their oil and gas division, they design and manufacture positive displacement pumps and associated

pumping equipment (such as valves, valve seats, plungers, choke valves, integral connectors. etc.) which are used in the hydraulic fracturing industry to transport the high pressure fluids into the well. The extreme operating conditions during hydraulic fracturing cause the positive displacement pumps and pumping equipment to experience a variety of material degradation issues such as corrosion [1.4, 1.5], erosion-corrosion [1.6, 1.7], cavitation [1.8, 1.9] and fatigue [1.6, 1.10]. Figure 1.1 illustrates a Weir SPM hydraulic fracturing pump (Destiny QWS 2800) with five cylinders, an inlet and two outlets. The fluid end is the wetted section of the pump which experiences severe corrosion and erosion-corrosion.

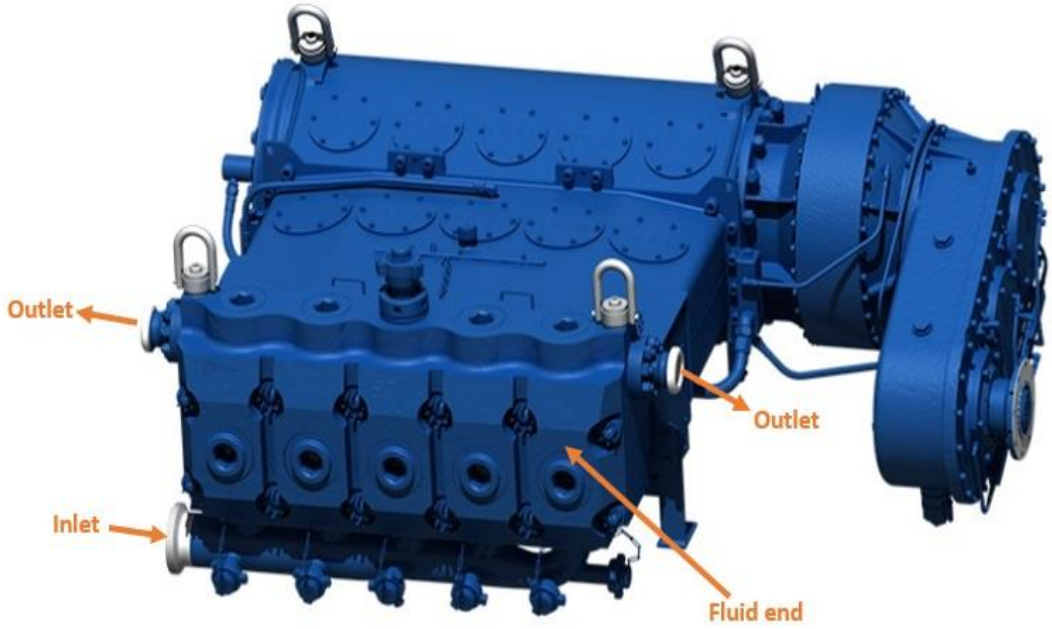

Figure 1.1: *WSPM Destiny QWS 2800 hydraulic fracturing pump (courtesy of WSPM)*

Figure 1.2 demonstrates the extreme corrosive wear which is commonly seen in engineering components, such as elbows in pipework, in the hydraulic fracturing industry. The 90° elbow shows severe corrosion damage throughout the inner bore, with large, deep pits occurring at the vicinity of the corner where the high pressure and turbulent fluid has caused extreme erosion-corrosion damage. The positive displacement pump casing (also referred to as the fluid end), also suffers significantly from erosion-corrosion damage.

Figure 1.2*: 90° elbow which has suffered severely from erosion-corrosion damage (courtesy of WSPM)*

The valve and valve seats located within the positive displacement pumps also experience corrosive wear from the hydraulic fracturing fluid (according to Figure 1.3). This is problematic as the wear process is so severe that the valve and valve seats cannot endure a full hydraulic fracturing cycle (the cycle involves various stages which include acid cleaning of the well, slickwater (proppant free), oil/gas recovery and flushing of the well) and so must be exchanged for new valves and seats in the field [1.11].

Figure 1.3: *Valve and valve seat which has experienced corrosive wear during the hydraulic fracturing process*

As the positive displacement pumps and associated equipment used in the hydraulic fracturing industry experience severe erosion-corrosion, there was a requirement to characterise these material degradation processes. To mitigate these deterioration mechanisms it was clear that alternative materials and/or surface engineering treatments (heat treatments, diffusion processes, weld claddings, etc.) were necessary to be substituted for the currently used materials or manufacturing processes. Attempts to improve performance by design/material selection strategies, particularly of valve seats, have been impeded by a lack of detailed comprehension of the complex deterioration processes occurring during operation. Therefore, there is a need to examine and understand the fundamental mechanisms of the degradation processes occurring in the hydraulic fracturing pumping equipment.

The objective of this research work was to:

1. Understand the degradation processes which are occurring in the Weir Group PLC hydraulic fracturing pumping equipment.
2. Assess the effect of altering the water source (freshwater to brine) on the corrosive wear behaviour of the materials.

3. Assess the potential benefit of applying cathodic protection (impressed current and sacrificial anode/coating) to extend the life of the hydraulic fracturing pumping equipment.
4. Assess alternative materials, surface engineering treatments and alternative manufacturing methods to develop a material selection solution to assist with improving the life span of components.

The work reported in this thesis enhances the state of the art and innovation in the field of erosion-corrosion by utilising an advanced volumetric analysis technique which has been developed in-house at the Weir Advanced Research Centre (WARC) based at the University of Strathclyde [1.12]. The benefits of using this technique is the quantification of high angle erosion-corrosion damage occurring in the direct impingement zone as well as corrosive sliding abrasion wear during a 90° impingement test. Cathodic protection tests isolated the mechanical deterioration mechanisms - high angle erosion and sliding abrasion damage. The direct impingement zone and the outer area of test materials were electrically insulated through a segmentation technique which allowed electrochemical monitoring and, hence, quantification of the corrosion occurring in the two different flowing environments.

Also, a novel repetitive impact testing machine was developed to enhance the understanding of the wear mechanisms occurring on the valve seat during operation. The impact testing machine utilises a hydraulic machine with an impactor and a test coupon with an aqueous solution with hydraulic fracturing sand being “crushed” between the impactor and test coupon. The contact pressure between the impactor and test coupon, as well as the frequency of the rig, mimics real life operating conditions [1.11].

The work described herein, utilises the enhanced erosion-corrosion analysis technique and novel repetitive impact test rig to assess the performance of currently used materials as well as alternative materials, surface engineering treatments and manufacturing methods.

An outline of the thesis is as follows. Chapter 2 involves a brief overview of the hydraulic fracturing process and a detailed description of the fundamentals of erosion-corrosion and repetitive impact wear phenomena. Chapter 3 describes the pre-test, test and post-test methodologies used in this study.

Chapter 4 involves an assessment of alternative materials for positive displacement pump casings (referred to herein as fluid ends). The advanced erosion-corrosion analysis technique is used to assess the currently used fluid end material, low alloy steel, with three different stainless steel grades – austenitic, martensitic and Superduplex grades. Due to differing local water sources (in the field) and the use of treated flowback water which can be used in the hydraulic fracturing fluid composition, the effect of water salinity was also evaluated. The potential application of cathodic protection (both impressed current and sacrificial anode/coating) for the low alloy steel was also assessed due the broad use of low durability, low alloy steel in the hydraulic fracturing industry and due to it's potential as a cheaper alternative to stainless steels.

Chapter 5 describes the wear mechanisms found on a valve seat used in a typical hydraulic fracturing pump and discusses the development and validation of a repetitive impact wear test machine which mimics the conditions found on the valve seat. Chapter 6 explores the assessment of Stellite 6 weld claddings as an alternative surface engineering treatment for hydraulic fracturing pumping components such as valve seats. Single and double layer weld claddings as well as gas nitrided specimens of both were evaluated under erosion-corrosion and repetitive impact conditions.

Chapter 7 demonstrates the relative performance of four additive manufactured materials along with their equivalent wrought counterparts under solid-liquid erosion-corrosion conditions. The additive manufacturing process is attractive as it could improve material development for specific components vulnerable to wear and could also lead to enhanced repair techniques. This chapter assesses the corrosive and repetitive impact wear performance of four different metallic alloys. The final chapter contains a discussion of the durability and overall potential of the various surface engineering strategies examined in the project followed by concluding remarks and future work.

As the thesis discusses a wide variety of materials, surface engineering treatments and manufacturing processes, the chapters involving material assessment include a literature review, experimental results, detailed discussion with remarks on the relevance of the work for industrial design and material selection, concluding remarks and chapter references.

1.2 References

[1.1] M. K. Hubbert and D. G. Willis, “Mechanics of hydraulic fracturing,” *J. Pet. Technol.*, vol. 9, no. 6, pp. 153–166, 1957.

[1.2] K. B. Gregory, R. D. Vidic, and D. A. Dzombak, “Water management challenges associated with the production of shale gas by hydraulic fracturing,” *Elements*, vol. 7, no. 3, pp. 181–186, 2011.

[1.3] D. M. Kargbo, R. G. Wilhelm, and D. J. Campbell, “Natural gas plays in the Marcellus Shale : Challenges and potential solutions,” *Environ. Sci. Technol.*, vol. 44, no. 15, pp. 5679–5684, 2010.

[1.4] A. Hartsock, K. Bibby, R. D. Vidic, and K. B. Gregory, “Microbial Community Changes in Hydraulic Fluids and Produced Water from Shale Gas Extraction,” *Environ. Sci. Technol.*, vol. 47, pp. 13141–13150, 2013.

[1.5] P. Rajeev, A. O. Surendranathan, and C. S. N. Murthy, “Corrosion mitigation of the oil well steels using organic inhibitors – A review,” *J. Mater. Environ. Sci.*, vol. 3, no. 5, pp. 856–869, 2012.

[1.6] S. N. Shah and S. Jain, “Coiled tubing erosion during hydraulic fracturing slurry flow,” *Wear*, vol. 264, pp. 279–290, 2008.

[1.7] M. C. Vincent, H. B. Miller, D. Milton-Tayler, and P. B. Kaufman, “Erosion by Proppant: A Comparison of the Erosivity of Sand and Ceramic Proppants During Slurry Injection and Flowback of Proppant,” *J. Pet. Technol.*, vol. 57, no. 3, pp. 35–37, 2015.

[1.8] A. Iannetti, M. T. Stickland, and W. M. Dempster, “A CFD and experimental study on cavitation in positive displacement pumps : Benefits and drawbacks of the ‘full’ cavitation model,” *Eng. Appl. Comput. Fluid Mech.*, vol. 10, no. 1, pp. 57–71, 2015.

[1.9] A. Iannetti, M. T. Stickland, and W. M. Dempster, “A CFD Study on the Mechanisms Which Cause Cavitation in Positive Displacement Reciprocating Pumps,” *J. Hydraul. Eng.*, vol. 1, pp. 47–59, 2015.

[1.10] X. He, Q. Liu, M. Zhao, Y. Zhao, and J. Tian, “Fatigue Prediction for Pump End of High Pressure Fracturing Pump,” *Adv. Mater. Res.*, vol. 337, pp. 81–86, 2011.

[1.11] Private communication with Jacob Bayyouk, Senior Engineering Technical Steward, Weir Oil & Gas, Fort Worth, Texas, USA, 2015.

[1.12] L. Giourntas, T. Hodgkiess, and A. M. Galloway, “Enhanced approach of assessing the corrosive wear of engineering materials under impingement,” *Wear*, vol. 338–339, pp. 155–163, 2015.

Chapter 2

Overview of hydraulic fracturing and corrosive wear

2.1 Introduction

This chapter presents an overview of the hydraulic fracturing process as well as the chemical composition of the fracturing fluid and the possible types of proppants used during operation. The fundamental theories of corrosion, erosion-corrosion and repetitive impact wear will also be discussed.

2.2 Hydraulic fracturing process

Hydraulic fracturing is a well stimulation technique which uses highly pressurised fluid with suspended solid particles to fracture rocks. The process involves injecting a high pressure fluid (discussed further in Chapter 2.2.1) into the wellbore to establish fissures in the rock formation which then allows the natural gas and petroleum to flow freely.

The fracturing process can be traced back to the 1860's, however, it was not fully comprehended until Floyd Farris conducted an in-depth study into hydraulic fracturing which related well performance with treatment pressures [2.1]. As further wells have been discovered and with developments in technology, hydraulic fracturing is now being used extensively and it has been reported that 95% of new wells drilled in the USA are hydraulically fractured [2.2].

Before the hydraulic fracturing procedure can commence, it is necessary to drill down to the underground well. The oil and gas reservoirs can be generally 183-2591m (600-8500ft) underground depending on the location of the well [2.3]. Initially the drilling occurs vertically where several steel casings of different diameters are inserted within the well into depths of 91-305m (300-1000ft) [2.4]. Cement is pumped down the drilled hole and solidifies between gaps in the steel casings. This is conducted to stop contamination of groundwater and aquifers which are located close to the surface. The procedure is continued with smaller diameter casings being used each time. Once the drill is located 152m (500 feet) above the oil and gas reservoir, the horizontal drilling begins. There is an initial radius of curvature as the drilling is rotated through a 90° angle. The horizontal drilling can occur up to 1 mile (depending on location) from the well head site. Once the horizontal drilling process has been completed, the drilling tool is withdrawn from the well and the cementing operation is conducted [2.4].

Before the hydraulic fracturing process occurs, a perforating gun is lowered down the bore. An electrical current triggers the gun which perforates small holes through the cemented steel casing which is located at the reservoir. These small holes will then allow the high pressure fluid to enter the formation [2.5].

The hydraulic fracturing process differs slightly for various sites due to the particular condition of the rock formation. However, the general procedure is similar for the majority of operations. The composition of the fluid used also differs depending on location as not all additives are required and proportions can alter depending on the depth, thickness and other characteristics of the formation [2.4].

The first stage of the hydraulic fracturing operation involves pumping several thousand gallons of water combined with dilute hydrochloric acid. This serves to remove cement debris in the bore and dissolves carbonates to allow for opening of fractures near the bore [2.4].

The next stage is called the “pad stage” which consists of 100,000 gallons of slickwater which is proppant free. The slickwater solution contains chemicals (described in chapter 2.2.1) which reduce the pressure required to pump the water into the bore. This assists with the opening of the formation fissures which provides easier placement of the proppant.

The next stage may consist of several sub-stages of the fluid combined with proppant pumped into the wellbore. The proppant is used to keep open the fractures and can even enhance the existing fissures. The oil and/or gas can then be recovered. The proppant which is used can either be silica sand or ceramic balls. Several thousands of gallons of water can be used in this stage. As much as 20% of the water can return to the surface (known as “flowback”). This “flowback” water can be treated and reused for subsequent fracturing stages [2.6].

The final stage is called a “flushing stage” which consists of a volume of water sufficient to remove excess proppant from the wellbore [2.7].

The pumping operation for each stage may take from 20 minutes up to 4 hours [2.4] depending on the design and intent of the hydraulic fracturing process. The fluid return for

the first day or two after fracturing can produce 3-6 barrels per minute of flowback fluid, before falling to 1000 barrels per day. By the end of the second or third week the production decreases to a few hundred barrels per day [2.4].

2.2.1 Hydraulic fracturing fluid chemical composition

The chemical composition of the hydraulic fracturing fluid differs during the hydraulic fracturing operation [2.4]. The fluid consists of two parts; an aqueous solution and proppant (5-12% concentration). The aqueous solution is 98-99.2% water which is typically sourced locally to the hydraulic fracturing well site. The local source may be a surface river or lake, underground water, seawater or water produced with the oil and/or gas from the well. The temperature of the source water will depend upon geographical location and season. Therefore, a potential temperature range could be between 5°C-40°C. The pH of the solution is neutral, typically of pH between 7-8 [2.8].

Evidently, the Total Dissolved Salts (TDS) of the aqueous solution will vary depending upon the source of the water [2.9]. Until recently, the main source of water has been fresh water –less than 1000 parts per million (ppm) TDS, has been used for both the drilling and fracturing operation. This continues to be the preferred water source for the industry [2.10]. However, water shortage problems in areas which are susceptible to droughts such Texas, California and New Mexico [2.10], as well as environmental issues and public pressure has resulted in a growing impetus on the re-use of returned “flowback” water from the reservoir. However, there are many issues with re-using the “flowback” water as its constitution does not simply equate to the fluid which was used initially. Modification of the fluid is highly likely during the hydraulic fracturing operation as it interacts with the subsurface water and rock formations. This can often lead to instances where the “flowback” water contains complex compositions (such as scale forming ions - barium and calcium, as well as organic compounds) and can also yield extremely high TDS levels (up to 200,000ppm) [2.4]. Hence, the “flowback” water is typically treated to remove the undesirable constituents and to reduce the TDS level. The proportion of re-used “flowback” water can be up to 40% depending upon the hydraulic fracturing site [2.4].

In some hydraulic fracturing sites in the Gulf of Mexico and Saudi Arabia, heavy brines have been used for the hydraulic fracturing fluid. The formations are typically high temperature

and pressure, therefore, the high density fluid is used to assist with overcoming some of the pumping capability challenges [2.8].

Depending upon the hydraulic fracturing stage and operating environment, a concoction of additives may be added to the hydraulic fracturing fluid [2.8, 2.9]. A list of these additives is described below:

- Dilute acid (hydrochloric or citric acid – up to 0.3% concentration) is used in the initial fracturing sequence. This cleans out cement and debris around the rock perforations to facilitate the subsequent slickwater solutions employed in the fracturing formation. It is also occasionally used to reduce the fracture initiation pressure. The acid is typically used up within a few centimetres of the initial fracture entry point and yields calcium chloride, water and a small amount of carbon dioxide.
- Corrosion inhibitors (amines or amides with formic acid and methanol as well as oxygen scavengers - 0.05% concentration) are used to suppress corrosion of the carbon steel well casings and are only used when the dilute acid is added to the fluid.
- Gelling agents (guar gums - 0.5% concentration) are used in small amounts to thicken the water-based solution to assist with transporting the proppant.
- Friction reducing agents (potassium chloride/polyacrylamide-based compounds – 0.05% concentration) - are used to reduce tubular friction and pressure required to pump fluid into the well bore, thereby reducing pump horsepower output and air emissions from the pumps. This is the “Slickwater” component of the fluid solution.
- Cross-linking agents (boric acid or ethylene glycol – 0.0032% concentration) these are used at the latter stage of the hydraulic fracturing process to cause the gelling agent to break down into a less viscous fluid so it can be removed from the wellbore without transporting the proppant.
- Biocides/disinfectants (bromide and phosphonium-based solutions - 0.001% concentration) are used to prevent growth of bacteria which may deposit on fissure walls and hence obstruct fluid flow. Microbes could potentially interact and reduce the effectiveness of friction reducers and gelling agents by consuming them as a

food source. The microbes may even promote corrosion by creating sour gas (hydrogen sulphide) in the reservoir.

- Scale inhibitors (carboxylic acid-base or acrylic acid-base polymers – 0.023% concentration) are used to control the precipitation of carbonate and sulphate minerals, which may cause blockage in equipment or within the rock fissures which would lead to a reduction in permeability.
- Clay inhibitors (sodium/potassium chlorides or quaternary amines – tetramethylammonium chloride – 500-2000ppm) are used when there are concerns with swelling of clay constituents in the formation which would lead to obstructions of the hydraulic fracturing fluid.
- Iron control/stabilising agents (citric/hydrochloric acid – 0.004% concentration) are used to inhibit the precipitation of iron compounds (such as iron oxide) in the wellbore by keeping them soluble.

2.2.2 Proppants used

As discussed previously, the proppant has a significant role in the hydraulic fracturing process as it ensures that the fissures remain open to allow the oil and/or gas to be recovered. There are three proppant materials which are commonly used: natural silica sand, resin coated silica sand and ceramic balls. Figure 2.1 shows the distribution of the proppant materials with respect to their oil/gas recovery efficiency (termed conductivity), mechanical strength and shape.

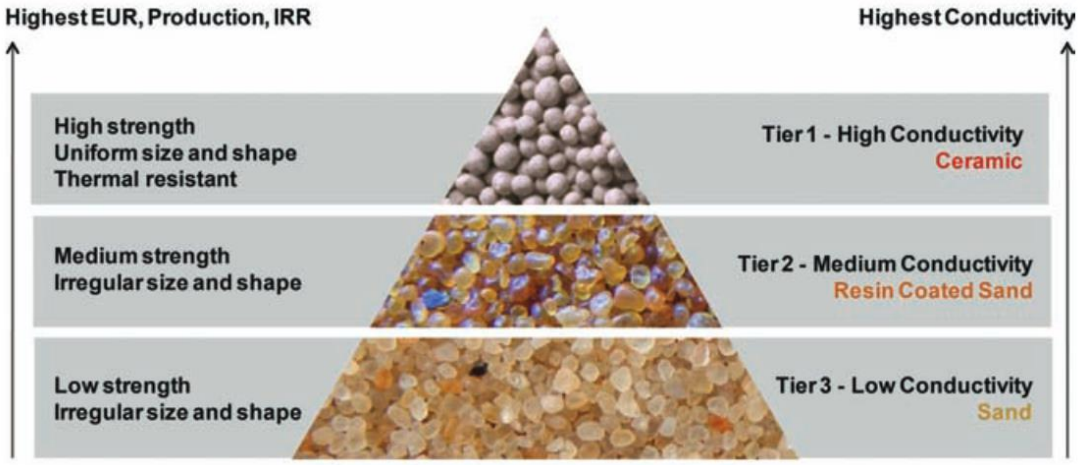

Figure 2.1: *Distribution of proppants in accordance with mechanical strength and oil/gas flow/conductivity [2.11]*

There are various properties that the proppant must demonstrate in order for it to function effectively and efficiently during the hydraulic fracturing operation. These characteristics include shape, size, compressive strength, acid solubility and turbidity. Standards and recommended practices (ISO 13503-2 [2.12] and API RP (Recommended Practice) 19C [2.13]) have been produced to ensure that used proppants meet specified requirements.

The shape and size are important as these determine the flow/conductivity of the oil and/or gas being extracted from the formation (Figure 2.2). If the proppant is irregular in shape and size then the flow rate of the oil and/or gas will be considerably lower when compared to spherical proppants. The tight packing arrangement of the irregular shaped proppant reduces the permeability of the oil/gas.

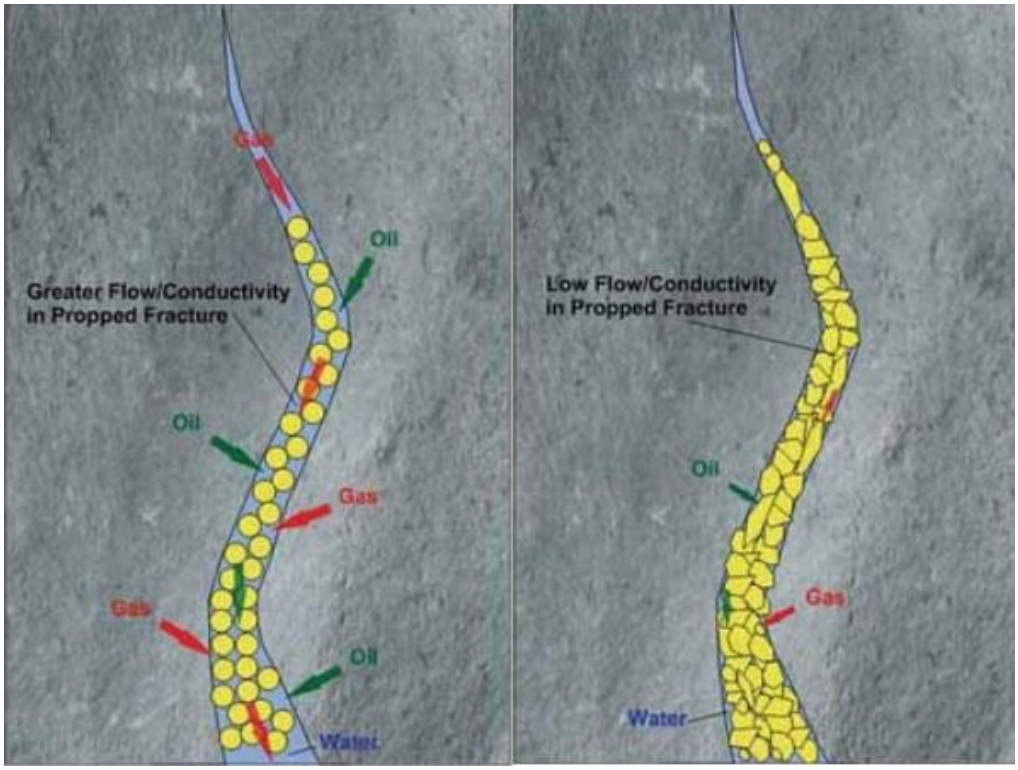

Figure 2.2: *Oil and gas conductivity with different proppant shape and size [2.14]*

In order to control the range of shapes and sizes of the proppant, methods have been developed to select preferential spherical shapes which will lead to greater conductivity. One such method utilises the Krumbein-Sloss chart (Figure 2.3), produced by studying the shape of sedimentary particles [2.15]. This chart can be used to visually measure the sphericity and roundness of the proppant.

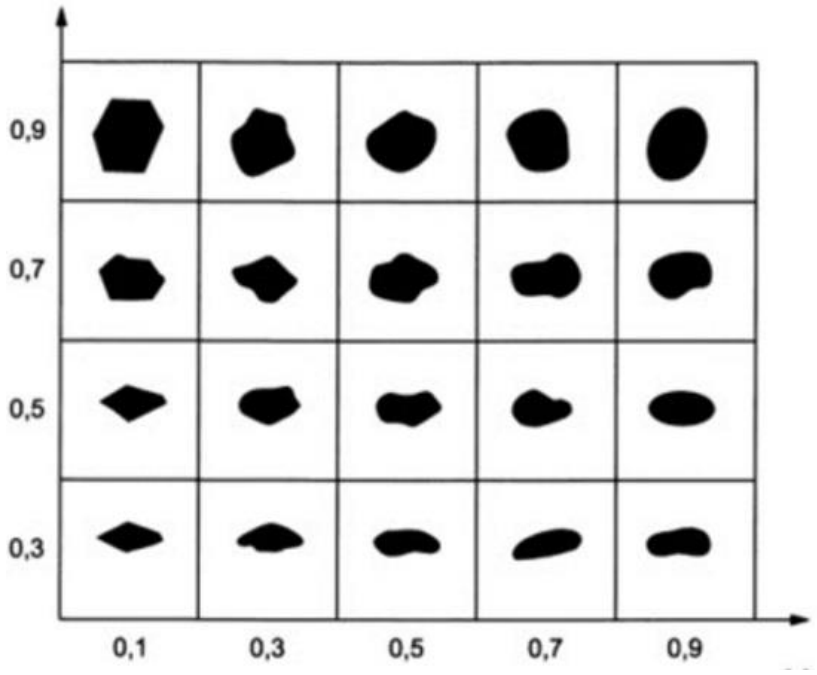

Figure 2.3: *Krumbein-Sloss chart for measuring sphericity and roundness [2.15]*

Both the ISO 13503-2 and API RP 19C standards recommend that both the sphericity and roundness for proppants must be greater than 0.6 and for high strength proppants they must both be greater than 0.7.

The compressive strength of the proppant is crucial as it is required to withstand high stresses applied by the fracture attempting to close. These stresses can exceed 68.9MPa (10,000 psi). The compressive strength of the proppants is generally between 41.3-96.5MPa (6,000-14,000psi)[2.12].

A variety of chemicals are used during the hydraulic fracturing process, including acids, which could potentially dissolve the proppant. Dissolved proppants would lead to reduced production rates, therefore, the proppant must not dissolve when in contact with the acidic solution. The API RP 19C standard states that hydraulic fracturing and resin coated sand should have a maximum acid solubility weight percentage of 2% for proppants larger or equal to 30/50 mesh size and 3% for proppants smaller than 30/50 mesh size. For ceramic proppants the maximum acid solubility weight percentage is 7% [2.13].

Turbidity is the cloudiness of a fluid caused by a large number of dissolved particles. This can give an indication of the amount of clays present in a proppant. The presence of clays in

proppants has two detrimental effects. The clay can dissolve into the hydraulic fracturing fluid which can obstruct leakage paths for the oil and natural gas. Also, clays present on the surface of the proppant can create friction which reduces the conductivity of the oil and/or gas. API RP 19C recommends that the turbidity of the proppant should not exceed 250 Formazin Turbidity Units (FTU) [2.13].

2.2.3 Pumping equipment used in the hydraulic fracturing process

Reciprocating positive displacement pumps are utilised to pump high pressure fluid to hydraulically fracture a well. A schematic cross section diagram of a typical reciprocating positive displacement pump is illustrated in Figure 2.4.

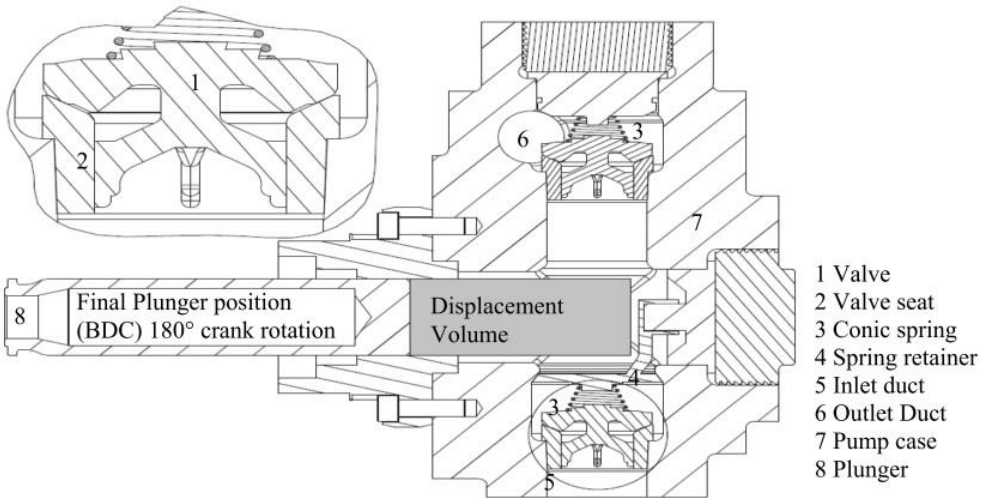

Figure 2.4: *Cross section schematic of a reciprocating positive displacement pump [2.16]*

A power source, such as an electric or diesel engine, is connected to a pinion gear which in turn causes the bull gear to operate the crankshaft which causes the plunger (8) to operate linearly within a cylinder located in the pump case (7), which is commonly referred to as the fluid end. As the plunger strokes outwards, fluid is brought into the chamber by the inlet duct (5) and discharged at a higher pressure out of a discharge port. Suction and discharge valves (1) open and close which results in fluid being drawing and discharging out from the chamber.

The pressure of the fluid within the hydraulic fracturing pump and associated equipment can be between 41-83MPa (4,000-12,000psi). The pumps operate between 1-5Hz and with sand loadings up to 15,900kg/hr (35,000 lbs/hr). Pumps are designed to withstand a rod

loading up to 1.2MN (275,000lbf) and have a capacity of pumping up to 4320 litres per minute (950gpm) [2.17].

2.3 Fundamentals of Erosion-Corrosion

As hydraulic fracturing pumps are used to transport high pressure corrosive fluids containing solid particles, it is clear that these pumps and associated equipment experience material degradation from erosion-corrosion processes. Erosion-corrosion is defined as a surface degradation mechanism that is caused by a flowing fluid, which may or may not contain solid particles. The erosion-corrosion phenomena is complex as it is made up of several degradation processes; mechanical wear (erosion), electrochemical damage (corrosion) and the combined interaction of the two processes (synergy). The relationship for erosion-corrosion damage is defined by some researchers as [2.18–2.20]

$$TML = E + C + \Delta C + \Delta E \quad \text{Eq. 2.1}$$

Where, the total mass loss (TML) is equal to the mechanical damage (E), the electrochemical corrosion in static conditions (C), ΔE is the enhanced erosion by corrosion damage and the ΔC is the enhanced corrosion by the erosion process.

For the purpose of this thesis, the erosion-corrosion damage phenomena will be described by Eq. 2.2, which is a simplified version of Eq. 2.1.

$$TML = E + C + S \quad \text{Eq. 2.2}$$

In this second approach, the C term is equivalent to the (C +ΔC) component in Eq. 2.1 as it is measured in-situ during testing and hence it is the total mass loss due to electrochemical corrosion processes. The term S is defined as the synergy component and is equivalent to the ΔE in Eq. 2.1.

Although there are only three constituents which contribute to the total material loss in Eq. 2.2, each of these degradation mechanisms have several parameters and influential factors. Hence, the subsequent sections will go into detail describing each of the three processes – corrosion, erosion and synergy.

2.4 Fundamentals of Corrosion

2.4.1 Background

In the most general form, corrosion is the degradation of a metal by a chemical or electrochemical reaction with its environment. The majority of metals have a tendency to corrode in aqueous environments as they are converted from an unstable state (alloy) to a stable condition which represents the ore from which the metal had been extracted. The tendency for a metal to corrode can be expressed as a thermodynamic property called free energy. A spontaneous reaction is associated with a reduction on the free energy of the system, hence, when a metal converts to corrosion product the change in free energy is negative. The transformation of a metal to corrosion product requires two electrochemical reactions, anodic and cathodic. Examples (Eq. 2.3-2.7) for both types of reactions are stated below.

Anodic Oxidation: $$Fe \rightarrow Fe^{2+} + 2e^{-}$$ Eq. 2.3

The surface on which chemical reduction occurs is called the cathode. The cathodic reaction which occurs in aqueous solutions varies depending on the pH of the environment. In acidic environments, the following cathodic reactions may take place:

In the absence of oxygen: $$2H^{+} + 2e^{-} \rightarrow H_2$$ Eq. 2.4

In the presence of oxygen: $$4H^{+} + O_2(aq.) + 4e^{-} \rightarrow 2H_2O$$ Eq. 2.5

"*Water reduction reaction*" $$2H_2O + 2e^{-} \rightarrow 2(OH^{-}) + H_2$$ Eq. 2.6

In neutral or alkaline environments, where the pH is greater than 7, the most common reaction is the oxygen reduction reaction which consumes dissolved oxygen to release hydroxyl ions.

Oxygen reduction: $$O_2(aq.) + 2H_2O + 4e^{-} \rightarrow 4(OH)^{-}$$ Eq. 2.7

The level of dissolved oxygen in the aqueous solution greatly dictates this reaction. In well aerated conditions the dissolved oxygen content can be typically between 5-10ppm which is sufficient for the oxygen reduction reaction to occur at finite rates – especially if the water is non-quiescent. By combining Eq. 2.3 and 2.7, this results in Eq. 2.8.

$$Fe^{3+} + 3(OH)^{-} \rightarrow Fe(OH)_3$$ Eq. 2.8

The brown scale formed from this reaction is commonly known as rust ($Fe(OH)_3$), which is caused by the corrosion of iron in aqueous environments. Factors which influence corrosion in aqueous solutions include oxygen content, pH, chloride content, Total Dissolved Solids (TDS), temperature, flow velocity, organic compounds and biological organisms [2.21].

Figure 2.5 illustrates the process which occurs when iron corrodes in an aqueous environment. The anodic oxidation and oxygen reduction reactions (Eq. 2.3 & 2.7) occur simultaneously to produce hydroxyl and iron ions which precipitate and form corrosion product on the surface. Pits are formed on the surface as a result of dissolution of iron ions from the surface of the material.

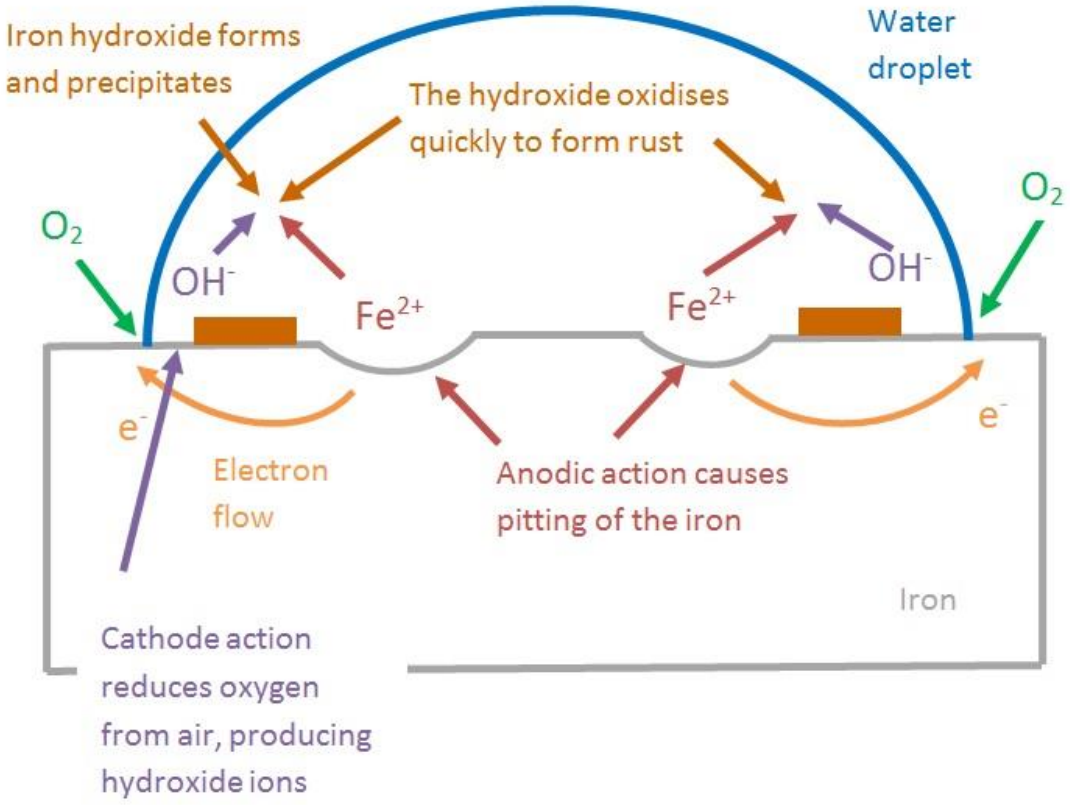

Figure 2.5: *Schematic diagram of iron corroding at the surface in an aqueous environment*

The mixed potential theory is a well-established concept which states that when a metal is exposed to an aqueous environment it will attain an electrode potential, E_{corr}, which is determined by the anodic and cathodic reactions occurring at the surface [2.22]. This is the potential that is observed when the electrode potential of a metal is measured with a

reference electrode. The mixed potential of a corroding metal alloy is greater (more positive) than its equilibrium potential, E_o.

When a metal is corroding freely in an aqueous solution it exhibits a mixed potential, E_{corr}, at which the subsequent corrosion current density, I_{corr}, can be used to determine the rate at which the metal corrodes in that particular environment. This can be conducted by using Faraday's Law of electrolysis. Therefore, measuring I_{corr} is a powerful tool for monitoring the rates of corrosion for metals. Faraday's Law for weight loss is given in Eq. 2.9.

$$m = \frac{M \cdot i \cdot t}{n \cdot F} \qquad \text{Eq. 2.9}$$

where, *m* is the mass loss of the corroded metal (g/s), *M* is the molar mass of the metal (g/mole), *i* is the current (A), *t* is the time (s), *n* is the number of electrons produced by the anodic oxidation reaction and *F* is Faraday's constant (96500 C/mole).

2.4.2 Corrosion monitoring

Corrosion monitoring in aqueous solutions has been developed over several decades and a variety of well-established techniques is widely used for corrosion research and practice [2.23]. The advantages of using such techniques include the sensitivity to low corrosion rates, short duration of experiments and good understanding of electrochemical theory. A brief description of some techniques will be highlighted in this section.

2.4.2.1 Potentiodynamic polarisation measurements

The corrosion current density, i_{corr}, is established by an accelerated polarisation test which procedure involves scanning, of the material under study, the potential away from its free corrosion potential, E_{corr}, by way of a potentiostat and a three electrode cell (shown in Figure 2.6). A reference electrode (Saturated Calomel Electrode or Silver/Silver chloride electrode) is used to measure the potential across the "working" electrode (material under study). An auxiliary electrode which is inert (typically platinum) performs as an electrical connection for the current to flow between it and the "working" electrode whenever the electrode potential is shifted from E_{corr}.

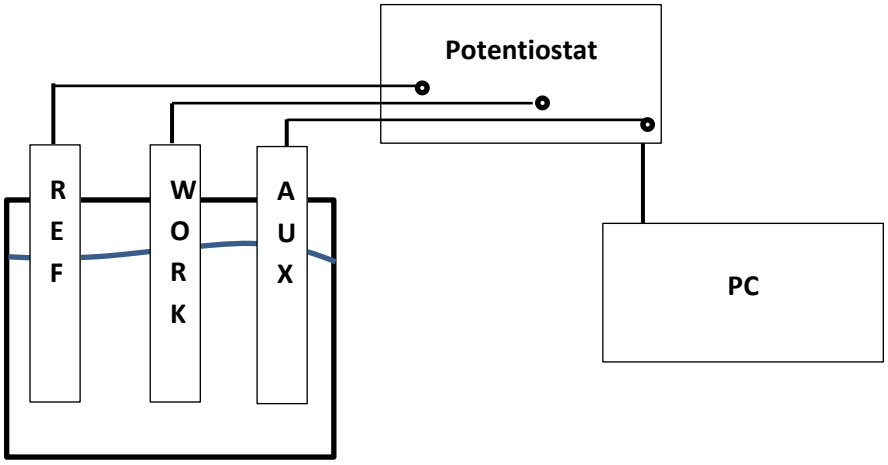

Figure 2.6: *Schematic diagram of a three electrode electrochemical cell: Ref – reference electrode, Work – working electrode, Aux – auxiliary electrode*

The procedure for polarisation involves shifting the potential of the working electrode in the anodic direction (i.e. to a more positive potential than E_{corr}) or in the cathodic direction (i.e. to a more negative potential than E_{corr}). The relationship between potential and current can then be plotted for both the anodic and cathodic reactions, as shown in Figure 2.7.

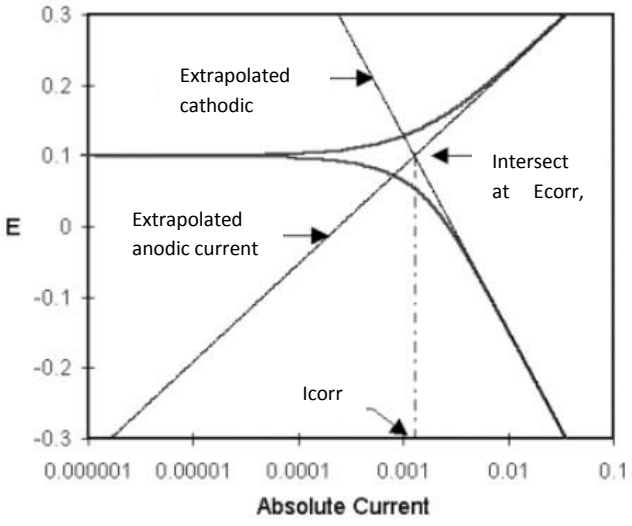

Figure 2.7: *Schematic diagram of determining i_{corr} by Tafel extrapolation method*

The anodic and cathodic curves are plotted on a potential (E) against current (log i) graph. The curves can then be extrapolated back to E_{corr} to find the current density, I_{corr}. The Tafel extrapolation method is commonly used to establish the corrosion rate of metals in freely

corroding conditions. When the potential is close to E_{corr}, activation polarisation occurs. This is due to a slow electrode reaction caused by the strong bonding forces of the atoms in the metal resulting in a resistance in charge transfer. As the difference between the applied potential and E_{corr} increases the magnitude of the current also increases (as indicated in Figure 2.7). Once the potential is significantly away from E_{corr} (typically greater than 50mV) the Tafel relationship (Eq. 2.10) is applicable.

$$E - E_{corr} = b_a \log\left(\frac{i_a}{i_{corr}}\right) \quad \text{Eq. 2.10}$$

b_a is known as the Tafel constant, i_a is the anodic current density and i_{corr} is the corrosion current density which represents the current density equivalent to the equal forward and reverse reactions under free corrosion conditions.

Another type of electrode polarisation is concentration polarisation. This phenomenon occurs as the electrode reaction rate is affected by either the supply rate of reactants or the removal rate of the electrode reaction. If the electrode is being anodically polarised, corrosion product forms on the surface of the electrode which can result in a limit at which the anodic reaction can occur. If the electrode is being cathodically polarised, the rate at which the oxygen reduction reaction occurs increases until it reaches a limit due the reduction in the amount of dissolved oxygen available for the reaction. Once these limiting current densities have been reached the polarisation tends towards infinity. In reality, this is not the case as another electrode reaction establishes itself at a more active potential.

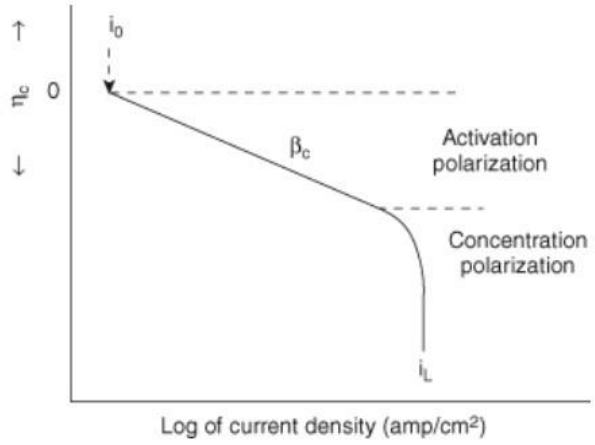

Figure 2.8: *Concentration polarisation slows down the cathodic reaction*

Figure 2.8 illustrates the initial activation polarisation regime with the decrease in potential, before concentration polarisation occurs, which results in a slowing down of the cathodic reaction rate.

2.4.3.2 Passivity

The definition of passivity is the ability of a metal to resist corrosion in a particular environment by restricting the electrolyte to the surface of the metal by way of a thin, adherent, non-conductive film. This film is typically an oxide such as aluminium oxide (Al_2O_3) or chromium oxide (Cr_2O_3). A metal can be defined as passive if it can substantially resist corrosion in a certain environment while under marked anodic polarisation (such as stainless steels) or if a metal resists corrosion in an environment even though it has a thermodynamic tendency to react (such as iron in inhibited pickling acid) [2.24].

Partial or complete breakdown of the passive film can be accomplished by many factors such as temperature, content of dissolved oxygen, film imperfections and mechanical removal (scratching, bending, stretching, impacting particles, etc.). The effectiveness of the passive film can be assessed through electrochemical monitoring techniques such as potentiodynamic polarisation scans. An anodic polarisation scan is typically conducted from E_{corr} to significantly more positive potentials until the passive film is broken down (Figure 2.9).

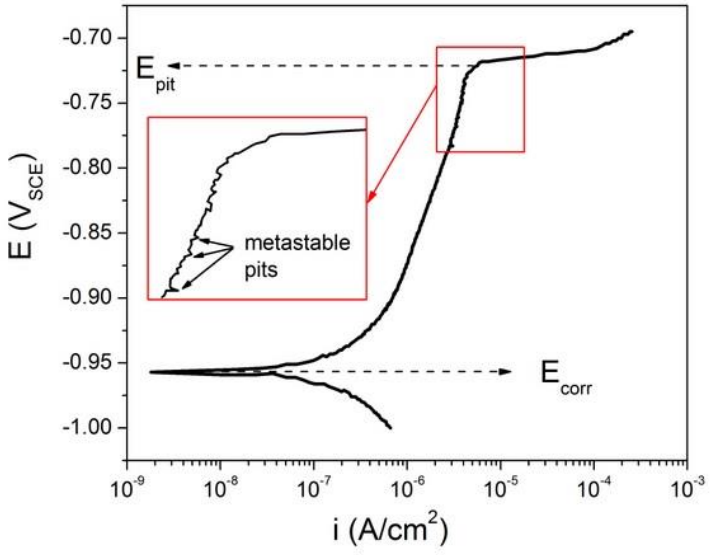

Figure 2.9: *Anodic polarisation scan demonstrating breakdown potential (E_{pit}) where a passive film has been partially or completely removed [2.25]*

This material would be deemed passive as the anodic current densities are extremely small even when the potential is significantly greater than E_{corr}. Once reaching the potential, E_{pit} or E_b, often referred to as the breakdown or pitting potential, the material begins to register high anodic currents. The breakdown of the passive film allows localised corrosion to occur on the surface of the material. To assess the extent of the localised corrosion damage, the scan can be continued until i_{max} is reached and the scan is reversed (as demonstrated in Figure 2.10).

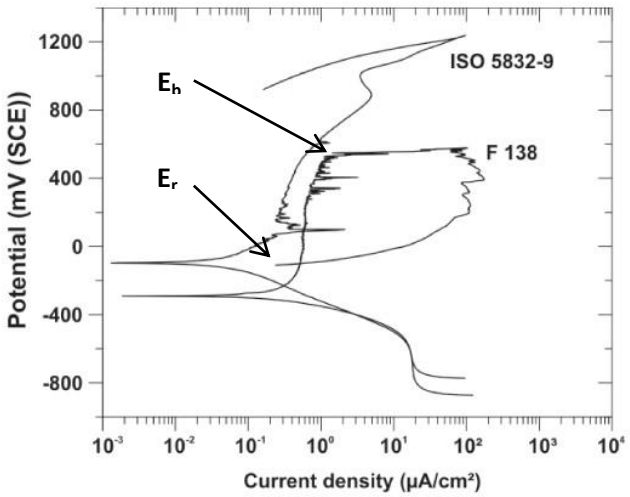

Figure 2.10: *Hysteresis loop produced by reversing the anodic polarisation scan. E_b – breakdown potential, E_r – repassivation potential [2.26]*

The difference between the E_r and E_{corr} or the area of the hysteresis loop are used to assess the likelihood of localised corrosion occurring. If the loop area is significantly small or negligible, then the material is less susceptible to localised corrosion.

2.4.3 Types of corrosion

2.4.3.1 Uniform Corrosion

As the name implies, uniform corrosion occurs evenly over the exposed metal surface. Essentially all metals are subjected to this type of corrosion under specified conditions. For example, the rusting of low alloy steels in atmospheric or aqueous conditions or the dissolution of stainless steels in acidic conditions. Generally for uniform corrosion, the initial corrosion rate is greater than that of subsequent rates. This type of corrosion is simpler to measure than localised corrosion and so life prediction of engineering components and structures can be more straightforward. Metals which have a corrosion

rate of less than 0.15mm/year are said to have good corrosion resistance, those between 0.15-1.5mm/year are deemed to have satisfactory corrosion resistance and those greater than 1.5mm/year are reckoned to have poor corrosion resistance [2.24].

2.4.3.2 Localised corrosion

Localised corrosion is more undesirable as it is more difficult to predict and so estimation of the life of engineering components and structures are typically more challenging. The various types of localised corrosion are discussed below.

2.4.3.2.1 Pitting corrosion

Pitting corrosion results in small "pits" which are characterised as small cavities or holes with small amounts of corrosion product formed over the cavity. The cavities are formed on the surface of the metal. There are three main causes of pitting:

- Localised corrosion or mechanical damage to the protective oxide film; such as water chemistry (acidic solutions, salinity or low concentrations of dissolved oxygen) which causes the passive film to breakdown or become less stable. Surface scratching or impacting particles can also breakdown the passive film.
- Localised damage or poor application of a coating
- Non-metallic inclusions and/or other non-uniformities present in the metal structure.

The mechanism for pitting in stainless steel is caused by anodic and cathodic sites forming on the exposed surface on ferrous metals. The anodic reaction is due to iron dissolution (Eq. 2.3), which supplies electrons to the nearby cathodic sites where they are discharged by the oxygen reduction reaction (Eq. 2.7). Iron ions released by the anodic reaction then react with hydroxyl ions to form corrosion product (Eq. 2.8) on the surface above the pit. Electrolyte enclosed in the pit becomes positively charged compared to the electrolyte out with the pit. The positively charged electrolyte tends to attract negatively charged chloride ions which increases the acidity of the electrolyte due to the following reaction

$$FeCl_2 + 2H_2O \rightarrow Fe(OH)_2 + 2HCl \qquad \text{Eq. 2.11}$$

The increase in acidity of the electrolyte within the pit enhances the corrosion (Eq. 2.11). Figure 2.11 illustrates the pitting corrosion mechanism in a stainless steel.

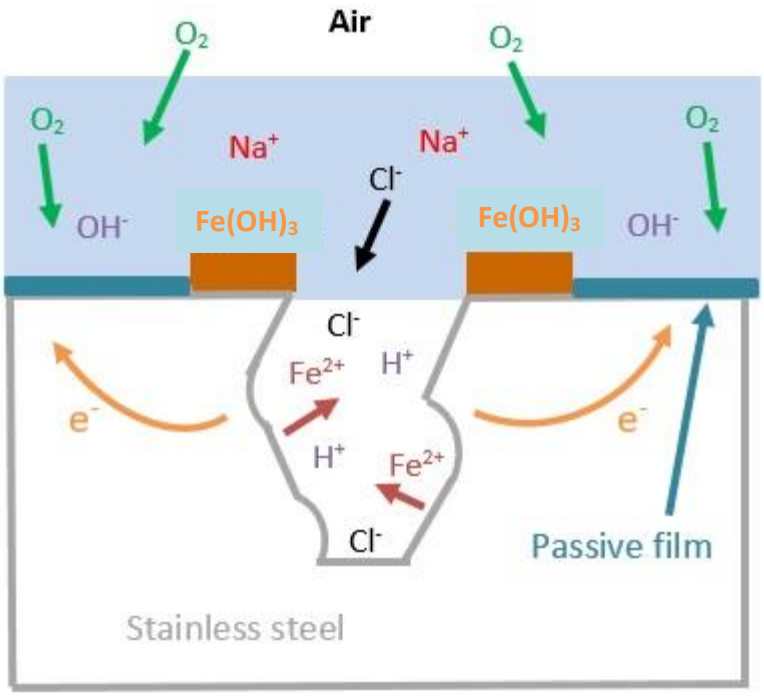

Figure 2.11: *Mechanism for corrosion pitting in stainless steels*

To aid material selection in seawater systems (such as offshore oil and gas production, power plants, desalination and petrochemical plants) the Pitting Resistance Equivalent Number (PREN) is used for austenitic and duplex stainless steels. These values are calculated from the chemical composition of the stainless steel and give an indication of the steels resistance to pitting and crevice corrosion. The PREN value can be estimated by the following empirical equation [2.27].

$$PREN = \%Cr + 3.3 * \%Mo + 16 * \%N \qquad \text{Eq. 2.12}$$

Chromium, molybdenum and nitrogen increase the pitting resistance of austenitic and duplex stainless steels. PREN values above 32 are considered to be corrosion resistant in seawater [2.24].

2.4.3.2.2 Crevice Corrosion

Crevice corrosion occurs when a stagnant or small quantity of electrolyte is shielded or confined between metallic surfaces while the remainder of the metallic surface is exposed to a large volume of electrolyte. Common applications where crevice corrosion occurs are washers, gaskets, fasteners, welded joints, rivets and seal interfaces between metal and

rubber. The initiation of crevice corrosion is instigated by environmental factors such as depletion of oxygen concentration, depletion of inhibitor, a local drop in pH to a more acidic solution and build-up of aggressive species such as chlorides.

Initially the oxygen content inside the crevice is similar to the content in the environment out with the crevice. However, as oxygen diffusion to the crevice is restricted, the oxygen content in the stagnant solution gradually diminishes by its consumption in the cathodic reaction (Eq. 2.7). Once the oxygen has been completely depleted, the cathodic reaction slows down and the generation of hydroxyl ions diminishes. The crevice now has an excessive amount of positive metal ions, which in turn attracts negative ions (such as chloride in saline solutions) to balance the anodic reaction. Inside the crevice, complex ions of metal chlorides and water molecules form, which undergo further hydrolysis to form corrosion product and generates hydrogen ions which reduces the pH in the crevice. Stainless steels which depend upon oxygen to form a stable passive oxide film are significantly affected by the depletion of oxygen. The oxide film becomes extremely unstable in the crevice and due to the increase of hydrogen and chloride ions within the crevice, the acceleration of metal dissolution drastically increase. Figure 2.12 illustrates the crevice corrosion mechanism for stainless steels.

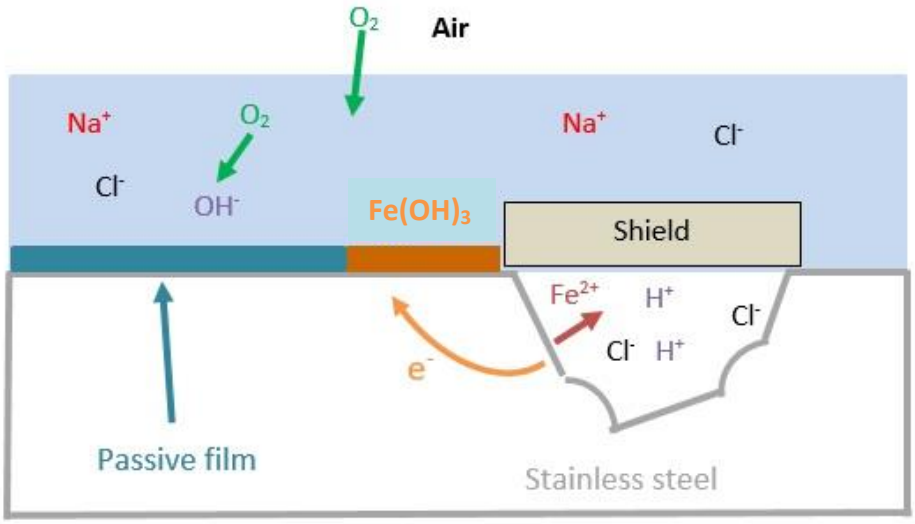

Figure 2.12: *Crevice corrosion mechanism for stainless steels*

2.4.3.2.3 Intergranular corrosion

Intergranular corrosion is a localised attack which occurs along or adjacent to the grain boundaries while the grains of the alloy are left mainly unaffected. Intergranular corrosion is typically associated with chemical segregation such as enriched impurities or specific phases that precipitate that have a tendency to form at grain boundaries.

When certain elements are segregated or if a compound is formed in the boundary, the preferential corrosion attack occurs on the grain boundary phase or on an adjacent region which has been depleted of an essential element which typically enhances corrosion resistance. This makes the grain boundary anodic relative to the grain. The corrosion typically follows a narrow path along the grain boundary. In severe circumstances, an entire grain may be dislodged due to the complete deterioration of the grain boundary.

For stainless steels, carbide precipitation occurs at the austenite grain boundaries as a result of sensitisation due to exposure at temperatures between 450-900°C. Corrosion occurs preferentially at the carbide-metal matrix interface due to the depletion of chromium in the solid solution near the grain boundaries. The depleted chromium zone becomes less noble than the carbide precipitates in the grain boundary and passive grains. Intergranular corrosion is also a prevalent issue with aluminium alloys [2.28, 2.29], which is mainly attributed to the interaction between intermetallic phases (located at grain boundaries) and the metallic matrix. Figure 2.13 illustrates the mechanism which occurs during intergranular corrosion.

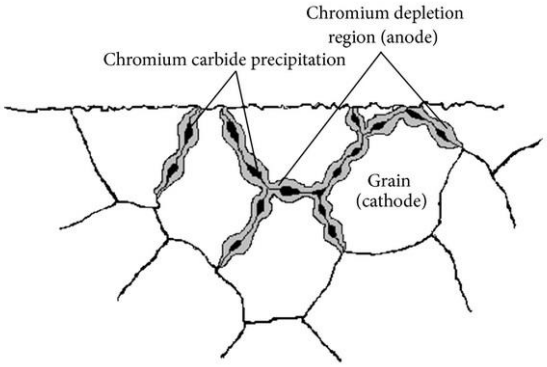

Figure 2.13: *Intergranular corrosion due to chromium depletion in the grain boundary as chromium carbide precipitates form. Grain boundary becomes an anode while the grain becomes a cathode [2.30]*

2.4.3.3 Bimetallic/galvanic corrosion

Galvanic (bimetallic) corrosion occurs when two dissimilar metals are coupled (via a welded joint, a bolt, electrical conductor, etc.) in a corrosive electrolyte. The galvanic effect occurs as one of the metals acts as the anode, while the other acts as a cathode. This occurs due to the potential difference between the two different metals.

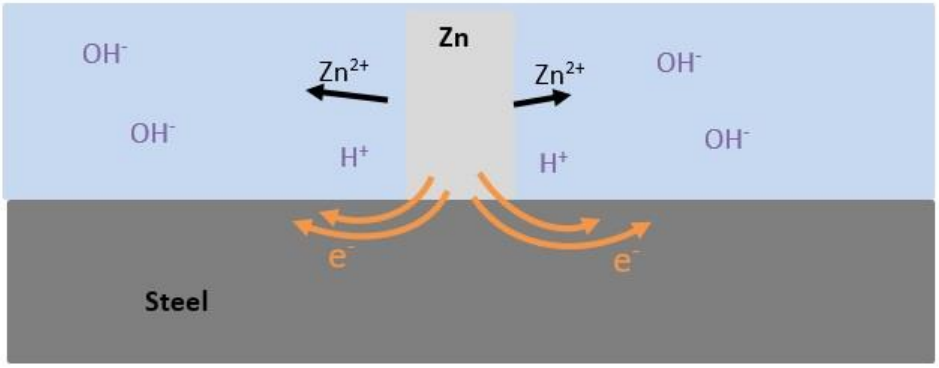

Figure 2.14: *A galvanic coupling of zinc and iron in a corrosive aqueous solution, where the zinc is the anode and steel is the cathode*

Figure 2.14 illustrates a galvanic couple between zinc and iron in an aqueous solution. The zinc is acting as the net anode while the steel acts as a net cathode. This type of galvanic couple is commonly used as a sacrificial anode cathodic protection (See Chapter 2.4.5.3) in engineering systems.

Another type of galvanic cell occurs when a material's surface experiences different hydrodynamic zones (i.e. one zone may be considerably more turbulent than another). In these regions, the material may have different free corrosion potentials (E_{corr}) which then results in a galvanic effect between the two different zones as one may be more electronegative than another (i.e. one zone in which anodic reactions are accelerated and another in which cathodic reactions are accelerated). This galvanic interaction between the two different zones could potentially lead to enhanced material removal. This has been observed during testing in this experimental study and will be discussed further in Chapter 7.5.2.

2.4.3.4 Flow-induced corrosion

In many engineering systems, the fluid which interacts with the surface of the component is often flowing. The term used to define this type of corrosion is flow-induced corrosion,

which predominately enhances the electrochemical reactions occurring at the surface of the exposed metal. There are three main causes which increase the corrosive effect of the fluid: replenishment of oxygen, replenishment of aggressive ions and removal of protective layers. Each of these causes will be discussed in turn.

For metals, which rely on oxygen to form a passive oxide film to protect them from corrosion (such as stainless steels), replenishment of oxygen is essential. However, the flow (dependant on velocity) may rupture the passive film and hence, expose the surface to the corrosive media. For active materials, the flow may continuously remove or prevent corrosion product forming on the surface. Hence, the exposed metal will be able to interact with the electrolyte with a constant supply of dissolved oxygen. Figure 2.15 illustrates a schematic diagram of the oxygen reduction reaction in both static and flowing conditions. The diagram indicates the increase in current from static to flowing conditions.

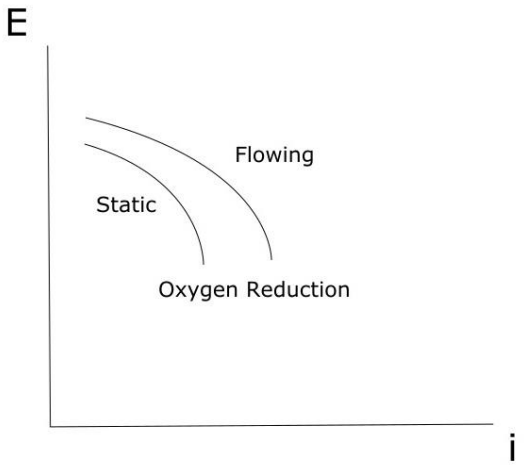

Figure 2.15: *Schematic representation of polarisation curves for oxygen reduction in static and flowing conditions*

Increases in corrosion rates in flowing conditions can also be attributed to the replenishment of aggressive ions such as chlorides, sulphides or hydrogen in acidic conditions. The protective oxide film will be removed if solid particles are introduced into the flow, as they will induce mechanical damage which will enhance the corrosion. This type of damage can occur through cavitation or impingement attack and is often referred to as erosion-corrosion.

2.4.4 Corrosion control, prevention and protection

Most metals will corrode naturally unless humans intervene and attempt to suppress or slow down the corrosion process. There are numerous methods which can be applied to control and prevent corrosion such as designing of engineering components and systems, material selection, controlling the corrosive environment, coating application and the application of electrochemical protection methods [2.31, 2.32]. Corrosion testing, monitoring, supervision and inspection are also essential in controlling corrosion.

2.4.4.1 Material selection

The role of material selection is a vital part in the design stages as a method of corrosion control. Although corrosion resistance in certain applications may be important, it is not the only parameter which may be considered. Other parameters include mechanical properties (such as fracture toughness, yield strength, tensile strength, elastic modulus, etc.), ease of manufacture, aesthetics, material availability and most importantly of all, overall cost.

A typical representation of relative material corrosion resistance in ambient temperature, low velocity, aerated seawater is illustrated in Figure 2.16. The line break between the copper and low alloy steel represents a large increase in corrosion rate.

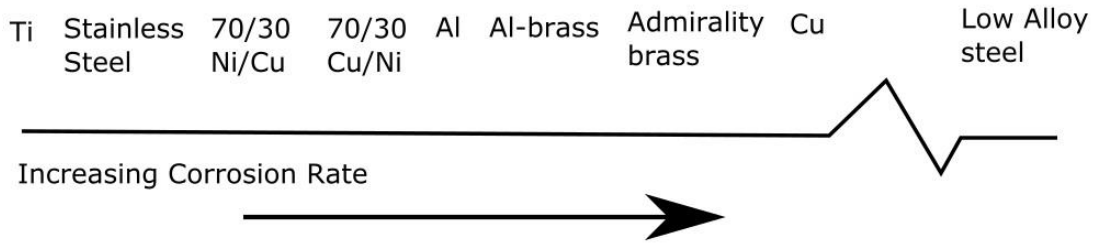

Figure 2.16: *Schematic diagram illustrating the relative corrosion resistance of metals in aerated, low velocity seawater in ambient temperatures*

The materials are categorised in two main groups: those with poor corrosion resistance in any aqueous environment, namely carbon, unalloyed and low alloy steels; and those with relatively superior corrosion resistance which form protective passive films. However, careful deliberation must be utilised when selecting materials for specific operating conditions as to avoid the onset of localised corrosion.

2.4.4.2 Coatings

Protective coatings have been used for centuries as a method of corrosion prevention for materials. Applied coatings to metals could offer a form of sacrificial protection, act as an inhibitor or crudely prevent the corrosive environment from contacting with the metal. Obviously for the latter to function, the coating must be impermeable to the corrosive environment, contain no cracks or defects to expose the metal and resistant to any mechanical damage. Table 2.1 demonstrates the most common types of coatings in four different categories.

Table 2.1: *Types of protective coatings and coating methods*

Metallic Coatings	Inorganic Coatings	Organic Coatings	Composite Coatings
Hot-dipping (e.g. galvanising) Cladding (welded or hot rolled) Electrodepositing Diffusion Thermal Spraying	Anodising Cement Phosphating Thermal Spraying	Conventional Paints (e.g. vinyl, acrylic) Epoxies Chloronated Rubber Polymer Linings Bitumen	Glass/ Flake Paint Sprayed Cermets

2.4.4.3 Cathodic Protection

The application of cathodic protection is one of the most important corrosion control methods. Cathodic protection is achieved by applying an electric current, which essentially reduces the corrosion rate of the metal to zero. There are two types of cathodic protection: Impressed Current Cathodic Protection (ICCP) or Sacrificial Anode Cathodic Protection (SACP) [2.24].

The external current supplied by either cathodic protection method, polarises the entire surface of the material which is being protected. Therefore, cathodic reactions become the more dominant reaction, while the anodic reaction is suppressed. Cathodic protection can be used to overcome both uniform and localised corrosion.

Impressed Current Cathodic Protection (ICCP) requires a DC source or an AC source with a rectifier along with an auxiliary electrode which can be either inert or expendable. Both the

metal component and the auxiliary electrode must be exposed to the electrolyte for the cathodic protection to function. Cathodic reactions occur at the surface of the component which is being protected, while the anodic reactions occur at the auxiliary electrode (which becomes the anode in the electrochemical cell). “Overprotection” of the component occurs if the applied electrode potential is significantly more negative than the required electrode potential for cathodic protection. This is of course wasteful of energy, but it can also lead to hydrogen embrittlement of some high strength alloys. The main advantage of ICCP is that it allows greater control over applying currents in the system.

Another option for applying cathodic protection, is using a metallic alloy which is more active than that of the metal alloy which is required to be protected, this produces a galvanic cell. Therefore, the current is supplied by the auxiliary electrode which is commonly called a sacrificial anode. Common materials used as sacrificial anodes are zinc-based alloys, aluminium-based alloys and magnesium-based alloys. The advantages of using sacrificial anodes are that there is no requirement for a power supply, hence, reducing the capital cost for power consumption and the sacrificial anodes are easier to install into the system. The main disadvantages of using sacrificial anodes are that they may need to be replaced periodically during scheduled maintenance and the galvanic current available is dependent upon the sacrificial anode area.

2.5 Fundamentals of Erosion

Erosion can be defined as the physical removal of material by way of mechanical processes. Dry erosion refers to material removal by solid particles in an airflow, whereas, aqueous erosion occurs when material is removed by an aqueous fluid with or without solid particles. In this section, ductile and brittle material erosion models are discussed as well as the key parameters which influence the erosion process.

2.5.1 Erosion mechanisms for ductile materials

There has been a vast amount of studies investigating the erosion mechanisms for ductile materials [2.33–2.39]. Although there has been much debate, the general acceptance is that there are three main types of mechanisms: ploughing, type 1 cutting and type 2 cutting (Figure 2.17) [2.34, 2.35, 2.38]. The shape denoted (a) in Figure 2.17 is defined as ploughing deformation caused by a spherical particle impacting at an angle of 30°. The formed lip represents only 10-25% of the total crater volume, the rest of the displaced material forms

less highly strained ridges around the sides of the crater. The shape denoted (b) in Figure 2.17 is termed Type 1 cutting. This is caused by a square particle impacting the surface at 30° with a rake angle (shown in Figure 2.18) of -35°. The rake angle is defined as the angle between the perpendicular to the target surface and the leading edge of the impacting particle. The material is displaced forward into a large lip at the particle exit. This lip is obviously vulnerable to subsequent impacting particles. The final shape denoted (c) is referred to as Type 2 cutting. At an impact angle of 30° and a rake angle between 0 and -17°, the particle rotates backwards which results in all the material being removed [2.38].

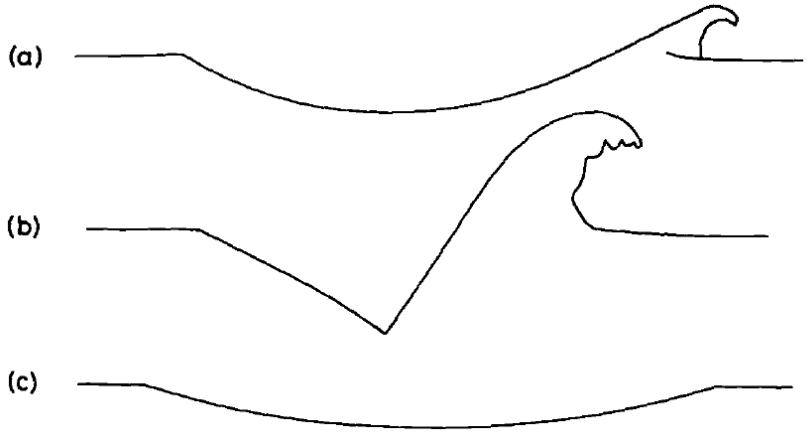

Figure 2.17: *Typical shapes of impact craters: (a) ploughing deformation of a sphere, (b) Type 1 cutting, (c) Type 2 cutting [2.38]*

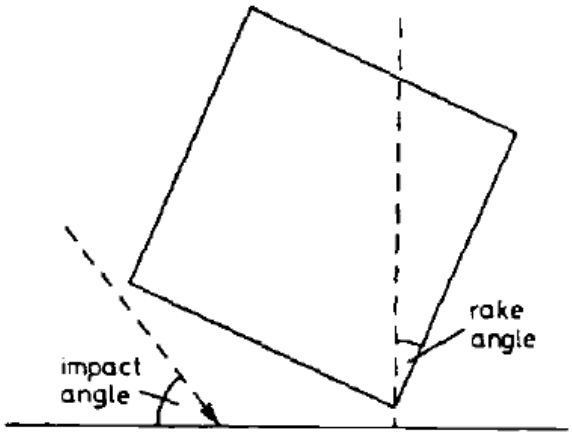

Figure 2.18: *Impact angle and rake angle definition [2.38]*

Hutchings [2.38] proposed that the variation in erosive behaviour due to the rake angle is the reason why previous erosion models proposed by Finnie [2.33] and Bitter [2.34, 2.35] struggled to accurately predict erosive damage of ductile materials at 90°.

Bellman Jr. and Levy proposed a slightly modified concept for the erosion mechanism of ductile materials [2.39]. Like Hutchings they also described three distinct types of craters: indentation, ploughing and smear (cutting). They postulated that the type of crater is irrespective of the impact angle and that the rotational component of the particle is the effective impingement angle. At low angles, smear craters are found as the velocity of particle is significantly greater than the rotational tendency of the particle. At intermediate impingement angles the ploughing crater (this is a combination of smearing and indentation) was found to be dominant. At high impingement angles, the indentation crater is dominant.

Continual impacting of the particles causes a roughening of the surface, this is attributed to plastic deformation caused by the large localised stresses in the area of the impacting particles. Metal platelets locally attached to the crater rim are forged-extruded. Some of the kinetic energy from the particles is converted into thermal energy, which heats the surface around the crater. This hot works the surface which results in a heated surface zone. This enhances the formation of the platelets. At a depth below the surface the metal temperature decreases and plastic deformation caused by the impacting particles causes work hardening.

Impact craters and platelets eventually cover the entire test surface. As the particles no longer have a fresh surface to impact, a steady increase in smear-type craters with platelets begin to form and erosion damage which is measureable commences. The particle easily penetrates through the softened layer, however, encounters resistance from the work hardened layer [2.39]. This enhances the formation of platelets as metal extrusion increases in the softened zone. The increase in platelets increases the erosion as they are easily removed by impacting particles. Once the development of the soft and hardened zones is completed, the erosion rate becomes a steady state mechanism of indentation, smearing platelet formation and extension and removal of platelets by several impact events.

2.5.2 Erosion mechanism for brittle materials

The erosion mechanisms for brittle materials are more widely accepted. Brittle materials are removed mainly as a result of crack formation and propagation. This was first proposed by Finnie who suggested that Hertzian stresses, which occur during solid particles impacting on the brittle material surface, would lead to cracking [2.33]. These cracks radiate from the point of impact in both lateral and radial directions. Cracking also occurs subsurface and these eventually join with surface cracks. Subsequent impacts of solid particles lead to material removal and also additional cracking [2.37]. A typical crater shape of a brittle material is shown in Figure 2.19.

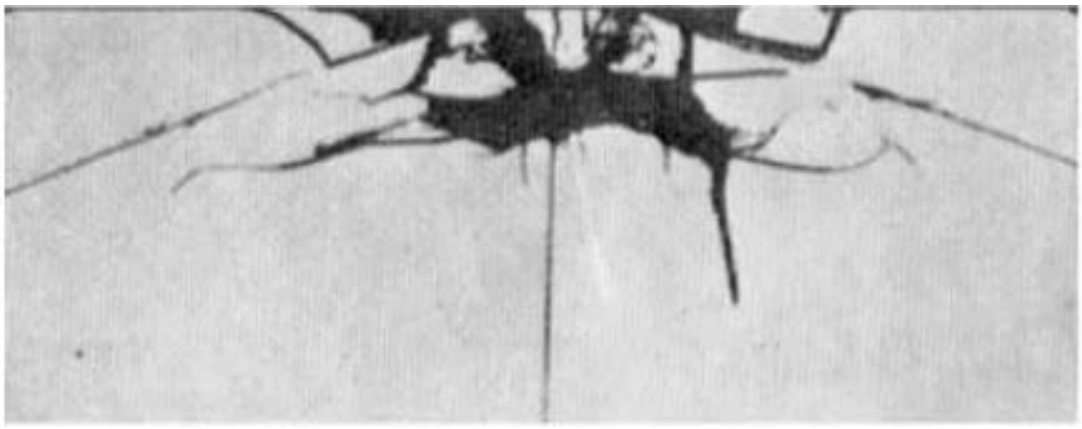

Figure 2.19: *Typical brittle material crater shape [2.40]*

2.5.3 Influential parameters of erosion

According to Hutchings [2.41] and Clark [2.42], there are three main groups of influential factors which contribute to erosion damage that can be categorised; flow parameters, particle properties and target material properties. The influential parameters of erosion are given in Table 2.2. Some of these parameters will be discussed in further detail in subsequent sections.

Table 2.2: *The three main groups of factors which influence erosion [2.41, 2.42]*

Flow parameters	Particle properties	Target material properties
Velocity	Size	Hardness
Impingement angle	Shape	Toughness
Viscosity	Hardness	Microstructure
Rebounding particles	Concentration	Work hardening effect

2.5.3.1 Effect of Velocity

Several studies have considered the effect of particle velocity on the erosion process [2.35, 2.38, 2.42–2.44]. They have all shown that the erosion of the material is linearly proportional to the velocity, as shown in Figure 2.20.

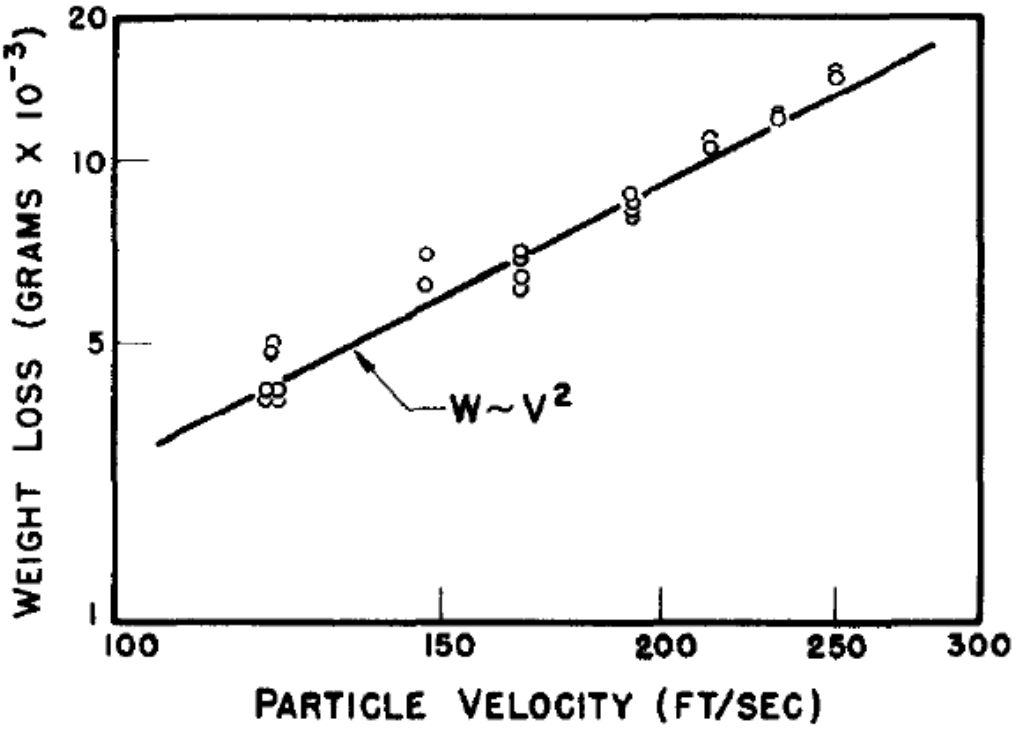

Figure 2.20: *Effect of particle velocity on erosion of a ductile material [2.33]*

The power exponent of the velocity term has been found to be between 2-2.5 depending on the test conditions and whether the material is ductile or brittle.

2.5.3.2 Effect of impingement angle

The influence of impingement angle has also been widely studied in the literature [2.35–2.38, 2.45–2.47]. The erosion phenomena for ductile and brittle materials at differing impingement angles can be seen in Figure 2.21. Ductile materials tend to have the greatest erosion at approximately 20° due to their susceptibility to the cutting action of abrasive particles, whereas, brittle materials have greatest erosion at high angles of impingement, although the highest rates of erosion of brittle materials are lower than those of ductile materials [2.46].

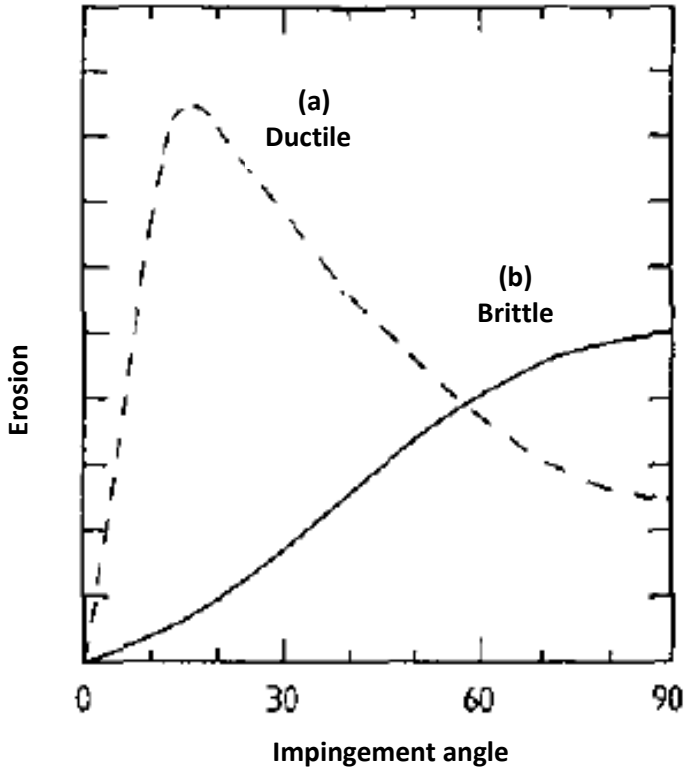

Figure 2.21: *Effect of impingement angle on erosion for ductile (dashed line) and brittle materials (solid line) [2.46]*

2.5.3.3 Effect of particle concentration

The erosion rate of materials is generally found to reduce as the sand concentration is increased. This is attributed to the turbulent flow conditions near the surface where particles are rebounding from the surface which help to protect the eroding surface. As the concentration increases, more particles will be rebounding from the surface which will increase the likelihood of collision between the solid particles. It has also been found that this screening effect is related with the angle of incidence of individual particles as they will deviate from the impacted surface [2.48, 2.49].

Frosell et al. also reported that the erosion rate reduced as slurry concentration increased, however, they also found that it was dependent on duration as the erosion rate was also linked with the erosion profile. The initial profile was “W” shaped before transitioning into a “U” shape at the minimum erosion rate. The profile remains “U” shaped for the remainder of the tests (Figure 2.22) [2.49].

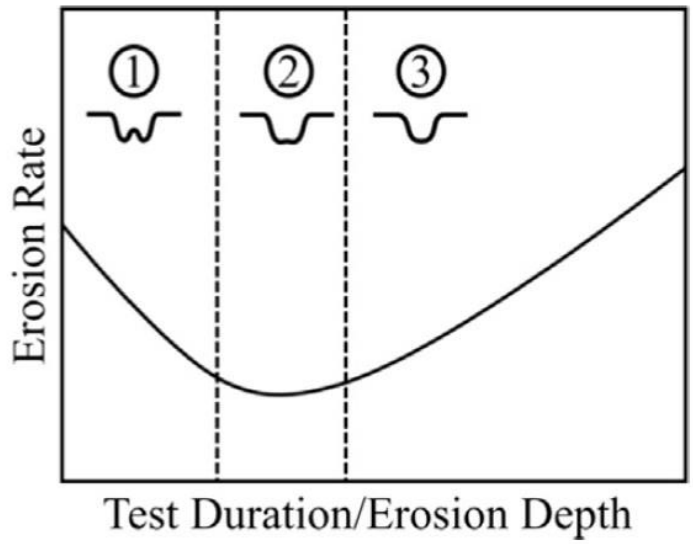

Figure 2.22: *Change in erosion rate with test duration and erosion depth [2.49]*

2.5.3.4 Effect of particle shape

Angular shaped particles have been found to cause greater erosion damage than spherical shaped particles. The explanation for these observations is that spherical particles will always impact the surface with negative rake angles; therefore, ploughing is the most likely mode of deformation. Whereas, an angular particle may impinge at a positive or negative rake angle, therefore, it is able to produce both micro-cutting and ploughing deformation. The micro-cutting mechanism leads to more material removal than the ploughing mechanism. This is the case as ploughing only displaces the material and cause it to form lips which are subsequently removed by particles, micro-cutting causes the material to be instantly removed [2.38, 2.50–2.52].

2.5.3.5 Effect of particle size

The effect of particle size on erosion rate is more complicated than the other parameters. Some researchers have found that increasing the particle size will result in increased erosion rates [2.51, 2.53]. Whereas, others have found that it depends on the type of particles which are being used as the erodent. Bahadur et al. reported that increasing the size of SiC and Al_2O_3 particles caused an initial increase in erosion rates before it became constant. However, increasing the particle size of SiO_2 particles was found to decrease the erosion rate [2.54].

The complex relationship between particle size and erosion rate was discussed by Clark et al. who found that although generally there was a decrease in erosion rate with decreasing particle size, a change in particle size produced a significant change in slurry flow conditions and particle motion [2.52].

The complex relationship between particle size and erosion rate was further evident in work conducted by Neville et al. [2.55] on high chromium cast irons. A change in particle size was found to alter the relative performance of the three white cast irons and austenitic stainless steel.

2.5.3.6 The relationship between the target material and particle properties

Many researchers have attempted to develop relationships between material properties (such as hardness, elastic modulus and microstructure) and abrasive particle properties to define the target material's erosion resistance.

A simple correlation between the hardness of the material and its erosion resistance has not been found in the literature. Under impingement slurry test conditions (3.5%NaCl, 17m/s, 90° impingement), Neville et al. found that a superaustenitic stainless steel, UNS S31254 (335HV), exhibited the poorest erosion-corrosion resistance than a Superduplex stainless steel (318HV) and another superaustenitic stainless steel, UNS S32654 (337HV) [2.56]. Similarly, Giourntas et al. did not find any correlation between material hardness and erosion resistance in impingement slurry conditions (3.5%NaCl, 24m/s, 90° impingement) [2.57]. A Superduplex, UNS S32760 (257HV), demonstrated a superior erosion resistance than a precipitation hardened martensitic stainless steel, UNS S17400 (358HV). Brownlie et al. also found no obvious linkage with target material hardness in 90° impingement slurry conditions (3.5%NaCl, 18m/s). An austenitic stainless steel, UNS S31600 (200HV), exhibited better erosion-corrosion resistance than a martensitic stainless steel, UNS S42000 (280HV and 480HV) and a Stellite 6 weld cladding, UNS R30006 (400HV) [2.58]. It should be noted that in these experimental conditions, material loss is also affected by corrosion effects.

However, there has been reasonable correlation found between abrasion resistance and material hardness. Llewellyn et al. utilised a Coriolis test to assess the abrasion resistance of a variety of high chromium cast irons [2.59]. There was a general trend of improved

abrasion resistance with increasing material hardness. A similar trend was found by Stevenson et al., who demonstrated, by a dry erosion jet with blast furnace sinter, that improved abrasion resistance is related to increased material hardness [2.60].

Another theory has suggested that the ratio of hardness (H) and elastic modulus (E) has a stronger linkage with wear (impact, erosion, abrasion, sliding) resistance. Matthews and Leyland proposed that this parameter was capable of defining the amount of deformation that could be absorbed elastically by a metal (i.e. the limit of deformation without material yield and, hence, resistance to wear) [2.61]. Further work by Cassac et al. found that a CrAlN coated Ti-6Al-4V sample had increased resistance to dry sliding wear compared to a nitrided Ti-6Al-4V alloy due its greater H^3/E^2 ratio. However, this parameter also appears to be inconsistent in predicting wear resistance as other studies by Leyland and Matthews [2.62] and Batista et al. [2.63] have found.

A more consistent relationship exists between the hardness of the target material and the hardness of the abrasive particle. Shipway and Hutchings first proposed this theory as a ratio between the hardness of brittle materials and abrasive particle hardness to model damage observed in an air blast erosion rig [2.64]. It was found that if the abrasive particle was harder than the target material, then an indentation-induced fracture mechanism occurred. However, when the particle was softer than the target material, then a less erosive chipping mechanism was induced. A similar correlation has also been found for ductile material. Desale et al. found that when the ductile material was softer than the abrasive particle then large craters were formed due to plastic deformation. Whereas, when the ductile material was harder than the abrasive particles, the particle penetration was smaller and small cracks were formed on the surface which lead to a smaller material loss [2.65].

2.6 Synergy

As described earlier in Chapter 2.2, synergy is not a separate degradation process but is actually a combined effect of corrosion and erosion deterioration mechanisms. In Eq. 2.2, the synergy term is a result of corrosion processes that enhances the mechanical damage.

An alternative method that has been used by investigators studying sliding wear (pin on disk) involves a mechanistic approach which distinguishes between two main degradation

contributions: corrosion occurring in sliding conditions and mechanical removal of material (mechanical wear) [2.66, 2.67]. For the mechanistic approach, the total wear volume loss (V_t) is equal to the sum of the metal loss due to electrochemical corrosion (V_{chem}) and the material loss due to mechanical wear (V_{mech}) as stated in Eq. 2.13.

$$V_t = V_{mech} + V_{chem} \quad \text{Eq. 2.13}$$

V_{chem} is the sum of the corrosion in the passive and de-passivated regions and is quantified by in-situ corrosion measurements. However, this approach is limited as the V_{mech} proportion of the wear cannot be determined experimentally, hence, the interactions between corrosion and mechanical wear are not considered. Due to this limitation, this mechanistic approach was not used in this study.

Another issue with quantifying synergy, is that it can only be calculated, it cannot be measured directly. In order to quantify the material damage associated with synergy, the overall material loss, pure mechanical and pure electrochemical damage must be measured. In order to measure the pure mechanical damage, three different test conditions have been used by researchers – distilled water [2.68–2.70], alkaline solution [2.71], cathodic protection [2.56, 2.72, 2.73]. Electrochemical techniques such as potentiodynamic polarisation [2.56, 2.72] and AC impedence [2.70, 2.74], are used to measure the in-situ corrosion rates of test materials. Experimental error in these test measurements inevitably leads to some uncertainty in the quantification of the synergy mechanism.

The synergy process is dependent upon the specific details of the erosion-corrosion system such as the material which is experiencing the erosion-corrosion phenomena. Work by Aminul Islam et al. found that an API X-70 pipeline steel suffered severely from synergy [2.75, 2.76]. The work hardened layer which had formed on the steel was removed by corrosion which exposed a stress free surface which was more vulnerable to mechanical damage, resulting in an increase of material loss.

Similarly, Wood et al. found that an austenitic stainless steel (UNS S31600) underwent a phase transformation (from austenite to martensite) as a result of work hardening effects by the sand particles. However, the work hardened surface was more vulnerable to

corrosion attack which in turn reduced the work hardening effect and, hence, increased the erosion-corrosion rate [2.68].

The influence of microstructure on synergy effects was also shown by Jones and Llewellyn [2.77]. Tests conducted in a slurry pot rig demonstrated that a hypereutectic high chromium white cast iron with a complex microstructure (duplex stainless steel matrix with distributed carbides) had significantly greater material loss due to synergy than a single phase austenitic stainless steel (UNS S31603). This is likely to be attributed to the corrosion occurring at the carbide-matrix interface in the white cast iron. However, the total material loss for the hypereutectic white cast iron was less than that of the austenitic stainless steel.

Synergy damage can also be a significant proportion of the overall erosion-corrosion damage for wear resistant materials and superalloys. Work by Neville and Hodgkiess [2.78] reported that the proportion of synergy damage of a Superduplex stainless steel (UNS S32760) was 12%. However, for Stellite 6 (UNS AMS5387) and Inconel 625 (UNS N00625) there was a significant proportional increase in synergy damage, 22% and 24% respectively. This further shows the influence of complex multiphase microstructure in altering the damage mechanisms proportionally.

2.7 Repetitive impact wear

Percussive (repetitive) impacting wear is described as repetitive solid body impacts, where the contacting surfaces are wearing [2.79]. There are two types of repeated impacts, when there is a tangential or rotational element which results in sliding or rolling then this is referred to as compound impact. When there is no rotational or tangential element then this is normal impact.

This is a major issue for valve and seats used in the positive displacement hydraulic fracturing pumps. The impact energy on the valve seat is created due to the closure of the valve body. As the valve body is abruptly stopped by the seat, the kinetic energy of the valve is instantaneously converted into impact energy. Therefore, the large kinetic energy of the valve leads to a quick deterioration rate of the valve and seat, hence, shortening the life of both the valve and seat.

During repetitive impact with sliding wear, different wear zones have been found occurring beneath the surface [2.80]. This is indicated in Figure 2.23.

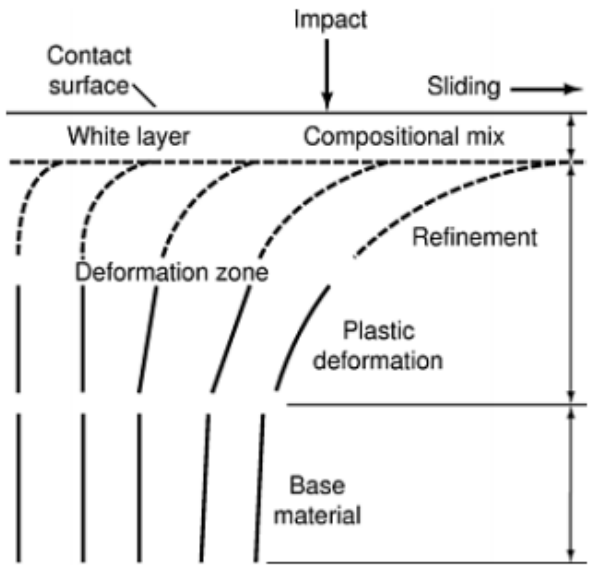

Figure 2.23: *Zones found beneath the surface of a material experiencing repetitive impacts and sliding wear [2.80]*

The subsurface zones are formed on both impacting bodies and occur rapidly within a few hundred impacts [2.81]. The white layer is formed due to adhesion, mechanical transfer of material and diffusion. It is a combination of material from both impacting bodies. This layer is extremely thin (a few micrometres) and could possibly be removed by abrasive wear. The region directly beneath the white layer is an intermediate deformation zone, which consists of plastically deformed base material. The severity of deformation ranges from zero (located at the interface between base material and intermediate zone) to a maximum which is located between the intermediate zone and the compound white layer. The base material is undisturbed as it is furthest from the impact contact area. These zones move closer to the surface as the coefficient of friction is increased. This is reported to be caused by a reduction of plastic strain in the subsurface in lubricated conditions [2.82]. The hardness of both the surface and subsurface (deformation zone) have been found to increase during repetitive impact tests as the material is being cold worked [2.83]. For brittle materials, the subsurface zones differ slightly (Figure 2.24). The white top layer is still present; however, the deformation zone does not form. This is attributed to brittle materials being more vulnerable to cracking and spalling.

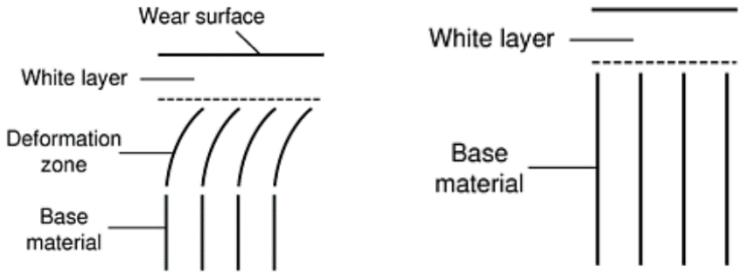

Figure 2.24: *Subsurface zones present in ductile (L) and brittle (R) materials under repetitive impact conditions [2.80]*

Material removal due to repetitive impact occurs by various forms of mechanisms depending on the size of impact energy [2.84]. The mechanisms are:

- Oxidative wear
- Adhesion
- Abrasion
- Surface fatigue
- Plastic deformation

The probability of these mechanisms is determined upon the stresses and sliding conditions which are occurring. During low stress conditions, it is possible for oxide films to stay intact and reduce the metal to metal contact wear as oxide films have a lubricating effect. This is the mildest wear regime. Adhesion and abrasion result in more severe wear regimes during impact. Adhesion is a result of material being transferred between the impacting bodies and abrasion occurs due to solid particles (such as sand) contacting with the surface. This typically leads to increasing surface roughness. Surface fatigue is more severe and leads to crack nucleation and delamination or spalling of the surface [2.85]. Fatigue and cracking is most likely to occur in the white compound layer. The impacting force will also lead to plastic deformation which increases with increasing impacting energy. The likelihood of each material loss mechanism with increasing impacting energy is indicated in Figure 2.25 [2.85].

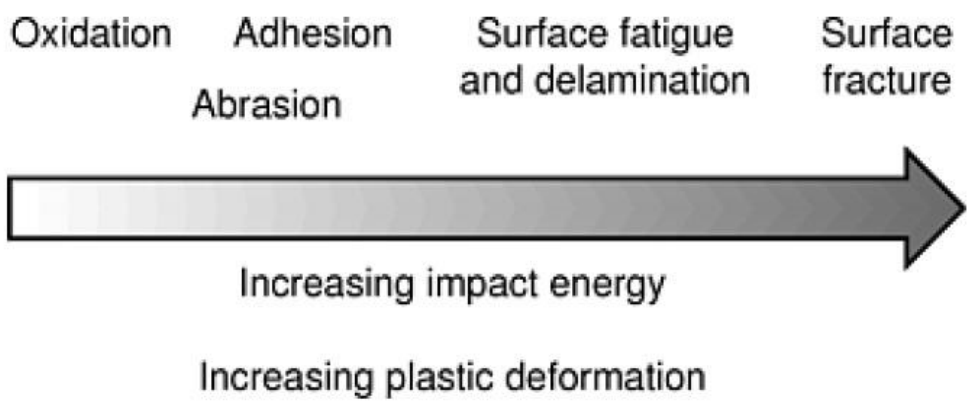

Figure 2.25: *Material loss mechanisms evolution with increasing impact energy [2.85]*

2.8 References

[2.1] C. T. Montgomery and M. B. Smith, “Hydraulic fracturing: History of an enduring technology,” *J. Pet. Technol.*, pp. 26–32, 2010.

[2.2] U.S. Department of Energy, “How is Shale Gas Produced?”, 2012.

[2.3] J. B. Curtis, “Fractured shale-gas systems,” *Am. Assoc. Pet. Geol. Bull.*, vol. 86, no. 11, pp. 1921–1938, 2002.

[2.4] G. E. King, “Hydraulic Fracturing 101: What Every Representative, Environmentalist, Regulator, Reporter, Investor, University Researcher, Neighbor and Engineer Should Know About Estimating Frac Risk and Improving Frac Performance in Unconventional Gas and Oil Wells. S,” in *Proceedings of the SPE Hydraulic Fracturing Technology Conference*, 2012.

[2.5] M. M. Molenaar, D. J. Hill, P. Webster, E. Fidan, and B. Birch, “First Downhole Application of Distributed Acoustic Sensing for Hydraulic-Fracturing Monitoring and Diagnostics,” *SPE Drill. Complet.*, vol. 27, no. 1, pp. 32–38, 2012.

[2.6] S. M. Rimassa, P. R. Howard, and K. A. Blow, “Optimizing Fracturing Fluids From Flowback Water,” in *SPE Tight Gas Completions Conference*, 2009.

[2.7] W. Al-Tailji, N. Northington, M. Conway, and B. Davidson, “Minimizing Over-Flush Volumes at the End of Fracture-Stimulation Stages - An Eagle Ford Case Study,” in *SPE Annual Technical Conference and Exhibition*, 2014.

[2.8] J. Wood, A. M. Galloway, T. Hodgkiess, B. Davies, A. Taheri, and G. Schnier, “The use of weld cladding in WeirSPM fracking pumps,” WARC internal report, 2012.

[2.9] K. B. Gregory, R. D. Vidic, and D. A. Dzombak, “Water management challenges associated with the production of shale gas by hydraulic Fracturing,” *Elements*, vol. 7, pp. 181–186, 2011.

[2.10] T. J. Gallegos, B. A. Varela, S. S. Haines, and M. A. Engle, “Hydraulic fracturing water use variability in the United States and potential environmental implications,” *Water Resour. Res.*, vol. 51, no. 7, pp. 5839–5845, 2015.

[2.11] W. Abdulrazzaq, B. Zoghbi, W. Suzart, and M. Salem, "Systematic Workflow for Characterizing Frac Sand : An Integrated Approach," in *GEO 2016, 12th Middle East Geosciences Conference and Exhibition*, 2016.

[2.12] ISO 13503: Petroleum and natural gas industries — Completion fluids and materials Part II: Measurement of properties of proppants used in hydraulic fracturing and gravel-packing operations, 2006.

[2.13] American Petroleum Institute, "API RP 19C.", 2014.

[2.14] C. Kelley, "Wet and Dry Frac Sand Processing," in *Frac sand insider*, 2013.

[2.15] W. C. Krumbein, "Measurement and geological significance of shape and roundness of sedimentary particles," *J. Sediment. Petrol.*, vol. 11, no. 2, pp. 64–72, 1941.

[2.16] A. Iannetti, M. T. Stickland, and W. M. Dempster, "A CFD Study on the Mechanisms Which Cause Cavitation in Positive Displacement Reciprocating Pumps," *J. Hydraul. Eng.*, vol. 1, pp. 47–59, 2015.

[2.17] Private communication with Jacob Bayyouk, Senior Engineering Technical Steward, Weir Oil & Gas, Fort Worth, Texas, USA, 2015.

[2.18] R. J. K. Wood, "Erosion-corrosion interactions and their effect on marine and offshore materials," *Wear*, vol. 261, no. 9, pp. 1012–1023, 2006.

[2.19] S. Zhou, M. M. Stack, and R. C. Newman, "Electrochemical studies of anodic dissolution of mild steel in a carbonate-bicarbonate buffer under erosion-corrosion conditions," *Corros. Sci.*, vol. 38, no. 7, pp. 1071–1084, 1996.

[2.20] M. M. Stack, H. W. Wang, and W. D. Münz, "Some thoughts on the construction of erosion-corrosion maps for PVD coated steels in aqueous environments," *Surf. Coatings Technol.*, vol. 113, no. 1–2, pp. 52–62, 1999.

[2.21] F. P. Ijsseling, "General guidelines for corrosion testing of materials for marine application," *Br. Corros. J.*, vol. 24, no. 1, pp. 55–78, 1989.

[2.22] N. Perez, "Mixed Potential Theory," in *Electrochemistry and Corrosion Science*, Springer US, pp. 155-166, 2004.

[2.23] L. Yang, *Techniques for monitoring corrosion*. Woodhead Publishing Limited, 2008.

[2.24] R. W. Revie and H. H. Uhlig, *Corrosion and Corrosion Control: An Introduction to Corrosion Science and Engineering, Fourth Edition*. Wiley, 2008.

[2.25] N. L. Sukiman, X. Zhou, N. Birbilis, A. E. Hughes, J. M. C. Mol, S. J. Garcia, and G. E. Thompson, "Durability and Corrosion of Aluminium and Its Alloys: Overview, Property Space, Techniques and Developments," in *Aluminium Alloys - New Trends in Fabrication and Applications*, 2012.

[2.26] E. J. Giordano, N. Alonso-Falleiros, I. Ferreria, and O. Balancin, "Electrochemical behavior of two austenitic stainless steel biomaterials," *REM R. Esc. Minas*, vol. 63, no. 1, pp. 159–166, 2010.

[2.27] E. Alfonsson and R. Qvarfort, "Investigation of the Applicability of some Pre Expressions for Austenitic Stainless Steels," *Mater. Sci. Forum*, vol. 111–112, pp. 483–492, 1992.

[2.28] W. Tian, S. Li, X. Chen, J. Liu, and M. Yu, "Intergranular corrosion of spark plasma sintering assembled bimodal grain sized AA7075 aluminum alloys," *Corros. Sci.*, vol. 107, pp. 211–224, 2016.

[2.29] T. Ramogopal, P. . Gouma, and G. S. Frankel, "Role of Grain-Boundary Precipitates and Solute-Depleted Zone on the Intergranular Corrosion of Aluminum Alloy 7150," *Corrosion*, vol. 58, no. 8, pp. 687–697, 2002.

[2.30] A. Almubarak, W. Abuhaimed, and A. Almazrouee, "Corrosion Behavior of the Stressed Sensitized Austenitic Stainless Steels of High Nitrogen Content in Seawater," *Int. J. Electrochem.*, pp. 1–7, 2013.

[2.31] M. Matsumura, *Erosion-Corrosion: An Introduction to Flow Induced Macro-Cell Corrosion*. Bentham Science Publishers, 2012.

[2.32] S. Papavinasam, "Electrochemical polarisation techniques for corrosion monitoring," in *Techniques for corrosion monitoring*, pp.49-85, 2008.

[2.33] I. Finnie, "Erosion of surfaces by solid particles," *Wear*, vol. 3, pp. 87–103, 1960.

[2.34] J. G. A. Bitter, "A Study of Erosion Phenomena: Part 1," *Wear*, vol. 6, pp. 5–21, 1963.

[2.35] J. G. A. Bitter, "A Study of Erosion Phenomena: Part 2," *Wear*, vol. 6, pp. 169–190, 1963.

[2.36] I. Finnie, "Some observations on the erosion of ductile materials," *Wear*, vol. 19, no. 1, pp. 81–90, 1972.

[2.37] G. P. Tilly and W. Sage, "The Interaction of Particle and Material Behaviour in Erosion Processes," *Wear*, vol. 16, pp. 447–465, 1970.

[2.38] I. M. Hutchings, "Mechanisms of the Erosion of Metals by Solid Particles," *Eros. Prev. Useful Appl. ASTM STP 664*, W. F. Adler, Ed., American Society for Testing Materials, pp. 59-76, 1979.

[2.39] R. Bellman and A. Levy, "Erosion mechanism in ductile metals," *Wear*, vol. 70, no. 1, pp. 1–27, 1981.

[2.40] D. Aquaro and E. Fontani, "Erosion of Ductile and Brittle Materials," *Meccanica*, vol. 36, pp. 651–661, 2001.

[2.41] I. M. Hutchings, "Wear by Particulates," *Chem. Eng. Sci.*, vol. 42, no. 4, pp. 869–878, 1987.

[2.42] H. M. Clark, "Particle velocity and size effects in laboratory slurry erosion measurements OR… do you know what your particles are doing?," *Tribol. Int.*, no. 35, pp. 617–624, 2002.

[2.43] G. L. Sheldon and A. Kanhere, "An Investigation of Impingement Erosion Using Single Particles," *Wear*, vol. 21, pp. 195–209, 1972.

[2.44] Y. I. Oka, M. Nishimura, K. Nagahashi, and M. Matsumura, "Control and evaluation of particle impact conditions in a sand erosion test facility," *Wear*, vol. 250, pp. 736–743, 2001.

[2.45] Y. I. Oka, H. Ohnogi, T. Hosokawa, and M. Matsumura, "The impact angle dependence of erosion damage caused by solid particle impact," *Wear*, vol. 203–

204, pp. 573–579, 1997.

[2.46] I. M. Hutchings, "Ductile-brittle transitions and wear maps for the erosion and abrasion of brittle materials," *J. Phys. D. Appl. Phys.*, vol. 212, pp. A212–A221, 1991.

[2.47] S. Turenne, M. Fiset, and J. Masounave, "The effect of sand concentration on the erosion of materials by a slurry jet," *Wear*, vol. 133, no. 1, pp. 95–106, 1989.

[2.48] T. Deng, A. R. Chaudhry, M. Patel, I. Hutchings, and M. S. A. Bradley, "Effect of particle concentration on erosion rate of mild steel bends in a pneumatic conveyor," *Wear*, vol. 258, no. 1–4, pp. 480–487, 2005.

[2.49] T. Frosell, M. Fripp, and E. Gutmark, "Investigation of slurry concentration effects on solid particle erosion rate for an impinging jet," *Wear*, vol. 342–343, pp. 33–43, 2015.

[2.50] A. V Levy and P. Chik, "The effects of erodent composition and shape on the erosion of steel," *Wear*, vol. 89, pp. 151–162, 1983.

[2.51] R. S. Lynn, K. K. Wong, and H. M. Clark, "On the particle size effect in slurry erosion," *Wear*, vol. 149, no. 1–2, pp. 55–71, 1991.

[2.52] H. M. Clark and R. B. Hartwich, "A re-examination of the 'particle size effect' in slurry erosion," *Wear*, vol. 248, no. 1–2, pp. 147–161, 2001.

[2.53] R. Brown, S. Kosco, and E. J. Jun, "The effect of particle shape and size on erosion of aluminium alloy 1100 at 90° impact angles," *Wear*, vol. 88, pp. 181–193, 1983.

[2.54] S. Bahadur and R. Badruddin, "Erodent particle characterization and the effect of particle size and shape on erosion," *Wear*, vol. 138, pp. 189–208, 1990.

[2.55] A. Neville and F. Reza, "Erosion-corrosion of cast white irons for application in the oilsands industry," in *Nace International Corrosion 2007 conference & expo*, 2007.

[2.56] A. Neville and X. Hu, "Mechanical and electrochemical interactions during liquid–solid impingement on high-alloy stainless steels," *Wear*, vol. 251, pp. 1284–1294, 2001.

[2.57] L. Giourntas, T. Hodgkiess, and A. M. Galloway, "Comparative study of erosion–corrosion performance on a range of stainless steels," *Wear*, vol. 332–333, pp. 1051–1058, 2015.

[2.58] F. Brownlie, T. Hodgkiess, A. Pearson, and A. M. Galloway, "Corrosive wear behaviour of various stainless steel alloys and stellite 6 weld cladding," in *The 17th Nordic Symposium on Tribology*, 2016.

[2.59] R. J. Llewellyn, S. K. Yick, and K. F. Dolman, "Scouring erosion resistance of metallic materials used in slurry pump service," *Wear*, vol. 256, no. 6, pp. 592–599, 2004.

[2.60] A. N. J. Stevenson and I. M. Hutchings, "Wear of Hardfacing While Cast Irons By Solid Particle Erosion," *Wear*, vol. 186, no. 1, pp. 150–158, 1995.

[2.61] A. Matthews and A. Leyland, "Materials Related Aspects of Nanostructured Tribological Coatings," in *51st. SVC TechCon*, 2008.

[2.62] A. Leyland and A. Matthews, "On the significance of the H/E ratio in wear control: A nanocomposite coating approach to optimised tribological behaviour," *Wear*, vol. 246, no. 1–2, pp. 1–11, 2000.

[2.63] J. C. A. Batista, C. Godoy, G. Pintaúde, A. Sinatora, and A. Matthews, "An approach to elucidate the different response of PVD coatings in different tribological tests," *Surf. Coatings Technol.*, vol. 174–175, pp. 891–898, 2003.

[2.64] P. H. Shipway and I. M. Hutchings, "The role of particle properties in the erosion of brittle materials," *Wear*, vol. 193, no. 1, pp. 105–113, 1996.

[2.65] G. R. Desale, B. K. Gandhi, and S. C. Jain, "Slurry erosion of ductile materials under normal impact condition," *Wear*, vol. 264, no. 3–4, pp. 322–330, 2008.

[2.66] A. Igual Munoz and N. Espallargas, "Tribocorrosion mechanisms in sliding contacts ," in *Tribocorrosion of Passive Metals and Coatings*, pp. 115-152, 2011.

[2.67] S. Mischler, E. A. Rosset, and D. Landolt, "Effect of Corrosion on the Wear Behavior of Passivating Metals in Aqueous Solutions," *Tribol. Ser.*, vol. 25, pp. 245–253, 1993.

[2.68] R. J. K. Wood, J. C. Walker, T. J. Harvey, S. Wang, and S. S. Rajahram, "Influence of

microstructure on the erosion and erosion-corrosion characteristics of 316 stainless steel," *Wear*, vol. 306, no. 1–2, pp. 254–262, 2013.

[2.69] J. Basumatary and R. J. K. Wood, "Synergistic effects of cavitation erosion and corrosion for nickel aluminium bronze with oxide film in 3.5% NaCl solution," *Wear*, vol. 376–377, pp. 1286–1297, 2017.

[2.70] J. Basumatary and R. J. K. Wood, "Different methods of measuring synergy between cavitation erosion and corrosion for nickel aluminium bronze in 3.5% NaCl solution," *Tribol. Int.*, pp. 1–12, 2017.

[2.71] S. S. Rajahram, T. J. Harvey, and R. J. K. Wood, "Erosion–corrosion resistance of engineering materials in various test conditions," *Wear*, vol. 267, no. 1–4, pp. 244–254, 2009.

[2.72] L. Giourntas, T. Hodgkiess, and A. M. Galloway, "Enhanced approach of assessing the corrosive wear of engineering materials under impingement," *Wear*, vol. 338–339, pp. 155–163, 2015.

[2.73] R. C. Barik, J. A. Wharton, R. J. K. Wood, K. S. Tan, and K. R. Stokes, "Erosion and erosion – corrosion performance of cast and thermally sprayed nickel – aluminium bronze," *Wear*, vol. 259, pp. 230–242, 2005.

[2.74] A. Neville and C. Wang, "Erosion-corrosion of engineering steels-Can it be managed by use of chemicals?," *Wear*, vol. 267, no. 11, pp. 2018–2026, 2009.

[2.75] M. Aminul Islam, Z. N. Farhat, E. M. Ahmed, and A. M. Alfantazi, "Erosion enhanced corrosion and corrosion enhanced erosion of API X-70 pipeline steel," *Wear*, vol. 302, no. 1–2, pp. 1592–1601, 2013.

[2.76] M. Aminul Islam and Z. N. Farhat, "The synergistic effect between erosion and corrosion of API pipeline in CO2 and saline medium," *Tribol. Int.*, vol. 68, pp. 26–34, 2013.

[2.77] M. Jones and R. J. Llewellyn, "Erosion-corrosion assessment of materials for use in the resources industry," *Wear*, vol. 267, no. 11, pp. 2003–2009, 2009.

[2.78] A. Neville and T. Hodgkiess, "Characterisation of high-grade alloy behaviour in severe erosion-corrosion conditions," *Wear*, vol. 233–235, pp. 596–607, 1999.

[2.79] P. A. Engel, "Percussive impact wear: A study of repetitively impacting solid components in engineering," *Tribol. Int.*, vol. 11, pp. 169–176, 1978.

[2.80] S. L. Rice, H. Nowotny, and S. F. Wayne, "Characteristics of metallic subsurface zones in sliding and impact wear," *Wear*, vol. 74, pp. 131–142, 1982.

[2.81] S. L. Rice, H. Nowotny, and S. L. Wayne, "Formation of Subsurface Zones in Impact Wear," *ASLE Trans.*, vol. 24, pp. 264–268, 1981.

[2.82] P. L. Menezes and S. V. Kailas, "Subsurface deformation and the role of surface texture — A study with Cu pins and steel plates," *Sadhana*, vol. 33, pp. 191–201, 2008.

[2.83] S. L. Rice, "The role of microstructure in the impact wear of two aluminum alloys," *Wear*, vol. 54, no. 2, pp. 291–301, 1979.

[2.84] P. A. Engel, *Impact Wear of Materials*. Amsterdam: Elsevier, 1976.

[2.85] R. Lewis and R. Dwyer-joyce, "Impact Wear Failures," *ASM Handb. Faliure Anal. Prev.*, vol. 11, pp. 965–974, 2002.

Chapter 3

Methodology

3.1 Introduction

This chapter will discuss the materials investigated and the experimental methods used during this study. The chapter has been divided into three main sections; pre-test methodology, erosion-corrosion and repetitive impact testing procedures as well as post-test analysis techniques.

3.2 Pre-test methodology

3.2.1 Test material sources

A variety of materials were assessed during the course of this study. Some of the selected materials were chosen specifically by the industrial sponsors due to their mechanical properties (yield strength, etc.) while other materials were chosen by the author for better appreciation of fundamental wear mechanisms. Table 3.1 is a list of materials and the corresponding chapters in which their test results are presented.

Table 3.1: *List of tested materials and their corresponding chapters*

Material	Corresponding chapter(s)
Stainless steel - UNS S31600 (rolled bar)	Chapters 4,5,6,7
Low alloy steel - UNS G43400 (rolled bar)	Chapter 4
Stainless steel - UNS S15500 (forged)	Chapter 4,7
Stainless steel - UNS S32760 (rolled bar)	Chapters 4 & 5
Sacrificial anode zinc alloy (rolled bar)	Chapter 4
Carburised UNS G86200 (rolled bar)	Chapter 5
Induction hardened UNS G52986 (rolled bar)	Chapter 5
Quench & Tempered UNS G52986 (rolled bar)	Chapter 5
Induction hardened UNS G41400 (rolled bar)	Chapter 5
Nitrided 905M39 steel (rolled bar)	Chapter 5
Stainless steel - UNS S42000 (rolled bar)	Chapter 5
HVOF WC-10Ni (commercially sprayed)	Chapter 5
Stainless steel - UNS S44003 (rolled bar)	Chapter 5
Stainless steel - UNS S44004 (rolled bar)	Chapter 5
27%Cr cast iron (cast engineering component)	Chapter 5
37%Cr cast iron (cast engineering component)	Chapter 5

Stellite 6 (UNS R30006) weld claddings (HWTIG process)	Chapter 6
Nitrided Stellite 6 (UNS R30006) weld claddings (HWTIG process)	Chapter 6
Titanium 6Al-4V alloy - UNS R56400 (rolled bar & additive manufactured)	Chapter 7
Inconel 718 alloy - UNS N07718 (rolled bar & additive manufactured)	Chapter 7
Stainless steel - UNS S31600 (additive manufactured)	Chapter 7
Stainless steel - UNS S15500 (additive manufactured)	Chapter 7

Most of the test materials were in the form of commercially available rolled bars which were sectioned into 17mm thick cylindrical samples with a diameter of 38mm. The UNS G86200, UNS G41400 and UNS G52986 test samples were then heat treated by commercial vendors with the following heat treatment procedures shown in Table 3.2. The 905M39 steel was gas nitrided in a furnace with ammonia gas at 520°C for 72 hours.

Table 3.2: *Heat treatment processes for the surface engineered steels*

Material	Heat treatment process
Carburised UNS G86200	1. 930°C at 1%C content for 24 hours 2. 850°C at 0.8%C content for 1 hour 3. Oil quenched 4. Tempered at 165°C for 2 hours
UNS G41400 induction hardened	1. 850°C for 15 seconds 2. Water quenched 3. Tempered at 180°C for 2 hours
UNS G52986 induction hardened	1. 870°C for 25 seconds 2. Water quenched 3. Tempered at 160°C for 4 hours
UNS G52986 quenched and tempered	1. 870°C for 2 hours 2. Oil quenched 3. Tempered at 160°C for 4 hours

A forged block of UNS S15500 was used as the source for test material. A Maxiem abrasive waterjet 1515 cutting machine was used to produce 38mm diameter cylindrical bars which were then sectioned to 17mm thick test samples. The white cast irons (27%Cr and 37%Cr) specimens were also machined by an electro-discharge machine (EDM) from an industrial quality frame plate liner insert. The final dimensions of the samples were 38mm diameter with a thickness of 17mm.

The Stellite 6 (UNS R30006) weld claddings were produced using a Hot Wire Tungsten Inert Gas (HWTIG) welding technique. The substrate used for the welding technique was a plate of UNS G43400 low alloy steel. A single layer (1.4mm depth) and a double layer (3.1mm depth) of the HWTIG Stellite 6 weld cladding were manufactured for comparison purposes. Following cladding, the test samples were manufactured by EDM (38mm diameter, 17mm thick) from the HWTIG Stellite 6 weld cladded plates. 10 samples of both single and double layer Stellite 6 weld claddings received the same nitriding heat treatment as the 905M39 steel in order to achieve a surface hardened layer.

The HVOF WC-10Ni cermet coating was sprayed onto cylindrical samples of UNS S31600 substrate. The spray coatings were deposited by an external supplier in accordance with appropriate industrial standards.

The additive manufactured (AM) test samples (UNS S31600, UNS S15500, UNS R56400 and UNS N07718) were produced by the powder bed fusion process (PBF). Each of the additive manufactured samples was required to be heat treated after the PBF process. The heat treatments for each of the materials are shown in Table 3.3.

Table 3.3: *Heat treatments of the additive manufactured materials*

Material	Heat treatment
UNS S31600	870°C for 60 minutes followed by a fast cool below 70°C
UNS S15500	545°C for 240 minutes followed by a fast cool below 70°C
UNS R56400	800°C for 240 minutes followed by a fast cool below 70°C
UNS N07718	980°C for 60 minutes followed by a fast cool below 70°C

3.2.2 Test samples surface preparation

The samples were surface prepared prior to testing in order to remove any scratches or other defects which may have occurred during the sample machining process. This also ensured that each test sample had the same surface finish before testing. The surface preparation procedure involved a grinding process with 500, 800 and 1200 SiC grit papers which produced a surface finish of 0.07µm Ra. The samples which were heat treated (carburising, nitriding, induction hardening and quench and tempering) were tested as-received (0.1-0.2µm Ra) in order to assess their industrially relevant surface finishes.

3.2.3 Preparation for metallurgical examination

The microstructure of each test material was examined by using standard metallurgical examination techniques. The first step in the process was to mechanically section the samples by a Struers Discotom-2 abrasive cutting machine. The samples were then hot mounted in Bakelite by a Struers PromtoPress-10 mounting machine and finally the samples were ground to 1200 grit paper and then polished on a Struers Rotopol-21 to 1µm diamond paste. After polishing, the samples were etched with an appropriate etching agent (Table 3.4) to highlight their microstructure before examination under an Olympus GX-51 light optical microscope.

Table 3.4: *Etching agents used for the materials*

Material	Etching agent
UNS G43400, carburised UNS G86200, UNS G52986 (Induction hardening and quench & tempered), UNS G41400, nitrided 905M39	2% Nital
UNS S31600 (rolled bar and AM), UNS S15500 (rolled bar and AM), UNS S37260, 37% cast iron	10% oxalic acid (Electrolytic 1V DC)
UNS S42000, UNS S44003, UNS S44004, 27%Cr cast iron	Kalling's reagent
UNS R30006 (weld cladding and lost wax cast)	Murakami's reagent
UNS R56400 (rolled bar and AM), UNS N07718 (rolled bar and AM)	Keller's reagent

3.2.4 Material characterisation

3.2.4.1 Energy-dispersive X-ray Spectroscopy (EDS)

A high resolution Hitachi S-3700 Scanning Electron Microscope (SEM) with an accelerating voltage of 20kV was utilised for pre-test and post-test microstructure images as well as Energy-dispersive X-ray Spectroscopy (EDS) analysis. The EDS enabled a semi-quantitative comparison of the chemical composition for the AM materials with their rolled bar counterparts.

3.2.4.2 X-ray Diffraction (XRD)

A Bruker AXS-D8 Advance equipped with Davinci X-ray diffractometer (XRD) and Göbel mirror optics was utilised to identify metallic and ceramic phases of the nitrided and non-nitrided Stellite 6 weld claddings as well as the additive manufactured alloys. A Cu tube was used with a two theta range from 20° to 100°, a step size of 0.05° and a step time of 1s at 40kV and 40mA.

3.2.5 Hardness measurements

A calibrated Vickers hardness testing machine with a 5kgf load was used to obtain macro-hardness measurements of the testing surfaces for the materials. A minimum of 5 measurements were taken and the average value was used as the macro-hardness of the materials testing surface. A Mitutoyo MVK-G1 micro-hardness testing machine with a 200gf load was used to determine the micro-hardness profiles for the gas nitrided and non-nitrided Stellite 6 weld claddings.

3.2.6 Surface roughness measurements

A Mitutoyo SurfTest machine was used to conduct the surface roughness measurements in accordance with BS EN ISO 4288 [3.1]. The standard recommends that the stylus pin move at a minimum distance of 4mm for accurate measurements. The measurements conditions that were used during the surface roughness measurements are shown in Table 3.5.

Table 3.5: *Surface roughness measurement conditions*

Measurement length	5mm
Stylus pin speed	0.5m/s
Measurement range	800µm
Number of points	5,000

3.2.7 Sand characterisation

As silica sand is the most commonly used proppant in the hydraulic fracturing industry, it was decided that this type of proppant would be used for testing instead of resin coated silica sand or ceramic proppants. The hydraulic fracturing silica sand possesses a hardness of 7 mohs, which is equivalent to approximately 1,160HV. The hydraulic fracturing silica sand is also required to be within a certain size and shape according to ISO 13503-2 [3.2] and API RP 19C [3.3]. In order to assess the shape of the hydraulic fracturing silica sand, images of the sand particles were taken on the Olympus GX-51 light optical microscope at x50 magnification (Figure 3.1). Image J, a scientific multidimensional software programme, was used to measure the area (A) and perimeter (P) of the sand particles. These values could then be used to calculate the circularity factor (CF) of the sand particles (Eq. 3.1)

$$CF = \frac{4\pi A}{P^2} \qquad \text{Eq. 3.1}$$

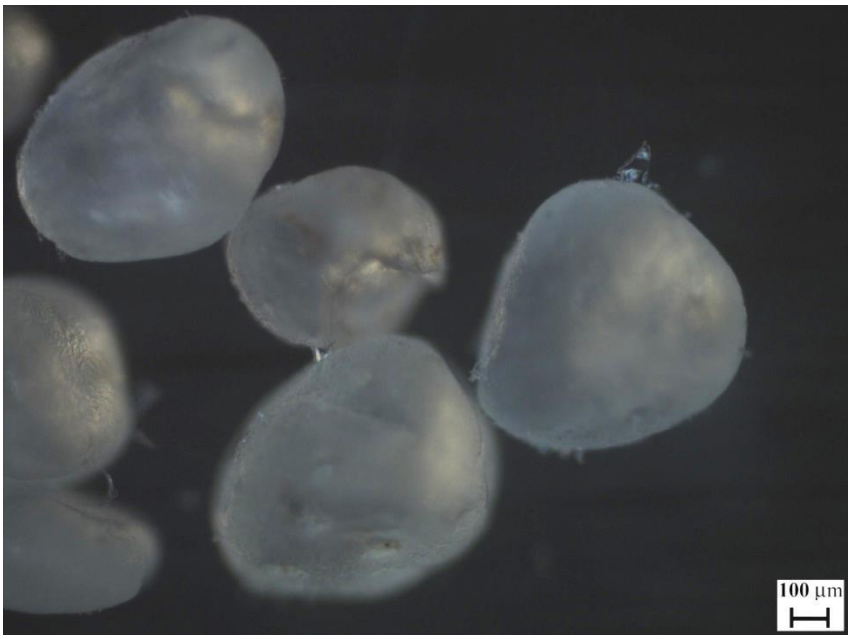

Figure 3.1: *Hydraulic fracturing sand used in erosion-corrosion testing*

100 untested hydraulic fracturing sand particles were analysed using this technique to assess the average shape of the particles and if they meet the expected shape standards. Figure 3.2 demonstrates the amount of sand particles found to have CF values below 0.8,

between 0.8 and 0.9 and above 0.9. A schematic demonstrating the defined CF shapes of particles ranging from 0.5-0.95 is also shown in Figure 3.2. Both ISO and API standards state that high strength proppants must have a CF value above 0.7, there was only 1 particle which was below 0.8 (CF value - 0.76), therefore, this batch of hydraulic fracturing sand met the standards criteria.

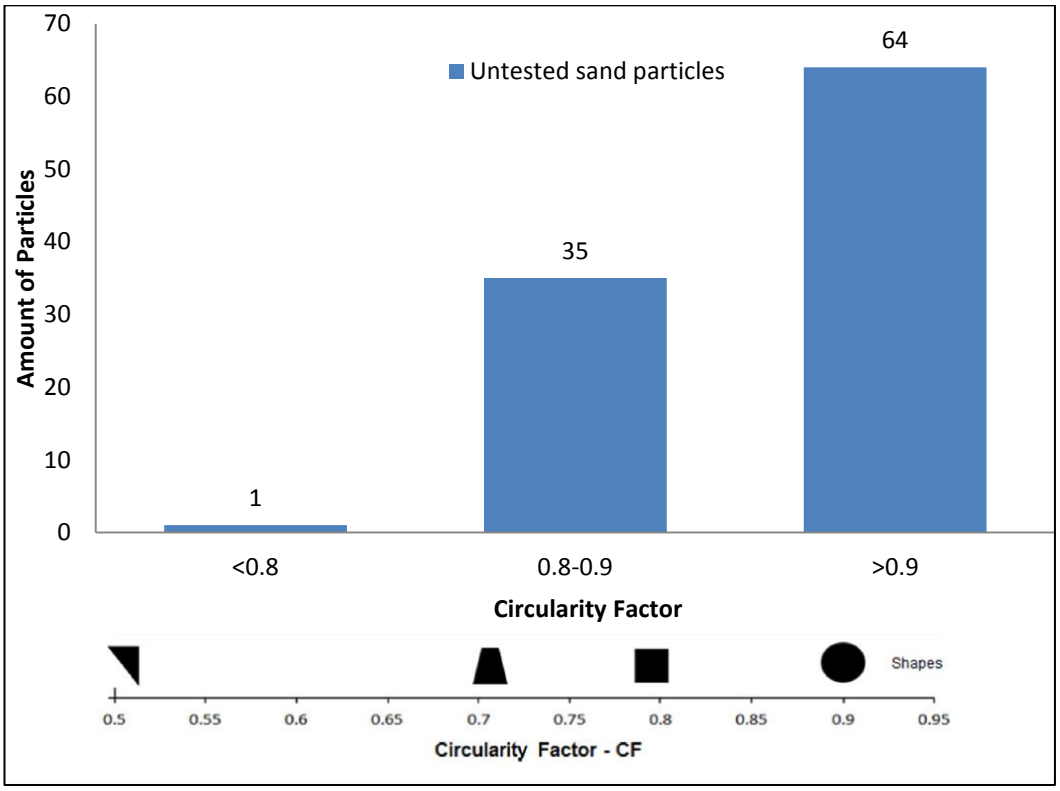

Figure 3.2: *Circularity factors for 100 untested hydraulic fracturing particles*

To measure the size of the sand particles, a sand size distribution (Figure 3.3) was attained through a sand sieving process. The sand was sieved through mesh sizes of 710µm, 600µm, 500µm, 410µm, 325µm, 250µm and 180µm.

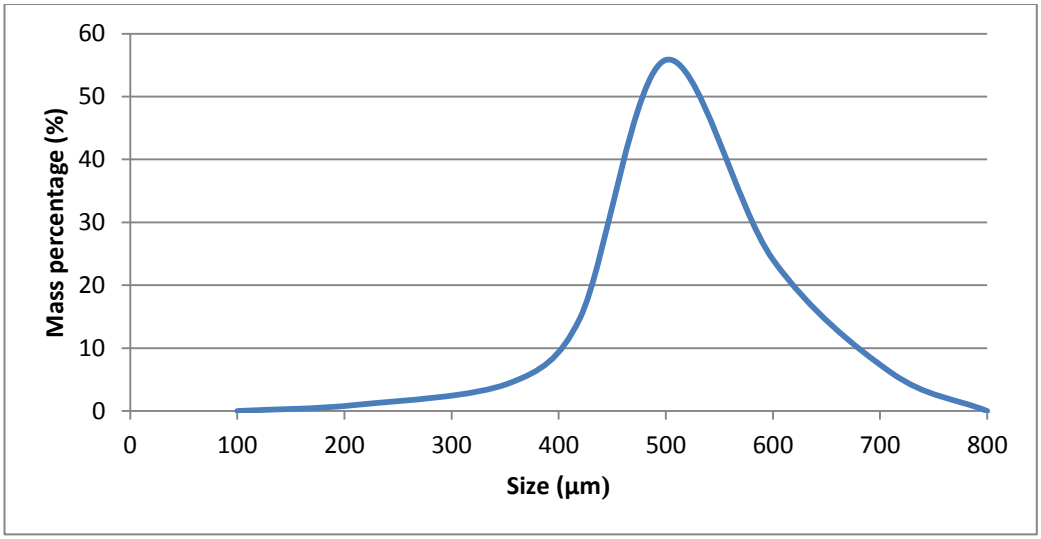

Figure 3.3: *Average sand size distribution of the hydraulic fracturing silica sand*

3.3 Erosion-corrosion testing procedures

3.3.1 Testing protocol

Before testing, the surface preparation procedure described in 3.2.2 was conducted. After the grinding process, the samples were cleaned in methanol to remove any debris and dried with pressurised air. The test samples were then weighed in a Sartorius Entris mass balance. The mass balance was calibrated to an accuracy of ±0.1mg. A minimum of five measurements per sample were taken before and after each test in order to assess the scatter in measured readings. A scatter of less than 0.5mg between the measurements was deemed acceptable.

The erosion-corrosion impingement tests were conducted in a closed loop submerged jet impingement rig, demonstrated in Figure 3.4. The vessel was filled with 33L of pre-heated (40°C) water which avoided any temperature changes occurring during the experiments. Sodium chloride (NaCl) was dissolved into the pre-heated water, the amount of dissolved sodium chloride differed between the test phases described in each of the chapters. In the study described in chapter 4, three NaCl concentrations were used; 0.05% (fresh water), 3.5% (sea water) and 10%. Whereas, the experiments described in chapters 6 and 7, were conducted with 3.5% NaCl only. A Hanna HI 9033 multi-range conductivity meter was used to measure the conductivity of each aqueous solution to ensure the salinity was kept constant for each experiment (2mS for 0.05% NaCl, 50mS for 3.5% NaCl and 62mS for 10% NaCl). In order to conduct electrochemical monitoring (Chapter 3.3.4) and Impressed

Current Cathodic Protection (3.3.5), a Gill AC potentiostat and a three electrode cell (auxiliary electrode, reference electrode and working electrode) was used.

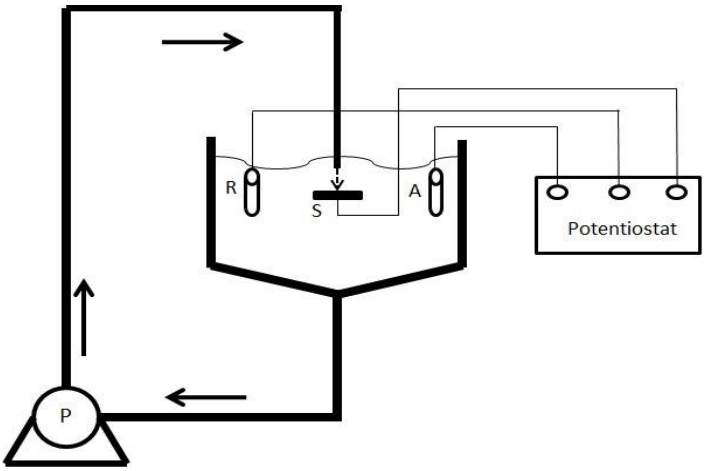

Figure 3.4: *Schematic diagram of the submerged jet impingement test rig with electrochemical monitoring equipment (A – auxiliary electrode, R – reference electrode and S – working electrode)*

The studies forming the basis of chapters 4, 6 and 7, erosion-corrosion tests were conducted at an impingement angle of 90°. For the 90° impingement tests, the test coupons were placed in the centre of the Perspex specimen holder (Figure 3.5) inside a 40mm diameter extruded hole with 15mm thickness. For the study described in chapter 4, a sacrificial anode was used to provide cathodic protection. The sacrificial anode was located in an extruded hole (40mm diameter, 15mm thick) adjacent to the test coupon (Figure 3.6). An electrical-connection wire was soldered to the base of the sacrificial anode specimens and then the specimen was encapsulated in epoxy resin. Electrical contact between the sacrificial anode specimen and the test specimen was achieved via a wire in contact with the base of the test specimen. This arrangement facilitated measurement of the galvanic potential of the electrically coupled specimens which was measured using an Ag/AgCl reference electrode.

For all tests, a 5mm thick disk was used to ensure that a 5mm offset distance between the nozzle and test coupon was kept constant. The specimen holder was then connected to the slurry jet impingement rig and the test coupon was submerged in the aqueous solution.

Once the pump was turned on, the hydraulic fracturing sand particles were loaded gradually into the aqueous solution within the first few seconds of the experiment. The test durations for all slurry jet impingement experiments was 1 hour. After testing, the test coupon was cleaned with methanol and dried with pressurised air before being weighed. Once the test was completed, the impingement rig was drained and cleaned. New slurry (aqueous solution and sand) was used for each experiment. For each experimental phase, to ensure consistency during tests, a UNS S31600 stainless steel was used to calibrate the rig and was used as a reference material due to its generally good corrosion resistance in various environments.

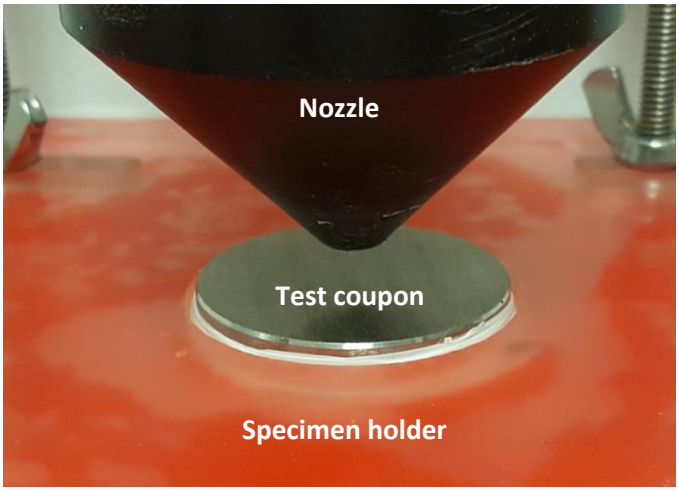

Figure 3.5: *90° angle of impingement specimen holder with test coupon*

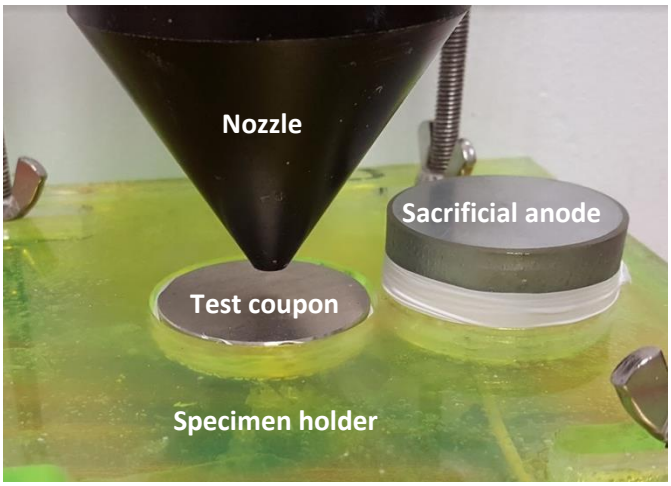

Figure 3.6: *Modified 90° angle of impingement specimen holder with test coupon and sacrificial anode*

3.3.2 Flow velocity and sand concentration measurements

The measurement of the flow velocity and sand concentration was conducted by filling the impingement rig vessel with 33L of water and the same amount of sand loading as would occur in an impingement experiment. The pump was switched on and after 15 minutes, a plastic hose was placed underneath the exit of the submerged nozzle and the slurry was collected in a 10L beaker for 20 seconds. The sand particles were collected in a 250µm sieve which was located between the hose and the beaker. The velocity of the jet was calculated using Eq. 3.2.

$$V = \frac{Q}{20 \times \pi {R_n}^2} \quad \text{Eq. 3.2}$$

Where, V is the flow velocity (m/s), Q (m^3/s) is the flow rate per 20 seconds and R_n is the radius of the nozzle (m). The sieve was then placed in a pre-heated oven to remove the moisture from the sand particles. The dried sand particles were then weighed with the Satorius Entis mass balance. The sand concentration was then obtained through the flow rate in mg/L. The velocity and sand concentration tests were conducted before and after each experimental phase to ensure repeatability of the impingement test apparatus. It was observed that there was no variation in flow velocity or sand concentration throughout the testing programmes.

3.3.3 Segmentation of the test samples

In order to determine the corrosion rates of the zone directly underneath the jet and the adjacent region, the 38mm diameter test coupon was segmented into two separate specimens. A 5mm diameter sample with a surface area of 0.2cm^2 was removed from the test coupon, this represented the direct impinged zone (DIZ). The remainder of the test coupon had a surface area of 11cm^2 and this represented the outer area (OA). The segmentation process was conducted by a Maxiem abrasive waterjet 1515 cutting machine which removed the 5mm diameter sample at the centre of the test coupon, shown in Figure 3.7. A more elaborate form of segmentation has been developed by Adegbite et al. [3.4], who have segmented the different zones of a welded sample within a specific hydrodynamic zone in order to investigate galvanic effects between the parent material (PM), Heat Affected Zone (HAZ) and weld metal.

Both sections (DIZ and OA) were connected to separate electrical wires via a spot welding machine to form electrodes. Before the small specimen was placed back inside the test coupon, a heat shrink tube of 0.8mm thickness was placed around the small specimen to ensure that both sections were electrically insulated. The segmented sample was then encapsulated in resin inside a 40mm diameter mould, which also aided as an additional insulating barrier between the DIZ and OA. Figure 3.8 demonstrates an Inconel 718 (UNS N07718) sample which has been segmented.

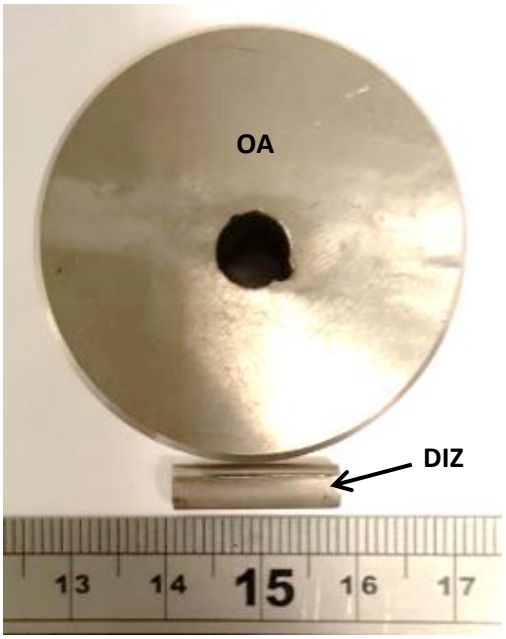

Figure 3.7: *The two segments (DIZ and OA) following waterjet machining*

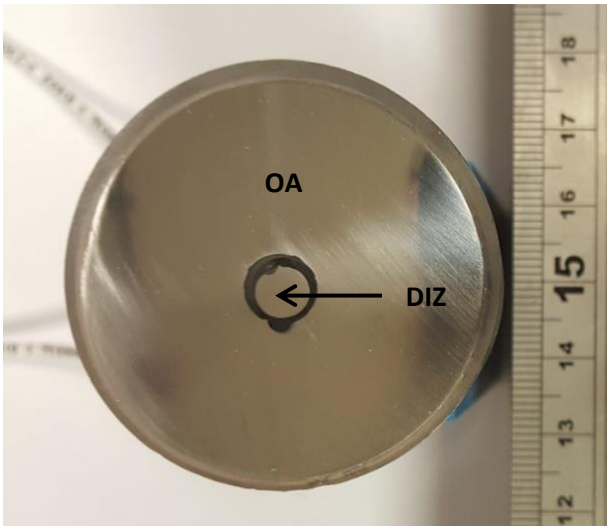

Figure 3.8: *Segmented sample encapsulated in epoxy resin*

3.3.4 Potentiodynamic polarisation scans

Potentiodynamic polarisation scans were used to indirectly measure the corrosion rates of the test specimens (both full and segmented) in static, flowing (solid free) and in-situ of the slurry jet impingement tests. The potentiodynamic polarisation scans utilised the standard three electrode cell (Ag/AgCl reference electrode, the working electrode (test coupon) and a platinum auxiliary electrode) with an ACM Instruments Gill AC electrochemical potentiostat.

Before conducting the polarisation scans, the free corrosion potential (E_{corr}) was measured 15 minutes after the test coupon was immersed in the aqueous solution in order for it to stabilise. Polarisation scans were conducted by shifting the initial electrode potential either 20mV more positive (cathodic) or 20mV more negative (anodic) than the free corrosion potential, hence, ensuring that the transition point would occur. Scans were then made 300mV more negative (for cathodic scans) or 300mV more positive (for anodic scans) at a sweep rate of 15mV/min. The chosen ranges were sufficient to evaluate corrosion current measurements by way of Tafel extrapolation. The measured current densities were then used to evaluate the associated mass losses due to corrosion via calculation by Faraday's Law, Eq. 2.9.

3.3.5 Application of cathodic protection

Cathodic protection was applied by impressed current cathodic protection (ICCP) and sacrificial anode cathodic protection (SACP). ICCP was applied using the three electrode cell (Ag/AgCl reference electrode, working electrode (test coupon) and the platinum auxiliary electrode) with an ACM Instruments Gill AC electrochemical potentiostat. Two methods were used to apply the SACP, the first utilised a piece of commercially-procured zinc alloy which was specifically designed for SACP and a commercially available zinc-particle-containing paint (Zinga).

ICCP was applied in the experimental studies described in chapters 4, 6 and 7 to assess the erosion damage occurring during the slurry impingement tests. An electrode potential of -800mV was selected as this was considered suitable to suppress anodic reactions occurring at the test coupons surface. This was supported by back extrapolation of the anodic polarisation scans of each material which demonstrated that the residual anodic current

densities at -800mV were negligible. An example of the back extrapolation method is shown in Figure 3.9.

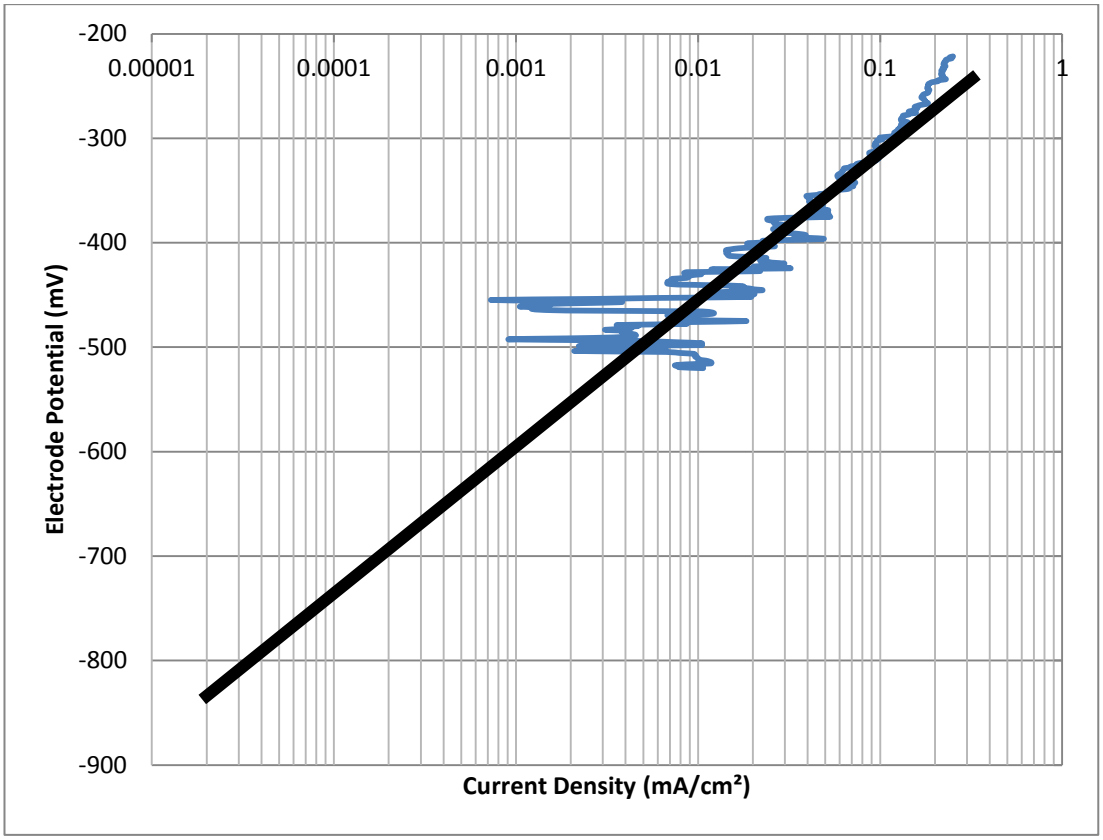

Figure 3.9: *Example of the back extrapolation technique used to determine the residual current densities at -800mV cathodic protection potential (material – UNS S31600)*

The SACP methods were only used in the experimental study described in chapter 4, to establish if they could be used in erosion-corrosion test conditions to cathodically protect a low alloy UNS G43400 steel. The Zinga coating was applied to the side of the 38mm diameter test samples, shown in Figure 3.10. As the coating was on the sides of the test coupon, this reduced the effect of the coating being removed by the abrasive particles and contributing to the overall material loss.

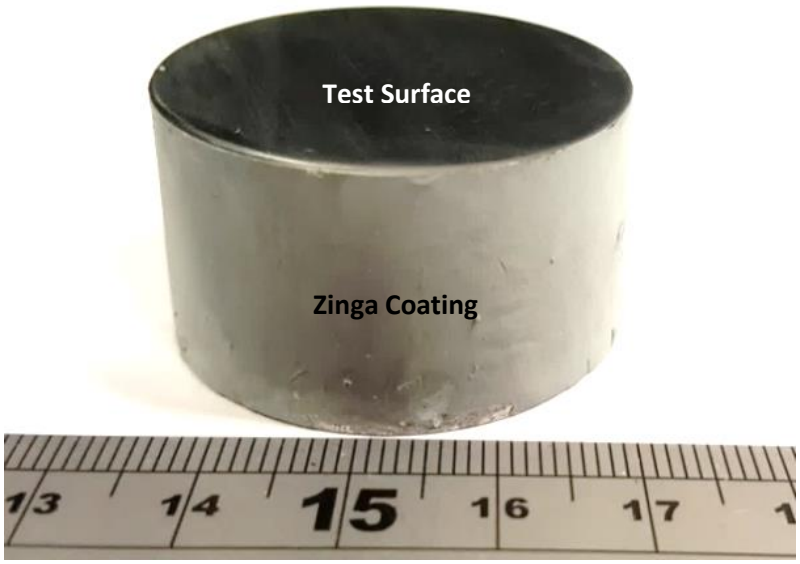

Figure 3.10: *UNS G43400 steel test coupon with Zinga coated side*

The measured coupled electrode potential between the UNS G43400 and the sacrificial anodes are given in Table 3.6. Both SACP methods were effective in achieving desire electrode potentials to adequately provide cathodic protection to the UNS G43400 low alloy steel.

Table 3.6: *Measured coupled potentials between the UNS G43400 steel and sacrificial anode/coating*

Coupled material	Coupled potential (mV)
UNS G43400 – Zinc anode	-1025
UNS G43400 – Zinga coating	-820

3.4 Repetitive impact testing procedures

A test rig was designed and manufactured in order to assess repetitive impact wear between two material surfaces. The test rig was designed to test coupons of the same size as the erosion-corrosion test samples. As the sizes of the specimens were small, this allowed materials to be tested quickly and inexpensively. This would assist with establishing suitable material candidates for the valve seat (Chapter 5).

The test rig was designed to mimic the service conditions of the valve seat during operation. Finite Element Analysis (FEA) data was supplied by engineers from Weir Group PLC. This information included the metal-metal contact pressure, metal-metal contact area, metal-metal contact force and contact angle. These are indicated in Table 3.7.

Table 3.7: *Valve seat operating parameters [3.5]*

Parameter	Value
Metal-metal contact pressure	$4.1x10^8 N/m^2$
Metal-metal contact area	$0.0044m^2$
Metal-metal contact force	1.8MN
Contact angle	40°

The high load required to replicate the force of the valve impacting on the surface of the valve seat was unrealistic to achieve in small scale laboratory testing. Therefore, a smaller contact area and applied load was chosen for testing. Hence, the contact pressure between the impactor and specimen would be the same pressure as the valve applies to the seat. The repetitive impact rig test parameters are shown in Table 3.8.

Table 3.8: *Repetitive impact test rig parameters*

Parameter	Value
Impactor-specimen contact area	$7.9\ x10^{-5} m^2$
Impactor-specimen contact force	32kN
Impactor-specimen contact pressure	$4.1x10^8 N/m^2$

A Zwick Roell 2061 hydraulic tensile testing machine was used for the repetitive impact testing. This was capable of applying a compressive load up to 50kN; hence, it was capable to produce the 32kN contact force required for testing. The valve operates at a frequency of approximately 5Hz; hence, the hydraulic tensile testing machine operated at a frequency of 5Hz. A custom-made impactor (Figure 3.11) is connected to the hydraulic tensile testing machine. The material used for the impactor was carburised 8620 steel, which is the same as the valve material.

Figure 3.11: *Custom made impactor for repetitive impact test rig*

As there are also sand particles which are crushed between the valve and seat during the operation of the valve closing, it was also important to incorporate this aspect into the rig. Therefore, a constant supply of hydraulic fracturing sand was fed between the impactor and specimen to replicate the crushing of sand. The proppant was mixed with a cellulose gel which was capable of holding the sand in suspension. The suspended sand was supplied to the sample through a Verderflex peristaltic pump. The sand concentration of the rig was 54g/l. The specimen holder contained a guard with an inlet and outlet for the slurry. The repetitive impact test set up is shown in Figure 3.12.

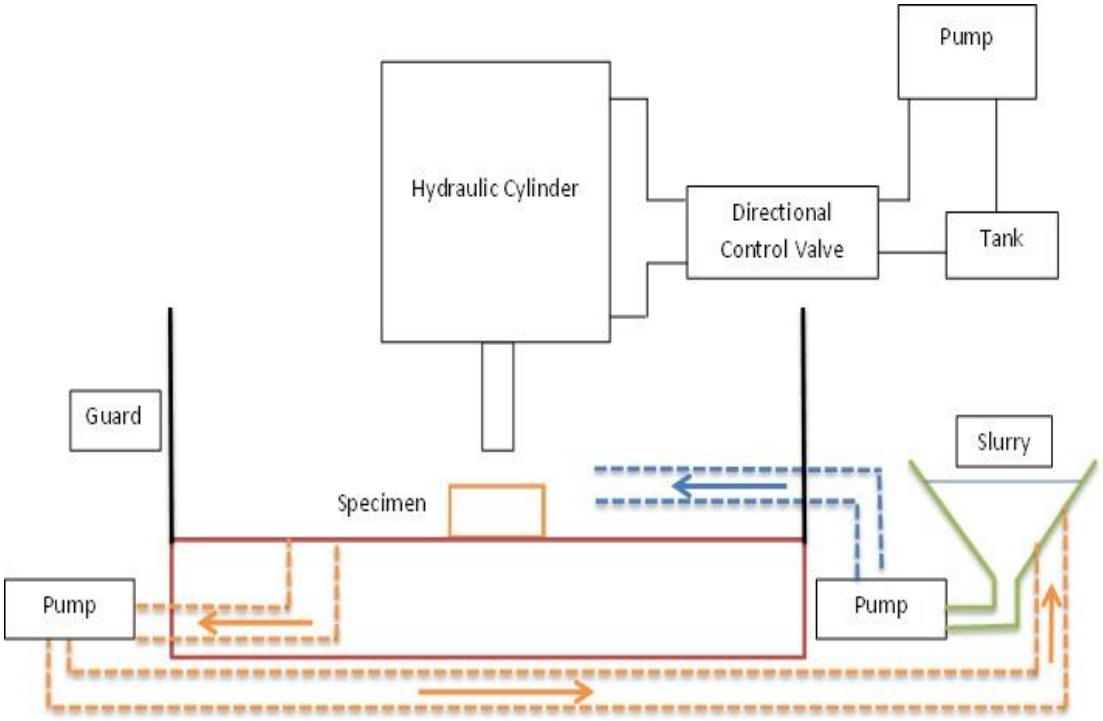

Figure 3.12: *Schematic of repetitive impact test rig*

The operation of the test rig was as follows:

- The in-feed pump was switched on and supplied a constant flow of slurry with suspended sand particles to the specimen.
- Once there was a constant flow of slurry, the hydraulic piston was activated which impacted with the specimen and crushes the sand at a rate of 5Hz.
- The used slurry was then drained through the drainage hole in the holder which is fed through the second peristaltic pump.

3.5 Post-test analysis techniques

3.5.1 Macro and micro examination of the tested surfaces

Macro-examination images were taken with a single-lens reflex (SLR) camera of the post-test surfaces for both erosion-corrosion and repetitive impact testing to record the overall surface damage. The test surfaces were also examined under an Olympus GX-51 light optical microscope to assess the degradation processes which occur in the different wear regions during erosion-corrosion testing.

3.5.2 Surface topography

An Alicona InfiniteFocus Optical Microscope was used to conduct the post-test surface topography. The Alicona operates with an X, Y and Z coordinate system which enabled a 3D scan of the test coupon's wear scars, i.e. the area directly underneath the impingement jet (erosion-corrosion testing) and also the area underneath the impactor (repetitive impact testing). An optical magnification of 5x and a vertical resolution of 800nm was used to scan the test coupons. The error in the 3D scan was stated (by the manufacturer) as ±1µm in terms of surface texture and ±0.02mm^3 in terms of volume loss.

The benefits of using the Alicona over a conventional stylus profilometer is that the surface texture analysis tool can be used to conduct multiple line scans to establish the deepest wear scar profile. The 3D scan could also be converted into a colour contour map (Figure 3.13) which enabled higher precision profile scans. The volume loss measurements provided a further understanding of the degradation processes as it was used in developing a quantitative tool (Chapter 3.5.3). The volume loss was measured by constructing a polygon around the area of interest, the volume below the surface was then calculated to yield the volume loss.

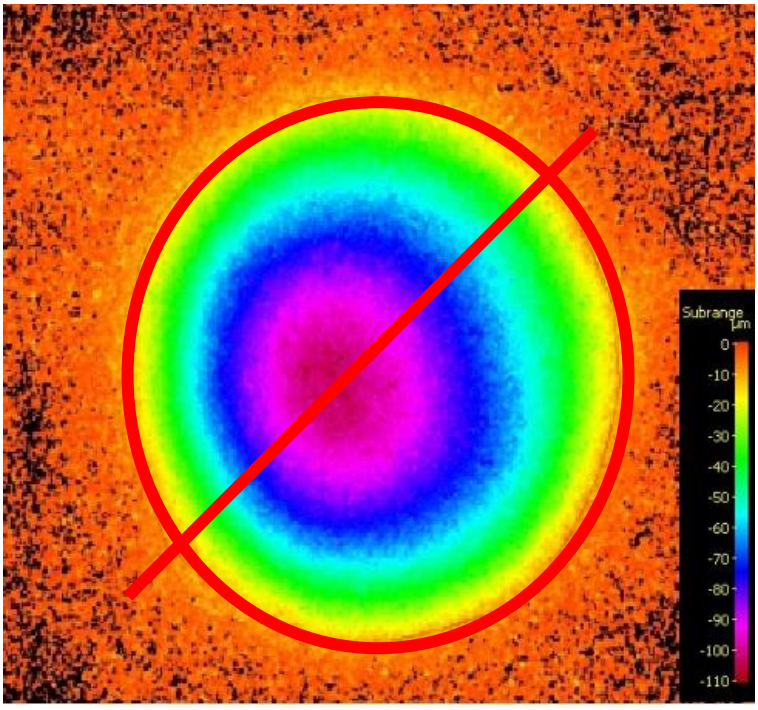

Figure 3.13: *Example of the colour contour map created by Alicona to establish wear scar depth and volume loss for test coupons*

To ensure the accuracy of the Alicona machine, a calibration test was conducted by Giourntas [3.5] prior to the volumetric analysis of the test coupons. A test coupon with a 90µm blind hole CNC machined from its centre, was used for calibration. Table 3.9 shows the measured Alicona volume loss and the theoretical volume loss from mathematical calculation of a cylinder. The error in the measurement was 7%.

Table 3.9: *Volume loss measurements for the calibration sample*

Measurement method	Volume of hole (mm^3)
Theoretical	1.76
Alicona	1.63

Another consideration was the error which may occur due to thickness loss outside of the wear scar during testing due to sliding abrasion, corrosion and synergy. Figure 3.14 demonstrates an example of a typical wear scar profile illustrating the outer area thickness loss which occurs due to sliding abrasion and corrosion related damage. Table 3.10 illustrates the estimated profilometer measurement error, which demonstrates that the error is negligible.

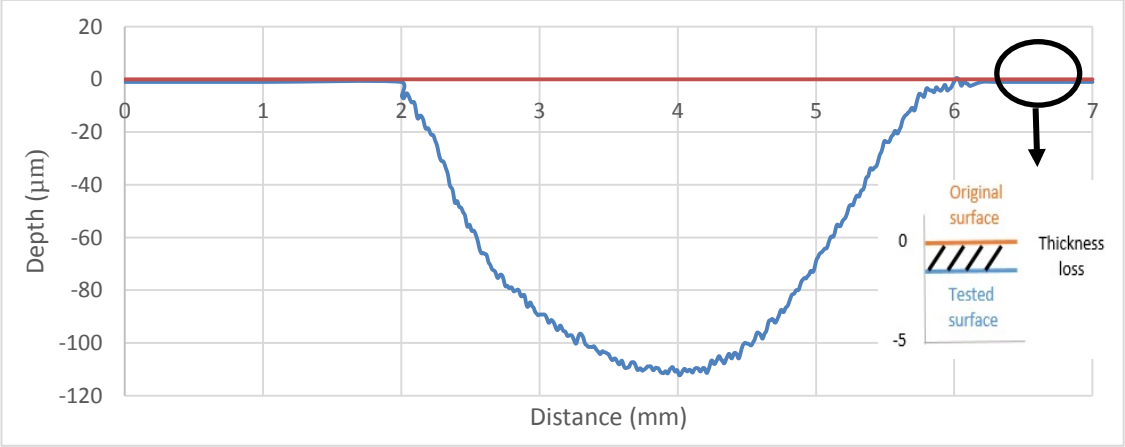

Figure 3.14: *Example of a 2D wear scar profile demonstrating the outer area thickness loss resulting from sliding abrasion and corrosion related damage*

Table 3.10: *The estimated error in volume loss measurement as a result of the thickness loss in the outer area and the measured wear scar depth*

Material	Wear scar depth (μm)	Thickness loss outside of the wear scar (μm)	Error (%)
UNS S31600	112	0.32	0.29

3.5.3 Volumetric analysis technique

As the test coupon was 38mm diameter and the exit of the nozzle was 4mm, two distinct wear regions were found during erosion-corrosion testing (Figure 3.15).

- The direct impinged zone (DIZ) is formed directly underneath the jet and is often referred to as the wear scar. Recent studies [3.7, 3.8] have found that the particles impact at angles that vary from 85° in the centre to 45° at the edges of the wear scar. Figure 3.16 shows the predicted impact angle with respect to the distance from the centre of the nozzle. The higher impact angles tend to cause crater-type damage as shown in Figure 3.15.
- The second region is referred to as the outer area (OA), where the particles are impacting the test surface at low angles and producing a sliding abrasion action. The intensity and damage of the abrasive scratches decreases towards the outer edges of the test coupon.

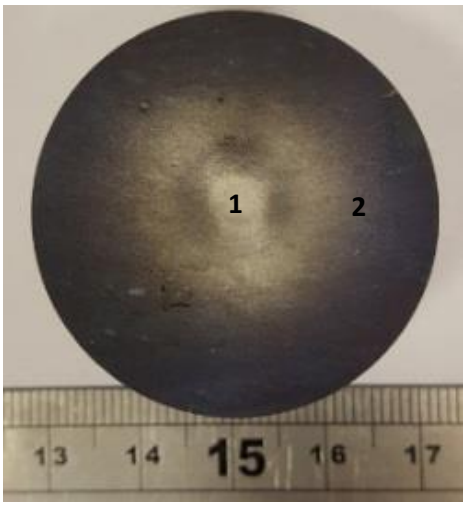

Figure 3.15: *Test coupon after erosion-corrosion testing demonstrating the DIZ (1) and the OA (2)*

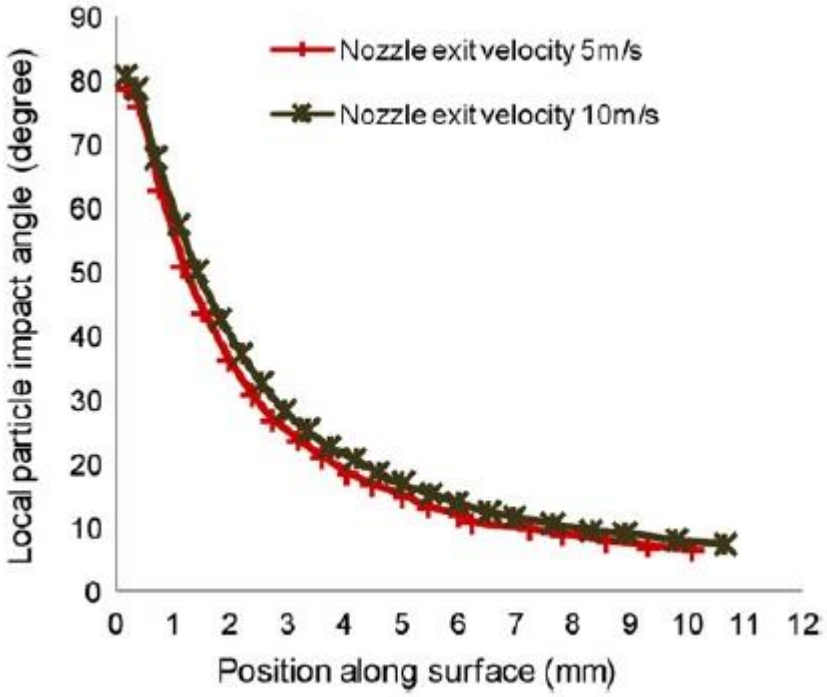

Figure 3.16: *CFD models predicting the impact angle of the particles with respect to the distance from the nozzle centre during solid-liquid impingement conditions [3.8]*

In the erosion-corrosion testing, the volume loss from the direct impinged zone (VL_{DIZ}) and the volume loss from the outer area (VL_{OA}) equate to the total volume loss (TVL), as shown in Eq. 3.3.

$$TVL = VL_{DIZ} + VL_{OA} \quad \text{Eq. 3.3}$$

The volume loss in the outer area was calculated by subtracting the direct impinged zone volume loss from the total volume loss, which was measured by Alicona InfiniteFocus 3D optical scanner, (Eq. 3.4).

$$VL_{OA} = TVL - VL_{DIZ} \quad \text{Eq. 3.4}$$

For a more comprehensive understanding of the degradation processes occurring during the erosion-corrosion testing, the damage mechanisms occurring in each wear region were quantified (Eq. 3.5). The contributing mechanisms to erosion-corrosion were shown in Eq. 2.2.

$$TML\ (FEC) = E_{DIZ} + C_{DIZ} + S_{DIZ} + SA_{OA} + C_{OA} + S_{OA} \quad \text{Eq. 3.5}$$

Where, E_{DIZ} is the pure mechanical erosion damage occurring within the wear scar, C_{DIZ} Is the corrosion damage occurring within the wear scar, S_{DIZ} is the synergy occurring within the wear scar, SA_{OA} is the sliding abrasion occurring in the outer area, C_{OA} and S_{OA} is the corrosion and synergy occurring in the outer area. When cathodic protection is applied, only mechanical damage occurs (E_{DIZ} and SA_{OA}), shown in Eq. 3.6.

$$TML\ (CP) = E_{DIZ} + SA_{OA} \quad \text{Eq. 3.6}$$

As the TML (CP) and the E_{DIZ} are measurable, the SA_{OA} can be simply obtained through Equation 3.6. The mass losses due to corrosion (C_{DIZ} and C_{OA}) are calculated from Faraday's Law, by Tafel extrapolation, using the potentiodynamic polarisation curves generated by the segmented sample (Chapter 3.3.3). Hence, the synergy terms (S_{DIZ} and S_{OA}) can be easily calculated.

The enhanced approach allows a better appreciation for comparing the corrosive wear performance of various materials under solid-liquid impingement conditions, than can be attained from a single measurement parameter (i.e. total mass loss) [3.8]. The technique also enables a differentiation between two different types of mechanical degradation processes (high angle erosion and sliding abrasion). The employed technique has yielded significant improvements in the understanding of erosion-corrosion behaviour and has demonstrated the complexity of this phenomenon, through cases where material rankings have changed dependent upon the material degradation process of interest, as demonstrated in Chapter 4.6.1.

3.6 References

[3.1] 4288:1999 British standard for geometric specification and surface texture, 1998.

[3.2] ISO 13503: Petroleum and natural gas industries — Completion fluids and materials Part II: Measurement of properties of proppants used in hydraulic fracturing and gravel-packing operations, 2006.

[3.3] American Petroleum Institute, "API RP 19C.", 2014.

[3.4] M. A. Adegbite, M. J. Robinson, and S. A. Impey, "The Influence of Hydrodynamics on the Preferential Weld Corrosion of X65 Linepipe Steel in Flowing Brine Containing Carbon Dioxide," in *NACE Int. Corros. Conf. Expo*, 2014.

[3.5] Private communication with Jacob Bayyouk, Senior Engineering Technical Steward, Weir Oil & Gas, Fort Worth, Texas, USA, 2015.

[3.6] L. Giourntas, "Investigation of erosion-corrosion behaviour of pump materials," Ph.D. Thesis, University of Strathclyde, 2016.

[3.7] A. López, W. Nicholls, M. T. Stickland, and W. M. Dempster, "CFD study of Jet Impingement Test erosion using Ansys Fluent® and OpenFOAM®," *Comput. Phys. Commun.*, vol. 197, pp. 88–95, 2015.

[3.8] A. Gnanavelu, N. Kapur, A. Neville, J. F. Flores, and N. Ghorbani, "A numerical investigation of a geometry independent integrated method to predict erosion rates in slurry erosion," *Wear*, vol. 271, no. 5–6, pp. 712–719, 2011.

[3.9] L. Giourntas, T. Hodgkiess, and A. M. Galloway, "Enhanced approach of assessing the corrosive wear of engineering materials under impingement," *Wear*, vol. 338–339, pp. 155–163, 2015.

Chapter 4

Assessment of fluid end materials and effect of environmental conditions

4.1 Introduction

The durability of fluid ends (which are the positive displacement pump casings) is essential to the life of the hydraulic fracturing positive displacement pumps. The fluid ends can experience a broad range of operating conditions (different pumping pressures, proppant loading, etc.) as well as various hydraulic fracturing fluid chemical compositions. These extreme operating conditions can cause severe corrosive wear (as demonstrated in Figures 4.1 and 4.2) to the wetted areas of the fluid end. A high strength low alloy steel (UNS G43400) is currently widely used as the fluid end material in hydraulic fracturing fluid ends. To increase the life expectancy of the fluid ends, it is clear that a reduction in the corrosive wear damage would be extremely beneficial.

Figure 4.1: *Corrosive wear damaged observed in valve lift area in fluid end (courtesy of Weir SPM)*

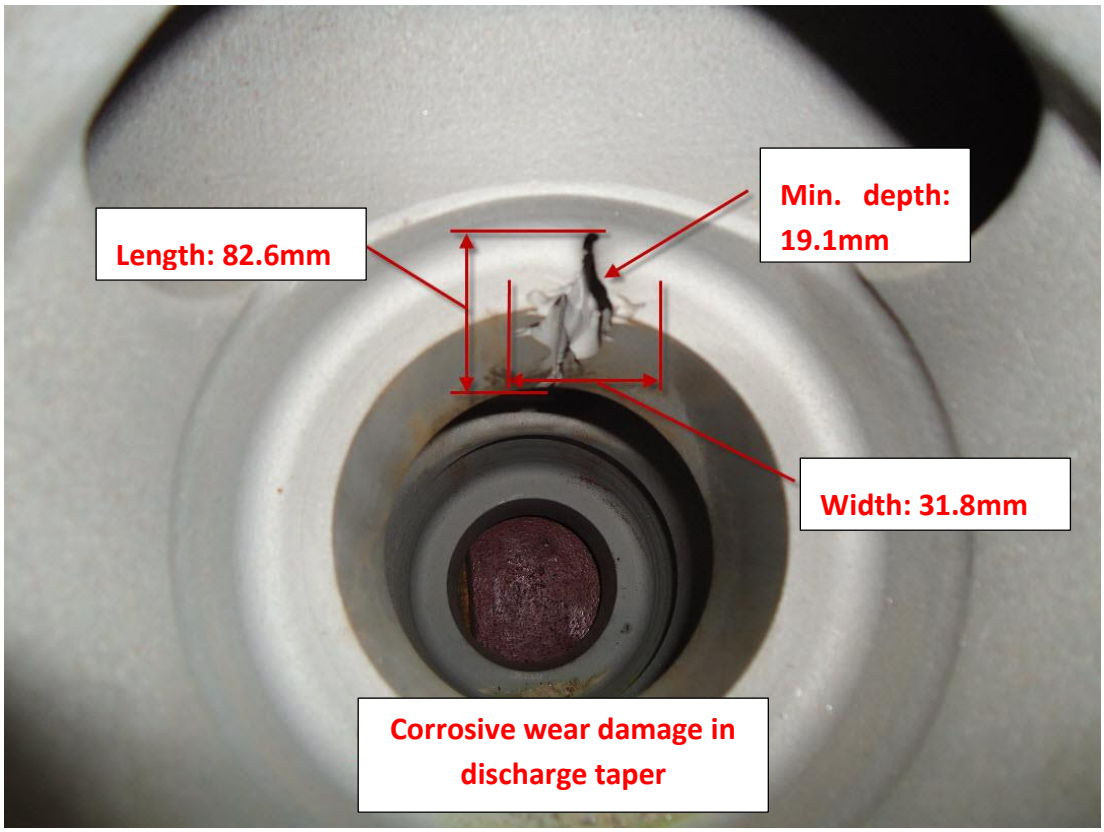

Figure 4.2: *Corrosive wear damage occurring in the discharge taper in a hydraulic fracturing pump fluid end (courtesy of Weir SPM)*

To combat the corrosive wear issue, two different approaches were selected. The first approach was to assess alternative materials with significantly improved corrosion resistance than the currently used low alloy steel. In this case, three stainless steels with different chemical compositions and microstructures were selected as the alternative materials. The second approach was to assess the potential of applying cathodic protection (both impressed current and sacrificial anode) to reduce the corrosive wear damage of the low alloy steel. As the water source for the hydraulic fracturing fluid varies between hydraulic fracturing sites and operational stages, the solid-liquid impingement experiments were conducted in three different levels of salinity (freshwater, seawater and brine) to assess the effect of salinity on the corrosive wear performance of the test materials.

4.2 Literature review

4.2.1 Comparative studies between stainless steels and low alloy steels

As low alloy steels have poor corrosion resistance, various grades of stainless steels have been developed to increase the service life of a variety of engineering components. As a result of stainless steel development, there have been numerous comparative studies which have demonstrated the superior erosion-corrosion resistance of stainless steels in comparison with low alloy steels. This was demonstrated by Neville et al. who studied a C-Mn steel and two stainless steels (austenitic - UNS S31603 and duplex - UNS S32205) in both liquid (100m/s, 3.5%NaCl, 50°C) and solid-liquid (25m/s, 3.5%NaCl and 1000ppm silica sand, 50°C) conditions at normal incidence [4.1]. There was a significant contribution of corrosion related damage in the solid-liquid erosion-corrosion tests (37% of the overall material loss for the C-Mn steel, 19% of the overall material loss for the UNS S31603 and 24% of the overall material loss for the UNS S32205). The passive film protected the stainless steels from substantial material removal in solid-free liquid conditions, whereas in such conditions the C-Mn steel experienced extensive erosion-corrosion damage. However, in solid-liquid conditions, the passive film was disturbed from the surface of the stainless steel, which then caused the stainless steels to exhibit corrosion related damage.

A similar trend was also found by Giourntas et al. [4.2]. This study compared four different grades of stainless steel (austenitic - UNS S31600, Superduplex - UNS S32760, martensitic - UNS S42000 and precipitation hardened - UNS S17400) and a low alloy steel grade UNS G10400 in normal incidence solid-liquid impingement conditions (24m/s, 200mg/l, 30-35°C). In free erosion-corrosion (FEC) conditions, the low alloy steel demonstrated average mass losses two times greater than that of the stainless steels. However, in cathodic protection (mechanical damage only) conditions, the increase was reduced to only 1.3 times greater average mass loss. The poor corrosion resistance of the low alloy steel resulted in greater corrosion related damage. This was evident from anodic polarisation monitoring, as the low alloy steel was found to be 6-33 times greater than the stainless steels (depending on grade), in terms of mass loss due to corrosion. The Superduplex (UNS S32760) was marginally (1.2 times) better than the other stainless steels, which all performed similarly to each other. This was due to the removal of the passive oxide film by the impacting sand particles.

Another study by Neville and Wang found that a low alloy steel (X65 pipeline steel – API-5L-X65) demonstrated approximately 4 times greater mass loss compared to two stainless steels (martensitic - UNS S41000 and Superduplex - UNS S32760) in solid-liquid impingement conditions (normal incidence, 500mg/l sand concentration, 20m/s, 50°C) [4.3]. The corrosion related damage of the overall damage for the carbon steel was about 40%, whereas it was about 25% for the martensitic stainless steel. This was attributed to the poorer corrosion resistance of the carbon steel. The corrosion component of the Superduplex was negligible and could not be quantified by calculating the charge transfer corrosion resistance from AC impedance results; hence, demonstrating the superior corrosion resistance of the stainless steels.

Rajahram et al. studied the erosion-corrosion resistance of a low alloy steel (UNS G10200 and a stainless steel (UNS S31603) in a slurry pot [4.4]. In distilled water with 1% sand concentration both the low alloy steel and austenitic stainless steel had similar mass losses. However, in 3.5% NaCl the low alloy steel demonstrated roughly 5 times greater mass loss than the austenitic stainless steel. Again, this study demonstrated that the low alloy steel and stainless steel have similar resistance to mechanical damage, however, when corrosion related damage becomes involved, there is a significant proportion of damage with the low alloy steel.

Giourntas et al. utilised an enhanced volumetric analysis technique to assess the erosion-corrosion damage of a low alloy steel (UNS G10400) and an austenitic stainless steel (UNS S31600) in normal incidence solid-liquid impingement conditions (3.5%NaCl, 19m/s and 150mg/l sand concentration) [4.5]. In terms of total mass loss, under FEC conditions, the low alloy steel was found to suffer a loss twice as great as the stainless steel. However, in pure erosion tests, the difference was reduced significantly to only 1.3 times. Anodic polarisation tests in the Direct Impinged Zone, DIZ (underneath the impinging jet), revealed that both materials exhibited similar free corrosion potentials, E_{corr} (-547mV for UNS S31600 and -574mV for UNS G10400) and a corrosion rate, I_{corr} (0.2mA/cm² for UNS S31600 and 0.5mA/cm² for UNS G10400). However, in the OA (outer area where the environment is less erosive) there was a significant difference between E_{corr} (-337mV for UNS S31600 and -524mV for UNS G10400) and I_{corr} (0.003mA/cm² for UNS S31600, 0.4mA/cm² for UNS

G10400). Once again, the erosion and abrasion resistance of the austenitic stainless steel was found to be similar to that of a low alloy steel but corrosion related damage significantly affected the low alloy steel. The study also demonstrated that when the passive film is removed, the stainless steel has similar corrosion rates to that of a low alloy steel because the passive film is periodically removed from the metal surface.

Foley and Levy conducted dry erosion experiments with Al_2O_3 particles at 30m/s on a low alloy steel (UNS G43400) and an austenitic stainless steel (UNS S30400) [4.6]. Both the low alloy steel and stainless steel demonstrated similar erosion resistance. However, another study by Levy and Hickey [4.7] found that a low alloy steel (UNS G10180) demonstrated poorer resistance to mechanical damage than an austenitic stainless steel (UNS S31600) when tested in a slurry pot with kerosene and 30%wt coal. This contradicts the findings from previous erosion-corrosion studies [4.2, 4.4, 4.5], however, abrasion is more likely to be the main wear mechanism for the slurry pot testing apparatus due to the low angle damage which occurs in the slurry pot testing device which may explain this discrepancy.

4.2.2 Comparative studies between stainless steels

Stainless steel is a general term to describe a wide variety of iron based materials which exhibit good corrosion resistance due to the presence of chromium (greater than 10.5%wt). The addition of alloying with elements such as molybdenum, nickel, tungsten and nitrogen also assist in increasing the corrosion resistance of the stainless steels. These alloying elements typically assist in improving resistance to localised attack such as pitting and crevice corrosion. Like low alloy steel grades, the microstructure of stainless steels can vary dependent upon the alloying elements and heat treatment process. The most common types of stainless steel microstructures are either austenitic (16-26%Cr, 6-24%Ni), ferritic (11-21%Cr, 0-2%Ni) or martensitic (11-18%Cr). However, with the requirement of combatting pitting and crevice corrosion in extremely corrosive environments, stainless steels have been developed further to high alloy stainless steel grades such as duplex (21-23%Cr), Superduplex (24-26%Cr) and superaustenitic (18-22%Cr, 17-30%Ni, 2-7%Mo, 0.18-0.26%N). The relative performance of these different stainless steel grades have been assessed under erosion-corrosion conditions and will be discussed in this section.

Al-Malahy and Hodgkiess compared the breakdown potentials of a martensitic stainless steel (UNS S43000), an austenitic stainless steel (UNS S31603) and a superaustentic stainless steel (UNS S31254) in flowing (3m/s with 35,000ppm TDS) and liquid jet impingement (95m/s with 35,000ppm TDS at 90° impingement) conditions [4.8]. In flowing conditions, the breakdown potentials of the austenitic stainless steel (220mV SCE) and martensitic stainless steel (-60mV) was significantly reduced compared to the superaustenitic stainless steel (900mV). The more aggressive nature of the liquid jet impingement conditions resulted in reductions in breakdown potentials for all stainless steels, both UNS S31603 and UNS S43000 were found to be active (no breakdown potential) and the breakdown potential of the UNS S31254 was reduced to 850mV.

A similar trend was also found by Neville and Hodgkiess [4.9]. In this study an austenitic stainless steel grade (UNS S31603) was compared in terms of breakdown potentials with two different grades of Superduplex (UNS S32760 and UNS S32205) in static (35,000ppm Total Dissolved Salts - TDS) and liquid jet impingement (100m/s with 35,000ppm TDS at 90° angle of impingement) conditions. In static conditions, the breakdown potential of UNS S31603 (505mV SCE) was significantly lower than the UNS S32760 (1083mV) and the UNS S32205 (1095mV). In liquid jet impingement conditions, the breakdown potentials substantially reduced due to the more aggressive environment but there was still a significant difference between the UNS S31603 (363mV) and the higher grade alloys (UNS S32760: 1005mV SCE and UNS S32205: 990mV) This was attributed to the more stable passive oxide film formed on the higher grade stainless steel alloys.

Hu and Neville assessed an austenitic stainless steel (UNS S31603) with a higher grade superaustenitic stainless steel (UNS S32654) under solid-liquid conditions (3.5%NaCl) with various solid loadings and fluid velocities [4.10]. The higher grade stainless steel (UNS S32654) demonstrated smaller corrosion rates under all conditions to the SS316. The smaller corrosion rates were attributed to the additions of Mo, Cr and N which reduced metal dissolution when the surface was de-passivated and exhibited better re-passivation properties. The study also demonstrated that, above a sand loading of 60mg/l and a velocity of 7m/s, there was a transition from flow induced corrosion to erosion-corrosion mechanisms. This was caused by the destruction of the passive oxide film by impacting

sand particles which resulted in a transition between nominally passive behaviour to de-passivation/re-passivation behaviour.

A further study by the same authors, assessed the erosion-corrosion resistance of two superaustenitic stainless steel grades (UNS S31245 and UNS S32654) and a Superduplex grade (UNS S32750) in solid-liquid conditions (17m/s, 600-640mg/l sand loading and 90° impingement) [4.11]. In terms of total weight loss, the UNS S32654 was found to be marginally better than the other high-alloy stainless steel grades (1.2 times better than UNS S31245 and 1.06 times better than UNS S32750). The marginal differences were found to be caused by the different proportions of corrosion related damage. The UNS S31245 demonstrated the greatest proportion of corrosion related damage (18%) compared to the UNS S32750 (13%) and the UNS S32654 (7%). This demonstrated that the addition of alloying elements effects the corrosion resistance of the stainless steels and does not assist with improving the resistance to mechanical damage.

Meng et al. also conducted experiments in solid-liquid conditions (3.5%NaCl, 20m/s with 500ppm sand loading) and compared UNS S31603 and UNS S32750 [4.12]. In terms of erosion damage, both stainless steels exhibited similar damage. However, there was a significant increase in corrosion related damage of the UNS S31603 when compared to the higher alloy grade, UNS S32750. This study is in agreement with previous findings [4.8–4.10].

Lopez et al. compared a martensitic stainless steel grade (UNS S42000) with an austenitic stainless steel grade (UNS S30400) in solid-liquid conditions (0.5M H_2SO_4, 3.5%NaCl and 30%wt quartz sand) [4.13]. Two impingement angles (30° and 90°) and two velocities (4.5m/s and 8.5m/s) were evaluated. The predominant material degradation mechanism for the UNS S30400 was mechanical damage at both angles and velocities. However, the martensitic stainless steel exhibited uniform, pitting and corrosion-assisted erosion attack at all angles and velocities. The austenitic stainless steel exhibited the better erosion-corrosion resistance due to its superior corrosion resistance.

4.2.3 Effect of salinity on low alloy and stainless steels

Due to the demand for the hydraulic fracturing industry to use salt water and recycled flowback water, the salinity of the water will greatly increase compared to using freshwater [4.14]. Therefore, the effect of salinity must be considered when assessing alternative materials for the fluid end, as the chloride content is one of the environmental factors which influences corrosion rates (Chapter 2.4.1).

A review of corrosion in the oil and gas industry by Brondel et al. states that the corrosion rate increases with increasing salinity until 5%NaCl content where it reaches a maximum [4.15]. Above this salinity, the solubility of oxygen in the water reduces and hence, reduces the corrosion rate. It also states that, above a salt content of 15%NaCl, the corrosion rates reduce below that of freshwater. As indicated by Figure 4.3 below.

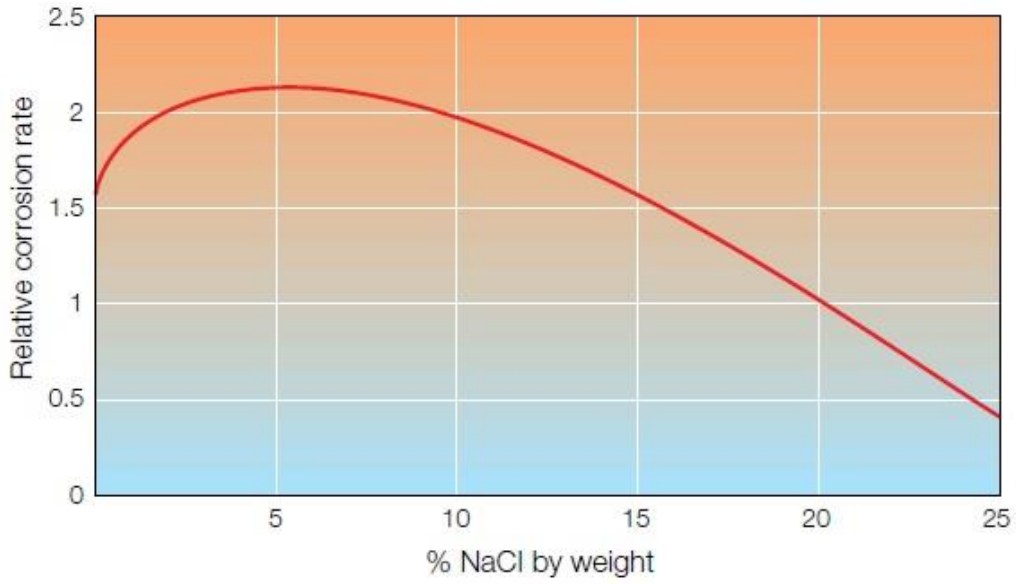

Figure 4.3: *Effect of salinity on corrosion rates for low alloy steels relative to freshwater conditions [4.15]*

A similar trend was found by Uhlig and Morrill who studied the effect of salinity on the corrosion rates for an 18Cr-8Ni stainless steel and a mild steel [4.16]. It was found that increasing the salinity, increased the corrosion rate for the mild steel (uniform corrosion) until approximately 3%NaCl, salinities above 4% actually reduced the corrosion rates below that of freshwater (Figure 4.4). However, for the stainless steel the corrosion rate (pitting corrosion) increased until 4%NaCl before decreasing at greater salinity levels. They also

attributed this trend with the limited solubility of oxygen with increasing salt concentrations.

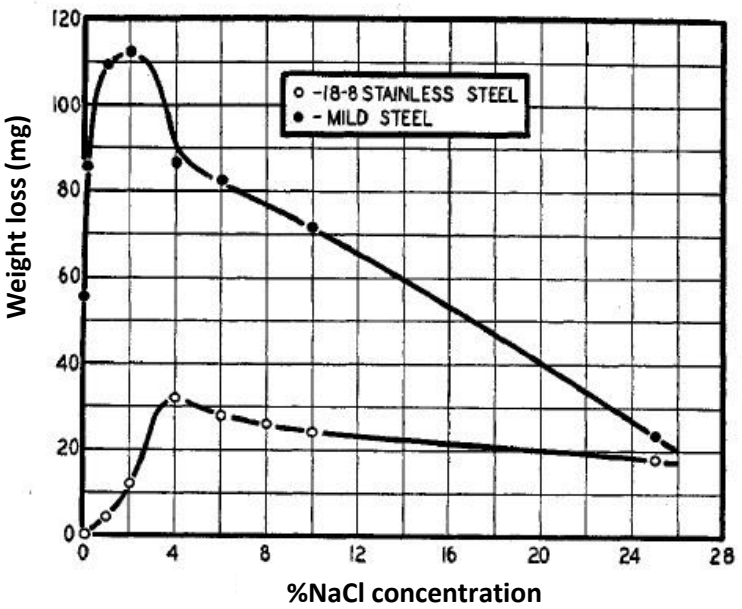

Figure 4.4: *Weight loss for a mild steel and stainless steel for different salt concentrations [4.16]*

Hasan compared the corrosion rates of a low alloy steel pipe in three different salinities (distilled water, 0.1N NaCl and 3%NaCl) in various turbulent conditions [4.17]. The corrosion rates were found to increase as the fluid became more turbulent. The study also found that higher salinity levels resulted in higher corrosion rates, with the greatest corrosion rate increase up to 1.5 times greater for 3%NaCl compared to distilled water in the most turbulent condition.

Al-Malahy and Hodgkiess compared the breakdown potentials of UNS S43000 and UNS S31603 in two different salinities (35,000ppm and 55,000ppm) at temperatures of 25°C and 45°C in static, flowing (3m/s) and liquid jet impingement (95m/s) conditions [4.8]. Results on the effect of salinity were inconclusive, in some situations there was a reduction in breakdown potentials, as would be expected, but there were also conditions where the breakdown potential increased with salinity.

It should be noted that there have only been limited studies assessing the effect of salinity under corrosive wear conditions. A study by Chen et al. assessed the effect of different salt

concentrations (0.5, 1, 2, 3 and 4%NaCl) on Inconel 625 and SS316 under pin on disk conditions [4.18]. In terms of corrosion rates, it was found that the corrosion rates increased until 3%NaCl salinity then began to decrease. This links with some of the previous studies conducted under static conditions.

Another study by Tomlinson and Talks compared a range of cast irons under cavitating conditions in three different salinities (distilled water, 0.02%NaCl and 3%NaCl) [4.19]. For all cast irons, the wear rate was found to increase with increasing salinity. A nitrided pearlitic cast iron with carbides demonstrated the largest wear rate increase, almost 20 times.

4.2.4 Effect of cathodic protection

Cathodic protection can be achieved by supplying a flow of negative charge aimed at eliminating any metal dissolution. As described in Chapter 2.4.5.3, there are two types of cathodic protection which can be applied – Impressed current (ICCP) and sacrificial anode (SACP). The ICCP method requires a DC or AC with rectifier power supply with an auxiliary electrode whereas the SACP method uses a zinc, aluminium or magnesium based alloy to create a galvanic cell which provides the electrical current required for cathodic protection.

Both types of cathodic protection systems are commonly used in the oil and gas industry to prevent corrosion occurring on offshore rig structures, and external corrosion on wells and pipelines [4.15]. Cathodic protection systems and coatings such as galvanising are also used on offshore wind energy devices to protect the structures from the corrosive seawater [4.20].

A study by Young and Hodgkiess found that a paint containing zinc particles could effectively protect austenitic stainless steels (UNS 304000 and UNS S31603) from crevice corrosion in static 3.5%NaCl aqueous solution [4.21]. The study also demonstrated that the zinc containing coatings could protect a low alloy steel in static conditions for a few days before the steel began to corrode.

Work by Okada et al. assessed a zinc coated S35C steel and the influence of cavitation erosion on corrosion fatigue [4.22]. The study found that the zinc coated steel increased the fatigue strength of the steel under the cavitation erosion conditions. Another study by Yaro

et al. found that the consumption of zinc anode protecting a copper pipe, increased when the salinity level, temperature and flow velocity increased [4.23].

ICCP has been used widely in studies to demonstrate the benefits of using cathodic protection in improving the erosion-corrosion resistance of a wide range of materials. However, there is no data in the literature demonstrating the use of SACP in solid-liquid erosion-corrosion conditions.

Giourntas et al. demonstrated that ICCP can reduce the mass loss for a low alloy steel (UNS G10400) and a stainless steel (UNS S31600) under normal impingement solid-liquid conditions (3.5%NaCl, 19m/s with 150mg/l sand concentration) [4.5]. Neville and Hodgkiess also demonstrated that ICCP could significantly reduce the erosion-corrosion damage of UNS S32760, UNS N00625 and UNS AMS5387) by eliminating the corrosion-related damage [4.24]. ICCP can also reduce the erosion-corrosion damage of a cermet (HVOF WC-Co) as demonstrated by Andrews et al. [4.25].

4.3 Literature review conclusions and experimental objectives

The review of the literature demonstrated that a significant amount of work has been conducted comparing the erosion-corrosion resistance of low alloy and stainless steels as well as comparing different stainless steel grades. The main observations were that the passive films caused the stainless steels to exhibit better erosion-corrosion resistance than the low alloy steel, however, under cathodic protection conditions (pure mechanical damage), the stainless and low alloy steels performed similarly. For higher alloy grade stainless steels, the higher alloying content resulted in better corrosion resistance than the lower grade stainless steels but had no effect on improving the resistance to mechanical damage.

From the literature, it is also evident that virtually no research has been conducted to assess the effect of salinity on the erosion-corrosion behaviour of low alloy steels and stainless steels. As the demand for the hydraulic fracturing industry to use more saline and recycled water increases, the corrosiveness of the fluid will increase dramatically. Therefore, a significant part of this study will assess the effect of salinity on the erosion-corrosion resistance of the current and potential fluid end materials.

It is also apparent, that there is a lack of research assessing the potential of using cathodic protection, in the form of sacrificial anodes/coatings, to reduce the erosion-corrosion damage of engineering steels.

4.4 Materials and methods

The alloys selected in this study are stated below:

- High strength low alloy steel (UNS G43400) which is the main alloy currently being used as the fluid end material.
- Precipitation hardened martensitic stainless steel (UNS S15500) which is considered as a possible alternative material due to its high yield strength and reasonable corrosion resistance. This alloy has been modified by the industrial sponsor to improve its yield strength and impact toughness.
- Superduplex stainless steel (UNS S32760) is also considered due to its excellent corrosion resistance.
- Austenitic stainless steel (UNS S31600) is used as a reference material due to its good corrosion resistance in various environments.

The nominal chemical compositions of the low alloy steel and stainless steels are illustrated in Table 4.1. Table 4.2 shows the densities and measured hardness of the test materials.

Table 4.1: *Nominal chemical composition (wt%) of the low alloy steel and stainless steels*

Material	C	Cr	Ni	Mn	Si	Mo	S	N	P	Cu	Fe
UNS G43400	0.37-0.43	0.7-0.9	1.65-2	0.6-0.8	0.15-0.3	0.2-0.3	0.04	-	0.035	-	Bal
UNS S15500	0.07 max	14-15.5	3.5-5.5	1 max	1 max	-	0.03 max	-	0.04	2.5-4.5	Bal
UNS S32760	0.03 max	24-26	6-8	1 max	1 max	3-4	0.01 max	0.2-0.3	0.03 max	0.5-1	Bal
UNS S31600	0.08 max	16-18	10-14	2 max	0.75 max	2-3	0.03 max	0.1 max	0.045 max	-	Bal

Table 4.2: *Densities and measured hardness values of the test materials*

Material	Density (g/cm^2)	Hardness (HV – 5kgf)
UNS G43400	7.85	300
UNS S15500	7.80	360
UNS S32760	7.80	265
UNS S31600	8.00	170

A commercially available zinc anode (supplied by MG Duff) and a zinc particle containing paint (Zinga) was used to assess the potential of SACP to reduce erosion-corrosion damage of the low alloy steel. Table 4.3 demonstrates the chemical composition of the zinc anode (supplied by vendor).

Table 4.3: *Chemical composition of the zinc anode*

Element	Cu	Al	Fe	Cd	Pb	Zn
Wt%	0.05	0.01-0.5	0.005	0.025	0.006	Bal

Figures 4.5-4.8 display the microstructures of the test materials. The low alloy steel (UNS G43400) and precipitation hardened UNS S15500 stainless steel comprises tempered martensite with retained austenite. The Superduplex (UNS S32760) stainless steel possesses the typical 50% ferrite and 50% austenite microstructure. The stainless steel (UNS S31600) demonstrates an austenitic structure with delta ferrite grain boundaries**.**

Figure 4.5: *The microstructure of UNS G43400 with tempered martensite and retained austenite*

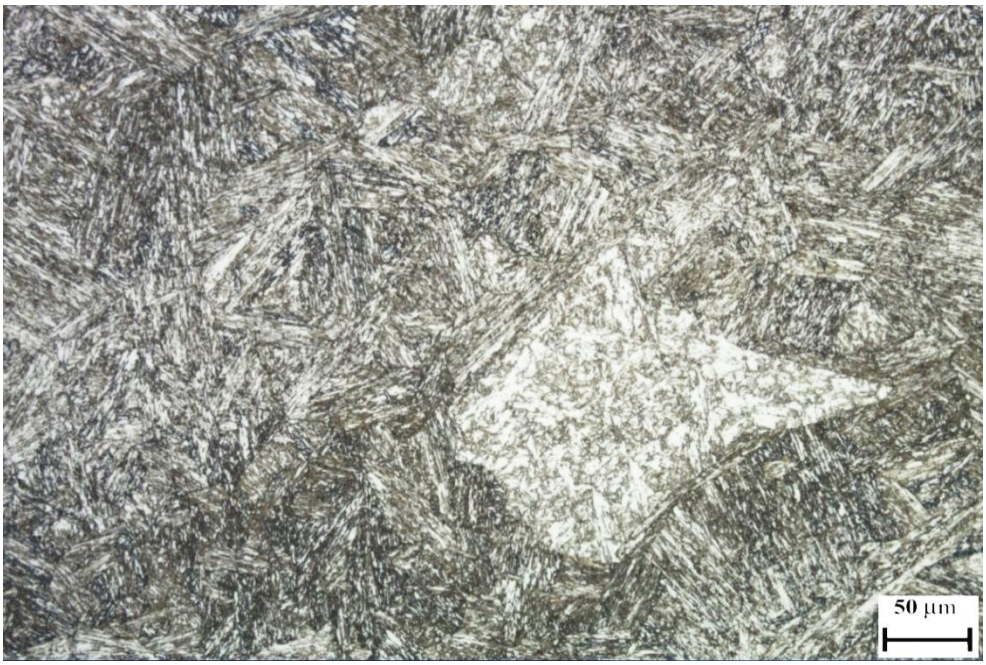

Figure 4.6: *The microstructure of UNS S15500 with tempered martensite and retained austenite*

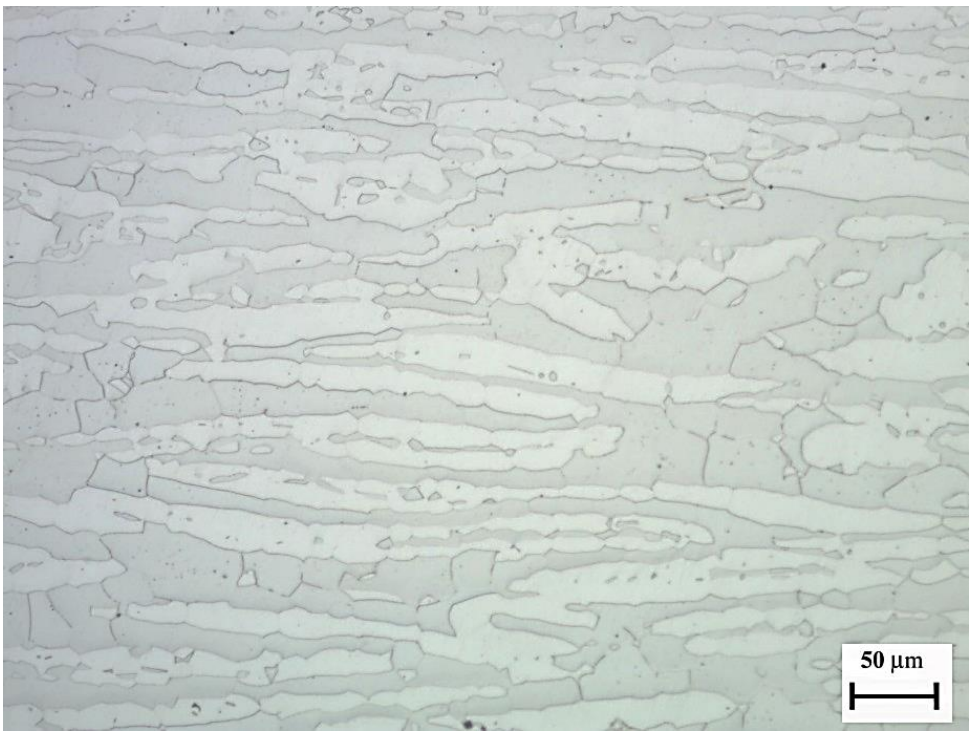

Figure 4.7: *The microstructure of UNS S32760 with equal grains of ferrite and austenite*

Figure 4.8: *The microstructure of UNS S31600 containing austenite with delta ferrite (dark phase) formed in the grain boundaries*

The erosion-corrosion testing was conducted in the slurry jet impingement test apparatus as described in Chapter 3.3.1. The duration of the tests was 1 hour and the nozzle diameter was 4mm. Three different salinity levels (0.05%NaCl - freshwater, 3.5%NaCl - seawater, and 10%NaCl – brine) were chosen to assess the effect of salinity on the erosion-corrosion behaviour of the test materials. The temperature of the aqueous solution was 40±2°C and the velocity of the impinging jet was 18m/s. The sand concentration was 0.5g/l. After FEC tests, the low alloy steel, UNS G43400 specimens, were immersed in an inhibited acidic solution (Clark's solution) in order to remove the corrosion product from the test surface prior to weighing. Cathodic protection was applied through the ICCP and SACP methods described in Chapter 3.3.5 and potentiodynamic polarisation scans were conducted using the methodology described in Chapter 3.3.4.

4.5 Results

4.5.1 Volume loss measurements

The measured mass losses for the test materials were converted into total volume losses by using the densities of the materials stated in Table 4.2. This facilitated a more accurate comparison between the test materials. Figure 4.9 demonstrates the total average volume losses with scatter bands representing the 4 replicates tested under the three different saline environments. It is evident that there were marginal increases in total volume loss for the stainless steels as the salinity of the solution was increased. For the low alloy steel (UNS G43400) there was a significant increase in total volume loss as the salinity was further increased from 0.05%NaCl to 3.5%NaCl. However, as the salinity was increased to 10%NaCl there was no discernible increase in erosion-corrosion damage. The Superduplex stainless steel (UNS S32760) demonstrated the lowest total volume loss compared to the other test materials in all salinity levels. When ICCP was applied, there was a significant reduction in total volume loss for the low alloy steel, as would be expected. A marginal reduction in total volume loss was observed for the stainless steel alloys when ICCP was applied.

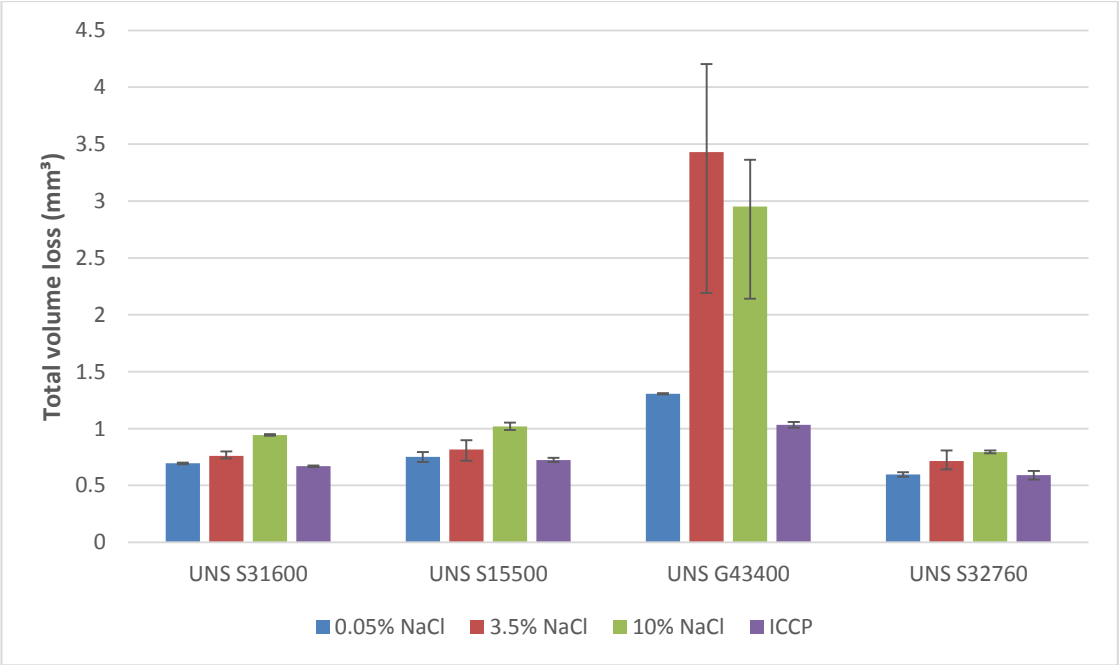

Figure 4.9: *Total volume losses of the test materials in the different saline conditions*

Erosion-corrosion tests (3.5%NaCl aqueous solution) were also conducted with the low alloy steel coupled with a sacrificial anode and also covered by a sacrificial coating. Figure 4.10 illustrates the total volume loss for the low alloy steel in FEC, ICCP and SACP conditions. A minimum of three replicates were conducted in each testing environment. A significant reduction in material loss was observed when ICCP and SACP were applied. The results demonstrate that SACP (anode and coating) is clearly as beneficial as applying ICCP.

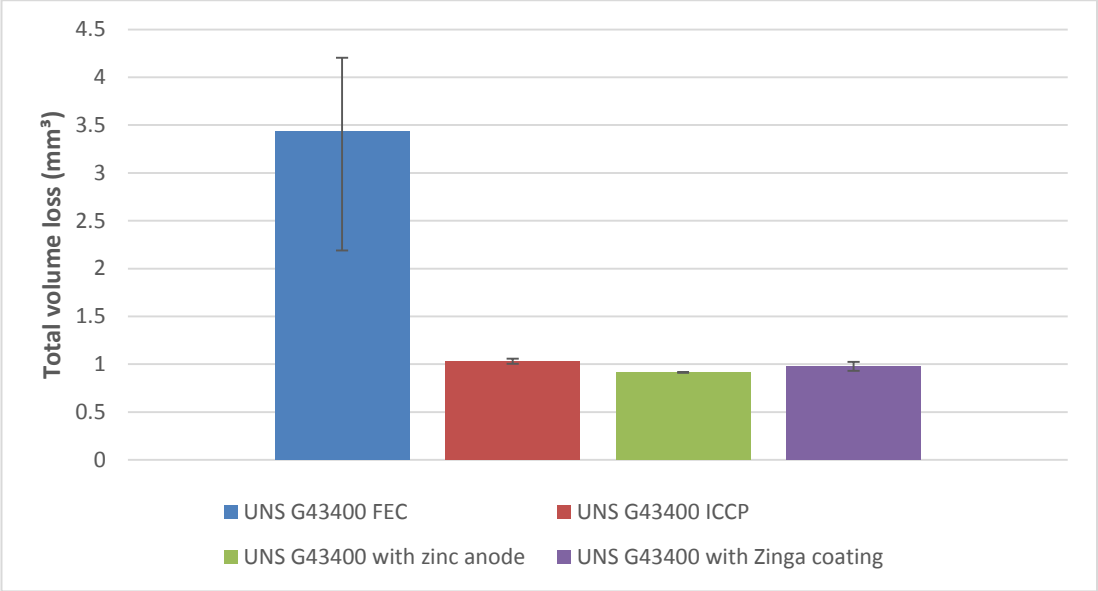

Figure 4.10: *Total volume losses for UNS G43400 in FEC, ICCP and SACP testing conditions*

4.5.2 Electrochemical monitoring

4.5.2.1 Potentiodynamic scans

Figures 4.11 – 4.13 show the anodic polarisation scans conducted for UNS S15500 in each wear region (DIZ and OA – discussed in Chapter 3.5.3) under solid-liquid conditions at the three different salinity levels. The anodic polarisations scans for the remaining test materials are shown in Appendix A. The anodic polarisation scans were conducted after the stabilisation of the free corrosion potential (E_{corr}) and by using the same methodology as described in Chapter 3.3.4. The electrode potentials have been normalised for better comparison purposes due to the large differences between the two areas and represents the electrode potential at a minimum of 25mV more negative than E_{corr}. The current densities were found to be greater in the direct impinged zone (DIZ) than the outer area (OA) for all materials and in all test environments. This can be attributed to the more aggressive nature of the solid-liquid conditions which occur directly beneath the impinging jet. The stainless steels also exhibited fluctuations in current density for all test environments due to de-passivation/re-passivation events occurring from the sand particles removing the passive oxide film and then the reforming of the oxide film. The low alloy steel exhibited active behaviour in both zones for all three salinity levels.

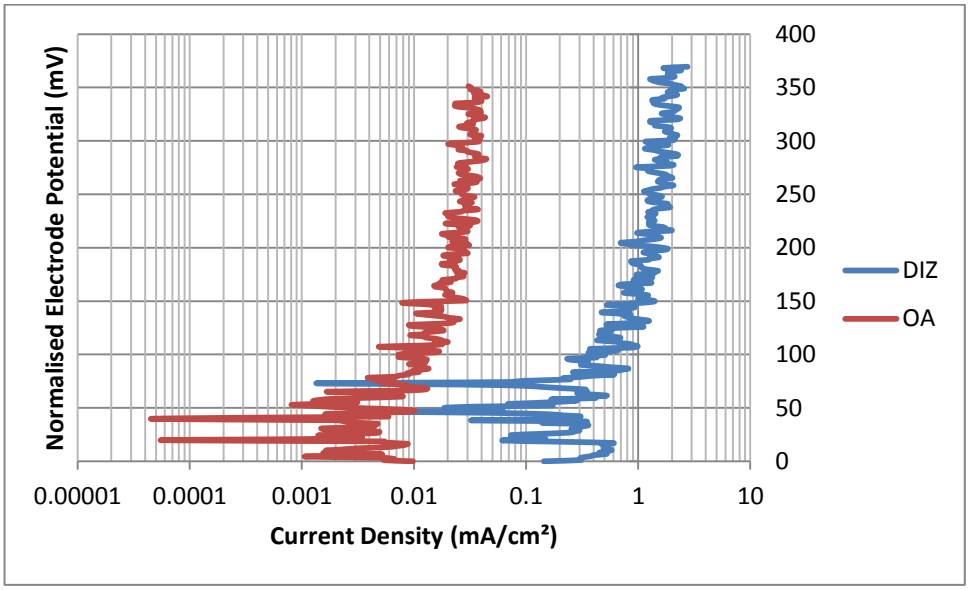

Figure 4.11: *Anodic polarisation scans on both wear regions of UNS S15500 in 0.05%NaCl solid-liquid conditions*

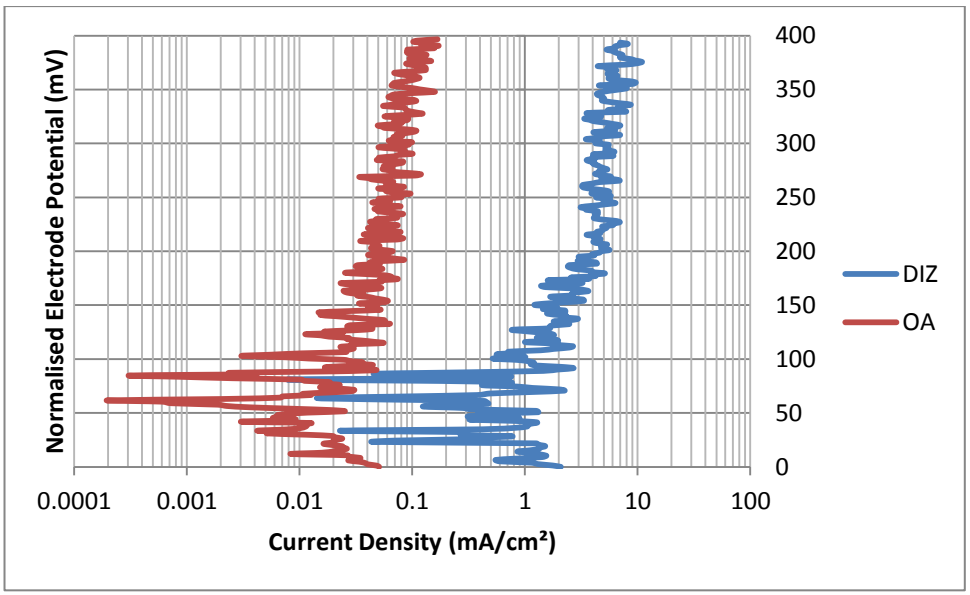

Figure 4.12: *Anodic polarisation scans on both wear regions of UNS S15500 in 3.5%NaCl solid-liquid conditions*

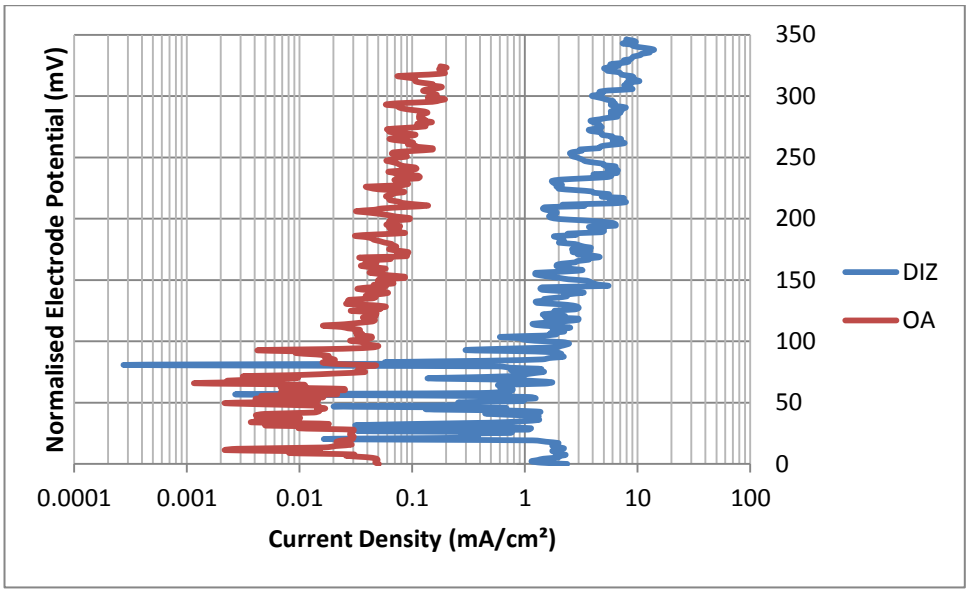

Figure 4.13: *Anodic polarisations on both wear regions of UNS S15500 in 10%NaCl solid-liquid conditions*

The E_{corr} values of both segmented regions as well as the Tafel extrapolated current densities for each test material in each test environment are given in Tables 4.4-4.6. Faraday's law (Chapter 2.4.1) was used to convert the corrosion current densities into mass loss which were then converted to volume loss through material densities. The corrosion current densities were found to be significantly greater in the DIZ compared to the OA for all test materials. This would be expected as the erosion-corrosion conditions are more severe directly underneath the nozzle. However, as the OA has a larger exposed surface area than the DIZ (11cm^2 compared to 0.2cm^2), the volume loss due to corrosion was found to be greater for the low alloy steel in each salinity level and similar for the stainless steels.

Table 4.4: *Measured free corrosion potentials (E_{corr}), corrosion current densities and calculated volume losses on both segmented wear regions for all materials in 0.05%NaCl solid-liquid conditions*

Material	DIZ (A=0.2cm^2)			OA (A=11cm^2)		
	E_{corr} (mV)	Corrosion current density (mA/cm^2)	Corrosion volume loss (mm^3/hr)	E_{corr} (mV)	Corrosion current density (mA/cm^2)	Corrosion volume loss (mm^3/hr)
UNS G43400	-470	0.20	0.005	-421	0.0500	0.073
UNS S15500	-414	0.22	0.006	-436	0.0120	0.017
UNS S32760	-525	0.22	0.006	-380	0.0090	0.007
UNS S31600	-380	0.21	0.006	-407	0.0045	0.013

Table 4.5: *Measured free corrosion potentials (E_{corr}), corrosion current densities and calculated volume losses on both segmented wear regions for all materials in 3.5%NaCl solid-liquid conditions*

Material	DIZ (A=0.2cm^2)			OA (A=11cm^2)		
	E_{corr} (mV)	Corrosion current density (mA/cm^2)	Corrosion volume loss (mm^3/hr)	E_{corr} (mV)	Corrosion current density (mA/cm^2)	Corrosion volume loss (mm^3/hr)
UNS G43400	-553	1.2	0.032	-530	0.900	1.323
UNS S15500	-438	1.1	0.029	-435	0.030	0.044
UNS S32760	-522	0.35	0.009	-312	0.006	0.009
UNS S31600	-437	1	0.026	-437	0.0150	0.022

Table 4.6: *Measured free corrosion potentials (E_{corr}), corrosion current densities and calculated volume losses on both segmented wear regions for all materials in 10%NaCl solid-liquid conditions*

Material	DIZ (A=0.2cm^2)			OA (A=11cm^2)		
	E_{corr} (mV)	Corrosion current density (mA/cm^2)	Corrosion volume loss (mm^3/hr)	E_{corr} (mV)	Corrosion current density (mA/cm^2)	Corrosion volume loss (mm^3/hr)
UNS G43400	-590	1.5	0.04	-555	0.600	0.882
UNS S15500	-437	0.6	0.03	-407	0.030	0.044
UNS S32760	-546	0.4	0.01	-350	0.004	0.006
UNS S31600	-419	1.1	0.03	-433	0.018	0.026

Figures 4.14 – 4.16 illustrate the anodic and cathodic polarisations for the full specimens (38mm diameter) of each test material under solid-liquid conditions for the three different salinity levels. The anodic and cathodic polarisations of the test materials under static and flowing conditions are given in Appendix A. The electrode potentials are normalised for an easier comparison. In each test condition and environment, the low alloy steel exhibited active behaviour and the largest current densities compared to the stainless steels. Under solid-liquid impingement conditions, the stainless steels exhibited the periodic de-passivation/re-passivation events caused by the impact of the sand particles. The cathodic polarisation curves for the low alloy steel and in some cases the stainless steels, exhibited concentration polarisation caused by the reduction of oxygen available at the surface for the cathodic reaction to occur.

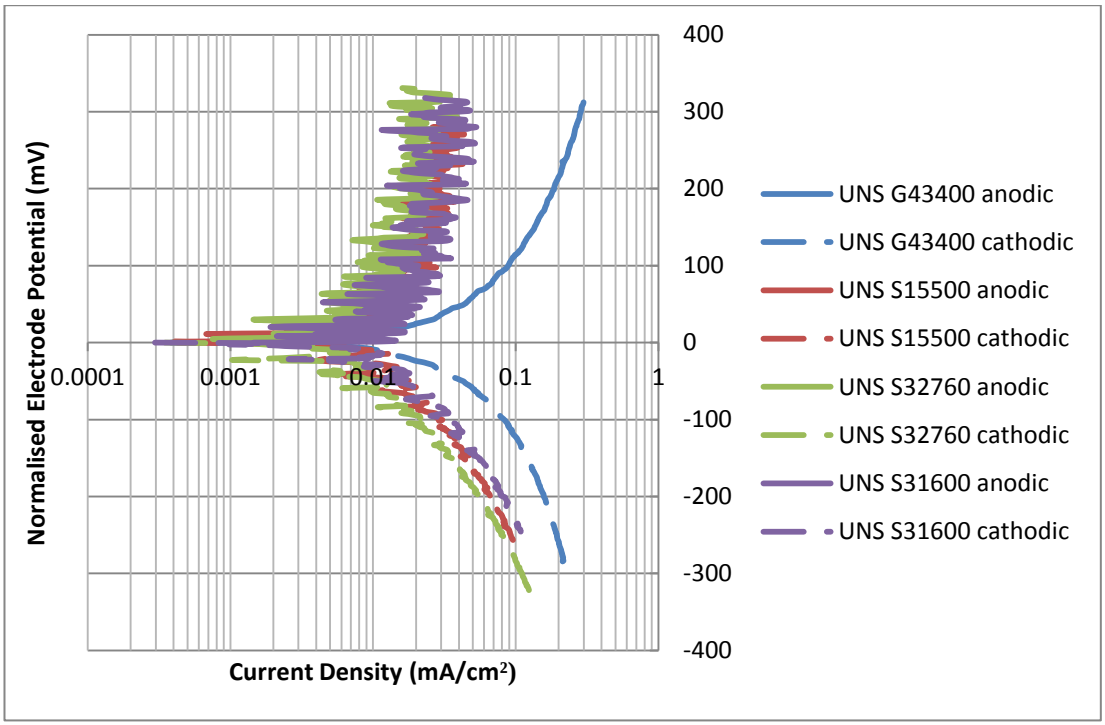

Figure 4.14: *Anodic and cathodic polarisation scans on the full specimen of the tested materials in 0.05%NaCl solid-liquid conditions*

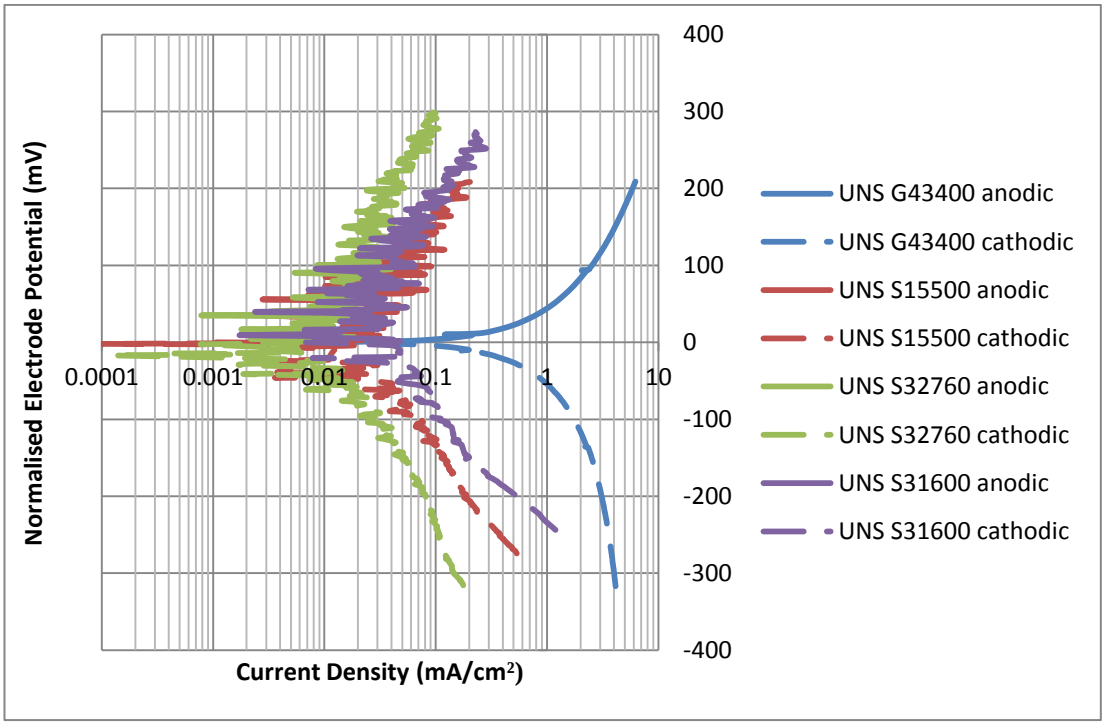

Figure 4.15: *Anodic and cathodic polarisation scans on the full specimen of the tested materials in 3.5%NaCl solid-liquid conditions*

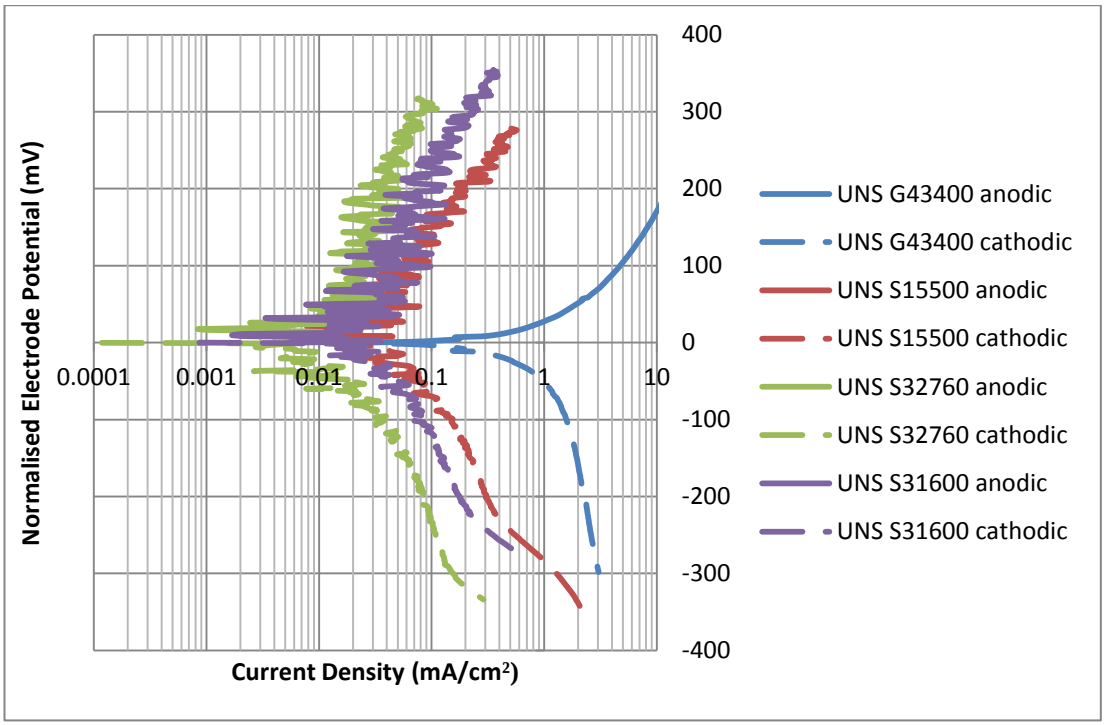

Figure 4.16: *Anodic and cathodic polarisations on the full specimen of the tested materials in 10% solid-liquid conditions*

The E_{corr} values along with corrosion current density and calculated volume loss for the full size specimens are given in Tables 4.7–4.15 for each test material under each test condition and salinity. In general, there was an increase (less negative) in E_{corr} values from static to liquid impingement conditions, this is due to the increase in oxygen available at the surface from the flowing water and hence, there will be increased cathodic rates. Generally, there was an increase in corrosion current density and hence, volume loss due to corrosion as the test conditions became more aggressive (from static to solid-liquid conditions). The low alloy steel exhibited the greatest corrosion rates compared to the other test materials in all environments as would be expected. In static conditions, the corrosion rates were found to increase with increasing salinity for all test materials, this observation is not in agreement with previous limited studies for low alloy and stainless steels [4.15, 4.16, 4.18]. In flowing conditions, there was found to be an increase in corrosion rates from 0.05%NaCl to 3.5%NaCl but corrosion rates were found to decrease or remain the same when the salinity was increased to 10%NaCl for all test materials (except UNS S15500 where the corrosion rates increased with increasing salinity). In solid-liquid conditions, the corrosion rates of the UNS S15500 and UNS G43400 were found to increase with increasing salinity, however, the

corrosion rates of the UNS S32760 and UNS S31600 were found to increase from 0.05%NaCl to 3.5%NaCl before decreasing slightly when the salinity was increased to 10%NaCl.

Table 4.7: *Measured free corrosion potential (E_{corr}), corrosion current density and calculated corrosion volume loss for the full specimen of the tested materials in 0.05% static conditions*

Material	E_{corr} (mV)	Corrosion current density (mA/cm^2)	Corrosion volume loss (mm^3/hr)
UNS G43400	-574	0.0320	0.0485
UNS S15500	-139	0.0005	0.0007
UNS S32760	-138	0.0004	0.0005
UNS S31600	-120	0.0005	0.0007

Table 4.8: *Measured free corrosion potential (E_{corr}), corrosion current density and calculated corrosion volume loss for full specimens of the tested materials in 0.05%NaCl flowing conditions*

Material	E_{corr} (mV)	Corrosion current density (mA/cm^2)	Corrosion volume loss (mm^3/hr)
UNS G43400	-404	0.0410	0.0621
UNS S15500	-112	0.0014	0.0020
UNS S32760	-62	0.0008	0.0012
UNS S31600	-33	0.0008	0.0012

Table 4.9: *Measured free corrosion potential (E_{corr}), corrosion current density and calculated corrosion volume loss for full specimens of the tested materials in 0.05%NaCl solid-liquid conditions*

Material	E_{corr} (mV)	Corrosion current density (mA/cm^2)	Corrosion volume loss (mm^3/hr)
UNS G43400	-393	0.050	0.076
UNS S15500	-404	0.009	0.014
UNS S32760	-412	0.006	0.009
UNS S31600	-369	0.010	0.014

Table 4.10: *Measured free corrosion potential (E_{corr}), corrosion current density and calculated corrosion volume loss for full specimens of the tested materials in 3.5%NaCl static conditions*

Material	E_{corr} (mV)	Corrosion current density (mA/cm^2)	Corrosion volume loss (mm^3/hr)
UNS G43400	-662	0.0700	0.106
UNS S15500	-269	0.0014	0.002
UNS S32760	-247	0.0015	0.002
UNS S31600	-187	0.0011	0.002

Table 4.11: *Measured free corrosion potential (E_{corr}), corrosion current density and calculated corrosion volume loss for full specimens of the tested materials in 3.5%NaCl flowing conditions*

Material	E_{corr} (mV)	Corrosion current density (mA/cm^2)	Corrosion volume loss (mm^3/hr)
UNS G43400	-541	0.825	1.250
UNS S15500	-287	0.007	0.01
UNS S32760	-290	0.007	0.01
UNS S31600	-66	0.002	0.003

Table 4.12: *Measured free corrosion potential (E_{corr}), corrosion current density and calculated corrosion volume loss for full specimens of the tested materials in 3.5%NaCl solid-liquid conditions*

Material	E_{corr} (mV)	Corrosion current density (mA/cm^2)	Corrosion volume loss (mm^3/hr)
UNS G43400	-530	0.540	0.818
UNS S15500	-359	0.013	0.019
UNS S32760	-400	0.009	0.013
UNS S31600	-375	0.028	0.042

Table 4.13: *Measured free corrosion potential (E_{corr}), corrosion current density and calculated corrosion volume loss for full specimens of the tested materials in 10%NaCl static conditions*

Material	E_{corr} (mV)	Corrosion current density (mA/cm^2)	Corrosion volume loss (mm^3/hr)
UNS G43400	-637	0.092	0.139
UNS S15500	-267	0.004	0.005
UNS S32760	-237	0.005	0.007
UNS S31600	-289	0.002	0.002

Table 4.14: *Measured free corrosion potential (E_{corr}), corrosion current density and calculated corrosion volume loss for full specimens of the tested materials in 10%NaCl flowing conditions*

Material	E_{corr} (mV)	Corrosion current density (mA/cm^2)	Corrosion volume loss (mm^3/hr)
UNS G43400	-547	0.460	0.697
UNS S15500	-314	0.011	0.017
UNS S32760	-265	0.007	0.010
UNS S31600	-299	0.006	0.008

Table 4.15: *Measured free corrosion potential (E_{corr}), corrosion current density and calculated corrosion volume loss for full specimens of the tested materials in 10%NaCl solid-liquid conditions*

Material	E_{corr} (mV)	Corrosion current density (mA/cm^2)	Corrosion volume loss (mm^3/hr)
UNS G43400	-542	1.300	1.97
UNS S15500	-399	0.032	0.05
UNS S32760	-419	0.008	0.01
UNS S31600	-431	0.023	0.03

The following findings can be made regarding the corrosion measurements:

- The corrosion rate of the low alloy steel generally increased with salinity due to the increased conductivity of the aqueous solution which caused an increase in corrosion current density.
- The corrosion rate of the stainless steels did not alter much with the increase of salinity with the exception in static conditions from 0.05%NaCl to 3.5%NaCl. The passive films of the stainless steels appear to be adequate to protect the stainless steels regardless of the salinity of the aqueous solution. An interpretation for the increase from 0.05%NaCl to 3.5%NaCl is that the increase in chloride concentration from freshwater to seawater brought about a slight reduction in integrity of passive film. It is well known that chloride ions are detrimental to passive films [4.26].
- In all salinities, the corrosion rate of the low alloy steel increased with the aggressiveness of the hydrodynamic conditions and was always substantially greater than the stainless steels. This would be expected as the increased turbulence of the fluid from static to solid-liquid conditions increases the availability of oxygen at the metal-fluid interface which would increase cathodic reactions and sand particles would be able to remove corrosion product from the surface which exposes a fresh steel surface.
- The corrosion rates of the stainless steels also increased with the aggressiveness of the hydrodynamic conditions, particularly in solid-liquid conditions as their passive films were removed which exposed the surface to the aqueous solution.
- The Superduplex alloy (UNS S32760) demonstrated the lowest corrosion rate at 10%NaCl in flowing and solid-liquid conditions due to its higher alloying content which resulted in a more passive film forming in the aggressive corrosive environment.

4.5.2.2 Open circuit potential measurements – SACP test conditions

Figure 4.17 illustrates the measured galvanic potentials between the low alloy steel and the sacrificial anode and coating during a one hour experiment under solid-liquid conditions. The galvanic potential between the low alloy steel and zinc anode was found to begin at around -940mV and decreased to around -1030mV and remained constant for the rest of

the experiment. This demonstrates that the zinc anode was able to provide full cathodic protection to the low alloy steel successfully under solid-liquid conditions. The galvanic potential between the low alloy steel and Zinga coating began more negative than -800mV before it increased to around -640mV at the end of the test. This increase can be attributed to the reduction in zinc particles within the paint as they are being consumed rapidly under solid-liquid conditions. However, as the galvanic potential is more negative than the free corrosion potential of the low alloy steel under solid-liquid conditions (-530mV), the Zinga coating will be providing some protection to the low alloy steel, although at longer test durations the Zinga coating will no longer be effective.

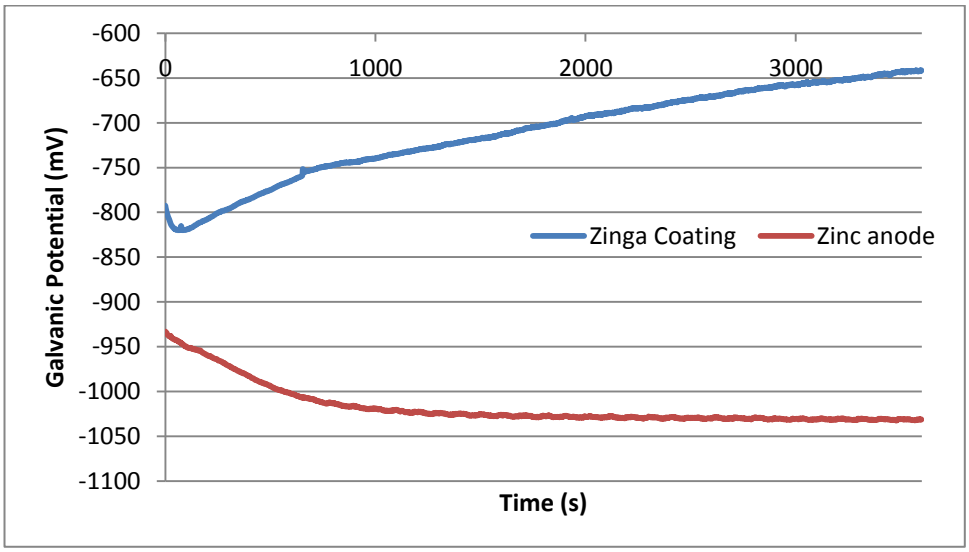

Figure 4.17: *Measured electrode potentials for the galvanic couples (UNS G43400 with zinc anode and Zinga coating) under solid-liquid conditions (3.5%NaCl)*

Further tests were conducted with the Zinga coated low alloy steel to assess how long the coating could provide protection in static and liquid impingement conditions (Figures 4.18 and 4.19). In static conditions (3.5%NaCl aqueous solution), the coating was able to provide full cathodic protection (more negative than -800mv) for about 100 hours before reaching the free corrosion potential of the low alloy steel under static conditions (3.5%NaCl aqueous solution). However, in liquid impingement conditions, full cathodic protection lasted for approximately 1 hour before increasing and reaching the free corrosion potential of the low alloy steel under liquid impingement conditions in 3.5%NaCl.

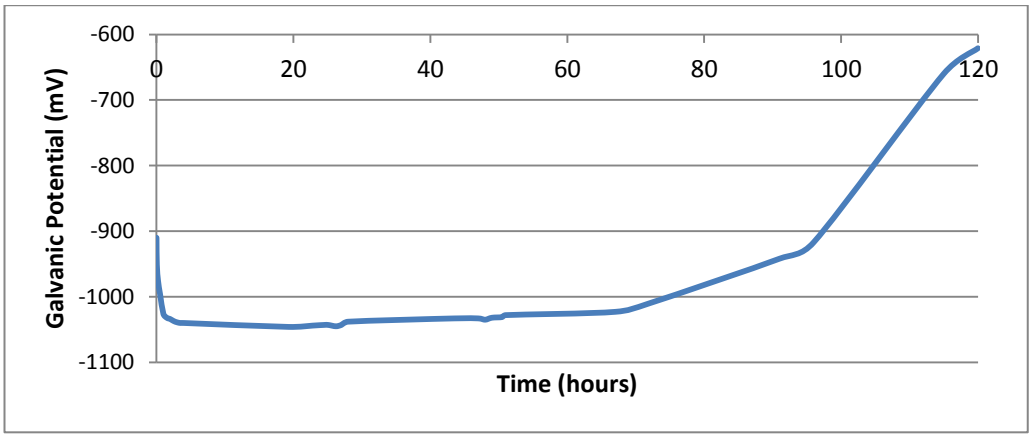

Figure 4.18: *Measured electrode potentials for the galvanic couple – UNS G43400 with Zinga coating under static conditions in 3.5%NaCl aqueous solution*

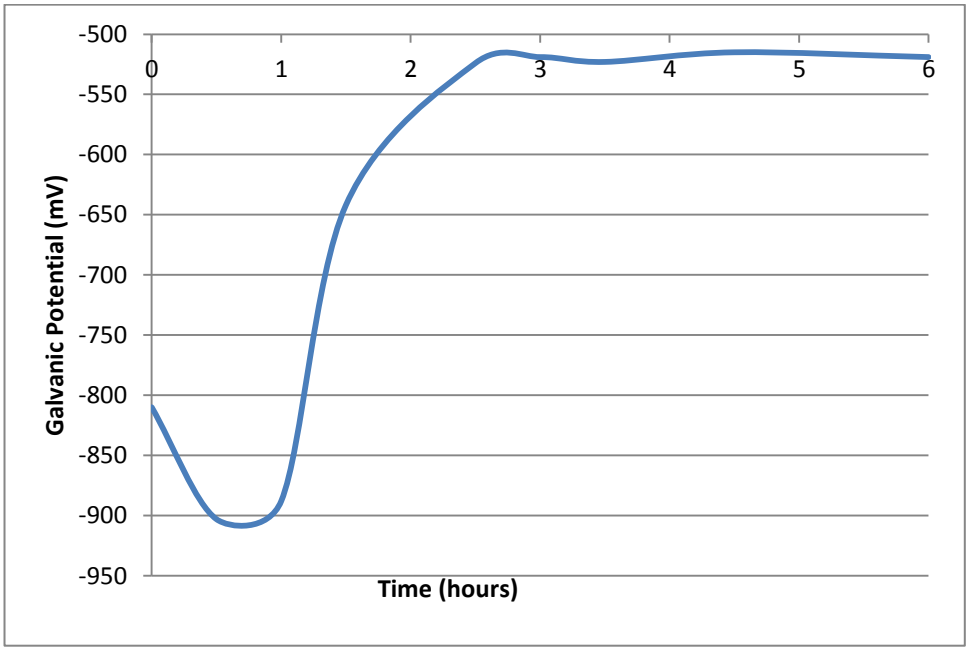

Figure 4.19: *Measured electrode potentials for the galvanic couple – UNS G43400 with Zinga coating under liquid impingement conditions in 3.5%NaCl conditions*

4.5.3 Post-test examination

4.5.3.1 Surface topography

4.5.3.1.1 Macro examination

Figure 4.20 illustrates the macroscopic views of the post-test surfaces directly after the one hour, free-erosion corrosion test (in 3.5%NaCl aqueous solution). The poor corrosion

resistance of the low alloy steel is demonstrated by the extensive corrosion damage outside the wear scar (Figure 4.20a). Whereas, it is evident that there are no corrosion products on the surface of the stainless steels (Figure 4.20b-d) which highlights their superior corrosion resistance.

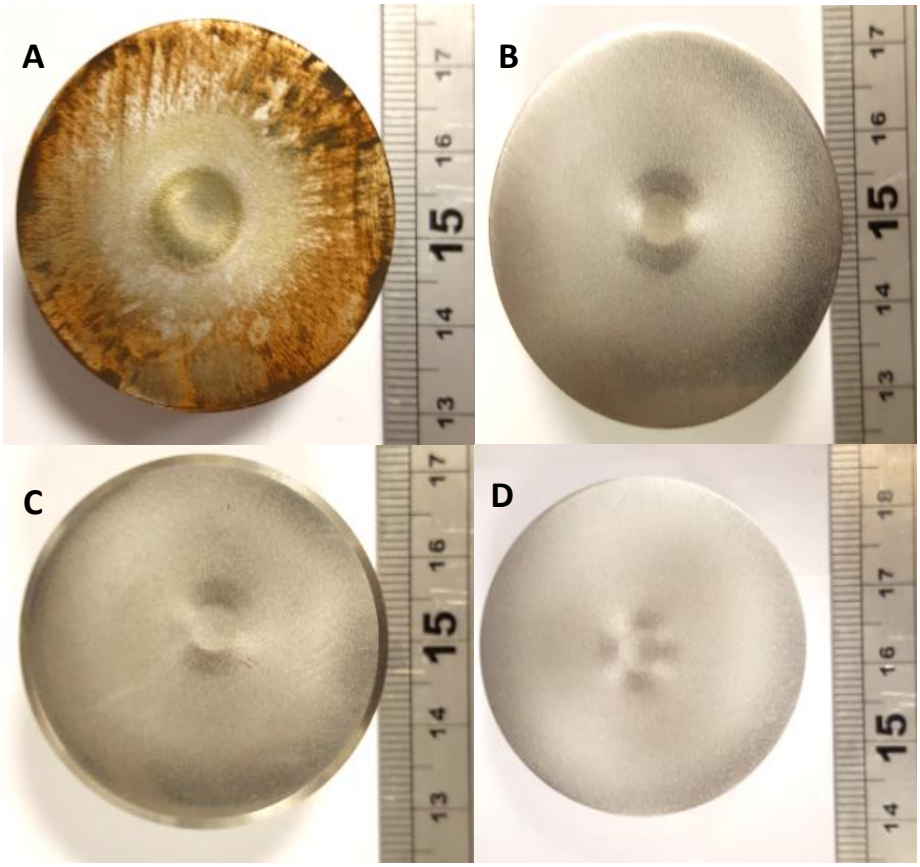

Figure 4.20: *Post-test surfaces of the test materials after 3.5%NaCl solid-liquid conditions: UNS G43400 – A; UNS S15500 – B; UNS S32760 – C; UNS S31600 – D*

Figure 4.21 shows the macroscopic post-test views of the low alloy steel after free erosion-corrosion conditions in 0.05%NaCl and 10%NaCl aqueous solutions. In 0.05%NaCl aqueous solution, the low alloy steel exhibited corrosion damage outside of the wear scar but to a lesser extent than that exhibited in 3.5%NaCl and 10%NaCl aqueous solutions.

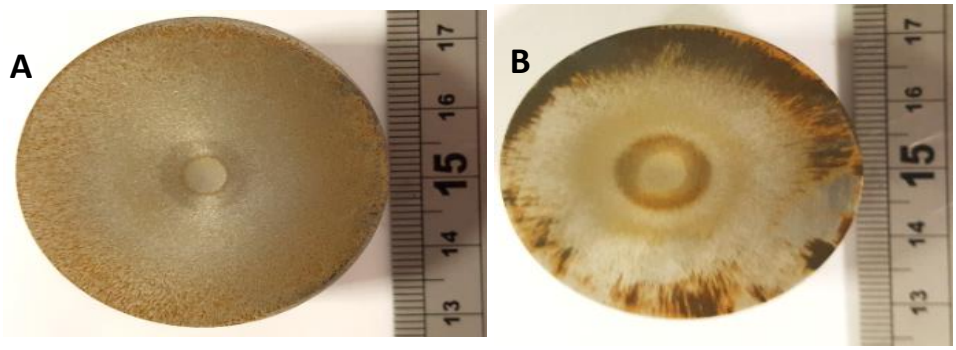

Figure 4.21: *Post-test surface of UNS G43400 after solid-liquid conditions in 0.05%NaCl; - A; 10%NaCl – B*

The beneficial effect of applying cathodic protection to the low alloy steel is highlighted in Figure 4.22. Each of the cathodic protection systems; ICCP, SACP with zinc anode and SACP with Zinga coating were able to suppress corrosion and, hence, no corrosion products were formed on the surface.

Figure 4.22: *Post-test surfaces of the UNS G43400 after solid-liquid conditions: ICCP – A; SACP with zinc anode – B; SACP with Zinga coating - C*

4.5.3.1.2 Micro examination

Microscopic views of the post-test surfaces after 3.5%NaCl solid-liquid experiments were also recorded to assess the corrosive wear damage in the DIZ and the OA. Figure 4.23 illustrates the typical crater-type damage associated with the sand particles impacting the surface at high impingement angles. This damage was observed on both the low alloy steel and stainless steels. However, in the OA, the sand particles impact the surface of the target material at significantly smaller angles and cause sliding abrasion damage, as indicated in Figures 4.24 and 4.25. The low alloy steel (Figure 4.24) also exhibited pitting damage in the OA due its poor corrosion resistance. The stainless steels only exhibited sliding abrasion damage, an example is demonstrated in Figure 4.25.

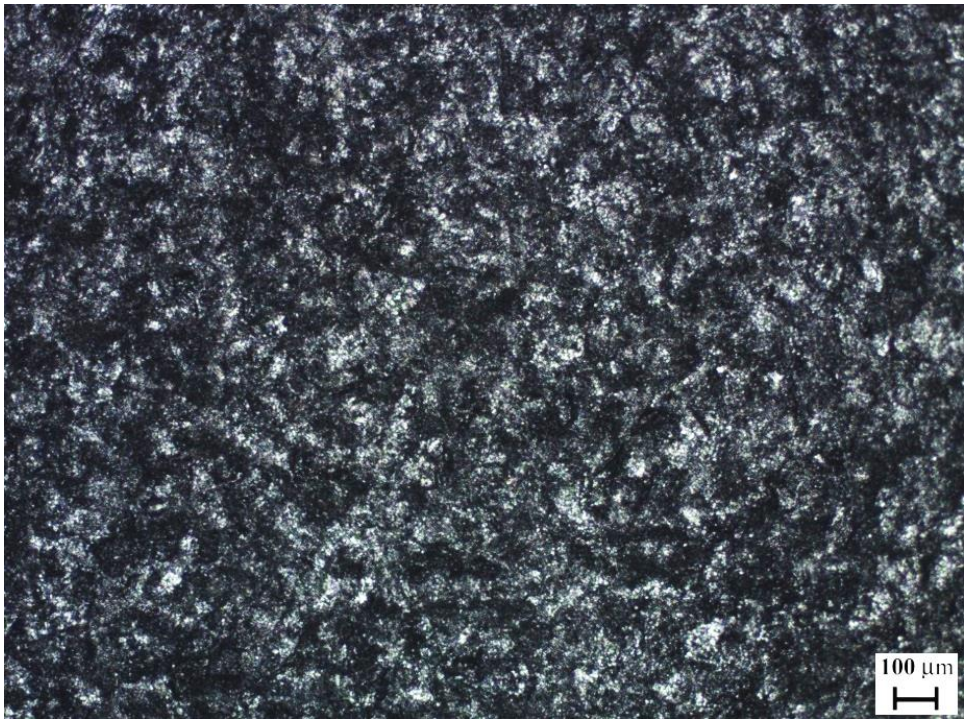

Figure 4.23: *Crater damage in the DIZ of the UNS G43400 in 3.5%NaCl solid-liquid conditions*

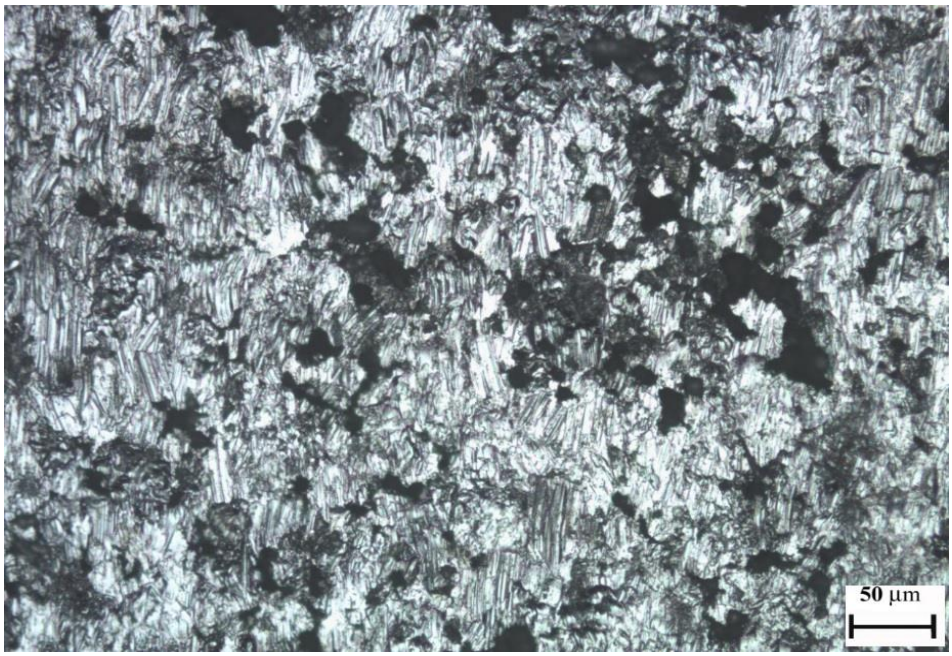

Figure 4.24: *Sliding abrasion marks and pitting damage in the OA of the UNS G43400 in 3.5%NaCl solid-liquid conditions*

Figure 4.25: *Sliding abrasion damage in the OA of the UNS S15500 in 3.5%NaCl solid-liquid conditions*

4.5.3.1.3 Wear scar profile scans

To assess the behaviour of the four alloys in the wear scar, surface profile scans were conducted on the post-test surfaces using the surface topography technique described in Chapter 3.5.2. The scans were conducted for each salinity level in FEC and also in ICCP conditions. Figure 4.26 shows a representative set of wear scar depth plots with the remaining graphs located in Appendix A. Figure 4.27 compares the wear scar profile scans for the low alloy steel in FEC, ICCP, SACP with the zinc anode and Zinga coating. The diameter of the wear scars was found to be about 4.5mm which corresponds to the diameter of the nozzle (4mm) which was used in this study.

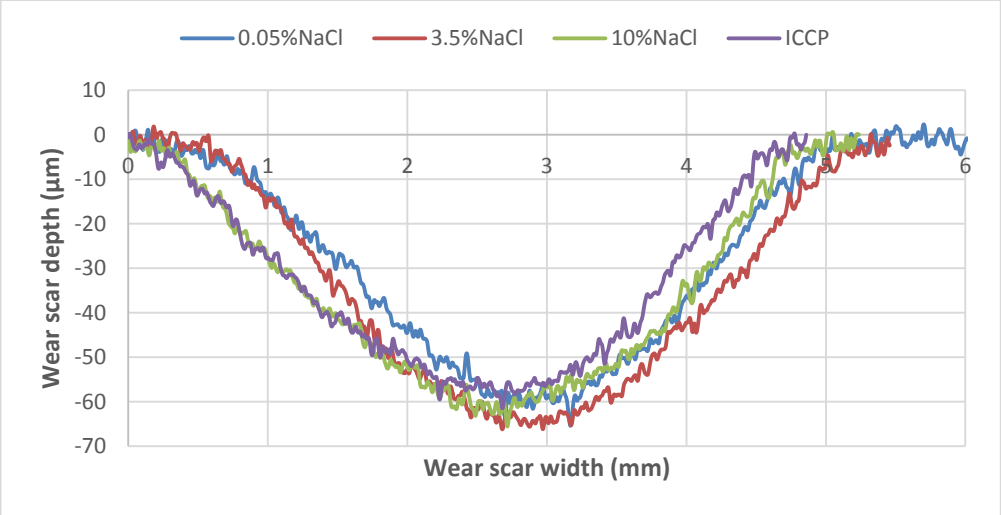

Figure 4.26: *Wear scar profiles for UNS S32760 in each testing environment in solid-liquid conditions*

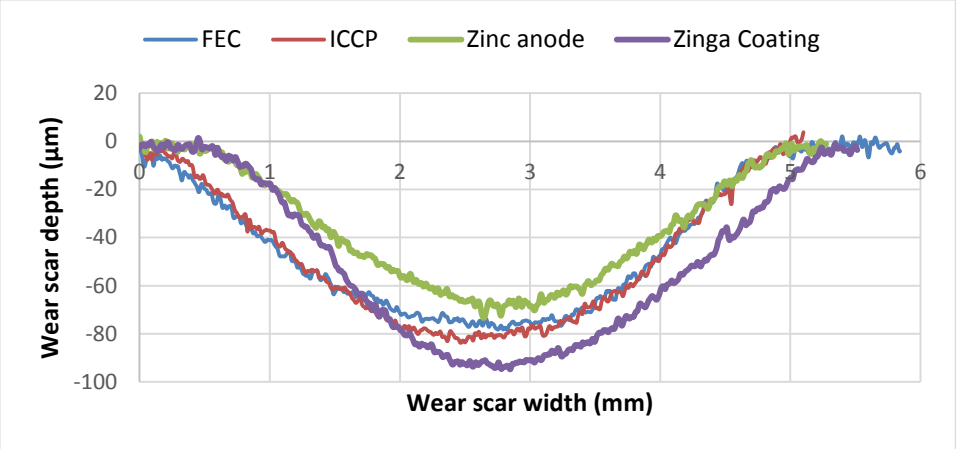

Figure 4.27: *Wear scar profiles for UNS G43400 with the effect of cathodic protection in 3.5%NaCl solid-liquid conditions*

The wear scar depths were broadly similar to the findings observed with the wear scar volume losses. Therefore, the measured wear scar depth graphs are located in Appendix A and the wear scar volume losses will be discussed in detail.

4.5.3.2 Volumetric analysis

The volume measurement of the UNS S15500 stainless steel in the direct impinged zone after a solid-liquid experiment is shown in Figure 4.28. The measurement for the volume was obtained within the region of the red ring which represents the area located directly beneath the nozzle. The surface topography method described in Chapter 3.5.2 was followed.

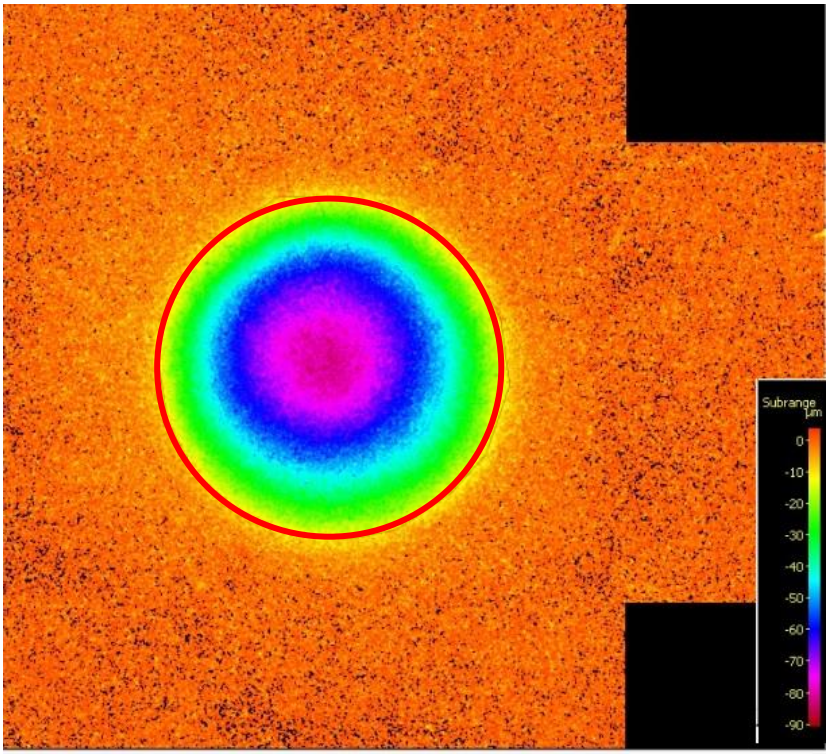

Figure 4.28: *Volumetric analysis on the wear scar of the UNS S15500 stainless steel surface after solid-liquid conditions*

The volume losses in the DIZ for each test material under each test condition is given in Figure 4.29. There were marginal increases in volume loss for the test materials as the salinity level was increased. The low alloy steel demonstrated the greatest volume loss in

the DIZ in all test conditions when compared to the stainless steels. Similar to the wear scar depths, there were marginal differences between the stainless steels in all test conditions. The effect of cathodic protection on the wear scar volume loss was observed to be minor for the tested materials.

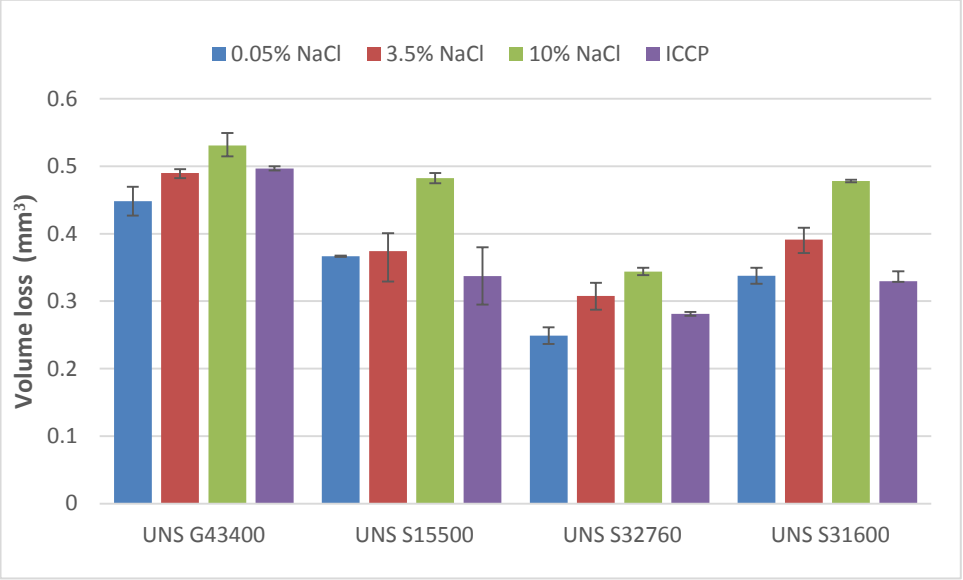

Figure 4.29: *Comparison of volume losses in the DIZ of the four test materials under solid-liquid test conditions in each level of salinity and in ICCP*

Figure 4.30 demonstrates the volume losses in the DIZ for the low alloy steel in FEC, ICCP and both SACP conditions. A similar trend was found with the wear scar depths as the volume losses were similar in all test conditions with an exception of the SACP with zinc anode, where there was a marginal decrease in volume loss compared to the other test conditions.

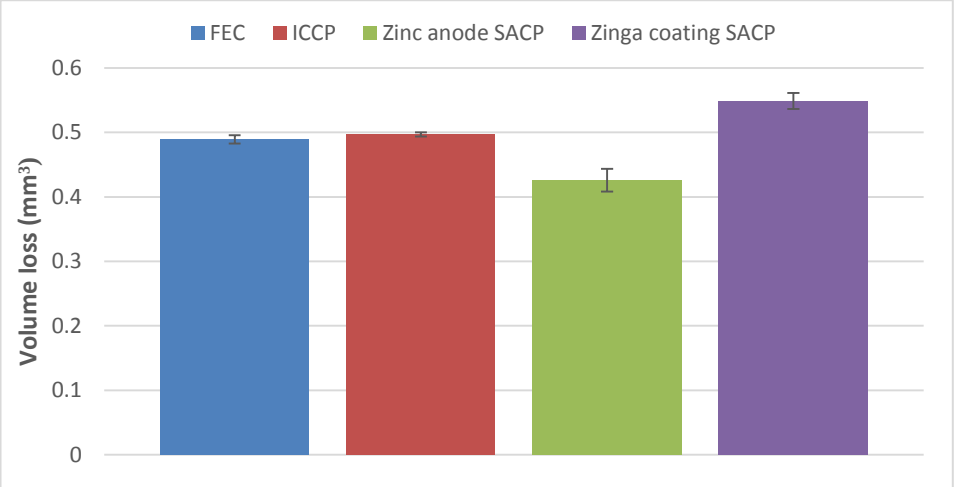

Figure 4.30: *Comparison of volume losses in the DIZ for the UNS G43400 under solid-liquid conditions in FEC and for the three different cathodic protection methods*

4.6 Discussion

4.6.1 Total Volume Loss (TVL) in free erosion-corrosion (FEC) conditions

As demonstrated in Figure 4.9, there were marginal increases with salinity in terms of total volume loss for the stainless steels. However, there was a substantial increase in total volume loss in the low alloy steel as the salinity was increased from freshwater (0.05%NaCl) to seawater (3.5%NaCl). When the salinity was increased to a brine (10%NaCl), the total volume loss of the low alloy steel was found to be similar to that of seawater conditions. The trend in this study of the stainless steel and the low alloy steel in increasing salinity matches well with findings from previous studies [4.18, 4.19]. The poor erosion-corrosion resistance of the low alloy steel compared to the stainless steels have also been observed in past studies [4.1–4.4]. The main cause of this finding is a result of the poor corrosion resistance of the low alloy steel which is detrimental to its overall erosion-corrosion performance, whereas, the passive film of the stainless steels provides some resistance to corrosion damage and, hence, results in an improved erosion-corrosion resistance.

Discrimination of the TVL in the DIZ and OA

The volume loss in the OA can be calculated from Eq. 3.4, as the total volume loss (TVL) is calculated from the measured total mass loss after the FEC experiments and from the measured volume losses in the direct impinged zone (DIZ), given in Figure 4.29. Figures 4.31-4.33 show the breakdown of the total volume into the volume losses in the two wear

regions under 0.05%, 3.5% and 10%NaCl solid-liquid conditions. In all test environments, the low alloy steel exhibited the greatest volume loss in both the DIZ and OA (particularly accentuated most in the OA) compared to the other test materials. The volume loss in the OA for the low alloy steel was found to be a substantial proportion of the overall damage. This can be mainly attributed to the poor corrosion resistance of the low alloy steel in FEC test conditions. Another notable difference is that the marginally improved erosion-corrosion resistance of UNS S32760 was found in the DIZ, where high angle erosion occurs, and that its erosion-corrosion performance was similar to the other stainless steels in the OA, where low angle erosion occurs. Previous studies have found that a strong link between sliding abrasion resistance and material hardness [4.27–4.29]. Therefore, the similar volume loss in the OA for the stainless steels is due to their similar hardness.

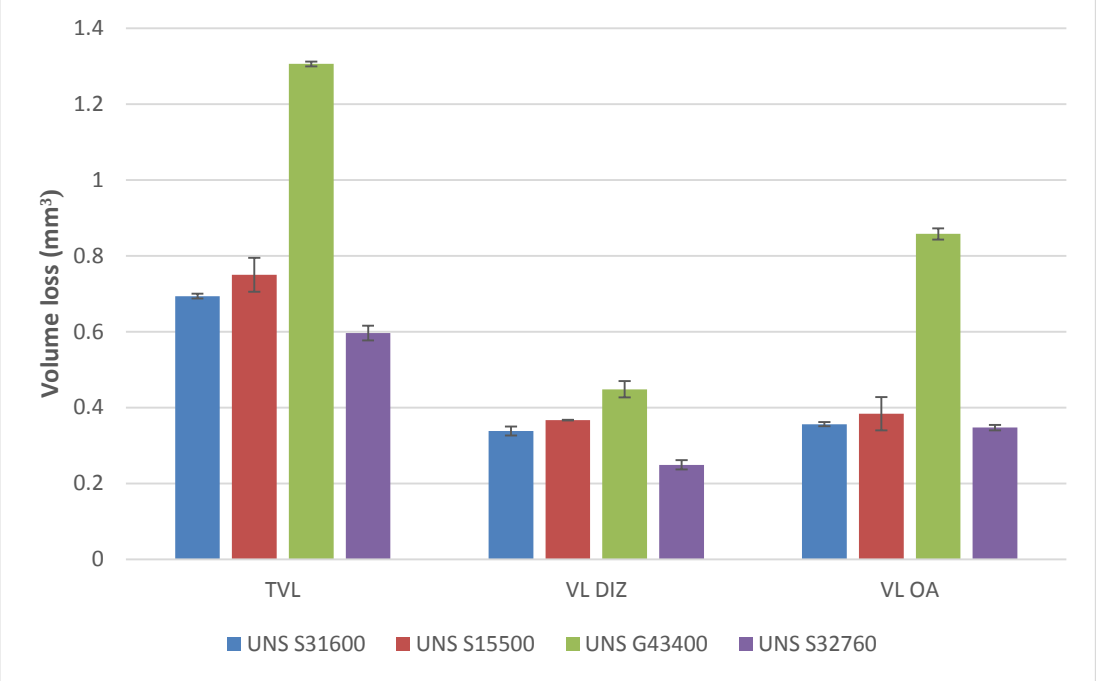

Figure 4.31: *Breakdown of the total volume loss into volume loss in the two distinct wear regions under 0.05%NaCl solid-liquid conditions*

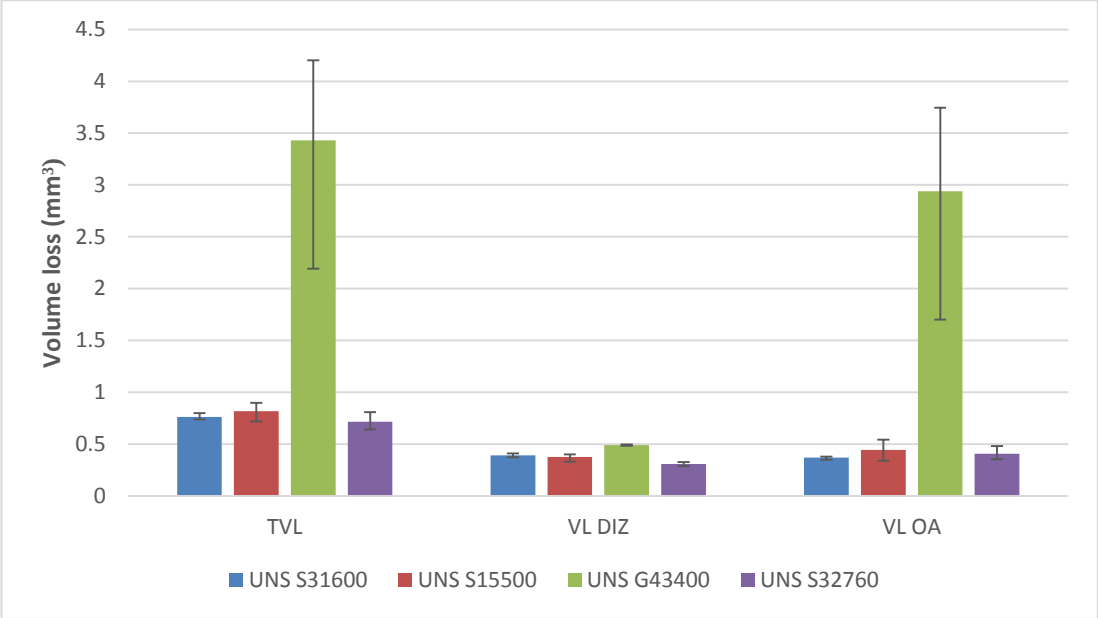

Figure 4.32: *Breakdown of the total volume loss into volume loss in the two distinct wear regions under 3.5%NaCl solid-liquid conditions*

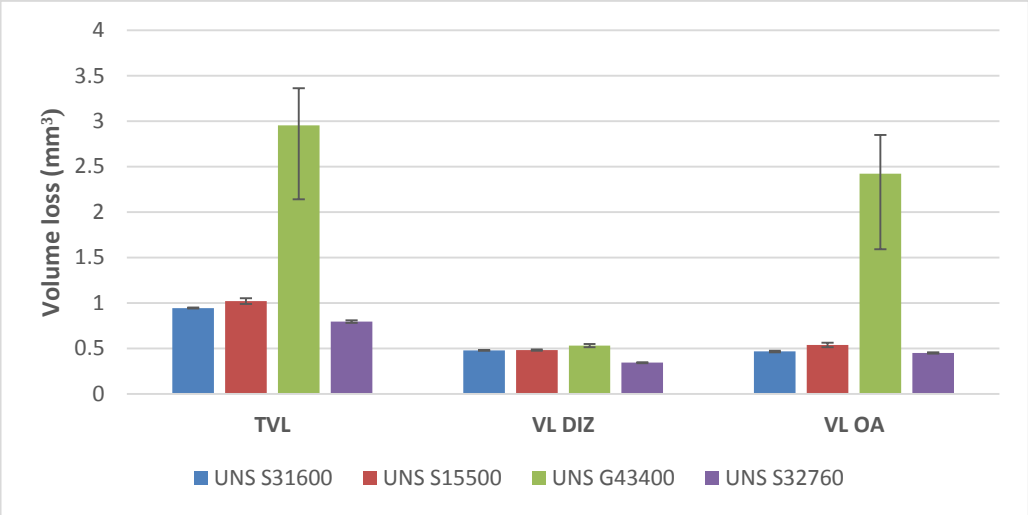

Figure 4.33: *Breakdown of the total volume loss into volume loss in the two distinct wear regions under 10%NaCl solid-liquid conditions*

Figures 4.34-4.36 show the quantitative volume losses of the different material degradation processes which were measured using the volumetric analysis technique described in Chapter 3.5.3. The technique was utilised for all test environments (0.05%NaCl, 3.5%NaCl and 10%NaCl). Each degradation process will be discussed separately in subsequent subsections.

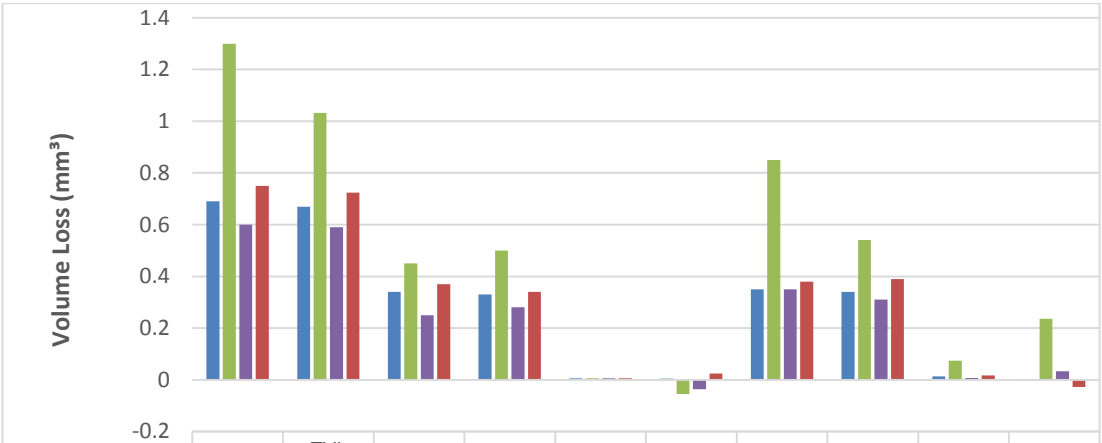

	TVL	TVL ICCP	VL DIZ	E DIZ	C DIZ	S DIZ	VL OA	SA OA	C OA	S OA
UNS S31600	0.69	0.67	0.34	0.33	0.0055	0.004	0.35	0.34	0.013	-0.003
UNS G43400	1.30	1.03	0.45	0.5	0.0053	-0.055	0.85	0.54	0.073	0.237
UNS S32760	0.60	0.59	0.25	0.28	0.0059	-0.036	0.35	0.31	0.007	0.033
UNS S15500	0.75	0.72	0.37	0.34	0.0058	0.024	0.38	0.39	0.017	-0.027

Figure 4.34: *Discrimination between the different material degradation processes on the tested materials under 0.05% NaCl solid-liquid conditions*

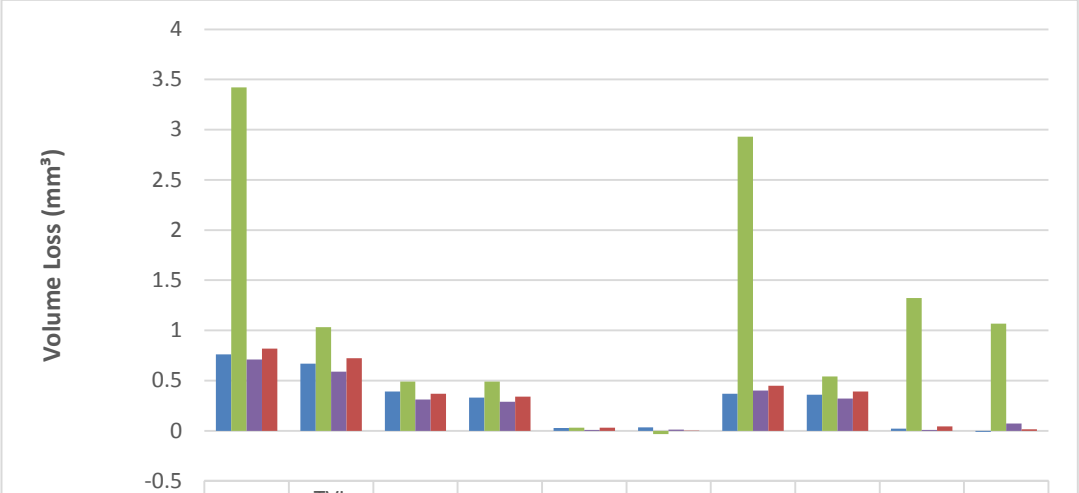

	TVL	TVL ICCP	VL DIZ	E DIZ	C DIZ	S DIZ	VL OA	SA OA	C OA	S OA
UNS S31600	0.76	0.67	0.39	0.33	0.026	0.034	0.37	0.36	0.022	-0.012
UNS G43400	3.42	1.03	0.49	0.49	0.032	-0.032	2.93	0.54	1.323	1.067
UNS S32760	0.71	0.59	0.31	0.29	0.009	0.011	0.4	0.32	0.009	0.071
UNS S15500	0.82	0.72	0.37	0.34	0.029	0.001	0.45	0.39	0.044	0.016

Figure 4.35: *Discrimination between the different material degradation processes on the tested materials under 3.5% NaCl solid-liquid conditions*

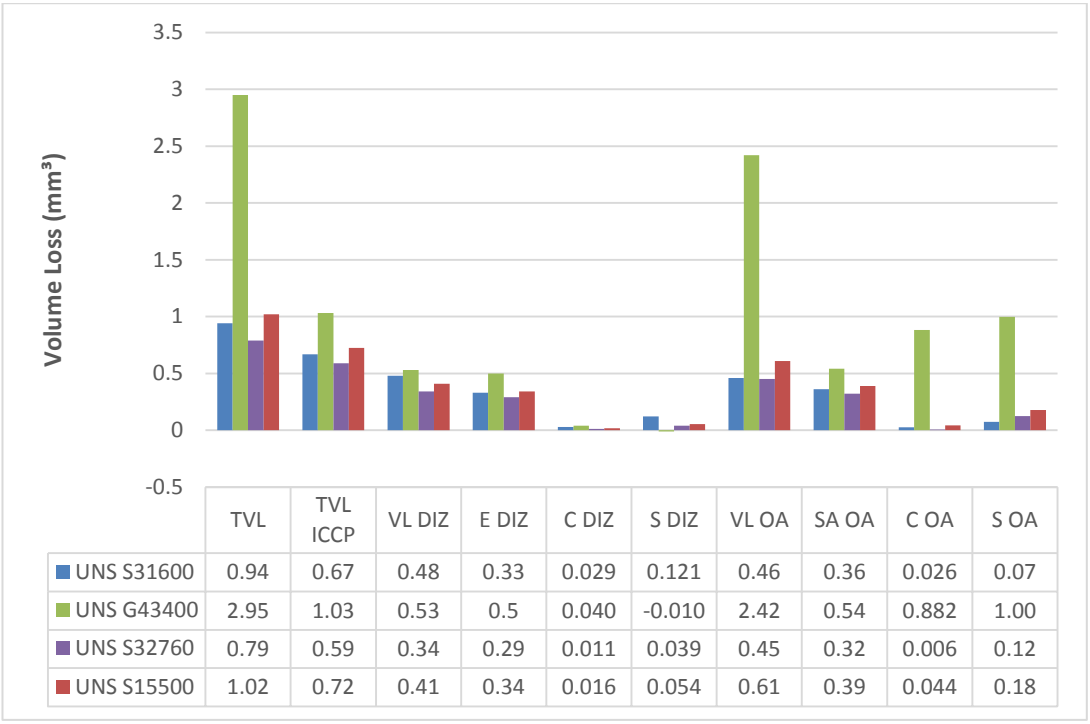

	TVL	TVL ICCP	VL DIZ	E DIZ	C DIZ	S DIZ	VL OA	SA OA	C OA	S OA
UNS S31600	0.94	0.67	0.48	0.33	0.029	0.121	0.46	0.36	0.026	0.07
UNS G43400	2.95	1.03	0.53	0.5	0.040	-0.010	2.42	0.54	0.882	1.00
UNS S32760	0.79	0.59	0.34	0.29	0.011	0.039	0.45	0.32	0.006	0.12
UNS S15500	1.02	0.72	0.41	0.34	0.016	0.054	0.61	0.39	0.044	0.18

Figure 4.36: *Discrimination between the different material degradation processes on the tested materials under 10% NaCl solid-liquid conditions*

4.6.2 Breakdown of total volume loss in cathodic protection (CP) conditions

The total volume losses for cathodic protection (ICCP) of the low alloy steel and stainless steels were calculated directly from the measured mass loss from the experiments (Figure 4.9). As the cathodic protection supresses' corrosion mechanisms, the total volume loss (TVL CP) represents the high angle erosion damage inside the wear scar (E_{DIZ}) and sliding abrasion occurring in the area outside of the wear scar (SA_{OA}), as shown in Chapter 3.5.3, Eq. 3.6.

The application of cathodic protection was effective in reducing the overall volume loss for all the materials in all three salinity levels. The reduction in overall volume loss of low alloy steels and stainless steels have been demonstrated in previous studies [4.2, 4.3]. The smallest reductions were found in 0.05%NaCl aqueous solution, where the overall mass loss of the low alloy steel was reduced by 21% and the reduction found for UNS S32760 was 2%. In 3.5% aqueous solution solid-liquid conditions, the greatest reduction in overall volume loss was found for the low alloy steel, with a reduction of 70%. The smallest reduction in total volume loss were found for UNS S31600 and UNS S15500 which both has a reduction

of 12%. In 10%NaCl aqueous solution solid-liquid conditions, the low alloy steel again demonstrated the largest reduction in overall volume loss with 65% and the UNS S32760 showed the smallest reduction with 25%. These findings demonstrate that the corrosion related damage (C+S) is a significant proportion of the overall material degradation processes for the low alloy steel in all salinity levels. The findings also show that the corrosion related damage for the stainless steels increases substantially when the salt content is increased, however, the proportion of damage is significantly smaller than that of the low alloy steel.

Figure 4.37 shows the breakdown of total volume loss into volume losses in the DIZ and the OA for the low alloy steel under FEC, ICCP and both SACP applications under 3.5%NaCl solid-liquid conditions. In terms of volume loss in the DIZ, all environments demonstrated similar volume losses which indicate that the mechanical deterioration mechanism is the dominant wear process. However, in the OA, there was a significant reduction (up to 85%) in volume loss when CP was applied.

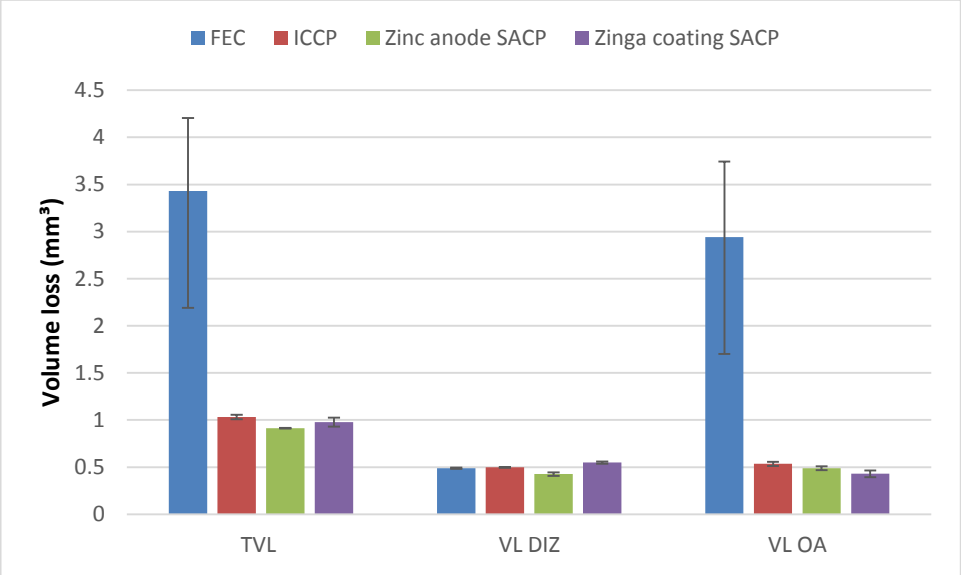

Figure 4.37: *Breakdown of the total volume loss into the two distinct wear regions for the low alloy steel in FEC, ICCP and both SACP under 3.5%NaCl solid-liquid conditions*

4.6.3 High angle erosion damage in the direct impingement zone (DIZ)

The high angle erosion damage occurring in the direct impinged zone (DIZ), was measured in terms of volume loss from the cathodically protected test samples. These measurements

were given in Figure 4.29. The low alloy steel exhibited greater volume loss due to the high angle erosion mechanism than the stainless steels. Similar trends have been observed by other studies [4.1, 4.2], where a medium carbon steel performed poorer than stainless steels under impingement erosion conditions. Marginal differences were observed when comparing the stainless steels, with the UNS S32760 demonstrating a slightly smaller volume loss than the UNS S15500 and the UNS S31600. The marginal differences between the stainless steels have been observed in terms of wear scar depths in a previous study [4.2].

By comparing the material's hardness in Table 4.2, no obvious linkage could be connected with the resistance to high angle erosion with material hardness. A more widely accepted notion is the relationship between sliding abrasion resistance and hardness, this will be discussed in Chapter 4.6.6. Another theory suggests that the elastic modulus is another material property is also important and that a high hardness (H) to elastic modulus (E) ratio is desirable. However, in this study there was also no clear relationship between the H/E ratio with the volume loss due to high angle erosion (Table 4.16).

Table 4.16: *H/E values and measured volume losses due to high angle erosion for the tested materials*

Material	H/E	Volume loss due to high angle erosion (mm^3)
UNS G43400	0.015	0.4968
UNS S15500	0.018	0.3373
UNS S32760	0.013	0.2813
UNS S31600	0.010	0.3294

The lack of correlation between conventional material properties and high angle erosion resistance may be attributed to the high-strain rate conditions which occur during a high velocity impingement erosion-corrosion experiment [4.30].

4.6.4 Corrosion and synergy in the direct impingement zone (DIZ)

From Figures 4.34-4.36, the volume losses due to corrosion and synergy in the wear scar were found to be negligible for all materials in each testing environment. This indicates that the material loss within the wear scar was purely mechanical. An exception to this finding

was the UNS S15500 in 10%NaCl solid-liquid conditions where 37% of the damage was attributed to synergy.

The negligible corrosion damage was shown by the estimated volume loss due to corrosion from the anodic polarisation scans of the segmented samples, shown in Tables 4.6-4.8. Even though the passive films were destroyed by impacting sand particles, it appears that the intermittent de-passivation/re-passivation events restricted the corrosion damage. The domination of erosion processes is likely to be associated with the size, shape and concentration of the sand as well as the velocity of the jet.

4.6.5 Sliding abrasion in the outer area (OA)

The sliding abrasion damage of the materials was calculated by rearranging Eq. 3.6, as shown below in Eq. 4.1.

$$SA_{OA} = TVL_{CP} - E_{DIZ} \quad \text{Eq. 4.1}$$

As described in Chapter 4.6.3, there is often a link between high hardness and improved sliding abrasion resistance. However, the low alloy steel, which exhibited the second greatest hardness, was found to have the poorest sliding abrasion resistance. This implies that the correlation between increased hardness and abrasion resistance is more complex than suggested in previous research [4.27–4.29]. Work conducted by Xu et al. suggests that an increase in hardness of steels does not necessarily increase abrasion wear resistance and is in fact influenced more by grain size, grain morphology and amount of retained austenite [4.31].

4.6.6 Corrosion in the outer area (OA)

The anodic polarisation scans conducted on the segmented samples (Figures 4.11 – 4.13 and in Appendix A) gave an indication of the corrosion damage occurring in the OA of the tested materials in each level of salinity. Using the Tafel extrapolation technique, it was found that in freshwater conditions, the corrosion in the OA of the low alloy steel was a small proportion of the overall damage (6%). However, in the higher salt content the proportion of the damage increased significantly (65% - 3.5%NaCl, 30% - 10%NaCl). The stainless steels exhibited negligible OA corrosion in freshwater, seawater and brine conditions (less than 5% of overall damage). As the conditions are less turbulent in the OA

compared to the direct impinged zone, the passive film was more stable and was able to protect the stainless steels. On the other hand, no passive film formed on the UNS G43400 due to its low alloying content and the greater conductivity of the solution resulted in substantial volume losses due to corrosion from 0.05%NaCl to 3.5%NaCl saline conditions. The decrease in volume loss due to corrosion from 3.5%NaCl to 10%NaCl for the low alloy steel in the OA may be explained by the reduction of oxygen in the aqueous solution. The poor corrosion resistance of low alloy steels under erosion-corrosion conditions were observed in previous studies [4.2–4.4].

4.6.7 Synergy in the outer area (OA)

The synergy in the OA was calculated by subtracting the sliding abrasion damage and the measured corrosion damage from the calculated total volume loss in the OA, as demonstrated below in Eq. 4.2.

$$S_{OA} = TVL_{OA} - SA_{OA} - C_{OA} \quad \text{Eq. 4.2}$$

In freshwater conditions, the stainless steels exhibited negligible synergy, whereas the low alloy steel exhibited significant synergy damage in the OA (19%). In 3.5%NaCl test conditions, the synergy in the OA decreased for the low alloy steel and was found to be only 6% of the overall damage. The synergy damage was found to increase for UNS S32760 to 10% of the overall damage. When the aqueous solution was increased to 10%NaCl, the synergy damage was found to increase for all materials (7% UNS S31600, 34% UNS G43400, 15% UNS S32760 and 18% UNS S15500). A reason for synergy in the austenitic stainless steel was suggested by Matsumura et al. who suggested that corrosion removes the work hardened layer which in turn causes the stainless steel to be more susceptible to mechanical damage [4.33]. Duplex stainless steel is an example of a multiphase material which can exhibit synergistic damage that is associated with micro-galvanic action at the phase boundaries. The latter phenomena has been shown in a number of erosion-corrosion systems, where the ferrite phase acts as an anode and the austenite phase acts as a cathode [4.34, 4.35]. Thus, an explanation for UNS S32760 and UNS S15500 is galvanic corrosion between the two different microstructures (ferrite and austenite for Superduplex and martensite and retained austenite for UNS S15500 steel) which allows easier removal of material from mechanical damage processes. For the low alloy steel, the synergy

mechanisms are attributed to the corrosion pits which are formed. The pits cause local turbulence which enhances the mechanical erosion damage. Corrosion roughens the surface causing micro-turbulence, this would be exacerbated by corrosion pits [4.36].

4.7 Relevance of work to the design and operation for a hydraulic fracturing pump fluid end

This study has demonstrated that increasing the salinity of the hydraulic fracturing fluid from freshwater to seawater, will dramatically reduce the life of the low alloy steel fluid end. However, above 3.5%NaCl there appears to be little effect to the erosion-corrosion resistance to the low alloy steel. This study has successfully demonstrated that the reduction in life of the currently used low alloy steel can be combatted by using stainless steel alloys which perform significantly better under erosion-corrosion conditions. Due to the significant costs associated with UNS S32760 (Superduplex), with only marginally better resistance to erosion-corrosion than the cheaper stainless steel alloys (UNS S15500 and UNS S31600) economically, selecting Superduplex as an alternative fluid end material is unrealistic. Another aspect which must be considered is the extremely high fluid pressures which are being pumped during the hydraulic fracturing process. Therefore, the fluid end material must have high strength properties in order to cope with the high mechanical stresses occurring during operation. The modified UNS S15500 alloy developed by Weir Oil and Gas was found to successfully increase the life of the fluid end by more than 5 times.

As anticipated, the application of cathodic protection through impressed current and sacrificial anode/coating were found to successfully reduce the erosion-corrosion damage of the low alloy steel in 3.5%NaCl test conditions. However, due to the complexities involved in designing and implementing an ICCP system for a fluid end and associated equipment then it is unlikely that this is the most appropriate cathodic protection technique. As the Zinga coating was found to last for only short durations then this is also not a viable option for these aggressive erosion-corrosion conditions. The most feasible option is zinc anodes which were found to effectively protect the low alloy steel from corrosion related damage and, therefore, enabled a significant increase in corrosive wear life. These could be designed and implemented much simpler into the fluid end and other components. For instance, recesses could be machined into the fluid end in which zinc

anodes could be placed and as long as the anode was in contact with the hydraulic fracturing fluid cathodic protection could be achieved. Another option is to incorporate the zinc anodes into the valve and seat which are located within the fluid end. Dependent upon the size of the fluid end there will be up to 10 valves and seats located within the fluid end which are in direct contact with the hydraulic fracturing fluid. The valves and seats are replaced at regular maintenance intervals which would allow also allow for unused anodes to be placed within the fluid end. The salinity of the hydraulic fracturing fluid must also be considered as this will dictate the anode material. In low salinity conditions, the appropriate anode material choice may be magnesium alloy as it produces a more negative electropotential than zinc and aluminium alloys. The positive findings in this research have enabled engineers in Weir Oil and Gas to initiate a project aimed at assessing the potential of SACP in fluid ends of hydraulic fracturing pumps.

4.8 Conclusions

1. The increase of salinity from freshwater to seawater was found to substantially increase (163%) the erosion-corrosion damage of the low alloy steel (UNS G43400). However, as the salinity was increased from 3.5%NaCl to 10%NaCl, the effect was found to be minimal as the overall volume loss was similar in both environments. The majority of the increase in damage was observed in the OA as a significant proportion of the material damage was corrosion related (8 times increase in corrosion and synergy for 3.5%NaCl and 6 times increase in corrosion and synergy for 10%NaCl compared to corrosion and synergy in 0.05%NaCl). The increased corrosion and synergy damage can be associated with the higher conductivity of the aqueous solution.
2. For the stainless steels, the increases in salinity were found to accelerate the overall damage marginally (less than 24%) but were found to have significant erosion-corrosion resistance when compared to the low alloy steel. This was attributed to the small amount of corrosion related damage associated with the stainless steels as they were erosion dominated.
3. As a result of the similar performance of the stainless steels under corrosive wear conditions and due to the lower associated costs, the high strength precipitation

hardened martensitic stainless steel (UNS S15500) is now finding application in fluid ends of hydraulic fracturing pumps.

4. The volumetric analysis technique applied in this study enabled a more comprehensive understanding of the corrosive wear material degradation processes involved during the impinging jet erosion-corrosion experiments. For instance, the marginal superiority of the UNS S32760 alloy over the other stainless steels is attributed to its direct impingement erosion resistance and not with its sliding abrasion resistance. Also, the volumetric analysis technique demonstrated that most of the corrosion damage on the low alloy steel is in the OA, which is not evident from just assessing full sized specimens. These conclusions would not have been evident by only considering the total volume loss under cathodic protection conditions.
5. The low alloy steel benefited substantially from cathodic protection with a reduction in overall volume loss up to 70%. In freshwater, cathodic protection was not found to have much benefit for the stainless steels. However, as the salinity was increased, cathodic protection provided some benefit with reductions in overall damage of 29% for UNS S31600, UNS S32760 and UNS S15500 in 10%NaCl aqueous solution.
6. The application of cathodic protection by impressed current and sacrificial anode/coating was found to be extremely beneficial to the low alloy steel in 3.5%NaCl aqueous solution under erosion-corrosion conditions. However, the Zinga coating could only effectively protect the low alloy steel in a relatively short time period as the zinc particles were rapidly consumed in the aggressive environment. Due to the complexities involved in design and implementing an ICCP system into a fluid end, zinc anodes offer great potential of increasing the life of the low alloy steel fluid end and are currently being assessed in operational conditions.

4.9 References

[4.1] A. Neville, T. Hodgkiess, and J. T. Dallas, "A study of the erosion-corrosion behaviour of engineering steels for marine pumping applications" *Wear*, vol. 186–187. pp. 497–507, 1995.

[4.2] L. Giourntas, T. Hodgkiess, and A. M. Galloway, "Comparative study of erosion–corrosion performance on a range of stainless steels" *Wear*, vol. 332–333, pp. 1051–1058, 2015.

[4.3] A. Neville and C. Wang, "Erosion-corrosion of engineering steels-Can it be managed by use of chemicals?" *Wear*, vol. 267, no. 11, pp. 2018–2026, 2009.

[4.4] S. S. Rajahram, T. J. Harvey, and R. J. K. Wood, "Erosion–corrosion resistance of engineering materials in various test conditions" *Wear*, vol. 267, no. 1–4, pp. 244–254, 2009.

[4.5] L. Giourntas, T. Hodgkiess, and A. M. Galloway, "Enhanced approach of assessing the corrosive wear of engineering materials under impingement" *Wear*, vol. 338–339, pp. 155–163, 2015.

[4.6] T. Foley and A. Levy, "The erosion of heat-treated steels" *Wear*, vol. 91, pp. 45–64, 1983.

[4.7] A. V. Levy and G. Hickey, "Liquid-solid particle slurry erosion of steels" *Wear*, vol. 117, no. 2, pp. 129–146, 1987.

[4.8] K. S. E. Al-Malahy and T. Hodgkiess, "Comparative studies of the seawater corrosion behaviour of a range of materials" *Desalination*, vol. 158, no. 1–3, pp. 35–42, 2003.

[4.9] A. Neville and T. Hodgkiess, "An assessment of the corrosion behaviour of high-grade alloys in seawater at elevated temperature and under a high velocity impinging flow" *Corros. Sci.*, vol. 38, no. 6, pp. 927–956, 1996.

[4.10] X. Hu and A. Neville, "The electrochemical response of stainless steels in liquid-solid impingement" *Wear*, vol. 258, no. 1–4, pp. 641–648, 2005.

[4.11] A. Neville and X. Hu, "Mechanical and electrochemical interactions during liquid–

solid impingement on high-alloy stainless steels" *Wear*, vol. 251, pp. 1284–1294, 2001.

[4.12] H. Meng, X. Hu, and A. Neville, "A systematic erosion-corrosion study of two stainless steels in marine conditions via experimental design" *Wear*, vol. 263, pp. 355–362, 2007.

[4.13] D. A. López, J. P. Congote, J. R. Cano, A. Toro, and A. P. Tschiptschin, "Effect of particle velocity and impact angle on the corrosion–erosion of AISI 304 and AISI 420 stainless steels" *Wear*, vol. 259, no. 1–6, pp. 118–124, 2005.

[4.14] T. J. Gallegos, B. A. Varela, S. S. Haines, and M. A. Engle, "Hydraulic fracturing water use variability in the United States and potential environmental implications" *Water Resour. Res.*, vol. 51, no. 7, pp. 5839–5845, 2015.

[4.15] D. Brondel, R. Edwards, A. Hayman, D. Hill, and T. Semerad, "Corrosion in the Oil Industry" *Oilf. Rev.*, pp. 4–18, 1994.

[4.16] H. H. Uhlig and M. C. Morrill, "Corrosion of 18-8 Stainless Steel in Sodium Chloride Solutions" *Ind. Eng. Chem.*, vol. 33, no. 7, pp. 875–880, 1941.

[4.17] B. O. Hasan, "Effect of Salt Content on The Corrosion Rate of Steel Pipe in Turbulently Flowing Solutions" *Nahrain Univeristy, Coll. Eng. J.*, vol. 13, no. 1, pp. 66–73, 2010.

[4.18] J. Chen, J. Wang, B. Chen, F. Yan, J. Chen, J. Wang, B. Chen, and F. Yan, "Tribocorrosion Behaviors of Inconel 625 Alloy Sliding against 316 Steel in Seawater" *Tribol. Trans.*, vol. 54, pp. 514–522, 2011.

[4.19] W. J. Tomlinson and M. G. Talks, "Erosion and corrosion of pure iron under cavitating conditions" *Ultrasonics*, vol. 29, no. 2, pp. 171–175, 1991.

[4.20] A. Momber, "Corrosion and corrosion protection of support structures for offshore wind energy devices (OWEA)" *Mater. Corros.*, vol. 62, no. 5, pp. 391–404, 2011.

[4.21] A. Young and T. Hodgkiess, "Use of sacrificial coatings for cathodic protection of low

alloy steel in aqueous environments." Unpublished work, University of Glasgow, 2008

[4.22] T. Okada, K. Awazu, and H. Kawasaki, "Influence of cavitation erosion on corrosion fatigue and the effect of surface coatings on resistance" *Wear*, vol. 63, pp. 51–70, 1980.

[4.23] A. S. Yaro, H. Al-Jendeel, and A. A. Khadom, "Cathodic protection system of copper-zinc-saline water in presence of bacteria" *Desalination*, vol. 270, no. 1–3, pp. 193–198, 2011.

[4.24] A. Neville and T. Hodgkiess, "Characterisation of high-grade alloy behaviour in severe erosion-corrosion conditions" *Wear*, vol. 233–235, pp. 596–607, 1999.

[4.25] N. Andrews, L. Giourntas, A. M. Galloway, and A. Pearson, "Erosion-corrosion behaviour of zirconia, WC-6Co, WC-6Ni and UNS S31600" *Int. J. Refract. Met. Hard Mater.*, vol. 48, pp. 229–237, 2015.

[4.26] S. Deng, S. Wang, L. Wang, J. Liu, and Y. Wang, "Influence of Chloride on Passive Film Chemistry of 304 Stainless Steel in Sulphuric Acid Solution by Glow Discharge Optical Emission Spectrometry Analysis" *Int. J. Electrochem. Sci.*, vol. 12, pp. 1106–1117, 2017.

[4.27] A. N. J. Stevenson and I. M. Hutchings, "Wear of Hardfacing While Cast Irons By Solid Particle Erosion" *Wear*, vol. 186, no. 1, pp. 150–158, 1995.

[4.28] R. J. Llewellyn, S. K. Yick, and K. F. Dolman, "Scouring erosion resistance of metallic materials used in slurry pump service" *Wear*, vol. 256, no. 6, pp. 592–599, 2004.

[4.29] L. Giourntas, F. Brownlie, G. Karafyllias, T. Hodgkiess, and A. M. Galloway, "Effect of corrosion on abrasive wear in a range of materials" in *BHR Group - 23rd International Conference on Fluid Sealing 2016*, 2016.

[4.30] G. Sundararajan, "The solid particle erosion of metallic materials: The rationalization of the influence of material variables" *Wear*, vol. 186–187, no. PART 1, pp. 129–144, 1995.

[4.31] X. Xu, W. Xu, F. H. Ederveen, and S. Van Der Zwaag, "Design of low hardness abrasion resistant steels" *Wear*, vol. 301, no. 1–2, pp. 89–93, 2013.

[4.32] L. Giourntas, T. Hodgkiess, and A. M. Galloway, "Enhanced approach of assessing the corrosive wear of engineering materials under impingement" *Wear*, vol. 338–339, pp. 155–163, 2015.

[4.33] M. Matsumura, *Erosion-Corrosion: An Introduction to Flow Induced Macro-Cell Corrosion*. Bentham Science Publishers, 2012.

[4.34] J.-S. Lee, K. Fushimi, T. Nakanishi, Y. Hasegawa, and Y.-S. Park, "Corrosion behaviour of ferrite and austenite phases on super duplex stainless steel in a modified green-death solution" *Corros. Sci.*, vol. 89, pp. 111–117, 2014.

[4.35] Y. H. Yau and M. A. Streicher, "Galvanic corrosion of duplex FeCr-10%Ni alloys in reducing acids." *Corrosion*, vol. 43, no. 6, pp. 366–373, 1987.

[4.36] T. J. Harvey, J. A. Wharton, and R. J. K. Wood, "Development of synergy model for erosion–corrosion of carbon steel in a slurry pot" *Tribology*, vol. 1, no. 1, pp. 33–47, 2007.

Chapter 5

Wear mechanisms of valve and valve seats and the validation of a novel repetitive impact test rig

Chapter 5: Wear mechanisms of valve and valve seats and the validation of a novel repetitive impact test rig

5.1 Introduction

Following the previous chapter which focused on fluid ends of hydraulic fracturing pumps, attention now turns to the specific components of valves and valve seats. This chapter will discuss the function as well as the material degradation processes occurring on valve and valve seats while in service. This is followed by a literature review of repetitive impact wear test machines and the validation of a novel repetitive impact wear test rig designed to mimic the repetitive impact wear occurring on a valve seat. The novel test rig was validated and was incorporated into the overall material degradation programme by testing a range of alternative valve seat material candidates.

5.2 Background

5.2.1 Valve seat operational problem

In a positive displacement pump, there are two valves and two seats located in each fluid end chamber (Figure 2.4). One valve and seat are situated in the suction end of the chamber and the other valve and seat is positioned in the discharge end of the chamber. A "triplex" (three chambers) positive displacement pump contains six valves and six seats, while a "quintex" (five chambers) positive displacement pump contains a total of ten valves and ten seats.

The operational life of the valve and seat has become one of the major issues with hydraulic fracturing pumping equipment due to their short life expectancy. The life of the valve and seat vary dependent upon the environmental conditions in which the pump is operating. The in-service valves and seats are typically exchanged for new valve and seats after 50-150 hours (2-6 days) of operation. A hydraulic fracturing operation may take 1-2 months to complete. Therefore, the valve and seats last only for a fraction of the hydraulic fracturing cycle [5.1].

There are several pumps which are in operation during the hydraulic fracturing process. Some hydraulic fracturing pumps handle only liquid (often termed as "clean" pumps) while other hydraulic fracturing pumps handle both the liquid and proppant (often termed as "dirty" pumps). At some stage during the hydraulic fracturing process, the "dirty" pumps require maintenance downtime in order to exchange the in-service valves and seats with new valves and seats. The procedure in order to remove the seats in the field is extremely

dangerous as the seat has to be removed under high pressure due to its tight interference fit inside the chamber. When the "dirty" pump(s) require maintenance, they are exchanged for spare pumps which are kept in reserve at the hydraulic fracturing site.

Figure 5.1 illustrates a valve seat prior to being in-service and Figures 5.2 and 5.3 show a valve seat and a valve which have been in-service.

Figure 5.1: *Valve seat prior to being in-service*

Figure 5.2: *Valve seat after being in-service showing step developed between areas A and B*

Figure 5.3: *Valve after being in-service showing enhanced damage in region C*

It is clear from Figures 5.2 and 5.3, that both the valve and seat display copious amounts of corrosive wear damage. On the surface of the seat, which is in contact with the valve, a deformation step (which is typical observed) was evident between the heavily corroded area (A) and the region which demonstrated less corrosion product (B). These two distinct damage regions could be easily related with the design of the valve. The region which experienced less corrosion damage was in contact with the urethane material (blue polymer (D) in Figure 5.3), while the area with extensive corrosion damage was in contact with the metal area of the valve (C). There was also extensive corrosion damage present inside the bore of the valve seat.

Solutions to the low operational lives of these components used in the “dirty” pumps have been hindered by a lack of understanding of the complex material degradation processes involved. Four possible material deterioration mechanisms were identified as:

- Corrosion due to the aqueous hydraulic fracturing fluid
- Erosion-corrosion caused by the opening of the valve which results in a high velocity flow of the hydraulic fracturing fluid with suspended solid proppants
- Repetitive metal-metal impact wear caused by the cyclic motion of the valve opening and closing onto the seat
- Impact-abrasive wear caused by the valve closing and “crushing” proppants onto the contact surface of the seat.

One or a combination of these mechanisms is a probable cause of the poor service life of the valve and seats. At this stage it is unclear which degradation process(es) is the major deterioration mechanism. Therefore, it is crucial to identify which mechanism(s) contributes to the most seat damage in order to distinguish alternative material candidates.

5.2.2 Previous studies of alternative valve seat materials in the WARC erosion-corrosion laboratory experiments

Previous experiments conducted at WARC focused on the erosion-corrosion resistance of various surface engineering treatments. The first experimental phase [5.2] compared: the current valve and seat material (carburised UNS G86200). Alternative materials investigated include; the base material (UNS G86200), boronised and carbo-boronised UNS G86200, nitrided 905M39 steel, hard chromium electroplated UNS G10400 and a martensitic stainless steel (UNS S42000). Erosion-corrosion tests were conducted for 1 hour at both normal incidence (90°) and low angle (20°) with a testing temperature between 19-26°C.

Two distinct groups of materials were observed, those which possessed poor corrosion resistance (untreated, carburised, boronised and carbo-boronised UNS G86200) and those which possessed good corrosion resistance (nitrided 905M39 steel, hard chromium electroplated UNS G10400 and UNS S42000). In terms of total mass loss, all the poor corrosion resistant materials demonstrated significant mass loss (greater than 25mg at 90° and greater than 12mg at 20°). Whereas, the good corrosion resistant materials performed substantially better with mass loss less than 10mg at 90° and less than 7.5mg at 20°.

However, when comparing wear scar depths, the carburised steel demonstrated the lowest wear scar depth of all the tested materials which highlighted its ability to withstand high angle erosion-corrosion. The carburised steel also demonstrated the second smallest wear scar volume. The martensitic stainless steel also performed well in terms of both wear scar depth and volume, with the second smallest depth and the smallest volume. The nitrided steel did not perform as well as the carburised steel or martensitic stainless steel, it did however, perform better than the other tested materials in terms of wear scar depth and volume loss. It was decided that further evaluation of both the nitrided steel and martensitic stainless steel was required in order to verify them as possible alternative valve seat materials.

The next industrial experimental phase in WARC [5.3] consisted of a hardened and tempered martensitic stainless steel UNS S42000 (480HV), three nitrided 905M39 steels with different nitriding durations (72 hours, 90 hours and 120 hours), a carburised UNS G93100 steel and an induction hardened UNS G52986 steel. Erosion-corrosion testing was conducted for 1 hour at normal incidence (90°) and low angle impingement (20°) and under similar conditions to the previous experimental phase.

Similarly with the previous industrial experimental phase in WARC, there were two distinct groups of materials, those with poor corrosion resistance (carburised steel and the induction hardened steel) and those which possess good corrosion resistance (nitrided steels and the martensitic stainless steel). This was demonstrated further when comparing mass loss of the materials in the erosion-corrosion tests with the carburised and induction hardened steels having mass loss greater than 9mg in 90° and 8mg in 20° tests. The nitrided steels and martensitic stainless steel demonstrated total mass losses less than 7mg in 90° and 3.5mg in 20° tests respectively.

The martensitic stainless steel and nitrided steel (72 hours) both demonstrated similar wear scar depths at both impingement angles which were the lowest when compared with the other test materials. The nitrided steel (120 hours) demonstrated the highest wear scar depth at 90° impingement angle, with the induction hardened steel demonstrating the highest wear scar depth at 20° impingement angle.

From both previous industrial experimental phases in WARC, the martensitic stainless steel (UNS S42000) and the nitrided steel (72 hours) exhibited the best erosion-corrosion resistance of the tested materials and so indicated that these may be attractive material candidates for the valve seat [5.2, 5.3]. It was decided that these two materials would be chosen for field trials. This represented the start of this research project.

5.2.3 Assessment of prototype valve seat field trials

Prototype valve seats using a nitrided 905M29 steel and a martensitic stainless steel were manufactured for field trials as a result of the erosion-corrosion studies previously conducted [5.2, 5.3]. A standard carburised UNS G86200 valve seat was used as the baseline. The operating conditions for each field trail are indicated in Table 5.1.

Table 5.1: *Field trial operating conditions*

Valve seat material	Run Time (hours)	Average Pressure (bar)	Sand per hour (kg/hr)
Carburised UNS G86200	33.5	312	15,895
Nitrided 905M39	42.1	361	13,346
UNS S42000	14.8	360	14,007

In order to obtain a reasonable comparison between the prototype valve seats, the data was assessed in terms of displacement rates. The post-service valve seats are illustrated in Figure 5.4. Cross sections were obtained from each valve seat to analyse the transition region from the metal-urethane to metal-metal contact regions and to assess the hardness profile for each region.

Figure 5.4: *Field Trial valve seats: carburised UNS G86200 (1), nitrided 905M39 steel (2), UNS S42000 (3). Showing metal-urethane region (denoted A) and metal-metal region (denoted B)*

The carburised UNS G86200 steel valve seat exhibited an extensive amount of corrosion product on both the valve contact surface and on the inner bore surface. The nitrided 905M39 steel valve seat exhibited corrosion product only on the metal-metal contact region. The martensitic stainless steel (UNS S42000) did not show any visible corrosion product. Another noticeable feature for all valve seats was that there was a clear displacement step between the metal-metal and metal-urethane contact regions. Figure 5.5 illustrates a cross section obtained from the carburised 8620 valve seat.

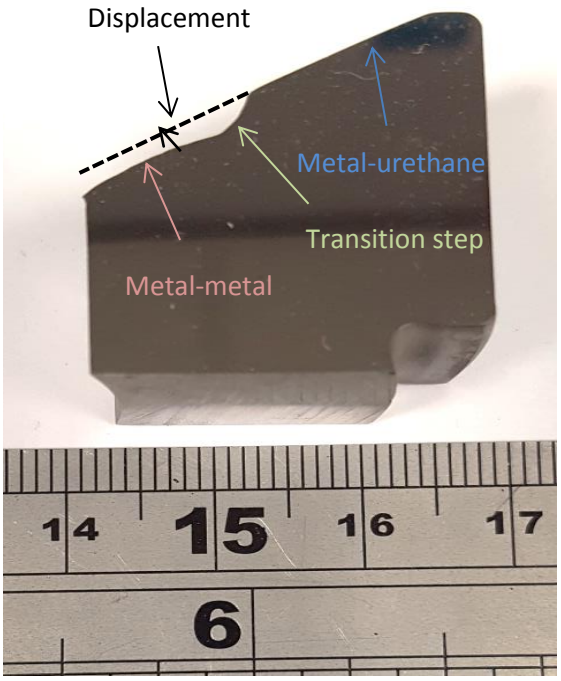

Figure 5.5: *Carburised UNS G86200 valve seat cross section*

The depths of the displacement steps (demonstrated in Figure 5.5) for each field trial material were measured using an Alicona InfiniteFocus 3D optical scanner. The average displacement depths and rates are given in Table 5.2. Displacement rates were used for more reasonable comparison purposes due to the different operational hours for each valve seat.

Table 5.2: *Average displacement and displacement rates of the valve seat*

Field trial valve seat material	Average Displacement (mm)	Displacement rate (mm/hr)
Carburised UNS G86200	0.64	0.019
Nitrided 905M39 steel	1.42	0.034
UNS S42000	0.83	0.056

The carburised UNS G86200 valve seat demonstrated the lowest displacement rate of all the field trial materials. The martensitic stainless steel (UNS S42000) performed the poorest with a significantly greater displacement rate. It should be noted that the rate of

displacement was assumed to be linear, however, this may not be the case particularly for surface hardened materials, when removing the hardened layer.

Roughness measurements were also obtained for each field test material on both metal-metal and metal-urethane contact regions. The roughness measurements are denoted in Table 5.3.

Table 5.3: *Average roughness values for each field trial material in both contact regions*

Field trial valve seat material	Average roughness (µm): metal-metal contact region	Average roughness (µm): metal-urethane contact region
Carburised UNS G86200	4.16	4.21
Nitrided 905M39 steel	3.22	0.72
UNS S42000	5.06	0.95

The carburised UNS G86200 valve seat demonstrated significant roughness in both contact regions; this was mainly attributed to the large amount of corrosion product which was found on the worn surface. Both the nitrided 905M39 steel and UNS S42000 demonstrated rough metal-metal contact surfaces which again are mainly attributed to corrosion product and plastic deformation from the valve seat wear mechanisms.

Microhardness profiling was also conducted to assess the hardness in both contact regions for each material. The microhardness profiles in the metal-urethane contact region are illustrated in Figure 5.6. The nitrided 905M39 steel initially had the greatest surface hardness (>1000HV), however, this sharply decreased with depth and the hardness of the untreated steel was similar to the martensitic stainless steel (approximately 380HV). After a depth of 0.4mm, the carburised UNS G86200 demonstrated the greatest hardness. The hardness of the carburised UNS G86200 was constant up to the measured depth of 1.5mm.

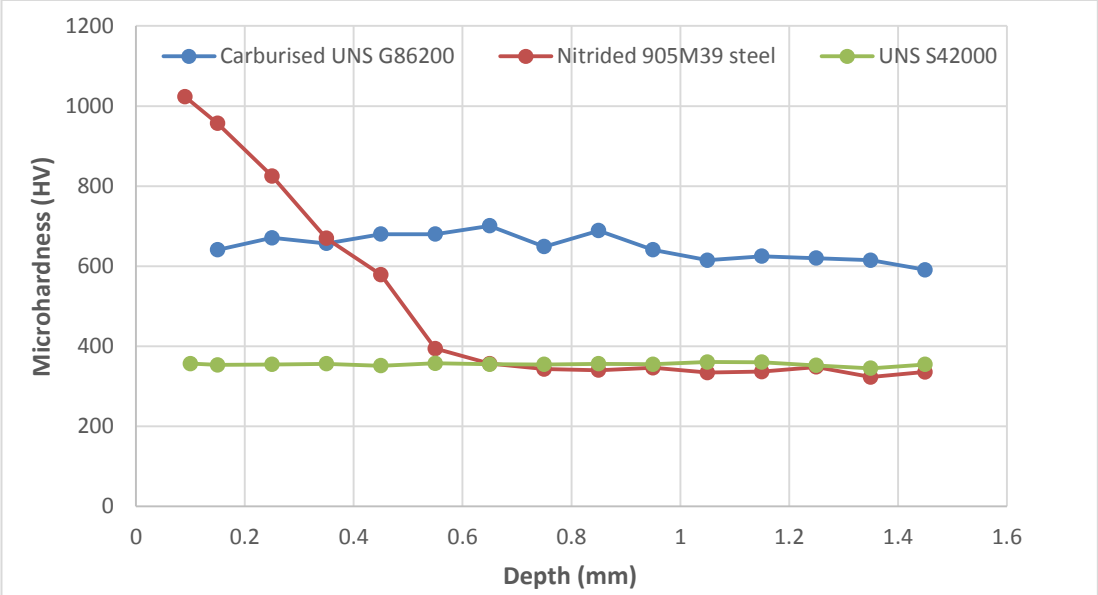

Figure 5.6: *Microhardness profile for each field trial material in the metal-urethane contact region*

The microhardness profiles for the field trial materials in the metal-metal contact region are shown in Figure 5.7. The carburised UNS G86200 exhibited the greatest hardness profile with a gradual decline indicating that the carburised layer was still present. An interesting feature was that the hardness at the surface of the carburised layer in the metal-metal contact region was approximately 200HV harder than the carburised layer in the metal-urethane contact region. The nitrided 905M39 steel and the martensitic UNS S42000 stainless steel illustrated similar hardness profiles. This indicated that the nitride layer had been removed and hence, exposed the untreated steel.

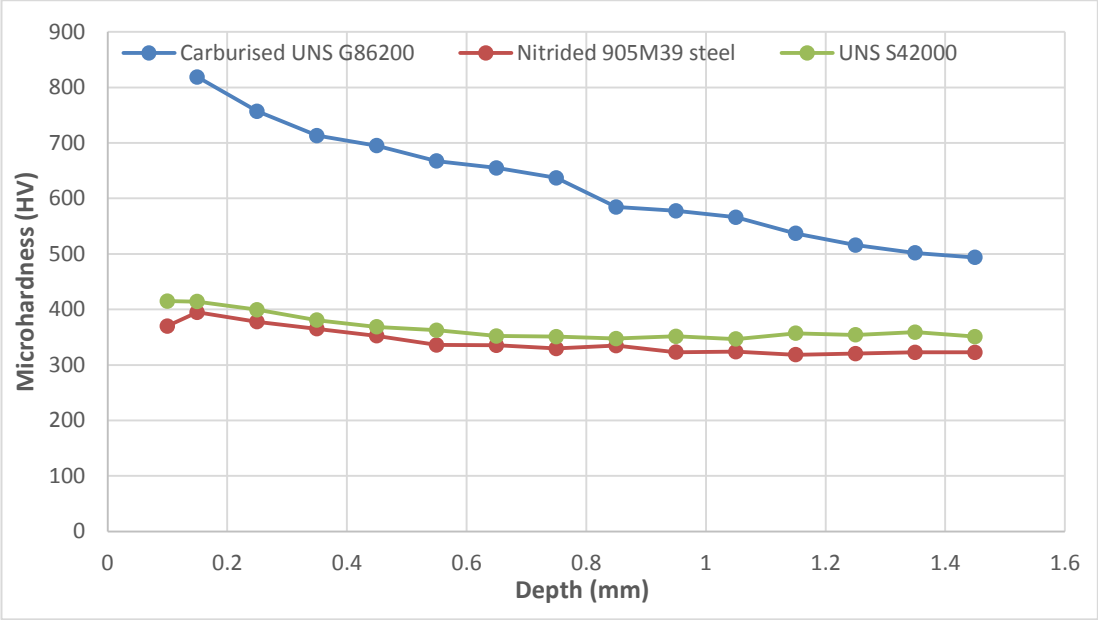

Figure 5.7: *Microhardness profile for each field trial material in the metal-metal contact region*

Figures 5.8 – 5.10 show SEM images for the carburised UNS G86200, nitrided 905M39 and UNS S42000 valve seats in the metal–urethane contact region. All valve seat materials exhibited subsurface cracking which led to material removal.

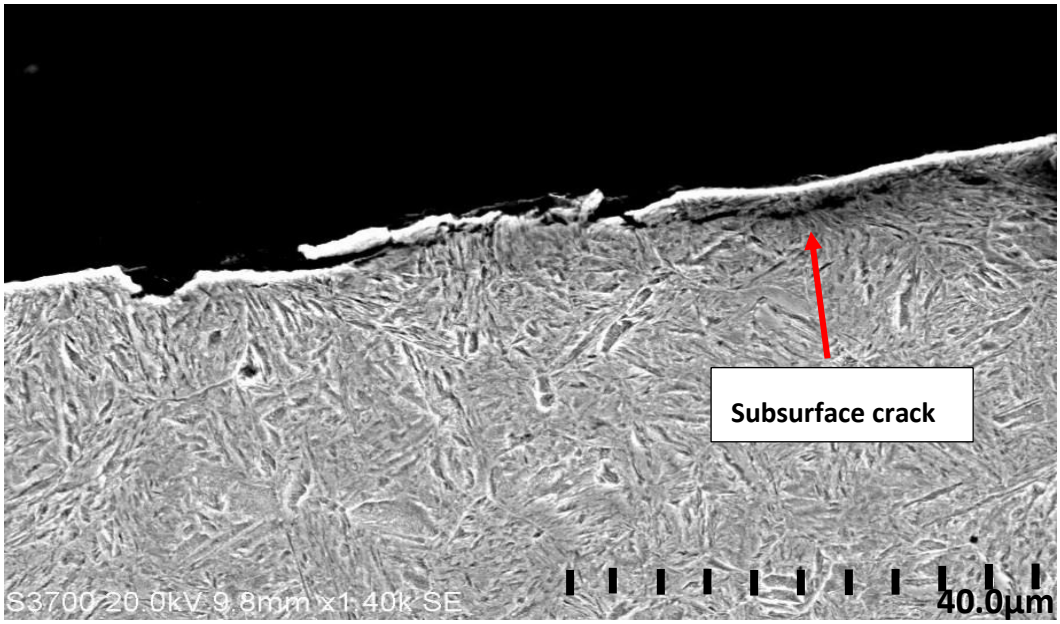

Figure 5.8: *Subsurface cracking leading to material removal in carburised UNS G86200 metal-urethane contact region*

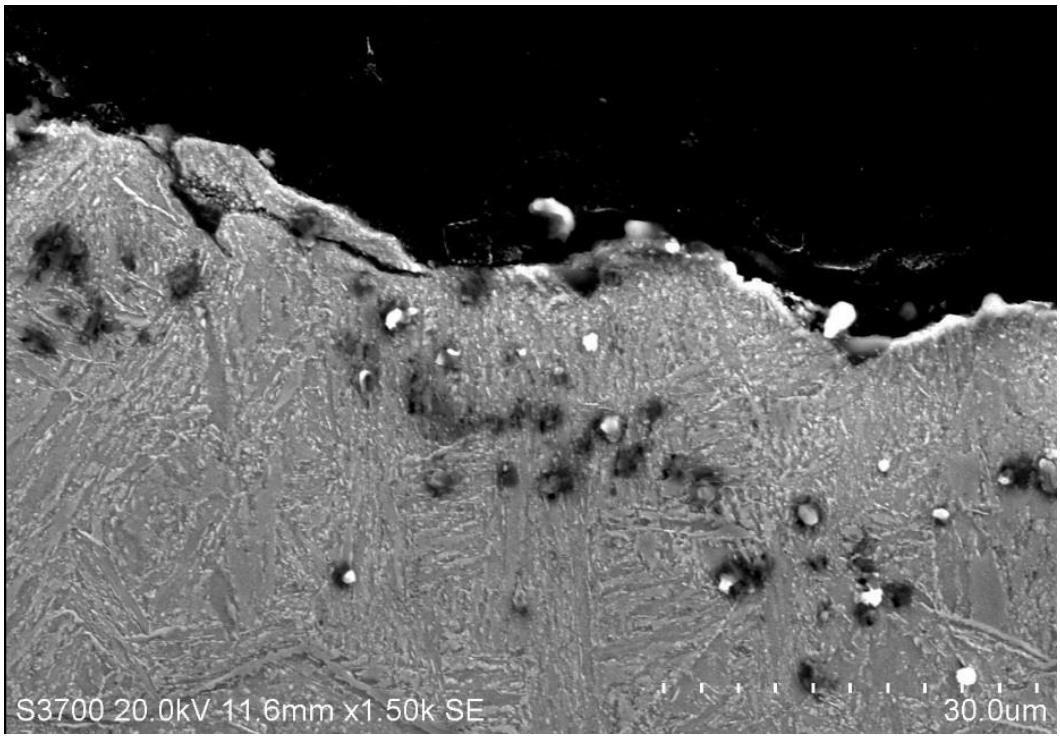

Figure 5.9: *Subsurface cracking leading to material removal in nitrided 905M39 metal-urethane contact region*

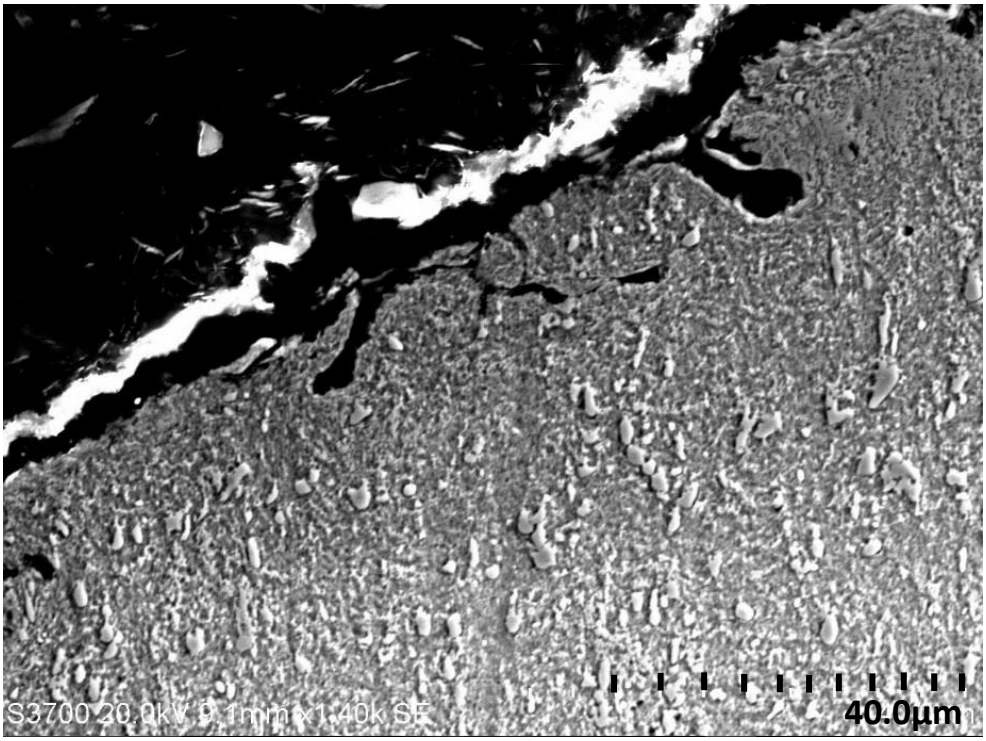

Figure 5.10: *Subsurface cracking leading to material removal in UNS S42000 metal-urethane region*

Figure 5.11 – 5.13 show SEM images of the carburised UNS G86200, nitrided 905M39 and UNS S42000 valve seat materials in the metal-metal contact region. The carburised UNS G86200 steel exhibited subsurface cracking (as the carburised layer is a hard/brittle material, hence, it has a low fracture toughness, therefore, it is more susceptible to cracking) which led to material removal, similar to the wear mechanisms observed in Figure 5.8. The nitrided 905M39 steel and the UNS S42000 exhibited an extensive network of subsurface cracks. The material near the surface and around the cracks is highly strained and plastically deformed.

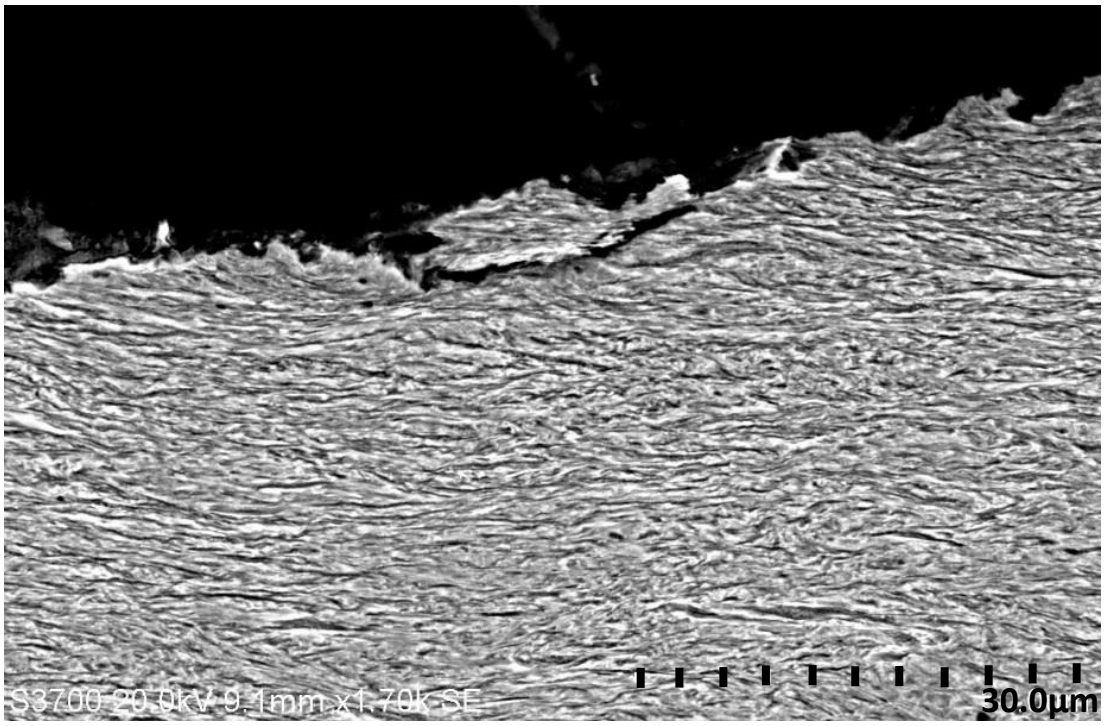

Figure 5.11: *Subsurface cracking leading to material removal in carburised UNS G86200 metal-metal contact region*

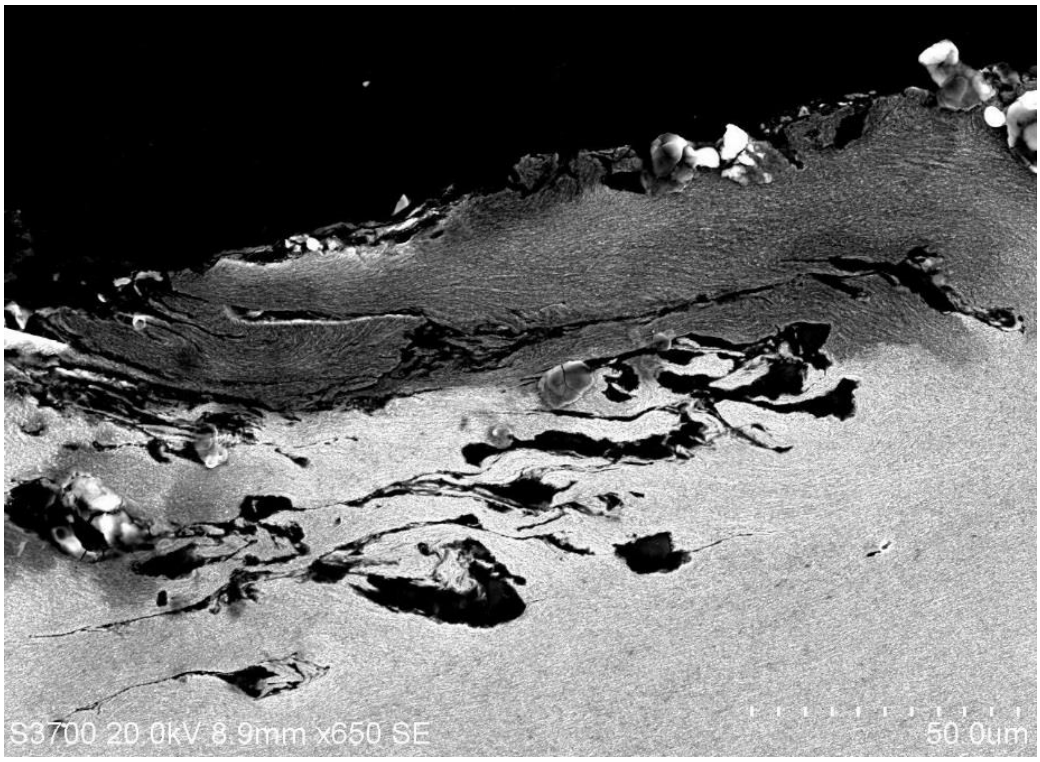

Figure 5.12: *Extensive network of subsurface cracking in nitrided 905M39 steel metal-metal contact region*

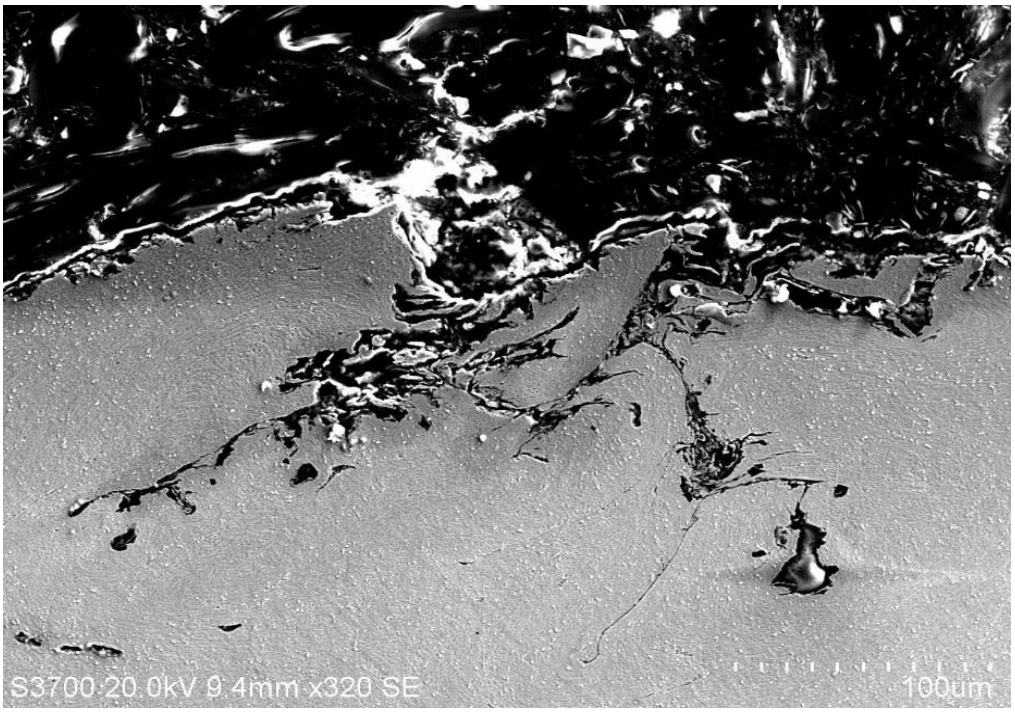

Figure 5.13: *Extensive network of subsurface cracking in UNS S42000 metal-metal contact region*

The field trial results indicate that the nitrided 905M39 steel and UNS S42000 performed better than the carburised UNS G86200 steel in the metal-urethane contact region. This was concluded through the macro-views of the post-field trial valve seats (Figure 5.4) as no visible corrosion product was present and from the roughness measurements presented in Table 5.3. The main wear mechanism observed in this region was small subsurface cracks which lead to material removal. However, the nitrided 905M39 steel and UNS S42000 were significantly poorer than the carburised UNS G86200 steel in the metal-metal region where the majority of the material degradation occurs. This is shown through the measured displacement (Table 5.2), the roughness measurements (Table 5.3) and the SEM images. Both the nitrided 905M39 steel and UNS S42000 exhibited an extensive network of subsurface cracks in the metal-metal contact region. This indicates that erosion-corrosion was not the only material degradation process in the metal-metal contact region as they would be expected to perform better than the carburised UNS G86200 steel (previous erosion-corrosion experimental programmes, Chapter 5.1.2) It was evident that further investigation was required into all of the complex deterioration mechanisms, highlighted earlier in Chapter 5.1.1, in order to identify attractive material candidates.

5.3 Repetitive impact test rig literature review

As repetitive impact wear was identified as one of the main material degradation processes, an in-depth literature review into repetitive impact wear was conducted. This was performed to assess the types of repetitive impact test rigs as well as the type of material degradation mechanisms which occur during repetitive impact wear. Five main types of repetitive impact test rigs were identified: modified pin on disk, pivot hammer, high velocity impact gun, ball on plate and repetitive impact with dry abrasion.

5.3.1 Modified pin on disk – compound and sliding impact tests

The pin on disk wear testing method is typically used to assess the sliding wear resistance and coefficient of friction of materials, however, this testing apparatus has been adapted by some researchers with the capability of testing both compound impact wear and transverse sliding wear (Figure 5.14). Testing parameters such as impacting velocity, sliding speed, number of cycles, load, frequency, lubrication, system damping and stiffness are all test variables [5.4]. However, the adapted testing apparatus was limited to small loads and

sliding velocities, less than 1kN and 21m/s respectively. These low loads and velocities mean that a large amount of cycles was required before any measurable damage occurred. From this reciprocating impact wear machine, three subsurface zones were found to be present after each test: non-deformed base material, plastically deformed base material and a white compound layer with a compositional mixture (Figure 2.24) [5.4–5.6].

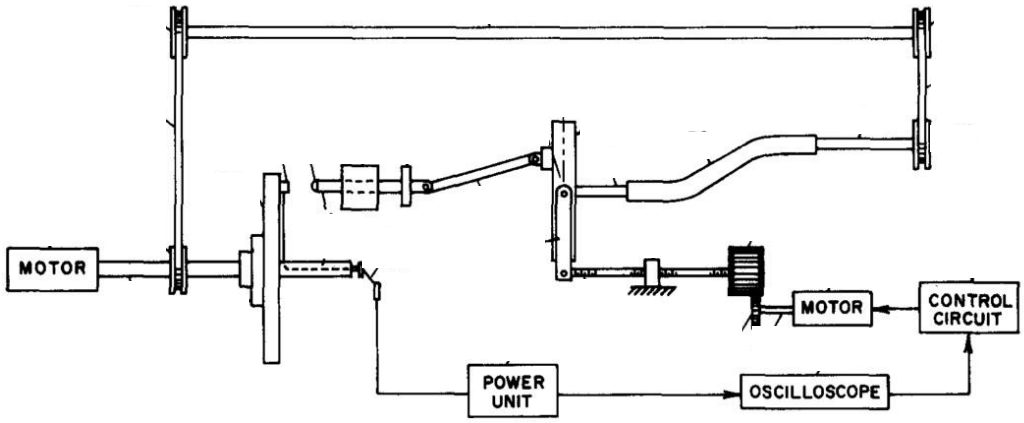

Figure 5.14: *Reciprocating pin on disk repetitive impact test rig [5.4]*

It was found that the three subsurface zones (non-deformed base material, plastically deformed base material and the white compound layer) were dependent upon velocity, stress, material, test duration and loading [5.5]. A greater velocity with a large number of cycles produced a thicker zone three (white compound layer). The depth of zone 2 (plastic deformation zone) was found to be deeper with a high velocity at a low number of cycles, however, as the number of cycles increased a lower velocity was also found to cause a deeper plastic deformed zone. In terms of stress, the white compound layer (zone 3) was found to be of same depth regardless of the stress which was applied. However, the plastically deformed zone was found to be slightly deeper with a larger applied stress. The subsurface zones were found to form quickly and are maintained in a state of equilibrium (same composition and morphology).

Another study by Rice et al. attempted to establish whether variations in hardness of precipitation hardened stainless steel (UNS S17400) influenced its repetitive impact wear behaviour [5.6]. A hard pin (44HRC/430HV) against a soft disk (30HRC/300HV) had a dramatic reduction in pin wear compared with a soft pin (30HRC) on a hard disk (44HRC).

However, there were issues with the soft pin due to a “mushrooming” effect and material transfer occurred at the contact interface. It was also found that all UNS S17400 steel specimens developed the three subsurface zones regardless of their original microstructure.

A different study by Rice found variations in wear resistance in different microstructures of UNS K92571 high strength low alloy steel during repetitive impact against a UNS S17400 pin [5.7]. The subsurface zones were also found on the high strength steel. However, ploughing and delamination were also found to contribute to the material degradation process. “Tough” specimens (aged at 400°F/204°C) had greater wear resistance than “strong” specimens (aged at 950°F/510°C).

Rice also observed the three subsurface zones in a titanium alloy (UNS R54560) and an aluminium-copper alloy (UNS A92011) [5.8]. However, there were only two clear zones (white compound layer and base material) found in aluminium alloy, UNS A92124. The aluminium-copper alloy (UNS A92011) favoured crack nucleation which resulted in voids and cracks forming in the compound layer and, hence, delamination occurred. The UNS A92124 alloy suppressed any crack nucleation due to its high fracture toughness.

Further work by Rice observed that short, stiff UNS K92571 pins produced the largest mass loss and deepest wear track; however, longer, ductile pins produced a very small amount of material loss and created irregular wear tracks due to material transfer [5.9]. It was stated that the irreproducibility for this kind of testing may be attributed to differing pin lengths which result in different stiffness and found that only stiff pins produced the compound layer.

The subsurface zones have also been observed by Menezes et al. [5.10]. The study was focused on plastic deformation and strain localisation in subsurface zones of copper pins and steel plates with surface texture was used as a variable. Plastic strain and deformed depth was found to be dependent upon the coefficient of friction and the transfer layer formation and both of these were found to depend heavily upon surface texture and lubrication. Strain was found to be greater under dry conditions than under lubricated conditions.

Nowotny et al. studied the repetitive impact sliding wear of a tool steel (CPM-10V crucible particle metallurgy) pin and a UNS S17400 counterface [5.11]. The tool steel exhibited a high resistance to compound impact wear and both materials exhibited the subsurface zones previously found in this type of repetitive impact sliding wear test. Material transfer from the UNS S17400 to the tool steel was observed and a phase transformation from ferrite to austenite was detected in the wear debris.

Nowotny et al. also assessed the characteristics of wear debris in impact sliding [5.12]. It was observed that debris could be produced from both the specimen and counterface and that the metallic particles were very small and/or distorted primary crystals. Oxides also formed during impact sliding wear and phase transformations were also observed.

Further work by Rice et al. has assessed material transfer in impact wear of titanium alloys with different beta phase content and morphology [5.13]. It was found that the material transport varied greatly and was dependent on a number of factors such as load, transverse velocity, duration and test environment. It was also observed that α and β phases in the titanium alloys were critical to the wear behaviour. For example, the predominately α alloys exhibited an increase in material transfer as the transverse velocity was increased, whereas, the predominately β alloy did not exhibit any material transfer until higher transverse velocities.

A study by Su et al. used an inclined impact-sliding wear testing apparatus to test a $TiN/Al_2O_3/TiCN$ multilayer coating on three different WC-TiC-Co cemented carbide substrates (commercially named – PM10C, PM25C and PM30C) [5.14]. The work showed that harder substrates produced more fatigue cracks in the coating, this was attributed to the lower substrate toughness. Tests also showed that in terms of sliding, the wear resistance of the coating decreased with the softer substrate. They also found that the wear was mainly influenced by applied loads and sliding speed. The multilayer coating with PM10C (1720HV) substrate was observed to have good wear resistance. The PM25C (1440HV) substrate with the multilayer coating offered good fatigue cracking resistance and the PM30C (1610HV) substrate with the multilayer coating was most effective in withstanding both impact and sliding wear components.

Li et al. conducted repetitive impact wear tests on Cr_3C_2–NiCr coatings prepared by plasma and HVOF sprays [5.15]. The HVOF coatings exhibited the best impact wear resistance as they were denser and had fewer defects. The main wearing process experienced by the coatings was impact fatigue which resulted in plastic smearing and breaking-off. Subsurface micro-cracks formed a network of cracks around the lamellae. The merging of these cracks resulted in the coatings breaking-off.

In summary, the modified pin on disk apparatus produces small loads and velocities which results in a large number of required cycles before any measurable wear occurs. In most studies, three subsurface zones are present – a white compound layer, a plastically deformed layer and un-deformed base material. These zones have been found to be present in low alloys steels, stainless steels, titanium, aluminium and copper alloys. These subsurface zones have been found to result in various wear mechanisms such as plastic deformation, ploughing, delamination, smearing and material transfer. Composite materials (HVOF sprays, etc.) exhibited fatigue cracks as well as plastic smearing as the main wear mechanisms.

5.3.2 Pivot hammer

Pivot hammer tests represent another test method used to assess repetitive impact wear extensively in the past (Figure 5.15). The test conditions for pivot hammer tests range from 2-200N applied load, up to 10^9 cycles and operate at a frequency up to 50Hz.

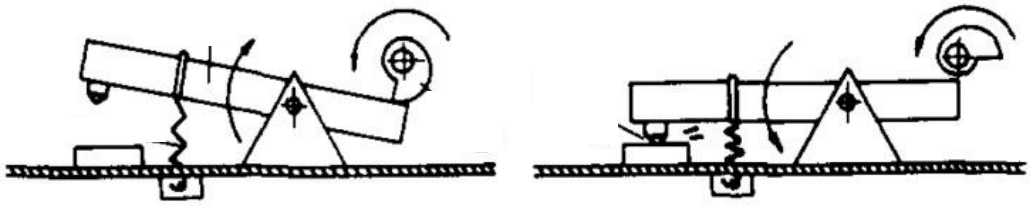

Figure 5.15: *Pivot hammer repetitive impact test rig [5.16]*

Engel and Millis studied surface topography due to repetitive impact wear on carbon steel test plates with tool steel hammers [5.17]. 2D and 3D surface profile scans exhibited plastic deformation and trends of the wearing surface deforming to the shape of the hammer.

Various surface finishes of the carbon steel test plates were also assessed (milled, ground, polished and bead-blasted); however, no benefits were found with any surface finish.

Engel and Yang, found that there were three main stages of wear during repetitive pivot hammer impacts: an initial wear stage followed by a zero wear stage and finally a measurable wear stage [5.18]. The initial wear stage was a result of initial plastic deformation and no material was lost, this occurred in less than 10 cycles. Between 10 to 2000 cycles the zero wear stage occurred, this was due to minor plastic deformation without any surface profile changes. The majority of wear occurred after 2000 cycles, where material was removed and more plastic deformation occurred.

Another pivot hammer testing device was developed by Mahoney et al. [5.19] who assessed EN42 (070A72) spring steel test samples with EN31 (534A99) steel as the hammer material. Craters were formed in the EN42 spring steel specimens after 10,000 impacts. A break-in period was observed before the material started to rapidly degrade. This observation also links with the findings by Engel and Yang [5.18].

Fricke and Allen were also interested in repetitive impact wear occurring in poppet valves and valves operating in hydropowered mining machinery [5.16]. The repetitive impact pivot hammer tests were performed in dry and wet environments on three stainless steels, UNS S43100, UNS S44004, UNS S30400, and 817M40 (EN24) steel. The materials were also tested in various heat treated forms. The study found that pitting and surface traction were the two wear mechanisms under lubricated conditions and surface heating was the main wear mechanism in dry impacting wear. Favourable material characteristics were observed to be high hardness, low coefficient of adhesion, toughness and good corrosion resistance. They also found that martensitic steels performed better than austenitic steels due to less plastic deformation and it was observed that austenite was transformed to martensite under repetitive impact conditions. The study concluded that the best way to reduce impacting wear was to keep impact velocities low.

Blau and Hanft also used a pivot hammer repetitive impacting device to investigate impact wear occurring in poppet valves and seats in automotive engines [5.20]. The materials which were assessed were alumina 995 and silicon nitride SN220M. Damage was visible in

both material after 1000 strikes, however, alumina demonstrated more micro-fracture and platelet formation than the silicon nitride test specimens.

The pivot hammer testing was conducted at low loads with a high number of cycles. The main findings were that metallic alloys exhibit an initial wear stage followed by a zero wear stage (plastic deformation only) and finally by a measurable wear stage. The main wear mechanisms for metallic alloys were plastic deformation, pitting and surface traction (wet conditions) and surface heating (dry conditions). For ceramic materials, the main wear mechanisms were micro-fracture and platelet formation.

5.3.3 High velocity impact guns

High velocity impact guns are used for impacting individual particles at extremely high impact velocities (Figure 5.16). This type of testing apparatus has been developed to study the erosion processes occurring in applications such as mining, coal gasification, helicopter parts and short take-off and landing aircraft. Particles vary in size from 100µm to 2cm and velocities range from 44m/s to 1210m/s. A variety of materials are used for the impacting particles such as zirconia, hardened steel, tungsten carbide and silicon nitride. The high velocity impact gun experiments are conducted in air.

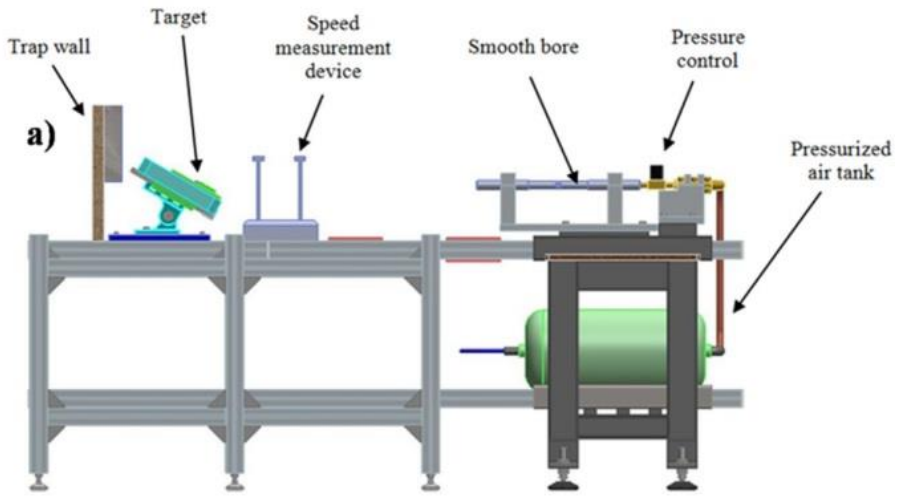

Figure 5.16: *High velocity impact gun test rig [5.21]*

A study by Cenna et al. evaluated mild steel (grade undefined) at 90m/s impact velocity and at three different impacting angles (30°, 60° and 90°) [5.22]. The study found that the

maximum crater depth occurred at 60° and smallest at 30°. A laser scanning confocal microscope (LSCM) was used to measure the craters. The measured craters from the LSCM were found to be in relation with a predictive wear model developed by Neilson and Gilchrist [5.23] as long as no plastically deformed lip occurred.

Lindroos et al. assessed four different types of wear resistant steels (grades undefined) at three different impact angles (15°, 30° and 60°) [5.21]. Spherical WC-Co cermet projectiles were used to impact the specimens. An impacting force of 2-15kN was observed during the high velocity impact testing. It was postulated that heat generated at the interface between the projectile and the sample could have led to thermal softening and potential changes in microstructure in a very thin layer on the test coupon surface. High shear deformation and strain localisation in the pile-up (lip) region was observed, as well as energy absorption and subsurface stresses due to the friction occurring during the impact event.

The authors also reported that martensitic steels strain harden at first before softening at high strain rates. This was explained by increased localisation of shear deformation into adiabatic shear bands (heat produced by the impacting particle causes narrow bands of highly sheared material to form) which rapidly change the strain hardening rate with increasing strain. This led to fracturing along the white shear bands (precursor for harder transformed bands at which failure tends to initiate [5.24]) which resulted in the main wear mechanism. Adiabatic shear bands were again used to explain the reason why the carbide reinforced steel had high strain rates. Small reinforcement particles were observed to affect the formation of white adiabatic strain bands and the high ratio of the reinforced particles had a strain hardening effect. The carbide reinforced steel experienced a low wear rate at the low angle as cutting was the main wear mechanism. However, a network of cracks in the adiabatic shear bands led to brittle fracture which initiated from the defects.

A deformation lip was also found to occur during the tests which increased in height with increase in angle. A formulation (Eq. 5.1) was developed to define how much material was “cut” and how much was plastically deformed. Where, V_{neg} is the volume below the surface (inside the wear scar) and V_{pos} is the volume above the surface. If the value is one then the material has been removed by cutting mechanisms and if the value is zero then the material has been plastically deformed.

$$\varphi = \frac{|V_{neg}| - |V_{pos}|}{|V_{neg}|} \quad \text{Eq. 5.1}$$

Murr et al. evaluated changes in microstructure of UNS R56400 titanium alloy impacted by UNS G43400 low alloy steel projectiles due to adiabatic shear band failure [5.25]. The impact velocities ranged from 633-1027m/s. The adiabatic shear bands contained martensite which increased in density with increased impact velocity. Crack nucleation and propagation inside the adiabatic shear bands also increased with impact velocity.

Duan et al. also assessed the microstructure and adiabatic shear bands formed during high velocity impact testing [5.26]. Sintered tungsten alloy (93W) projectiles were impacted on a medium carbon steel (undefined) and a 30CrMnMo steel. No adiabatic shear bands were observed on the carbon steel as the impact energy dissipated slowly. However, 30CrMnMo steel demonstrated evidence of adiabatic shear bands due to the quick dissipation of the impact energy.

Naim and Bahadur conducted a single particle impact testing using hardened steel balls (grade undefined) to impact on 70-30 brass (UNS C26000) specimens at 120m/s [5.27]. It was observed that the impact damage increased as the levels of cold working increased. Unsurprisingly, the damage caused by the impact, also increased with increasing kinetic energy. Two distinct mechanisms were observed to occur during the impact testing: flake formation and lip fragmentation. Flake formation was the dominant wear mechanism in normal impact conditions; whereas, lip fragmentation was the dominant wear mechanism at oblique impact conditions.

High velocity impact gun testing was conducted in air with particle sizes ranging from 100µm to 2cm and velocities between 44m/s and 1210m/s. A variety of wear mechanisms have been observed such as thermal softening, shear deformation, stain localisation, adiabatic shear bands, flake formation and lip fragmentation.

5.3.4 Ball on plate

Ball on plate testing devices (Figure 5.17) use spherical balls, which are often tungsten carbide as the ball material, to create repetitive impact damage. The loads used in these studies are less than 1kN and are often in the magnitude of 10^3-10^6 cycles. They are commonly used to assess the adherence of thin surface coatings such as Diamond-like Carbon (DLC) and Physical Vapour Deposition (PVD) coatings [5.28–5.35].

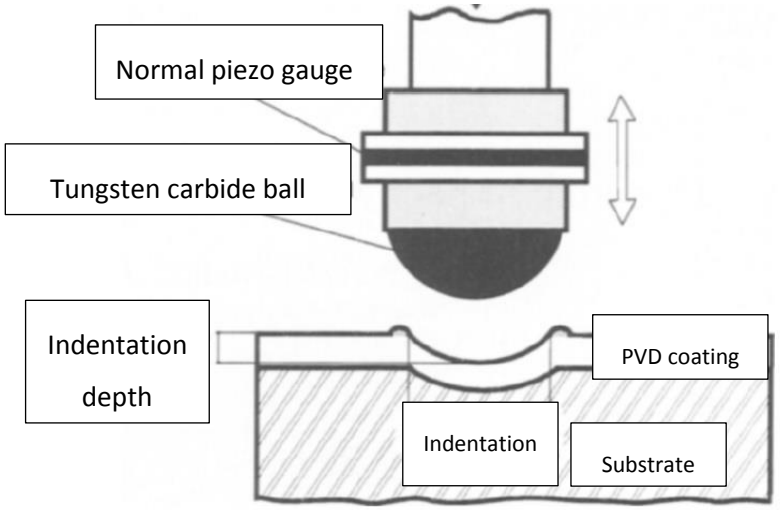

Figure 5.17: *Schematic of ball on plate impact testing machine* [5.35]

Kuptsov et al. assessed the corrosion and impact behaviour of TiCN, TiSiCN, TiCrSiCN and TiAlSiCN coatings which had been deposited via DC magnetron sputtering (PVD process) onto WC-6Co and alumina substrates [5.36]. Impact tests were conducted in air, distilled and saline (0.9%NaCl) water. The TiCN coating performed the poorest under dynamic impact conditions due to coating imperfections such as porosity and micro-cracking which dramatically reduced the mechanical properties of the coating. The TiAlSiCN coating was the only tested material which was able to withstand the dynamic impact loads in all three environments (dry, distilled and saline water).

La Vecchia and Lecis studied the effect of a duplex treatment (nitriding plus a CrN PVD coating) on a UNS G41400 substrate under repetitive impact conditions with a UNS G52986 steel ball [5.37]. A non-nitrided coating (CrN only) was found to fail after only 1000 cycles, however, the nitrided coating was found to exhibit no cracking up to 50,000 cycles. The

benefit of the nitriding treatment was attributed to the higher stiffness of the coating which suppressed the occurrence of adhesive coating failure.

Yoon et al. studied the repetitive impact wear behaviour of TiN and Ti-Al-N PVD coatings on UNS T30402 and WC-Co substrates against tungsten carbide balls [5.38]. The study found that the ratio, H^3/E^{*2} (defined as the plastic deformation resistance of the specimen, where H is the hardness and E* is the effective Young's modulus ($E^*=E/(1-\nu^2)$), note, ν is Poission's ratio), played an important role to the repetitive impact wear behaviour of the coating. A greater H^3/E^{*2} ratio altered the repetitive impact wear mechanism from plastic deformation to a brittle failure mode.

Cassar et al. assessed the repetitive impact wear behaviour of plasma diffusion treatments, PVD ceramic and duplex treated (combined plasma and PVD) coatings on a UNS R56400 substrate against a cemented carbide ball indenter [5.39]. The study observed that the resistance to repetitive impact wear of the UNS R56400 alloy could be increased from diffusion and PVD coating surface treatments. However, the duplex treated coatings with shallow diffusion treatments were found to have greatest resistance to repetitive impact.

Huang et al. studied the repetitive impact of high silicon (1.65 Si) bainitic cast irons [5.40]. Slightly modified bainitic cast iron (with alloying addition of <0.15Ti) was observed to improve the repetitive impact wear resistance by up to 50% compared to the unmodified bainitic cast iron. The formation of a white compound layer (Figure 2.24) was found on the surface of the tested cast irons.

Rastegar and Karimi assessed the repetitive impact wear resistance of four different wear resistant steels (grades undefined) with cemented carbide indenters [5.41]. The study found that subsurface deformation increased with increasing impact energy, impact velocity and decreasing steel hardness. The study also observed that localised deformation resulted in narrow adiabatic shear bands with a fine microstructure. Within the shear bands, intense shearing and nucleation of micro-voids were also observed. The growth and linkage of the voids resulted in crack formation along the length of the shear band which eventually lead to flake-like fragments becoming detached once the cracks reached the surface.

Yang et al. studied the failure modes induced by white layers formed on a medium-high carbon low alloy steel (grade undefined) during repetitive impacts with bainitic steel (grade undefined) balls [5.42]. Two wear zones were found to form subsurface of the low alloy steel during testing, a white compound layer and a plastically deformed zone. Two different failure modes were observed to occur on the low alloy steel. The first was due to delamination occurring when microcracks propagated along a path parallel to the white compound layer. The second failure mode occurred due to spalling when microcracks propagated along the flow lines of the plastically deformed zone.

Iturbe et al. studied the repetitive impact wear behaviour of a copper alloy (grade undefined) with hardened steel indenter (grade undefined) [5.43]. The study found that a substantial amount of plastic deformation occurred below the surface of the copper alloy. The material removal mechanism was found to occur due to surface cracking and flaking from a fatigue process caused by the sliding friction between the indenter and specimen and the formation of an inhomogeneous region formed from plastically deformed material.

The ball on plate impact testing was conducted at moderate loads and cycles and has been broadly used to assess the adherence of thin surface coatings. A white compound layer with a plastically deformed zone has been observed in some studies of metallic alloys as well as adiabatic shear bands. These often lead to nucleation of micro-voids as well as surface cracking and flaking.

5.3.5 Repetitive impact with abrasion

Due to the high wear rates found in hydraulic rock crushing equipment, repetitive impact test rigs have been designed to incorporate the dry abrasive “crushing” effects of rocks, as seen in Figure 5.18. The test conditions include high loads up to 86kN and test durations up to 1000 cycles.

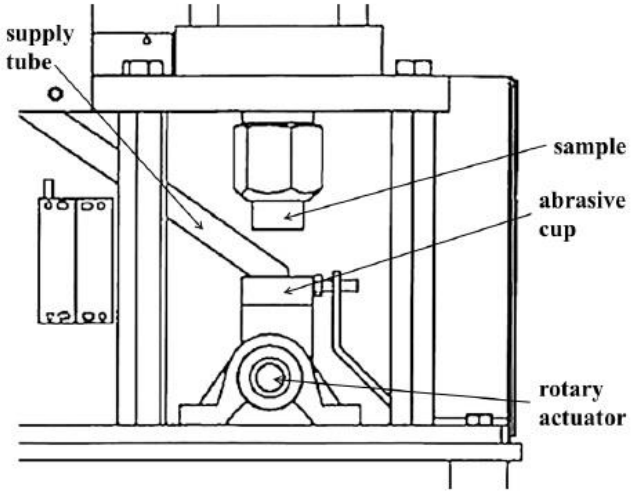

Figure 5.18: *Repetitive impact with abrasion test rig [5.44]*

Ratia et al. assessed the repetitive impact with dry abrasion wear behaviour of structural steel S355 and three martensitic wear-resistant steels (Raex 400, 450 and 500) with granite rocks as the abrasive particles [5.44]. The study observed that increasing hardness resulted in better repetitive impact wear resistance. The main wear mechanisms were observed to be indentation, plastic deformation and micro-scratches.

Work by Heino et al. studied the same materials as Ratia et al. [5.44] as well as WC-Co hard metal in a variety of compositions with granite as the abrasive particles [5.45]. A link with increasing hardness with improved impact resistance was also observed. Abrasion and plastic deformation were found to be the main wear mechanisms.

Lindroos et al. studied the repetitive impact with dry abrasion wear of high manganese Hadfield steel (grade undefined) with basalt, granite, tonalite and quartz abrasive particles [5.46]. It was observed that the abrasiveness of the rock had better correlation with material loss than rock hardness. The surface hardness of Hadfield steel was found to increase dramatically (400HV increase) after testing as a result of austenite to martensite phase transformation.

Kennedy and Hashmi studied the repetitive impact with dry abrasion wear behaviour of HVOF sprayed Ni-Cr and WC-Co on aluminium and mild steel substrates (grades undefined) with a tungsten carbide indenter [5.47]. The study found that coated and uncoated mild

steel samples exhibited greater resistance to impact wear than coated and uncoated aluminium alloy samples.

Osara and Tiainen studied the repetitive impact wear of variations of manganese steel, a white cast iron and two metal-matrix composites (MMCs) (50%WC with 50% high speed steel (high performance steel with high hardness at high temperatures up to 500°C) matrix and 70% high speed steel in manganese steel matrix) [5.48]. The MMCs and white cast iron exhibited the greatest resistance to repetitive impact with abrasion resistance compared to the manganese steels. The mix of hard wear resistant particles with a hardenable/tough matrix was attributed to the good performance of the MMCs. The high hardness of the white cast iron (650HV) was found to be beneficial in these test conditions.

Page et al. assessed the repetitive impact with dry abrasion wear of a Ni hard-4 cast iron (grade undefined) with quartz sand abrasive particles [5.49]. The main material degradation mechanism was found to be ploughing. As the tests continued, comminution of the sand particles reduced the wear rate significantly.

Qian and Chaochang studied the repetitive impact with dry abrasion wear of low alloy white cast irons with quartz sand as the abrasive [5.50]. The study observed that material loss increased with increased volume fraction of eutectic carbides. The network of eutectic carbides were found to fragment and gradually turn into microcracks after repeated impacts.

Repetitive impact with abrasion tests were conducted with high loads and a low number of cycles. A good correlation was observed with increased hardness with increased resistance to impact-abrasion. The main wear mechanisms were indentation, plastic deformation and micro-scratches. Micro-cracking was observed in materials with carbides.

In summary, the literature study of repetitive impact test machines, demonstrated (perhaps unsurprisingly) that the main damage processes occurring during repetitive metal-metal impact are interactions between plastic deformation and cracking. Although a large number of variations of testing equipment and conditions have been investigated, many of these (e.g. stress levels, no of cycles, dry conditions, etc.) are not especially relevant to the valve and seat deterioration situation. There appears to be no standard test rig which

incorporates repetitive impact with high compressive loads and abrasive sand particles in an aqueous solution. Therefore, it was clear that a purpose built rig was required to investigate this type of wear. The design and testing conditions of the custom built repetitive impact with slurry is discussed in Chapter 3.4 and 5.4.

5.4 Materials and methods

In order to obtain correlation between repetitive impact behaviour and material type/conditions a range of materials were assessed these are described by category below.

Heat treated/surface engineered low-alloy steel

- Carburised UNS G86200 – a carburised low alloy steel
- Induction hardened UNS G52986 – an induction hardened high carbon low alloy steel
- Quenched and tempered UNS G52986 – a quenched and tempered high carbon low alloy steel
- Induction hardened UNS G41400 – an induction hardened low alloy steel
- Nitrided 905M39 steel – an ammonia gas nitrided low alloy steel

Stainless steels

- UNS S31600 – austenitic stainless steel
- UNS S42000 – martensitic stainless steel, in heat treated and non-heat treated forms
- UNS S44003 – martensitic stainless steel with 0.75-0.95%C content
- UNS S44004 – martensitic stainless steel with 0.95-1.2% C content
- UNS S32760 – high alloy duplex stainless steel

Chromium cast irons

- Commercially available 27%Cr cast iron – hypoeutectic chromium cast iron with a martensitic metal matrix and hard M_7C_3 carbides
- Commercially available 37%Cr cast iron – hypoeutectic chromium cast iron with an austenitic metal matrix and hard M_7C_3 carbides

Cermet coating

- HVOF WC-10Ni – commercially available HVOF sprayed coating with 90% tungsten carbide and 10% nickel metallic binder

The nominal chemical composition (obtained from technical data sheets from the material supplier) for each test material is given in Table 5.4. The hardness, elastic modulus and yield strength of the test materials are shown in Table 5.5. These material properties were used to assess relationships between material properties and repetitive impact wear resistance.

Table 5.4: *Nominal chemical composition (wt%) of the test materials*

Material	C	Cr	Ni	Mo	S	Mn	Si	N	P	Fe
UNS G86200	0.18-0.23	0.4-0.6	0.4-0.7	0.15-0.25	≤0.04	0.7-0.9	0.15-0.35	-	≤0.035	Bal.
UNS G52986	0.98-1.10	1.3-1.6	-	-	≤0.025	0.25-0.45	0.15-0.30	-	≤0.025	Bal.
UNS G41400	0.38-0.43	0.8-1.1	-	0.15-0.25	0.04	0.75-1.00	0.15-0.30	-	0.035	Bal.
UNS S31600	≤0.08	16-18	10-14	2-3	≤0.03	≤2.0	≤0.75	≤0.1	0.045	Bal.
905M39 steel	0.35-0.43	1.4-1.8	-	0.15-0.25	≤0.025	0.40-0.65	0.1-0.4	-	0.025	Bal.
UNS S42000	≤0.15	12-14	-	-	≤0.03	≤1	≤1	-	≤0.04	Bal.
UNS S44003	0.75-0.95	16-18	-	≤0.75	≤0.03	≤1	≤1	-	≤0.04	Bal.
UNS S44004	0.95-1.20	16-18	-	≤0.75	≤0.03	≤1	≤1	-	≤0.04	Bal.
UNS S32760	≤0.03	24-26	6-8	3-4	≤0.01	≤1	≤1	0.2-0.3	≤0.03	Bal.

27%Cr cast iron	3	27	-	-	-	-	-	-	-	-
37%Cr cast iron	1.8	37	-	-	-	-	-	-	-	-

Table 5.5: *Hardness, elastic modulus and yield strength of the test materials*

Material	Hardness (HV)	Elastic modulus (GPa)	Yield strength (MPa)
Carburised UNS G86200	720	200	832
Induction hardened UNS G52986	720	200	1410
Quenched and tempered UNS G52986	825	200	1410
Induction hardened UNS G41400	655	200	-
UNS S31600	170	193	285
Nitrided 905M39 steel	1100	200	480
UNS S42000 – heat treated	480	200	1360
UNS S42000 – non-heat treated	280	200	345
HVOF WC-10Ni	1060	-	-
UNS S44003	580	200	1860

UNS S44004	630	200	1896
UNS S32760	265	200	795
27%Cr cast iron	765	-	650
37%Cr cast iron	365	-	250

The experiments were conducted in the repetitive impact test rig which is detailed in Chapter 3.4. The tests ran for 50,000 cycles with an applied load of 32kN and a frequency of 5Hz. A carburised UNS G86200 steel with a diameter of 6mm was used as the indenter material. A constant supply of hydraulic fracturing sand was fed between the impactor and the test sample with a sand concentration of 54g/l. Two replicates were assessed for each test material.

5.5 Results and discussion

This section discusses the test results and findings from the validation testing of the repetitive impact with slurry rig. The first part discusses some initial test results which assessed the contribution of damage by the "crushing" of the sand particles. The main section of test results evaluates a wide range of materials under repetitive impact conditions. The sand particles before and after testing were also assessed to evaluate their circularity. A metallographic examination of the wear scars of the tested materials was also conducted, along with an assessment of relationship between material properties and repetitive impact wear resistance.

5.5.1 "Crushing" effect of sand

It was necessary to assess the contribution of damage from the "crushing" effect of the sand. In order to evaluate this, tests were conducted with and without slurry. The material used in these initial tests was UNS S31600. The test parameters are stated in Table 3.8 and in Chapter 3.4. Figure 5.19 shows the appearance of the UNS S31600 test specimens after the exposure to repetitive impact with and without the slurry. The wear scar depths and volume losses for the tests are shown in Figures 5.20 and 5.21.

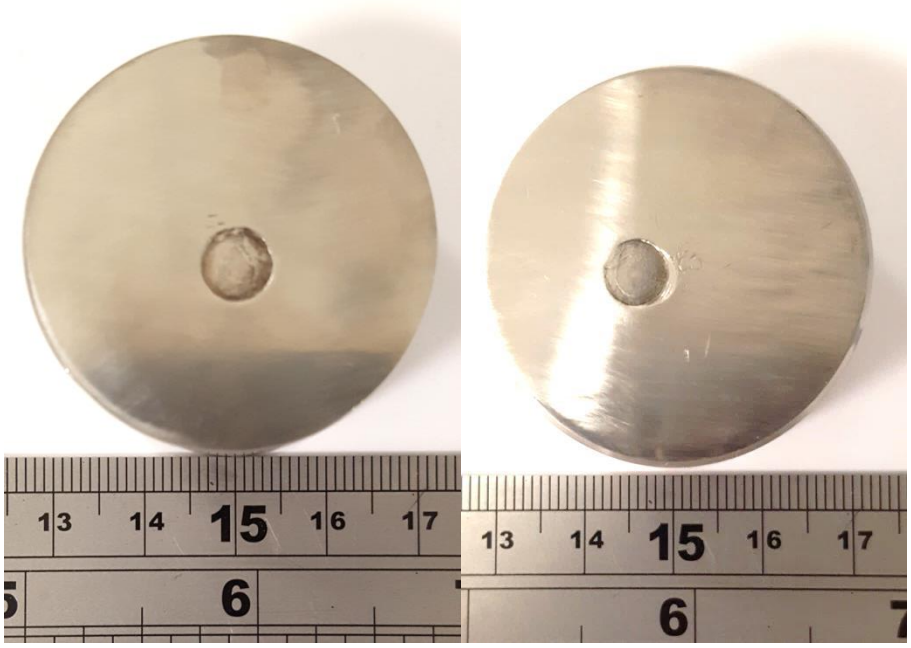

Figure 5.19: *UNS S31600 after testing: without slurry (left) and with slurry (right)*

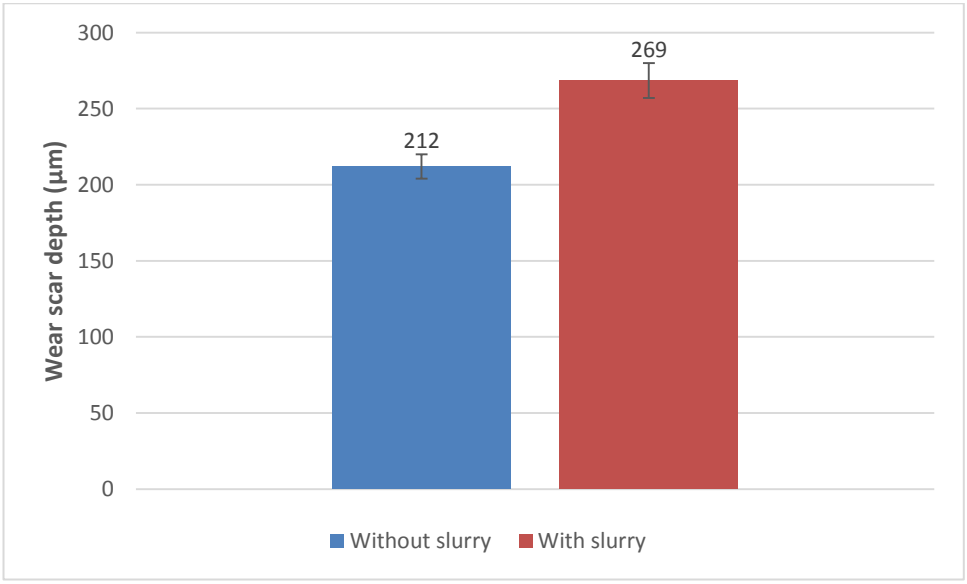

Figure 5.20: *Wear scar depth for UNS S31600 with and without slurry*

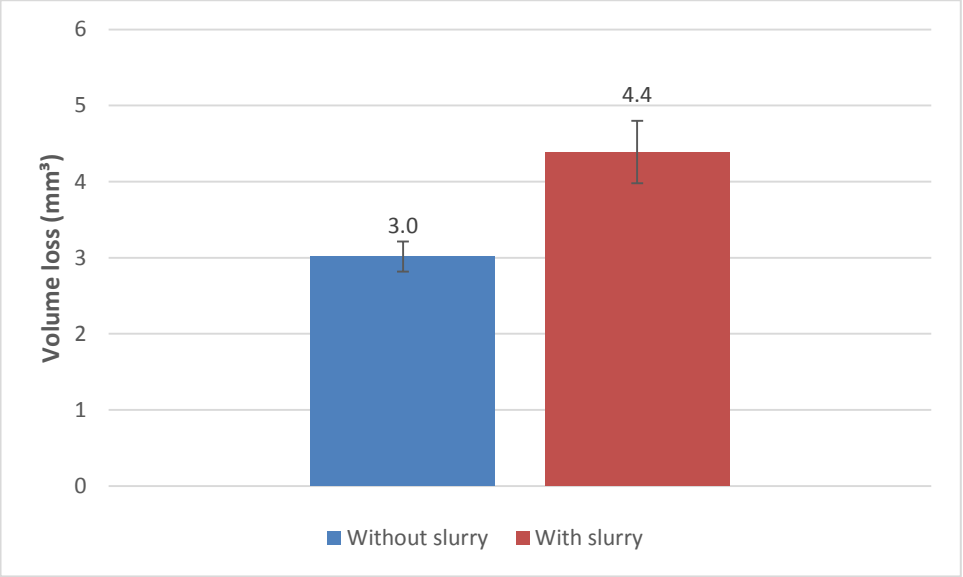

Figure 5.21: *Volume losses for the UNS S31600 with and without slurry*

Wear scar depths and volume losses both increased when sand particles were being crushed between the impactor and specimen demonstrating that the crushing of the sand particles contributes to the repetitive impact damage (20-30% of overall damage). However, it should be noted that a significant amount of the damage (70-80%) was attributed to only repetitive impact wear (without slurry).

5.5.2 Surface topography

5.5.2.1 Wear scar depth

The wear scar depths for all tested materials are shown in Figure 5.22. The scatter bands represent the scatter bands for two test replicates. The UNS S31600 stainless steel and HVOF WC-10Ni exhibited the greatest wear scar depths of all test materials. Whereas, the carburised UNS G86200 and 27%Cr cast iron demonstrated the lowest wear scar depths. In general, materials with a martensitic microstructure (carburised UNS G86200, 27%Cr cast iron, UNS S42000 (480HV), induction hardened UNS G52986, etc.) had lower wear scar depths than materials with an austenitic microstructure (UNS S31600 and 37%Cr cast iron). This observation has been perceived in previous studies [5.15, 5.41]. However, there were exceptions to this as the UNS S42000 (280HV), UNS S44003 and UNS S44004 all demonstrated wear scar depths greater than the 37%Cr cast iron and UNS S32760.

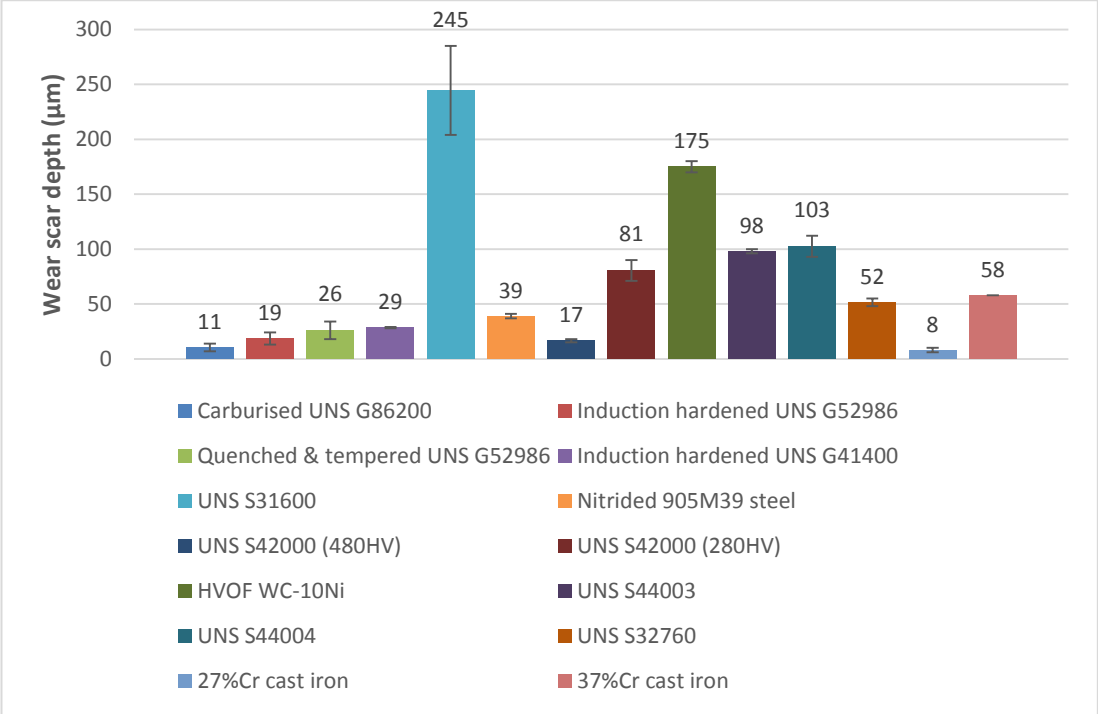

Figure 5.22: *Wear scar depths of the tested materials in repetitive impact with slurry conditions*

5.5.2.2 Wear scar volume loss

The wear scar volume losses for all test materials are given in Figure 5.23, materials with a volume loss with less than 0.2mm³ are also presented in Figure 5.24 for a better comparison. A similar trend to those found with wear scar depths was observed, as the UNS S31600 stainless steel and HVOF WC-10Ni exhibited the greatest wear scar volume losses and the carburised UNS G86200 and 27%Cr cast iron demonstrated the lowest wear scar volume losses.

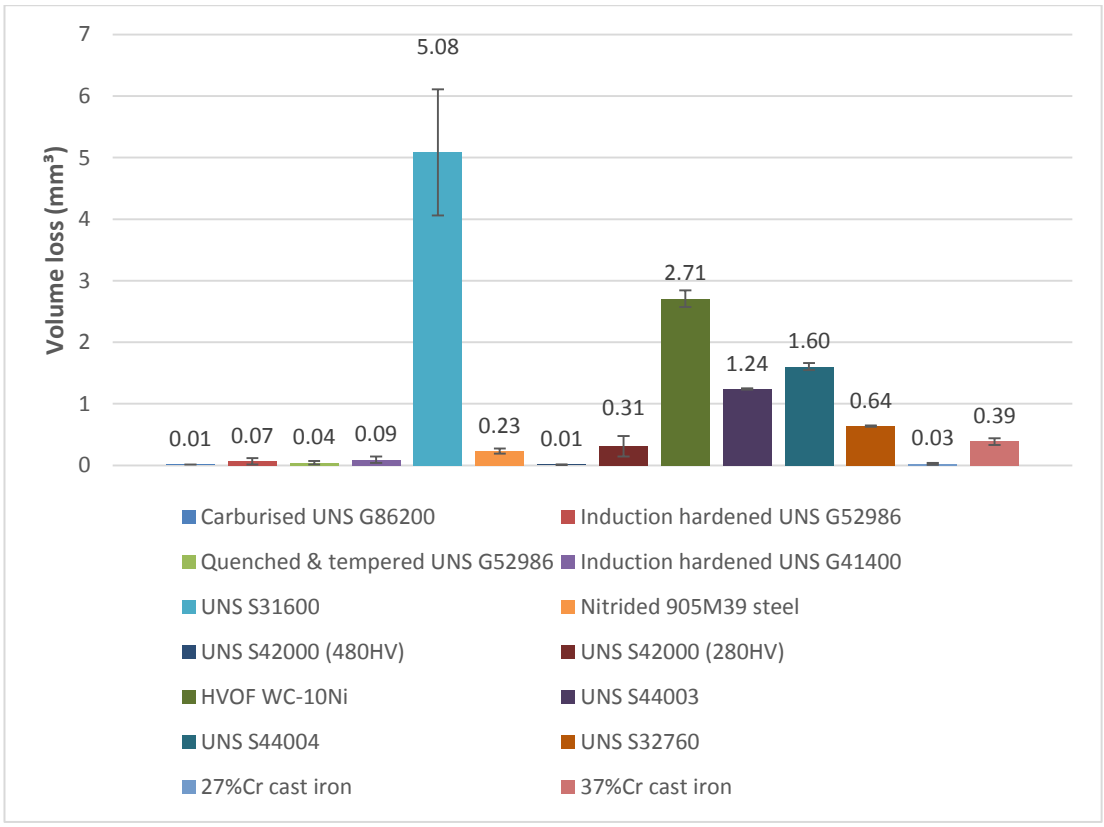

Figure 5.23: *Wear scar volume losses of tested materials in repetitive impact with slurry conditions*

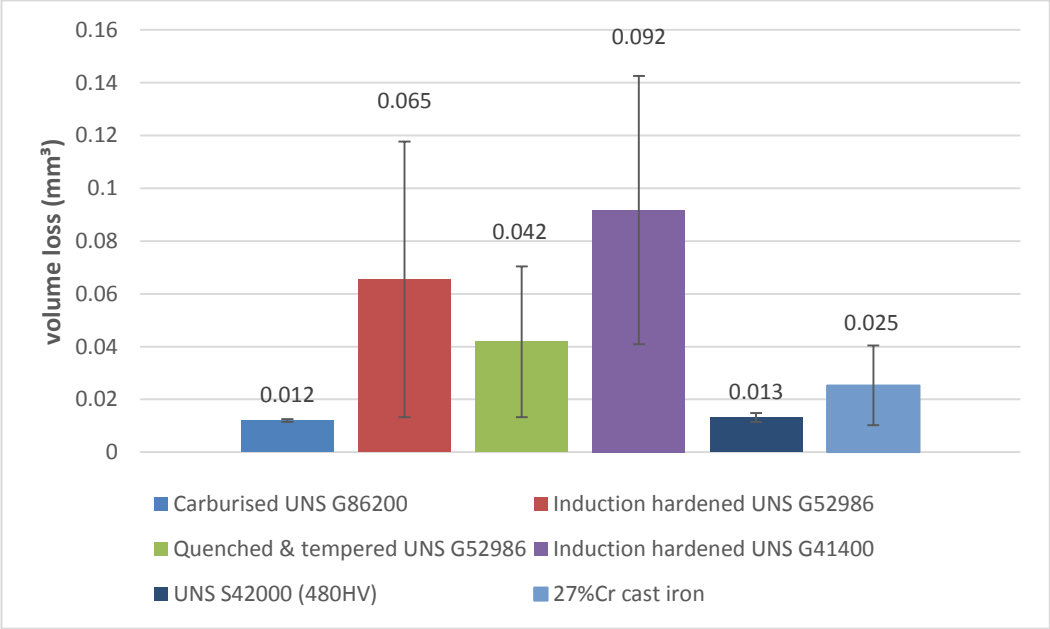

Figure 5.24: *Wear scar volume losses for tested materials (volume loss less than 0.2mm³) in repetitive impact with slurry conditions*

5.5.2.3 Wear mechanisms occurring in repetitively impacted zones

The material degradation mechanisms occurring inside the repetitively impacted wear scars were determined through SEM images of cross sectioned wear scars. A light microscope was used for an in-plane image of the HVOF WC-10Ni coating wear scar (Figure 5.38). A microhardness profile for the soft/ductile materials was also conducted to assess work hardening effects. A selection of soft/ductile and hard/brittle materials (listed below) were chosen to be analysed.

- Soft/ductile materials (170HV-580HV) – UNS S31600, UNS S42000 (280HV), UNS S44003, UNS S32760
- Hard/brittle materials (720HV-1100HV) – 27%Cr cast iron, carburised UNS G86200, Nitrided 905M39 Steel, HVOF WC-10Ni

UNS S31600

The main material degradation mechanism for the UNS S31600 was plastic deformation where regions within the wear scar suffered from a cutting/shearing effect from “crushing” sand particles (Figure 5.25). This type of damage is similar to cutting deformation wear as described by Hutchings [5.51], who stated that subsequent impacts will easily remove the vulnerable material displaced in the highly strained lip. Work by Ratia et al. attributed large amounts of plastic deformation of materials with low hardness and high ductility [5.44].

A hardness increase of 100HV was observed at the surface of the UNS S31600 impact wear scar (Figure 5.26). This strain hardening effect of UNS S31600 has been observed previously by a number of researchers [5.52–5.54]. Singh et al. conducted air blasting experiments at normal incidence and found that the surface hardness of UNS S31600 increased from 160HV to 430HV [5.53]. Similarly, Giourntas observed hardness increases of 100HK (Knoop hardness) in a wear scar of UNS S31600 after an impinging slurry jet experiment [5.54].

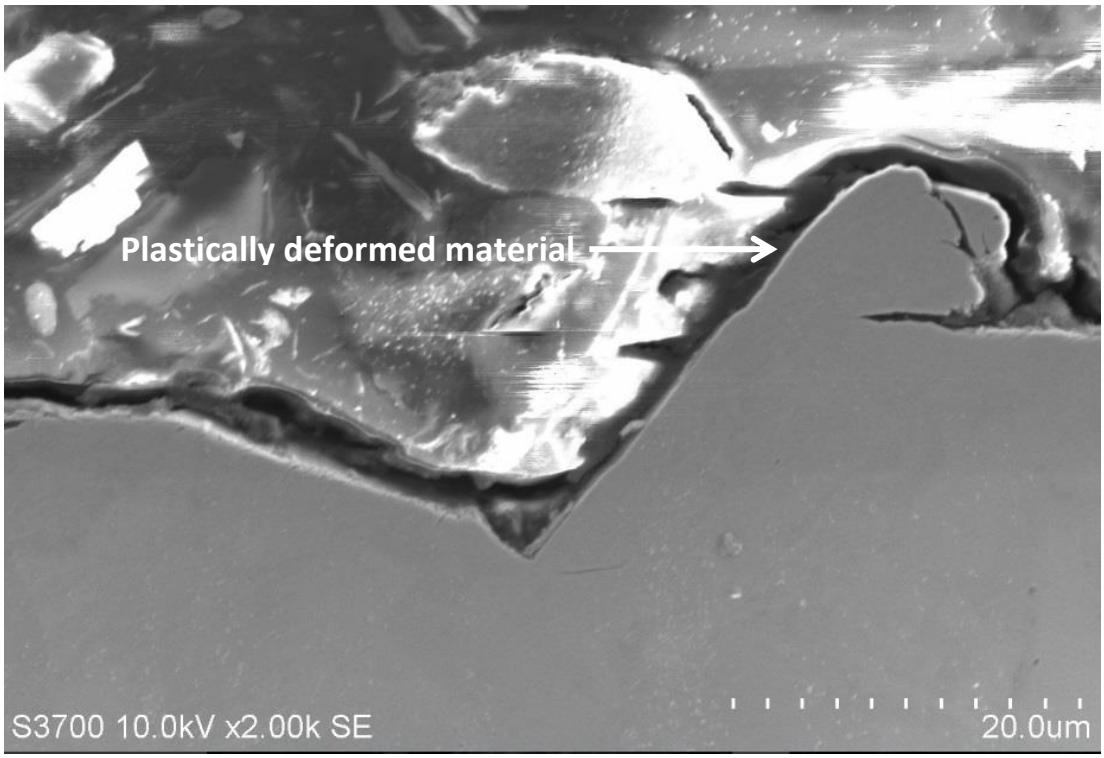

Figure 5.25: *Plastically deformed material in UNS S31600 wear scar following repetitive impact wear testing*

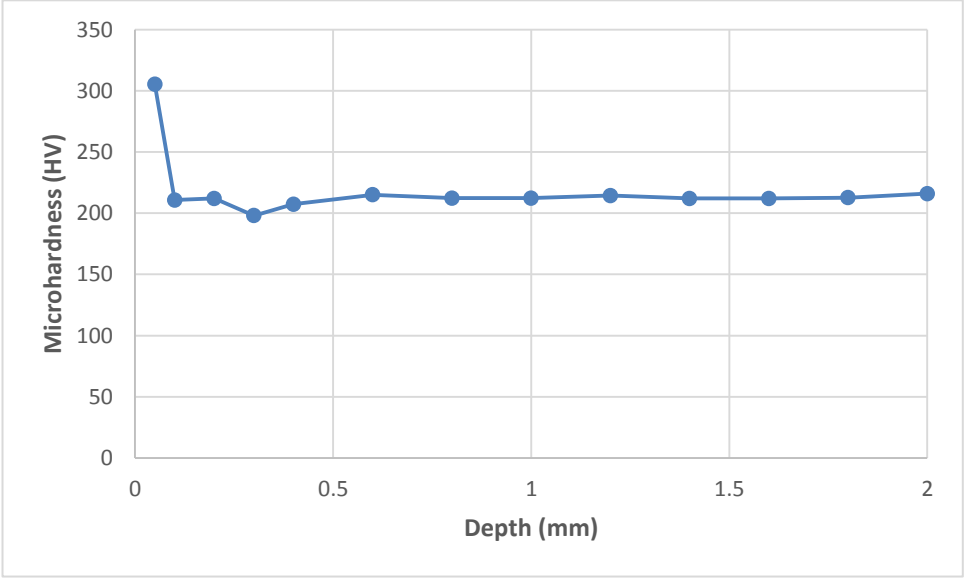

Figure 5.26: *Microhardness profile for UNS S31600 wear scar*

UNS S42000 (280HV)

For UNS S42000, the main degradation mechanism was found to be microploughing which has resulted in plastically deformed material (Figure 5.27). Localised regions in the wear scar exhibited heavily sheared material which is vulnerable to removal in subsequent impacts. No increase in surface hardness was observed for the UNS S42000 (Figure 5.28).

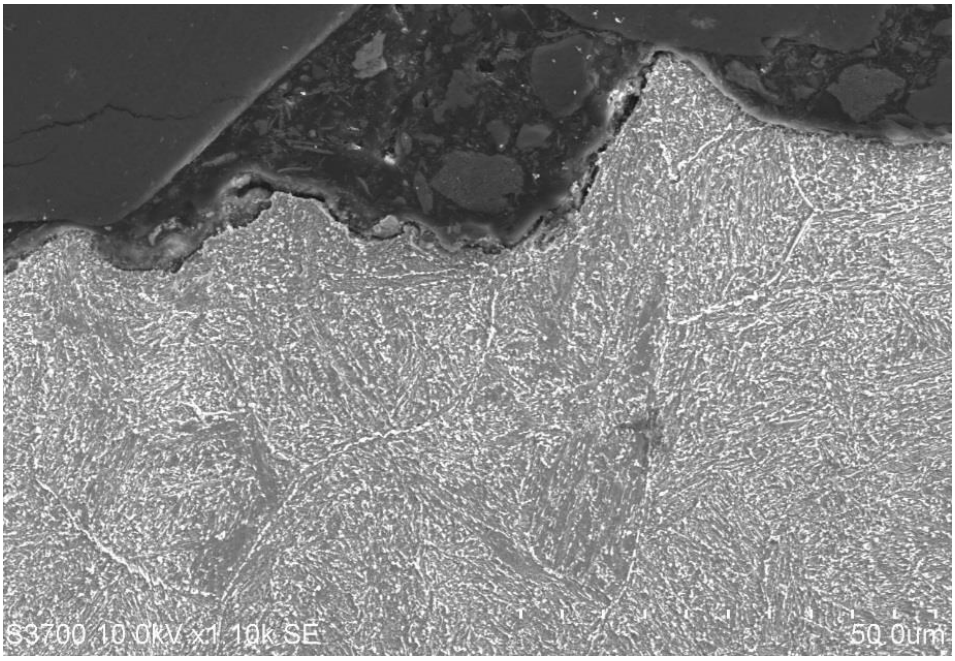

Figure 5.27: *Plastically deformed material in UNS S42000 (280HV) wear scar*

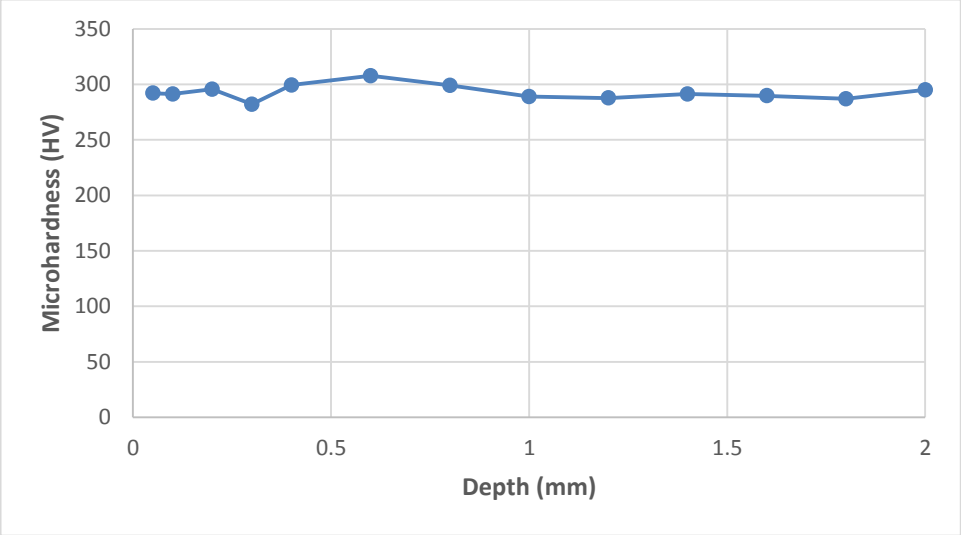

Figure 5.28: *Microhardness profile for UNS S42000 (280HV) wear scar*

UNS S44003

The UNS S44003 exhibited two different types of wear mechanisms. Figure 5.29 illustrates the cross section of the UNS S44003, where subsurface cracking was observed on a primary carbide. This feature illustrates that impact stresses, caused by the impactor and "crushed" sand particles, have transferred onto the carbides which has resulted in cracking. It is possible that the fractured carbides underneath the surface will increase the likelihood of spalling which has then caused material to be removed (Figure 5.30). It is also possible that martensite has also deformed and the combination of these degradation processes has led to the removal of material. No increase in hardness was observed for the UNS S44003 (Figure 5.31).

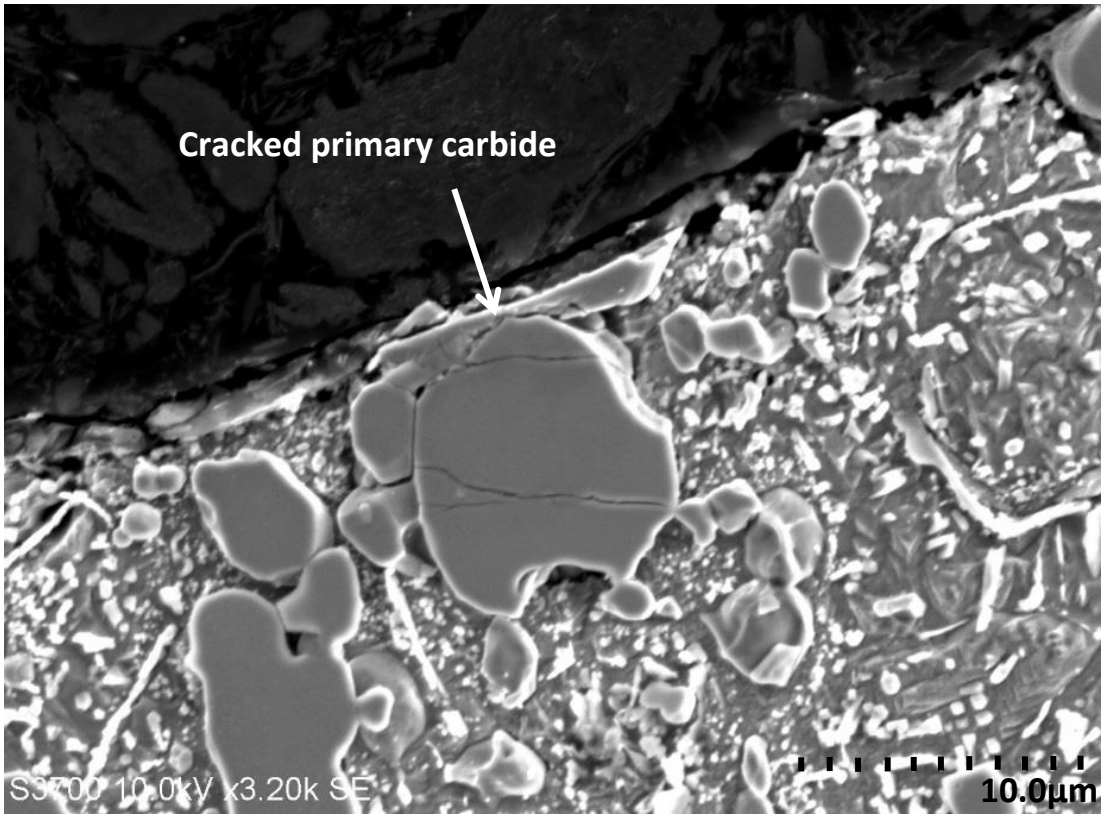

Figure 5.29: *Cracked primary carbide in UNS S44003 wear scar*

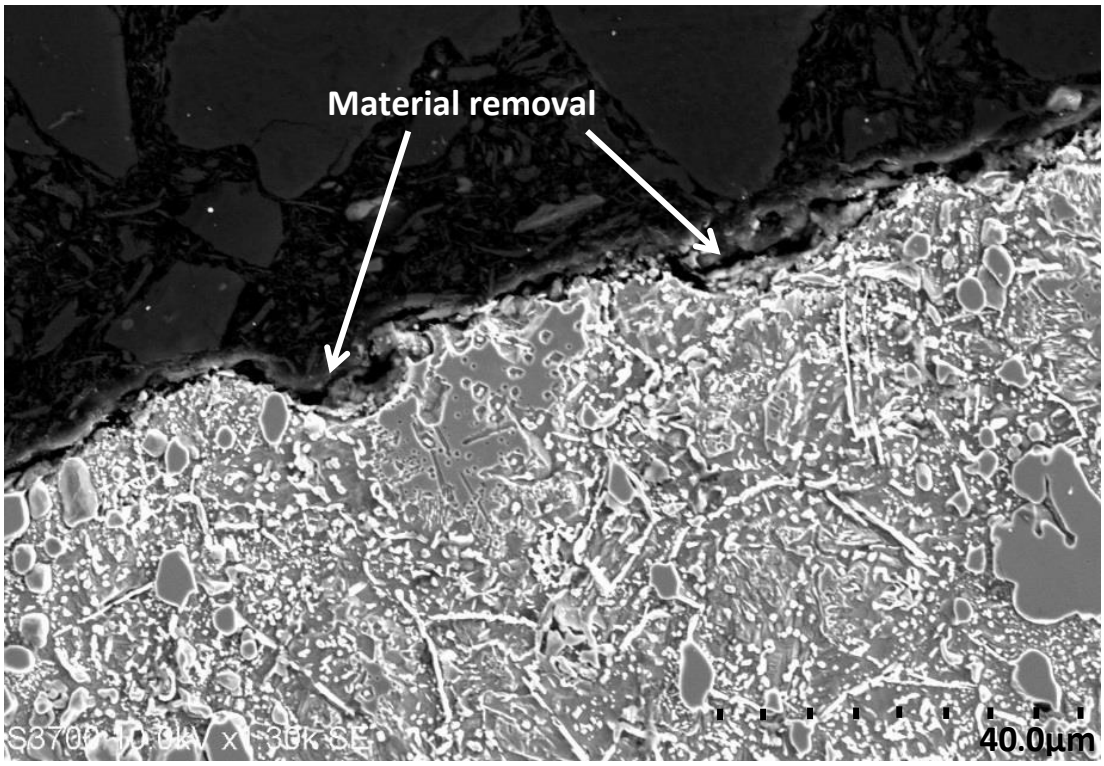

Figure 5.30: *Material removal in UNS S44003 wear scar*

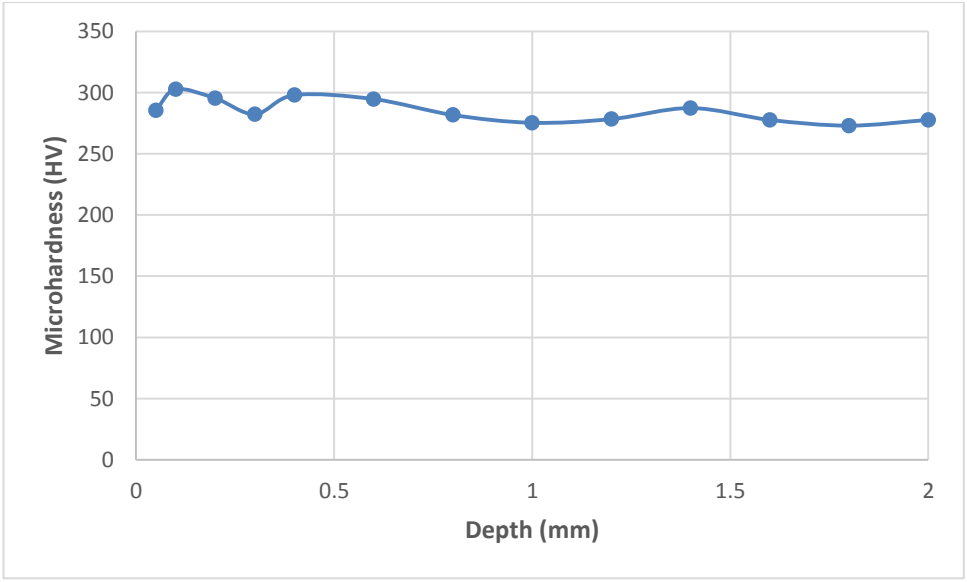

Figure 5.31: *Microhardness profile for UNS S44003 wear scar*

UNS S32760

Figure 5.32 shows the cross section of UNS S32760 wear scar, where sections of grains have been removed. The removal of these grain sections may be attributed to surface fatigue

caused by the high stresses applied by the repetitive "crushing" of sand particles into the surface of the material. Parts of the grain have been drawn out and orientated parallel to the surface. No increase in surface hardness was observed for UNS S32760 (Figure 5.33).

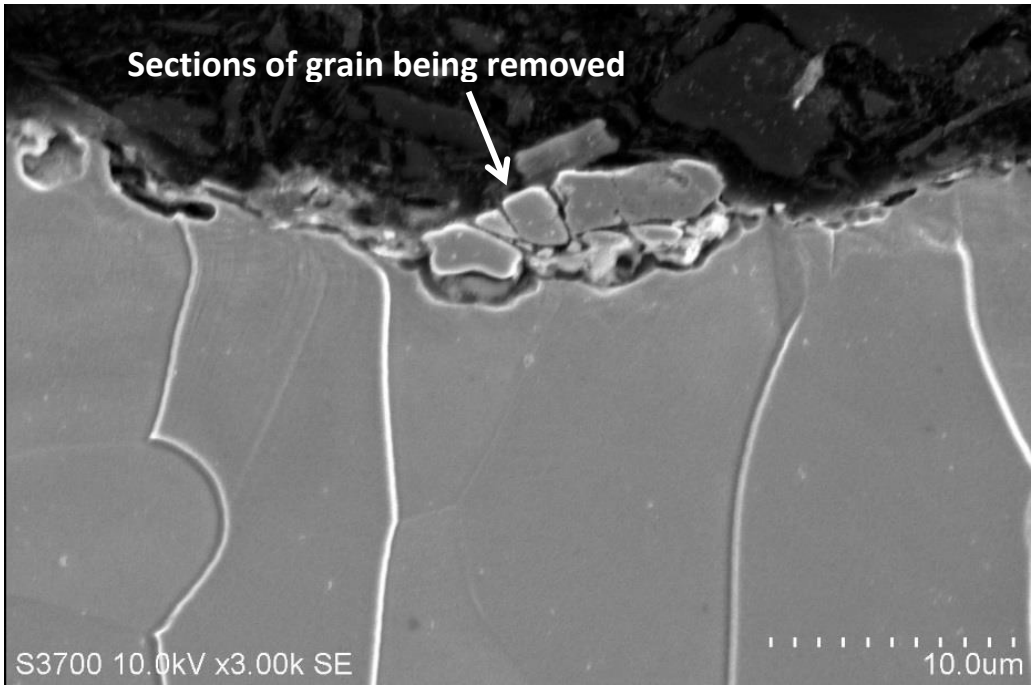

Figure 5.32: *Sections of grain being removed in UNS S32760 wear scar*

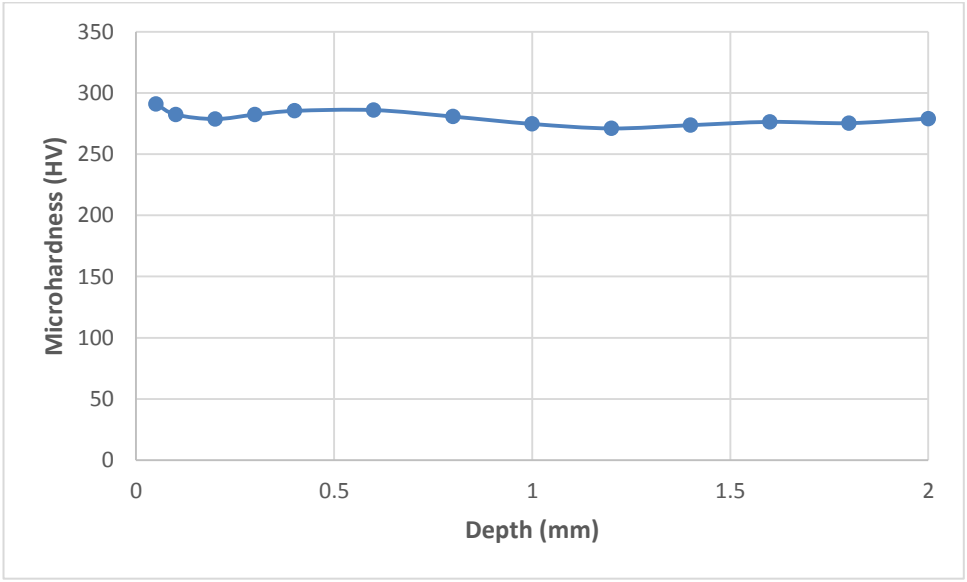

Figure 5.33: *Microhardness profile for UNS S32760 wear scar*

27% Cr cast iron

The 27%Cr cast iron exhibited a similar type of degradation processes as the UNS S44003. In localised regions within the wear scar, the martensitic matrix was heavily deformed (Figure 5.34) and cracks were observed in primary carbides (Figure 5.35). This is has been caused by the high impact stresses from "crushed" sand particles. Qian et al. have also observed severe fragmentation of carbides in a white cast iron caused by repetitive impact loading [5.47]. Further development of the fragmentation process resulted in the eutectic carbide spalling and also formed microcracks along the eutectic carbide network.

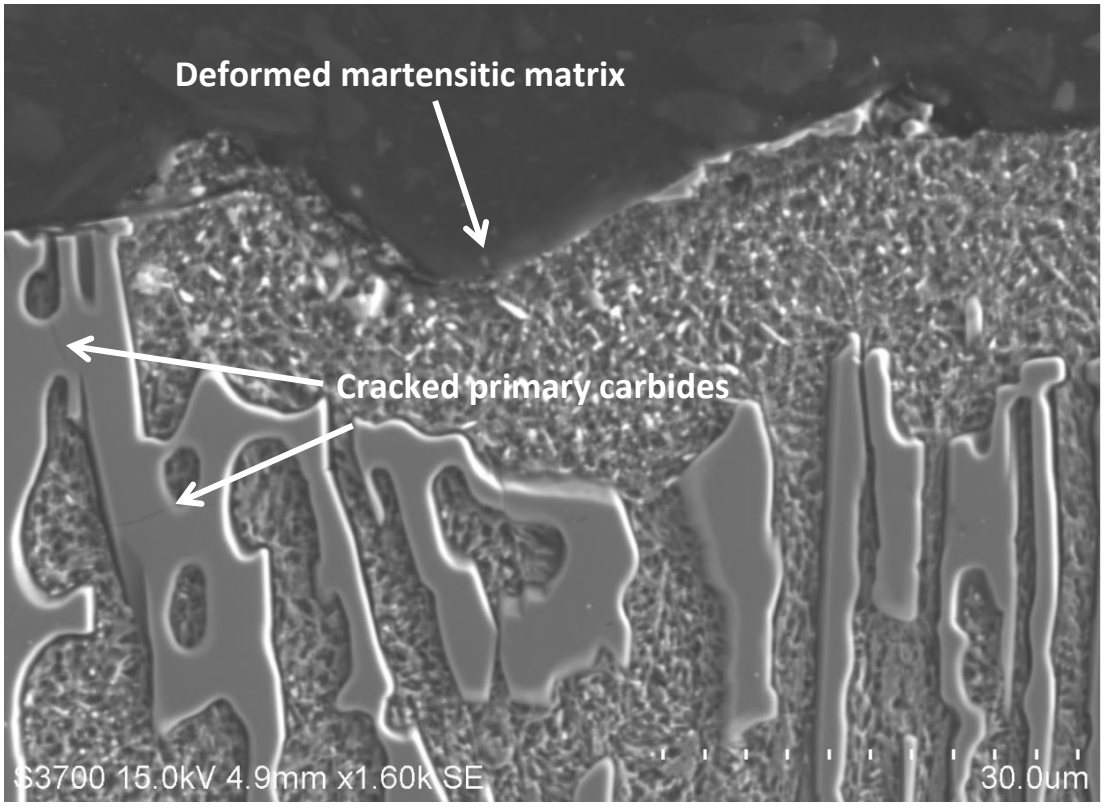

Figure 5.34: *Deformed martensitic matrix and cracked primary carbide in 27%Cr cast iron wear scar*

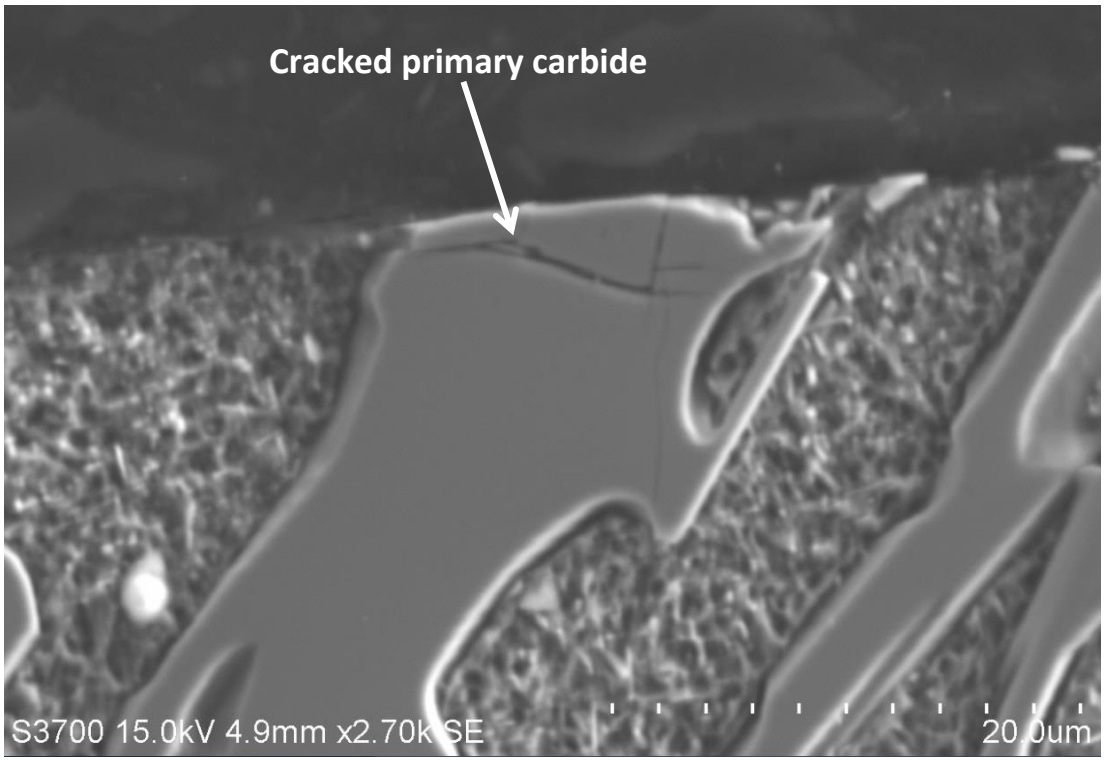

Figure 5.35: *Cracking in primary carbide in 27%Cr cast iron wear scar*

Carburised UNS G86200

The carburised UNS G86200 exhibited subsurface cracks, caused by the high impact stresses associated from the repetitive impact testing. Cracks were observed to occur parallel and perpendicular to the surface which will lead to material being spalled and/or delaminated from the surface of the carburised UNS G86200 steel (Figure 5.36). This wear mechanism was similar to that found on the carburised UNS G86200 steel field trial valve seat (Figures 5.8 and 5.11). Subsurface cracking caused by repetitive impact wear has previously been observed by various researchers [5.7, 5.19, 5.39, 5.40].

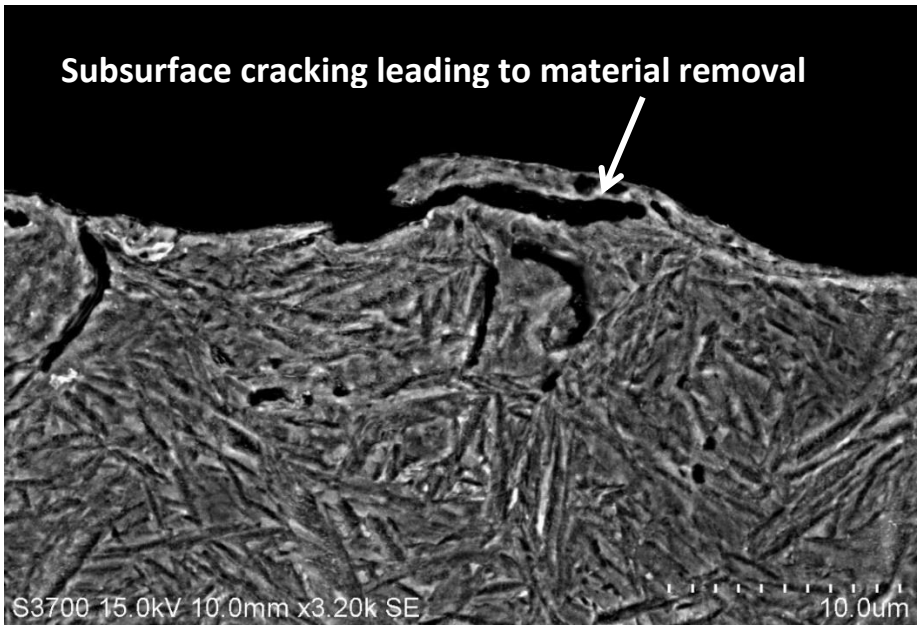

Figure 5.36: *Subsurface cracking leading to material removal in carburised UNS G86200 wear scar*

Nitrided 905M39 steel

The nitrided 905M39 steel also exhibited an extensive network of subsurface cracks which extend over 100µm in length (Figure 5.37). The vast crack network will eventually result in delamination and spalling of the nitride layer.

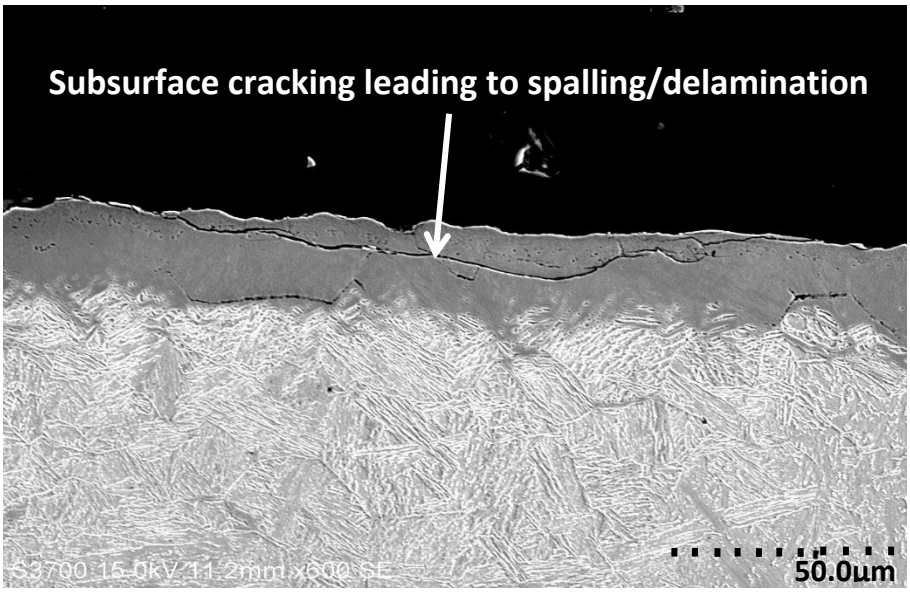

Figure 5.37: *Subsurface cracking leading to material removal in nitrided 905M39 steel wear scar*

HVOF WC-10Ni

Figure 5.38 demonstrates numerous cracking occurring at the surface of the HVOF WC-Ni coating. Cracks were observed within the wear scar and also radially outside the wear scar. Similarly to the carburised UNS G86200 and nitrided 905M39 steels, the coating material will be removed through spalling and delamination.

In summary, the damage mechanisms (plastic deformation and cracking) that have been observed in the current study correlate well with observations of investigators using repetitive impact machines described in Chapter 5.2.

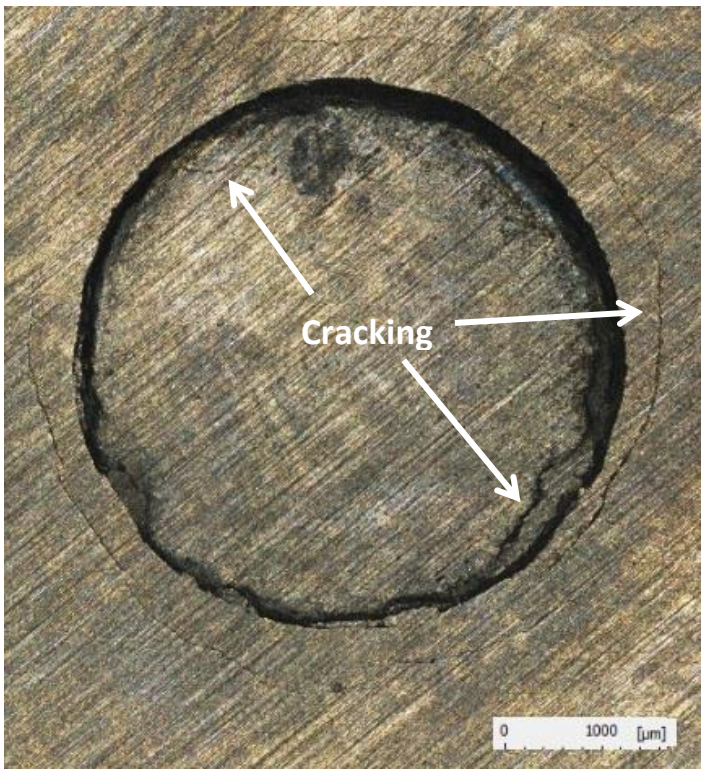

Figure 5.38: *Micro-cracking of the HVOF WC-10Ni in and around the circumference of the wear scar*

5.5.3 Circularity factor of tested sand particles

The shape of the proppant used in the hydraulic fracturing process is crucial as the proppant is required to be circular to allow for a faster flow of oil and/or gas. Therefore, it was important to assess the shape of the sand particles after a test to ensure that the proppant shape met standards and it also verified if the sand particles were being

"crushed" in the test rig. The post-test assessment was conducted through an image processing program called ImageJ. The measurement was taken by drawing a line around the circumference of the sand particle. The area (A) and perimeter (P) of the measured shape can then be used to calculate the Circularity Factor (CF), outlined in Eq. 5.2, of the sand particles.

$$Circularity\ Factor\ (CF) = \frac{4\pi A}{P^2} \qquad \text{Eq. 5.2}$$

100 sand particles were measured before and after each test to evaluate the effect of crushing the sand particles during a repetitive impact test. Figure 5.39 is an example of a typical sand particle with a CF value greater than 0.9, i.e. circular in shape. Figure 5.40 demonstrates an example of a sand particle with a CF value less than 0.8, i.e. irregular in shape.

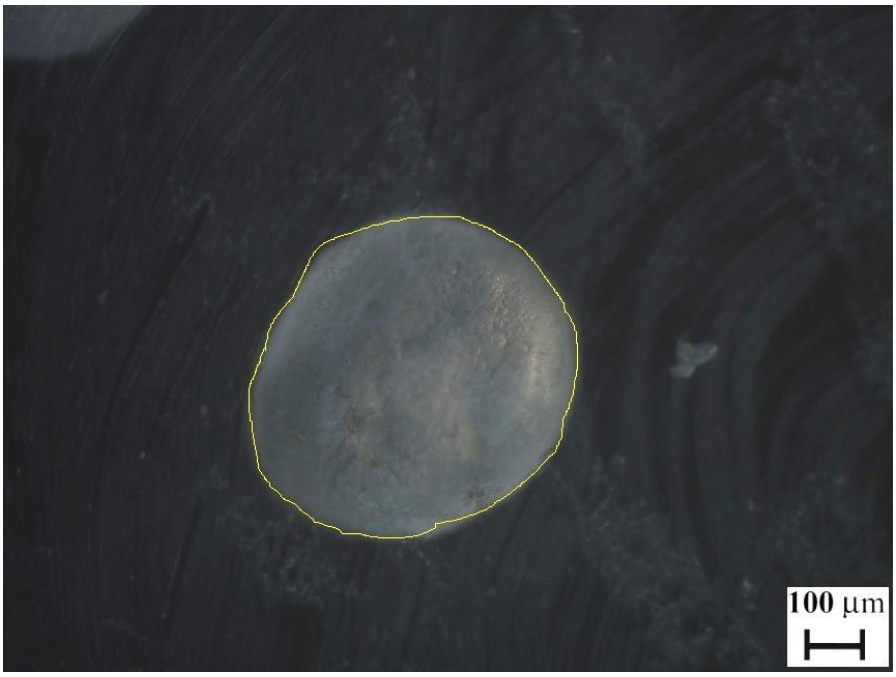

Figure 5.39: *Example of circularity factor measurement (>0.9)*

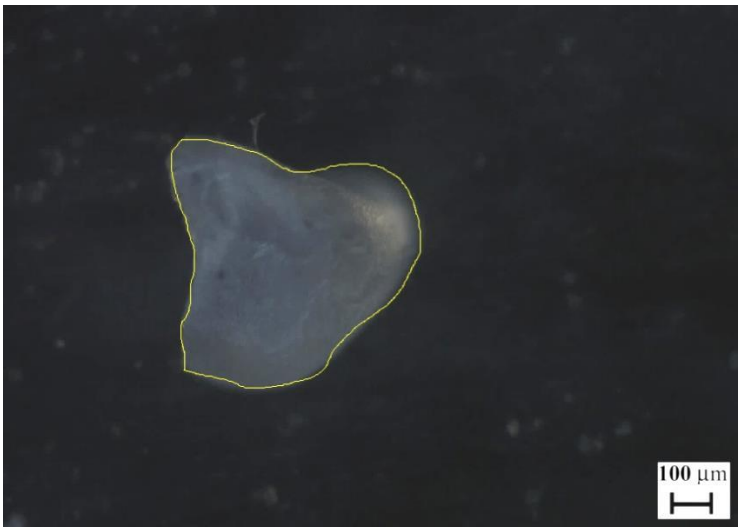

Figure 5.40: *Example of circularity factor measurement (<0.8)*

Table 5.6 shows the range of CF values (<0.8, 0.8-0.9 and >0.9) and the amount of particles found in each CF value range. A total of 100 sand particles were measured randomly after each experiment. The same process was followed for 100 untested sand particles which were used as a reference to compare with post-tested sand particles. From the results, it is clear that the repetitive impact conditions result in the sand particles becoming damaged. However, the majority of the sand particles have a CF value greater than 0.8, therefore, the particle would still met the requirements set by the ISO and API standards [5.55, 5.56]. The results also verify that sand particles were being "crushed" in the repetitive impact test rig.

Table 5.6: *Amount of sand particles for each CF range for all test materials in repetitive impact with slurry test conditions*

Material	CF value <0.8	CF value 0.8-0.9	CF value >0.9
Untested sand particles (reference)	1	35	64
Carburised UNS G86200	12	37	51
Induction hardened UNS G52986	8	47	45
Quenched and tempered UNS G52986	14	41	45
Induction hardened UNS G41400	7	49	44
UNS S31600	5	58	37
Nitrided 905M39 steel	9	55	36
UNS S42000 (480HV)	9	56	35

UNS S42000 (280HV)	4	54	42
HVOF WC-10Ni	7	48	45
UNS S44003	16	64	20
UNS S44004	15	67	18
UNS S32760	8	66	26
27%Cr cast iron	16	44	40
37%Cr cast iron	11	58	31

5.5.4 Relationship between repetitive impact resistance and material properties

To assist with material selection for valve seats, an assessment was conducted to establish relationships, if any, between repetitive impact resistance and material properties. The material properties which were used for the assessment were hardness, elastic modulus and yield strength. Figure 5.41 demonstrates the relationship between material hardness and repetitive impact wear scar depth. In general terms, as the hardness was increased the wear scar depth decreased up to a hardness of approximately 765HV. Above this hardness value the wear scar depths increased. This suggests that there is an optimum hardness where repetitive impact wear is at a minimum.

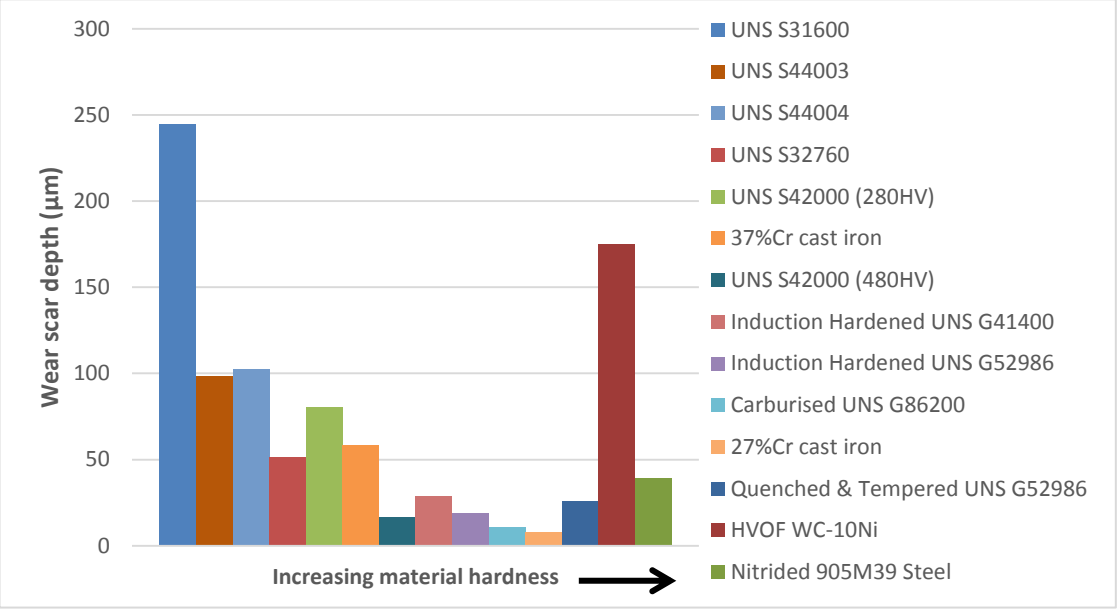

Figure 5.41: *Relationship between material hardness and repetitive impact wear scar depths*

Figure 5.42 demonstrates the relationship between yield strength and repetitive impact wear scar depth. The yield strength was selected as a criteria as this is indicative of the resistance of a material to plastic deformation. Therefore, the greater the yield strength, the greater the resistance to plastic deformation. However, no correlation was observed between yield strength and repetitive impact wear scar depth.

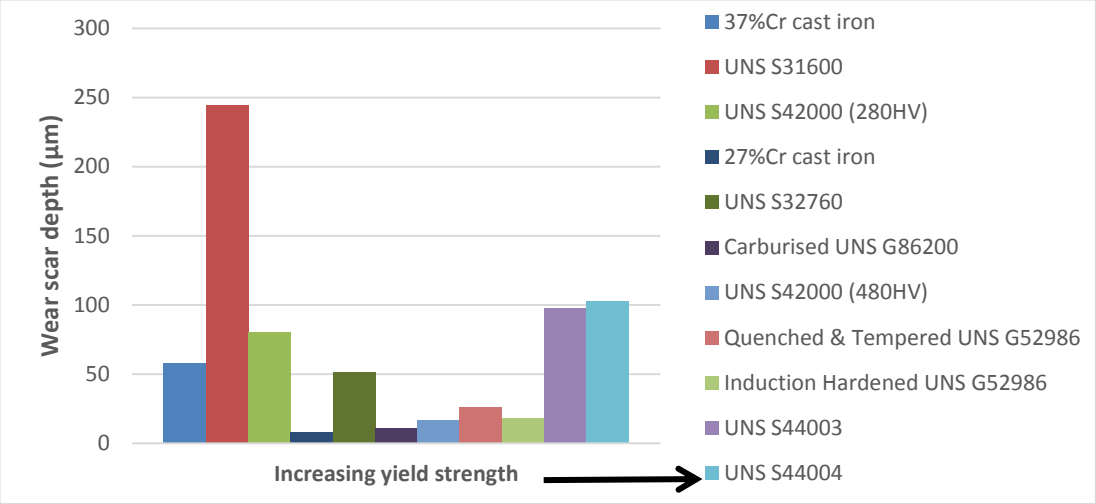

Figure 5.42: *Relationship between yield strength and repetitive impact wear scar depth*

Figure 5.43 exhibits the relationship between the hardness/elastic modulus (H/E) ratio with the repetitive impact wear scar depth. In general, there was a reduction in wear scar depth as the H/E ratio increased. However, there was no direct correlation which could be used to predict the behaviour of a material under repetitive impact conditions.

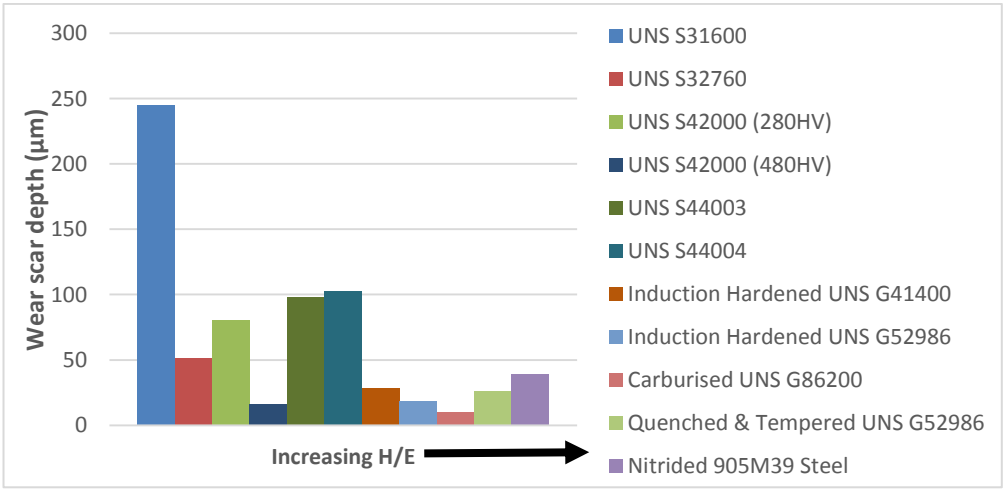

Figure 5.43: *Relationship between H/E and repetitive impact wear scar depth*

5.6 Relevance of work to design and operation for hydraulic fracturing pump valve and valve seat material

This study has shown that there appears to be an optimum hardness where the repetitive impact wear is reduced to a minimum. This suggests that the valve seat materials must be resistant to plastic deformation, however, must also be tough enough to not fail in a brittle manner. This explanation proposes why the hardened martensitic materials performed the best in the repetitive impact test rig.

SEM analysis of field trial valve seats and repetitive impact test samples exhibited similar type of wear mechanisms. The carburised UNS G86200 steel demonstrated small subsurface cracks which led to small amounts of material removal. Similar mechanisms were observed for the nitrided 905M39 steel and UNS S42000 in the metal – urethane contact region and the repetitive impact test samples. This indicates that the repetitive impact test rig could represent the wear mechanisms occurring in operating valve seats. Therefore, the repetitive impact test rig can be used to support assessment of candidate valve seat materials along with erosion-corrosion testing.

The currently used carburised UNS G86200 steel has been observed to be one of the best performing materials under repetitive impact conditions and yet does not seemingly possess good durability in operational valves and valve seats. This study has identified three main material degradation mechanisms occurring in valve and valve seats – corrosion, erosion-corrosion and repetitive impact with crushing sand particles. However, the deterioration process is complex due to the interaction between each of the wear mechanisms. Therefore, all of the wear mechanisms should be considered when designing valve and valve seats for hydraulic fracturing pumps. To develop the knowledge of how the wear mechanisms interact, controlled testing of prototype valves and valve seats should be considered in either a custom built test rig or in field trials. The results from laboratory testing and prototype valve seats should be compared to assess the combined effect of the wear mechanisms.

5.7 Conclusions

1. The wear mechanisms occurring on valve and valve seats are complex and involve the combined effect of corrosion, erosion-corrosion and repetitive impact with sand crushing.
2. A novel repetitive impact rig, incorporated with the effect of sand crushing, was successfully constructed and validated through experiments with a range of materials. A 30% increase in wear scar volume was attributed to the sand crushing effect for UNS S31600.
3. The materials which performed best under repetitive impact conditions were hardened with a martensitic microstructure, for example the 27%Cr cast iron was one of the best performing materials. These materials performed best due to their higher resistance to plastic deformation.
4. The material degradation mechanisms for soft/ductile materials, of lower repetitive impact resistance, were found to be plastic deformation through ploughing/cutting mechanisms caused by high impact stresses from “crushed” sand particles.
5. The material degradation mechanisms for hard/brittle materials, also with lower repetitive impact resistance were observed to be subsurface cracking which lead to delamination/spalling of the material.
6. Analysis of post-test sand particles observed some damage, however, the shape of the sand particles were found to meet the required industrial standards.
7. No distinct correlation was observed between material properties and repetitive impact resistance. This highlights the complexity of this type of wear process.
8. It has been demonstrated that the repetitive impact process is likely to be a determinant in valve seat life and the test method developed in this work has demonstrated a good sensitivity in comparative material performance. Nevertheless, it appears that all wear mechanisms (corrosion, erosion-corrosion and repetitive impact) significantly contribute to the degradation of the valve seat, therefore, all must be assessed to identify attractive alternative material candidates.

5.8 References

[5.1] Private Communication with Jacob Bayyouk, Senior Engineering Technical Steward, Weir Oil & Gas, Fort Worth, Texas, USA, 2015.

[5.2] E. Chrysochoos, L. Giourntas, T. Hodgkiess, A. M. Galloway, and A. Pearson, "Investigation of valve seat materials," WARC internal report, 2013.

[5.3] G. Karafyllias, L. Giourntas, T. Hodgkiess, A. M. Galloway, and A. Pearson, "Investigation of valve seat materials," WARC internal report, 2014.

[5.4] S. L. Rice, "Reciprocating impact wear testing apparatus," *Wear*, vol. 45, pp. 85–95, 1977.

[5.5] S. L. Rice, H. Nowotny, and S. F. Wayne, "Characteristics of metallic subsurface zones in sliding and impact wear," *Wear*, vol. 74, pp. 131–142, 1982.

[5.6] S. L. Rice, H. Nowotny, and S. F. Wayne, "Specimen-counterface bulk hardness effects in impact wear of 17-4 ph steel pairs," *Wear*, vol. 103, pp. 175–185, 1985.

[5.7] S. L. Rice, "Variations in wear resistance due to microstructural condition in high strength steel under repetitive impact," *Tribol. Int.*, vol. 12, no. 1, pp. 25–29, 1979.

[5.8] S. L. Rice, "The role of microstructure in the impact wear of two aluminum alloys," *Wear*, vol. 54, no. 2, pp. 291–301, 1979.

[5.9] S. L. Rice, "The role of specimen stiffness in sliding and impact wear," *Wear*, vol. 77, pp. 13–28, 1982.

[5.10] P. L. Menezes and S. V. Kailas, "Subsurface deformation and the role of surface texture — A study with Cu pins and steel plates," *Sadhana*, vol. 33, pp. 191–201, 2008.

[5.11] H. Nowotny, S. Rice, and S. Wayne, "Impact Wear of a Tool Steel.," *Wear*, vol. 81, no. 1, pp. 175–181, 1982.

[5.12] H. Nowotny, S. L. Rice, and S. F. Wayne, "Characteristics of wear debris in impact sliding," *Wear*, vol. 68, no. 2, pp. 159–167, 1981.

[5.13] S. L. Rice, S. F. Wayne, and H. Nowotny, "Material transport phenomena in the impact wear of titanium alloys," *Wear*, vol. 65, pp. 215–226, 1980.

[5.14] J. F. Su, D. Yu, X. Nie, and H. Hu, "Inclined impact-sliding wear tests of TiN/Al2O3/TiCN coatings on cemented carbide substrates," *Surf. Coatings Technol.*, vol. 206, no. 7, pp. 1998–2004, 2011.

[5.15] X. M. Li, Y. Y. Yang, T. M. Shao, Y. S. Jin, and G. Barbezat, "Impact wear performances of Cr3C2-NiCr coatings by plasma and HVOF spraying," *Wear*, vol. 202, pp. 208–214, 1997.

[5.16] R. W. Fricke and C. Allen, "Repetitive impact wear of steels," *Wear*, vol. 162–164, pp. 837–847, Apr. 1993.

[5.17] P. A. Engel and D. B. Millis, "Study of surface topography in impact wear," *Wear*, vol. 75, no. 2, pp. 423–442, 1982.

[5.18] P. A. Engel and Q. Yang, "Impact wear of multiplated electrical contacts," *Wear*, vol. 181–183, pp. 730–742, 1995.

[5.19] N. J. Mahoney, R. J. Grieve, and T. Ellis, "A simple experimental method for studying the impact wear of materials," *Wear*, vol. 98, pp. 79–87, 1984.

[5.20] P. J. Blau and T. A. Hanft, "Quantitative measurement of repetitive impact damage on ground silicon nitride surfaces," *Tribol. Int.*, vol. 27, no. 2, pp. 109–118, 1994.

[5.21] M. Lindroos, M. Apostol, V. Kuokkala, A. Laukkanen, K. Valtonen, K. Holmberg, and O. Oja, "Experimental study on the behavior of wear resistant steels under high velocity single particle impacts," *Int. J. Impact Eng.*, vol. 78, pp. 114–127, 2015.

[5.22] A. A. Cenna, K. C. Williams, and M. G. Jones, "Analysis of impact energy factors in ductile materials using single particle impact tests on gas gun," *Tribol. Int.*, vol. 44, no. 12, pp. 1920–1925, 2011.

[5.23] J. H. Neilson and A. Gilchrist, "Erosion by a stream of solid particles," *Wear*, vol. 11, no. 2, pp. 111–122, 1968.

[5.24] B. Dodd and Y. Bai, *Adiabatic shear localisation*. Elsevier Ltd, 2012.

[5.25] L. E. Murr, A. C. Ramirez, S. M. Gaytan, M. I. Lopez, E. Y. Martinez, D. H. Hernandez, and E. Martinez, "Microstructure evolution associated with adiabatic shear bands and shear band failure in ballistic plug formation in Ti-6Al-4V targets," *Mater. Sci. Eng. A*, vol. 516, no. 1–2, pp. 205–216, 2009.

[5.26] Z. Q. Duan, S. X. Li, and D. W. Huang, "Microstructures and adiabatic shear bands formed by ballistic impact in steels and tungsten alloy," *Fatigue Fract. Eng. Mater. Struct.*, vol. 26, no. 12, pp. 1119–1126, 2003.

[5.27] M. Naim and S. Bahadur, "The significance of the erosion parameter and the mechanisms of erosion in single-particle impacts," *Wear*, vol. 94, no. 2, pp. 219–232, 1984.

[5.28] K. D. Bouzakis, A. Asimakopoulos, and M. Batsiolas, "Characterization of fatigue and adhesion properties of a-C:H/CrN coatings on bearing rings by impact tests," *Surf. Coatings Technol.*, vol. 202, no. 24, pp. 5929–5935, 2008.

[5.29] J. F. Su, X. Nie, and T. Mulholland, "Combinative influence of impact and pressing forces on coating failure behaviour," *Surf. Coatings Technol.*, vol. 205, no. 5, pp. 1520–1526, 2010.

[5.30] K. D. Bouzakis, G. Skordaris, E. Bouzakis, S. Makrimallakis, S. Kombogiannis, and O. Lemmer, "Fatigue strength of diamond coatings' interface assessed by inclined impact test," *Surf. Coatings Technol.*, vol. 237, pp. 135–141, 2013.

[5.31] J. L. Mo, M. H. Zhu, A. Leyland, and A. Matthews, "Impact wear and abrasion resistance of CrN, AlCrN and AlTiN PVD coatings," *Surf. Coatings Technol.*, vol. 215, pp. 170–177, 2013.

[5.32] R. Bantle and A. Matthews, "Investigation into the impact wear behaviour of ceramic coatings," *Surf. Coatings Technol.*, vol. 74–75, no. 2, pp. 857–868, 1995.

[5.33] Y. Chen and X. Nie, "Study on fatigue and wear behaviors of a TiN coating using an inclined impact-sliding test," *Surf. Coatings Technol.*, vol. 206, no. 7, pp. 1977–1982,

2011.

[5.34] K. D. Bouzakis, A. Asimakopoulos, G. Skordaris, E. Pavlidou, and G. Erkens, "The inclined impact test: A novel method for the quantification of the adhesion properties of PVD films," *Wear*, vol. 262, no. 11–12, pp. 1471–1478, 2007.

[5.35] A. A. Voevodin, R. Bantle, and A. Matthews, "Dynamic impact wear of TiCxNy and Ti-DLC composite coatings," *Wear*, vol. 185, no. 1–2, pp. 151–157, 1995.

[5.36] K. A. Kuptsov, P. V. Kiryukhantsev-Korneev, A. N. Sheveyko, and D. V. Shtansky, "Comparative study of electrochemical and impact wear behavior of TiCN, TiSiCN, TiCrSiCN, and TiAlSiCN coatings," *Surf. Coatings Technol.*, vol. 216, pp. 273–281, 2013.

[5.37] G. M. La Vecchia and N. Lecis, "Impact test and tribological behaviour of duplex-treated low-alloy steel," *Surf. Coatings Technol.*, vol. 205, no. 2, pp. 614–619, 2010.

[5.38] S. Y. Yoon, S. Y. Yoon, W. S. Chung, and K. H. Kim, "Impact-wear behaviors of TiN and Ti-Al-N coatings on AISI D2 steel and WC-Co substrates," *Surf. Coatings Technol.*, vol. 177–178, pp. 645–650, 2004.

[5.39] G. Cassar, S. Banfield, J. C. Avelar-Batista Wilson, J. Housden, A. Matthews, and A. Leyland, "Impact wear resistance of plasma diffusion treated and duplex treated/PVD-coated Ti-6Al-4V alloy," *Surf. Coatings Technol.*, vol. 206, no. 10, pp. 2645–2654, 2012.

[5.40] J. F. Huang, H. S. Fang, and Y. K. Zheng, "Influence of Re-Ti modification on the high impact wear resistance of high Si bainitic cast steel," *Int. J. Miner. Metall. Mater.*, vol. 17, no. 6, pp. 756–762, 2010.

[5.41] V. Rastegar and A. Karimi, "Surface and Subsurface Deformation of Wear-Resistant Steels Exposed to Impact Wear," *J. Mater. Eng. Perform.*, vol. 23, no. 3, pp. 927–936, 2013.

[5.42] Y.-Y. Yang, H.-S. Fang, Y.-K. Zheng, Z.-G. Yang, and Z.-L. Jiang, "The failure models induced by white layers during impact wear," *Wear*, vol. 185, no. 1–2, pp. 17–22,

1995.

[5.43] E. B. Iturbe, I. G. Greenfield, and T. W. Chou, "The wear mechanism obtained in copper by repetitive impacts," *Wear*, vol. 74, no. 1, pp. 123–129, 1981.

[5.44] V. Ratia, K. Valtonen, A. Kemppainen, and V.-T. Kuokkala, "High-Stress Abrasion and Impact-Abrasion Testing of Wear Resistant Steels," *Tribol. Online*, vol. 8, no. 2, pp. 152–161, 2013.

[5.45] V. Heino, M. Kaipiainen, P. Siitonen, V. Ratia, K. Valtonen, T. Lepisto, and V.-T. Kuokkala, "Compressive Crushing of Granite with Wear- Resistant Materials," *Finnish J. Tribol.*, vol. 30, no. 1–2, pp. 21–28, 2011.

[5.46] M. Lindroos, M. Apostol, V. Heino, K. Valtonen, A. Laukkanen, K. Holmberg, and V.-T. Kuokkala, "The Deformation, Strain Hardening, and Wear Behavior of Chromium-Alloyed Hadfield Steel in Abrasive and Impact Conditions," *Tribol. Lett.*, vol. 57, no. 3, pp. 1–11, 2015.

[5.47] D. M. Kennedy and M. S. J. Hashmi, "Test rig design and experimental results of coated systems under impact abrasion conditions," *Surf. Coatings Technol.*, vol. 86–87, no. 2, pp. 493–497, 1996.

[5.48] K. Osara and T. Tiainen, "Three-body impact wear study on conventional and new PM/ + HIPed wear resistant materials," *Wear*, vol. 250–251, no. 1, pp. 785–794, 2001.

[5.49] N. W. Page, M. Yao, S. Keys, W. Mcmillan, and A. Cenna, "A high-pressure shear cell for friction and abrasion measurements," *Wear*, vol. 241, pp. 186–192, 2000.

[5.50] M. Qian and W. Chaochang, "Impact-abrasion behavior of low alloy white cast irons," *Wear*, vol. 209, pp. 308–315, 1997.

[5.51] I. M. Hutchings, "Mechanisms of the Erosion of Metals by Solid Particles," *Eros. Prev. Useful Appl. ASTM STP 664*, W. F. Adler, Ed., American Society for Testing Materials, pp. 59-76, 1979.

[5.52] R. J. K. Wood, J. C. Walker, T. J. Harvey, S. Wang, and S. S. Rajahram, "Influence of microstructure on the erosion and erosion-corrosion characteristics of 316 stainless steel," *Wear*, vol. 306, no. 1–2, pp. 254–262, 2013.

[5.53] T. Singh, S. N. Tiwari, and G. Sundararajan, "Room temperature erosion behaviour of 304, 316 and 410 stainless steels," *Wear*, vol. 145, no. 1, pp. 77–100, 1991.

[5.54] L. Giourntas, "Investigation of erosion-corrosion behaviour of pump materials," Ph.D Thesis, University of Strathclyde, 2016.

[5.55] ISO 13503: Petroleum and natural gas industries — Completion fluids and materials Part II: Measurement of properties of proppants used in hydraulic fracturing and gravel-packing operations, 2006.

[5.56] American Petroleum Institute, "API RP 19C.", 2014.

Chapter 6

Alternative materials and manufacturing options for hydraulic fracturing pump components – Stellite 6 weld claddings

6.1 Introduction

An option for prolonging the life of hydraulic fracturing pump components is to use more corrosive wear resistant materials and coatings. However, these alternative materials must also be cost effective. Hardfacing is the deposition of a hard, “wear resistant” material onto a worn or new component which is subsequently subjected to an aggressive environment during service. As the hardfacing is a surface engineering treatment, the bulk of the component can be made from a cheaper material. The hardfacing process can also be used to repair damaged components which have been in service. A variety of welding processes can be used for hardfacing materials these include; metal-inert gas (MIG), tungsten-inert gas (TIG), plasma transferred arc (PTA), submerged arc (SAW) and manual metal arc (MMA).

Stellite alloys are commonly used as hardfacing materials due to their generally good corrosion and “mechanical wear” resistance as well as their good weldability. The Stellite alloys are cobalt based with additions of Cr, C, W and Mo. Stellite 6 (UNS R30006) is one of the most commonly used Stellite alloys and so this was selected as the hardfacing material in this study. A single and double layer Stellite 6 weld cladding were studied to assess if weld dilution (change in chemical composition of the weld as a result of diffusion between the weld metal and base metal) has any effect on the corrosive- and repetitive-impact-wear resistance of the weld claddings. Little research has been conducted assessing this strategy on the durability of Stellite 6 weld claddings. A further modification, that was investigated, was the effect of nitriding on the corrosive and repetitive impact wear resistance of Stellite 6 alloys.

6.2 Literature review

6.2.1 Assessment of Stellite alloys under corrosion and wear conditions

Stellite alloys are a range of Co-Cr alloys which are specifically designed for mechanical wear resistance and generally have good corrosion resistance due to their high chromium content. The chemical composition of Stellite alloys results in them exhibiting high melting points (1285-1410°C) which also allows them to be used in high temperature applications. Due to the wide range in Stellite alloys and also with the possibility of altering the composition to tailor for specific types of wear, several studies, which will be discussed in

this section, have assessed the wear and corrosion resistance of Stellite alloys. The nominal chemical compositions for the discussed Stellite alloys are given in Table 6.1 [6.1–6.6].

Table 6.1: *Nominal chemical compositions for the Stellite alloys discussed in the literature review*

Material	Co	Cr	W	C	Ni	Mo	Fe	Si
Stellite 6	Bal.	30.0	4.0-5.0	1.20	<3.0	<1.0	<3.0	<2.0
Stellite 20	Bal.	33.0	16.0	2.45	<3.0	<1.0	<3.0	<2.0
Stellite 21	Bal.	28.0	-	0.25	3.0	5.2	<3.0	<1.5
Stellite X40	Bal.	25.0	7.0-8.0	0.50	3.0	5.2	<2.0	1.0
Stellite 706	Bal.	31.0	-	1.20	<3.0	4.0	<3.0	<1.0
Stellite 712	Bal.	31.0	-	1.55	<3.0	8.0	<3.0	<2.0

Stellite 6 (UNS R30006) has been widely assessed under corrosion and erosion-corrosion resistance. Neville and Hodgkiess assessed the erosion-corrosion behaviour of Superduplex stainless steel (UNS S32760), Inconel 625 (UNS N00625) and Stellite 6 (UNS AMS5387 – specific UNS number for investment casting of Stellite 6) under liquid impingement (3.5%NaCl, 100m/s, 18°C and 50°C) and under solid-liquid impingement (1000ppm sand, 25m/s, 50°C) conditions [6.1]. Under liquid impingement conditions, the passive films of the tested materials were observed to remain intact. The Stellite 6 exhibited the smallest total weight loss and smallest corrosion current density under solid-liquid conditions. The study also highlighted the importance of corrosion-related damage as a significant proportion of the overall wear was attributed to synergy (12-24%).

A further study by Andrews et al. assessed the effect of impingement angle on the erosion-corrosion resistance of two different cast Stellite 6 alloys and UNS S31600 with a slurry jet impingement rig (3.5%NaCl, 1.2g/l sand concentration, 19m/s and a range of impingement angles) [6.7]. Both Stellite 6 alloys performed similarly under conditions at all impingement angles, whereas the UNS S31600 performed substantially worse than the Stellite 6 alloys. As the maximum material loss for the Stellite 6 alloys occurred at 60°, then it was

concluded that they could not be described as either ductile or brittle. At low angle (20° and 45°) the main wear mechanism observed was sliding abrasion, whereas, at high angle (60° and 90°) the wear mechanism changed to crater and pit formation on the tested surface.

The effect of alloying molybdenum and tungsten on Stellite alloys has also been studied. Malayoglu and Neville evaluated the erosion-corrosion resistance of Stellite 706 (5% Mo) and Stellite 6 (4.8% W) in both cast and Hot Isostatically Pressed (HIPed) forms as well as UNS S31603 and UNS S32750 under slurry impinging jet apparatus (17m/s, 90° impingement angle and 200 and 500mg/l sand loading) [6.2]. The HIPed specimens performed slightly better than those produced by casting and the Stellite 706 performed slightly better than the Stellite 6 alloy. The cast alloys exhibited a coarser carbide size which resulted in large amounts of matrix removal which accelerated the erosion-corrosion wear rate. The main role of Mo and W in Co-based alloys is for solid solution strengthening, however, the higher Mo content in the Stellite 706 alloys led to formation of Mo-rich carbides which aided in its erosion resistance, hence, improving its overall erosion-corrosion resistance.

Liu et al. also evaluated the effect of molybdenum content on the erosion and corrosion resistance of cast Stellite alloys (two new low-C Stellite alloys along with Stellite 21 and Stellite 6) [6.3]. The dry erosion tests (ASTM G76) showed that the increased Mo content did not improve the resistance of the low-C Stellite alloys compared to the Stellite 21 and Stellite 6 (contradicts the findings observed by Malayoglu and Neville [6.2]). It was concluded that the carbides played a more crucial role in the erosion resistance then the intermetallic compounds formed with the additional Mo. The Stellite 21 and modified version (with greater Mo) were observed to have the best corrosion resistance. The poorer corrosion resistance of the Stellite 6 was attributed to the higher C content which is more likely to form large amounts of Cr-rich carbides, which reduces the Cr in the matrix, thus, resulting in a weaker passive film.

The effect of manufacturing process on the corrosion and wear resistance of Stellite alloys has also been studied. Yu et al. compared HIPed and cast forms of Stellite 6 and Stellite 20 under abrasive wear (ASTM G65), sliding wear (ASTM G133-02) and rolling contact fatigue

tests [6.4]. The HIPed alloys performed better under abrasive wear (higher hardness) and rolling contact fatigue (improved impact toughness due to finer microstructure which arrested crack propagation) conditions, but, performed poorer under sliding wear conditions. For the cast alloys, brittle fracture of the carbides and ploughing of the matrix were the main wear mechanisms. For the HIPed alloys, ploughing and carbide pullout were the dominant mechanisms.

The HIPed process has further been evaluated by Malayoglu and Neville who assessed the erosion-corrosion resistance of HIPed and cast Stellite 6 compared with UNS S31603 and UNS S32760 under slurry impingement conditions (17m/s, 200 and 500mg/l sand loading) [6.8]. Both forms of Stellite 6 performed significantly better than the stainless steel alloys under erosion-corrosion conditions. The HIPed alloy performed slightly better than the cast alloy. The cast alloy exhibited a network of interconnected brittle carbides and as the matrix material was preferentially being removed, this exposed the carbide network to subsequent impacting particles. This resulted in a rougher wear scar of the cast alloy compared to the HIPed alloy which wore more homogeneously.

The erosion-corrosion resistance of Stellite X40 was assessed by Neville et al. under liquid (17m/s, 90°, 3.5%NaCl) and solid-liquid conditions (17m/s, 90°, 3.5%NaCl, 0-600mg/l sand concentration) [6.5]. The weight loss was observed to increase with increased sand loading, increased salinity and increased temperature. The wear mechanism was observed to change in the different wear regions of the tested samples. In the central region of the wear scar, the matrix was removed leaving carbides protruding from the surface. In regions outside of the wear scar, low angle ploughing occurred which resulted in carbides being covered with plastically deformed matrix.

Reyes and Neville also assessed the erosion-corrosion resistance of Stellite X40 in comparison with a WC-Ni coating (K2550) and a WC-Cu coating in a slurry impingement jet apparatus under solid-liquid conditions (500mg/l sand concentration, 3.5%NaCl, 18°C, 17m/s and a range of impingement angles) [6.9]. The Stellite X40 exhibited better overall erosion-corrosion resistance than the WC coatings, as the coatings were found to be porous and most of the WC particles were subsurface, hence, mainly matrix was worn at the surface. At low angles (15° and 30°), the matrix of the Stellite X40 was observed to be

eroded away leaving carbides in relief. At high angles (75° and 90°), the wear scar of Stellite X40 was observed to deepen as both matrix and carbides were removed through erosion and corrosion processes.

The corrosion and erosion-corrosion resistance of Stellite X40 was further assessed and compared to an austenitic cast iron (BS 3468) under solid-liquid conditions (3.5%NaCl, 500ppm sand loading, 17m/s, 18°C) [6.10]. The Stellite X40 exhibited significantly better corrosion and erosion-corrosion resistance compared to the cast iron. Another important feature from this study was the proportion of corrosion related damage (corrosion and synergy) to the overall damage of the materials (45.8% - Stellite X40 and 41.6% - austenitic cast iron).

Stellite alloys are significantly more expensive than engineering steels due to their high alloying content. Therefore, in many practical engineering applications Stellite alloys are often used as a hardfacing material. Experimental studies have been conducted assessing the corrosion and wear resistance of Stellite weld cladding alloys. One such study by Nelson et al. investigated a range of high chromium cast irons and a Stellite 6 PTA weld overlay under slurry pot test conditions [6.11]. The high chromium cast irons performed significantly better than the Stellite 6 weld overlay. Impact craters were observed in the Stellite 6 weld overlay caused by the quartz particles which plastically deformed the matrix material.

Another study by Hattori and Mikami assessed the cavitation erosion resistance of Stellite weld overlays (Stellite 6 and Stellite 21) with a cavitation vibratory erosion and a cavitating liquid jet erosion testing equipment [6.12]. The Stellite 6 weld overlay exhibited the greatest cavitation erosion resistance in both testing environments when compared to the Stellite 21 alloy. The wear mechanism for the Stellite 6 weld overlay was observed as the softer cobalt matrix plastically deforming near the interface with carbides. The deformed matrix has a high stress concentration which initiates cracks and the matrix is removed. Subsequently, the unsupported carbide is removed.

Lee et al. also studied the cavitation erosion resistance of a Stellite 6 weld overlay (gas tungsten arc welding - GTAW) and a Fe-based alloy (grade undefined) with a vibratory

cavitation erosion testing apparatus [6.13]. Both materials exhibited similar weight loss during the early stages of the test. However, as the duration increased the Stellite 6 exhibited better cavitation erosion resistance. A similar wear mechanism (compared with Hattori and Mikami) was observed for the Stellite 6, cracks initiated at the interface between the hard carbide and soft matrix which leads to plastically deformed matrix being removed and subsequently carbide removal.

Benea et al. assessed the tribocorrosion resistance of plasma sprayed Stellite 6 in a pin on disk tribometer in a 0.5M sulphuric acid solution [6.14]. Potentiodynamic polarisations demonstrated depassivation and dissolution of the Stellite 6 alloy induced by friction in the wear track. A galvanic couple between the wear track (anode) and the untested surface (cathode) was observed and had an influence of the evolution of wear as the passive film on the areas not subject to friction were destabalised by cathodic polarisation induced by the coupling and corrosion appeared and spread over areas which were distant from the wear track.

Furthermore, So et al. assessed the tribocorrosion behaviour of laser clad Stellite 6 in a pin on disk testing apparatus with UNS G41400 and UNS G43400 alloys as materials for the pins [6.15]. The mean temperature at the contact surface was measured during testing, at low loads (78.4N) the mean contact surface temperature was 400°C and at high loads (156.8N) the mean contact surface temperature was 700°C. Oxidation wear was observed to be the main wear mechanism under the test conditions of the study. The oxides formed on the Stellite 6 alloy were described as tough and well bonded to the surface which resulted in a mild wear.

Another study by Singh et al. assessed the solid particle erosion and cavitation resistance of a laser cladded Stellite 6 alloy on stainless steel (UNS S13400) [6.16]. The Stellite 6 laser cladding was observed to perform significantly better than the untreated UNS S13400 alloy in both solid particle and cavitation erosion conditions. The lowest laser power weld ($32J/mm^2$) performed better than the higher laser weld powers in both solid particle and cavitation erosion conditions. The improved erosion resistance was attributed to its greater hardness.

Similarly with wrought alloys, the effect of molybdenum and tungsten on the corrosion and wear resistance of Stellite weld claddings has been evaluated. A study by Shin et al. evaluated the effect of Mo on the abrasion resistance on PTA welded Stellite 6, 3% Mo and 6% Mo Co-based alloys [6.17]. The addition of Mo was observed to increase the hardness of the Co-based alloy due to the additional formation of carbides. An increase in carbide volume fraction, refinement in microstructure and increase in hardness resulted in improved abrasion resistance.

A further study on the effect of alloying Stellite weld claddings was conducted by Yao et al. who evaluated the corrosion and wear (erosion, abrasion and adhesion) resistance of a variety of Stellite alloys (including Stellite 6) manufactured through the PTA welding method [6.6]. The corrosion tests (ASTM G-31) showed that the alloys containing W exhibited better corrosion resistance in oxidising acid (10% HNO_3) at boiling temperature, whereas, the Mo containing alloys exhibited better corrosion resistance in reducing acids (5%HCl at 40°C and 10%H_2SO_4). Under dry erosion conditions (ASTM G76), it was observed that at low impingement angles (20°) the tungsten-containing Stellite 12 performed better than the Mo-containing Stellite 712, however, this finding was reversed at high impingement angles (90°) where the Stellite 712 performed better than the Stellite 12. In the tested Stellite alloys, the improved corrosion resistance was found to be due to the Mo in solid solution and the wear resistance was improved by the formation of Mo carbides.

Romo et al. assessed the cavitation and slurry erosion resistance of SMAW Stellite 6 claddings and 13-4 stainless steel alloy [6.18]. The Stellite 6 cladding exhibited greater cavitation and slurry erosion resistance than the 13-4 stainless steel alloy. It should be noted that the slurry erosion tests lasted for only 5 minutes. At low impingement angles, the main wear mechanism was micro-cutting and micro-ploughing. At high impingement angles, the main wear mechanism was detachment of highly deformed plates due to repeated impingement of sand particles.

Jones and Llewellyn assessed the erosion-corrosion behaviour of a wide range of materials including Stellite 712 (PTA overlay), Stellite 6B (wrought plate) and Stellite 21 (wrought plate) with a slurry erosion jet (16m/s velocity and 45° impingement angle) and also a slurry pot erosion-corrosion testing apparatus [6.19]. The Stellite 6B alloy exhibited the best

overall erosion-corrosion resistance of the tested materials in the slurry jet conditions, whereas, Stellite 21 exhibited the poorest erosion resistance. The Stellite 6B (386HB) and Stellite 712 (462HB) overlay exhibited similar erosion-corrosion rates in the slurry pot testing conditions despite their differences in hardness.

Previous research work on corrosive wear of Stellite alloys has demonstrated that the behaviour of this group of Co-Cr-base materials is, to an extent, dependent upon the composition and manufacturing process with the role of alloying elements, such as W and Mo, involving carbide formation rather than solid solution effects. It is clear that Stellite alloys possess superior corrosive wear durability than a range of steels, (including stainless steels) and are promising as cladding materials for many ferrous components.

6.2.2 Effect of nitriding on the corrosion and wear resistance of materials

Nitriding is a thermochemical case hardening process which diffuses nitrogen into the surface of a metallic alloy. The main purpose of this process is to increase the wear resistance, surface hardness and fatigue life of the engineering component. Unlike other surface treatment process such as carburising, the nitriding process is conducted at lower temperatures (between 500°C and 550°C) which is below the austenising temperature for most ferritic steels, therefore, quenching is not required [6.20]. Gas nitriding is conducted in the presence of ammonia gas and produces a brittle nitrogen-rich compound zone which is commonly referred to as the white layer. Plasma nitriding is conducted in the presence of nitrogen and hydrogen gas at low pressures and a voltage is applied between the component and furnace walls. A glow discharge with high ionisation energy (plasma) is generated around the component. On the surface which is charged with ions, nitrogen-rich nitrides are formed and decompose which releases nitrogen into the surface of the component. Low alloys steels and stainless steels are the most common alloys which have been studied in the literature and these will be discussed initially in this section.

The sliding abrasive wear resistance of induction hardened, plasma and pulse plasma nitrided low alloy steel (UNS G41400) was studied by Podgornik et al. [6.21]. The plasma and pulse plasma nitrided steel exhibited greater sliding abrasion resistance than the induction hardened steel. At high loads the main wear mechanism was observed to be

subsurface fatigue, whereas, at low loads triboxidation along with surface fatigue was detected.

A further study by Podgornik et al. performed sliding (ball-on-flat) wear testing of a powder-metallurgy high-speed steel with various combinations of austenising temperature (1130 and 1230°C) and time (2 and 6 minutes), deep-cryogenic treatment temperature (-196°C) and immersion time (25 and 40 hours) and plasma nitriding treatment (520°C for 2 hours) [6.22]. The finer microstructure as a result of the separate deep-cryogenic treatment and plasma nitriding processes was observed to improve the sliding abrasion resistance of the steel alloy. However, when both treatments were combined they were observed to be detrimental to the wear resistance of the steel. The authors concluded that the reasons for this were unclear.

Karafyllias et al. evaluated the corrosive wear behaviour of various gas nitriding treatments (72, 90 and 120 hours duration) of a low alloy steel (905M39) under impinging slurry jet conditions [6.23]. In static and liquid impingement conditions, the nitriding treatment exhibited excellent corrosion resistance compared to an untreated alloy. However, in solid-liquid conditions, the shorter duration nitriding treatment resulted in a slightly better erosion-corrosion resistance compared to the other nitriding durations.

The erosion resistance of nitrided stainless steels have also been investigated. Mann and Arya evaluated the abrasive and erosive wear of plasma nitrided and HVOF sprayed stainless steels [6.24]. Under abrasion (ASTM G-65) and erosion conditions, the HVOF sprayed coating performed better than the plasma nitrided stainless steel. The better abrasion/erosion resistance of the HVOF sprayed coating was attributed to the greater hardness of the WC particles which did not wear as quickly as the nitride phase. The main damage mechanism for the HVOF coating was attributed to micro-cracking which is initiated from pores which result in de-bonding and removal of WC particles. The plasma nitrided stainless steel appeared to fail in a ductile manner with smooth removal of the nitride layer without the initiation of cracks.

The same authors also studied the erosion-corrosion behaviour of plasma nitrided UNS S17400, plasma nitrided 12Cr steel and various other materials under impinging slurry jet

conditions [6.25]. The plasma nitriding process provided a significant increase in erosion-corrosion resistance of the 12Cr steel. However, this benefit was not observed when comparing the untreated and plasma nitrided UNS S17400. Similarly, the nitrided stainless steels were observed to fail in a ductile manner as no cracking or chipping was detected.

The effect of surface treating Co-Cr alloys have also been studied. Chen et al. assessed the sliding wear resistance of untreated and various plasma surface alloyed (PSA – carbon and nitrogen mixture) Stellite 21 [6.26]. In dry sliding conditions, the wear resistance was found to increase with increasing treatment temperature, up to 500°C, after which the wear resistance decreased. For the treated samples, oxidation wear was observed to be the main wear mechanism. In wet conditions (3.5%NaCl), the optimum treatment temperature was observed to be 460°C and the wear rate increased dramatically as a result of the additional corrosion-related damage. Abrasive wear and pits due to corrosion was observed after testing in wet conditions.

Lutz and Mandl assessed the sliding wear resistance of untreated and various nitrogen plasma immersion ion implantation (PIII) treated UNS R30075 alloys under dry and wet (simulated body fluid) conditions [6.27]. In dry conditions, there was a significant increase in wear resistance with treated UNS R30075. However, under wet conditions, above a PIII process temperature of 400°C, the wear rate increased and even exceeded that of untreated UNS R30075. It was postulated that at low temperatures, the expanded austenitic structure with nitrogen in solid solution, generally maintained the passivating nature of the original CoCrMo alloy. Due to the strong affinity of nitrogen with chromium and the likelihood of chromium nitride formation at elevated temperatures, it was postulated that this resulted in depletion of chromium in solid solution, thus, compromising the corrosion resistance of the CoCrMo alloys.

A further study by Lutz et al. assessed the corrosion behaviour of untreated and PIII treated UNS R30605 (medical CoCr alloy L605) in Ringer's solution (saline solution) [6.28]. It was observed that the corrosion rates increased drastically when comparing the PIII processes with untreated UNS R30605. The increased corrosion rates were also attributed to the high affinity of nitrogen with chromium which reduces the chromium in the metallic matrix and hence, reduces the passivity of the UNS R30605 alloy.

It would thus appear that the results of nitriding Co-Cr-base alloys is a trade-off between he benefits associated with the protection of a hard nitrided surface layer and potential reductions in corrosion resistance in highly-corrosive aqueous environments. The final outcome might then be determined by the interplay between mechanical and corrosion deterioration processes.

6.3 Experimental objectives

The objective of this study was to assess the corrosion, erosion-corrosion and repetitive impact resistance of a single and double layer Stellite 6 (UNS R30006) hot wire tungsten inert gas (HWTIG) weld cladding on a low carbon steel (UNS G43400), in addition to determining the effect of nitriding Stellite 6 weld cladding under corrosion, erosion-corrosion and repetitive impact conditions. These two aspects of the study have never been considered previously in the literature.

6.4 Materials and methods

A Hot Wire Tungsten Inert Gas (HWTIG) welding process was used to produce a single and double layer Stellite 6 (UNS R30006) weld cladding on a low alloy steel (UNS G43400) substrate (Figure 6.1). The welding was undertaken by a qualified industrial welder and fully certified welding equipment. Test coupons of both single and double weld cladding layers were also ammonia gas nitrided (hereafter referred to as Nit.) at 520°C for 72 hours. A nitrided and untreated 905M39 steel were used as comparator materials during potentiodynamic polarisation experiments.

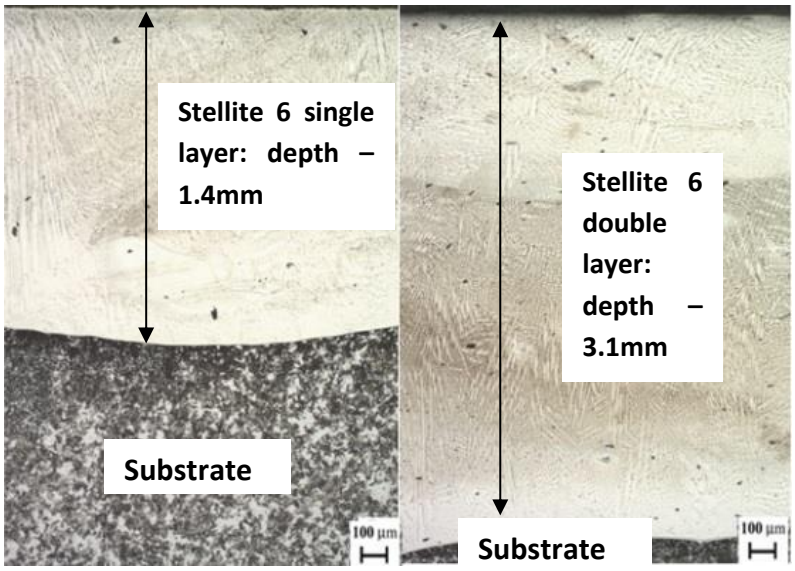

Figure 6.1: *Single (left) and double (right) layer Stellite 6 weld claddings*

Table 6.2 demonstrates the nominal density and measured macro-hardness of the test materials. The macro-hardness of the nitrided Stellite 6 was greater compared to the as-welded Stellite 6 as would be expected. Table 6.3 illustrates the chemical composition of the feedstock material (obtained from supplier) as well as the single and double layer Stellite 6 weld claddings. The chemical composition of the weld claddings were conducted using standard chemical analysis techniques (Infrared combustion (for C, S), volumetric analysis (for Cr) and inductively coupled plasma optical emission spectroscopy (for remainder)) by a commercial vendor. The chemical analysis indicates that the chromium, nickel, molybdenum and tungsten contents of the clad layers are all reduced compared to the feedstock material. There has also been an increase in manganese and iron in the Stellite 6 weld claddings. This indicates that the weld dilution has caused iron and manganese from the low alloy substrate to be absorbed into the Stellite 6 weld claddings. Whereas, chromium, nickel, molybdenum and tungsten have been diluted from the weld claddings and diffused into the low alloy steel substrate. As chromium, nickel and molybdenum are well known to increase the corrosion resistance of a material then the weld dilution might be expected to reduce the corrosion resistance of the Stellite 6 weld claddings.

Table 6.2: *Nominal densities and measured macro-hardness values of the test materials*

Material	Density (g/cm^3)	Hardness (HV)
Stellite 6 Single	8.7	400
Stellite 6 Double	8.7	440
Nit. Stellite 6 Single	8.7	680
Nit. Stellite 6 Double	8.7	685

Table 6.3: *Chemical composition of the feedstock material (nominal) and the measured chemical composition of the single and double layer Stellite 6 weld cladding*

Material	Si	Cr	Mn	Fe	Ni	Mo	W	C	Co
Feedstock	2.00	30.0	0.50	3.00	3.00	1.00	5.00	1.20	Bal.
Stellite 6 single	0.99	23.2	0.92	20.7	0.04	0.02	3.89	0.89	Bal.
Stellite 6 double	1.13	24.2	0.93	18.2	0.04	0.02	3.76	0.90	Bal.

Figure 6.2 demonstrates the microstructure of the Stellite 6 single layer weld cladding and Figure 6.3 displays the microstructure of the nitrided Stellite 6 single layer weld cladding. The Stellite 6 weld cladding has a typical dendritic type structure with a hypoeutectic microstructure. The microstructure contains primary Co-rich dendrites (light grey areas) which are surrounded by Cr-rich carbides (dark grey areas) in a solid solution cobalt-rich matrix. A small percentage of tungsten (white regions) and micro-pores (black regions) are also present. The depths of the single and double layer weld as well as the depth of the nitride compound layer were measured using Image J software. The depths for the single and double layer cross sections were found to be 1.4mm and 3.1mm respectively. The depth of the nitride compound layer was found to be 27µm.

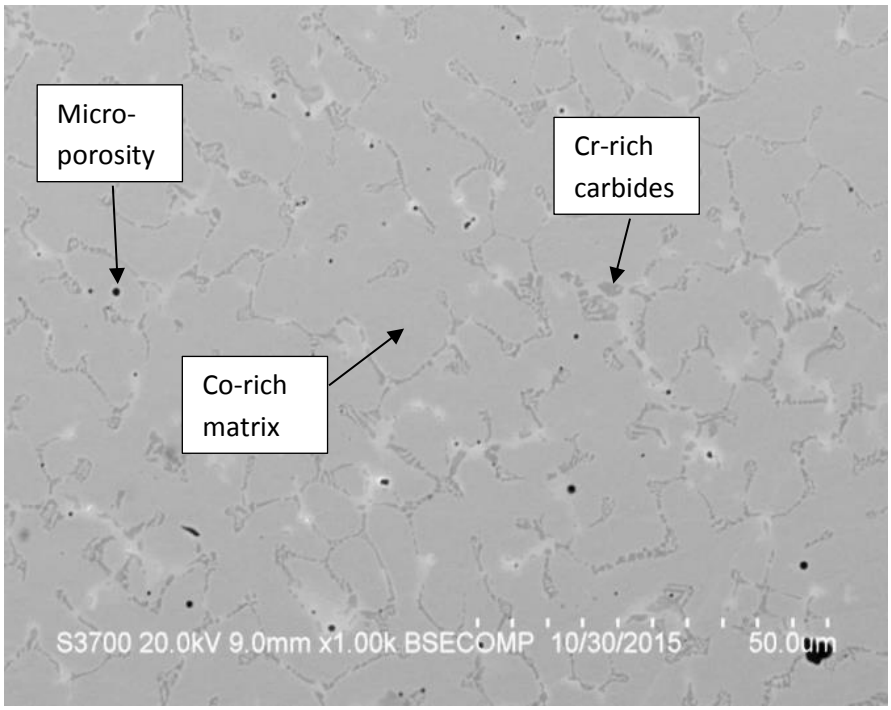

Figure 6.2: *Microstructure of Stellite 6 weld cladding single layer*

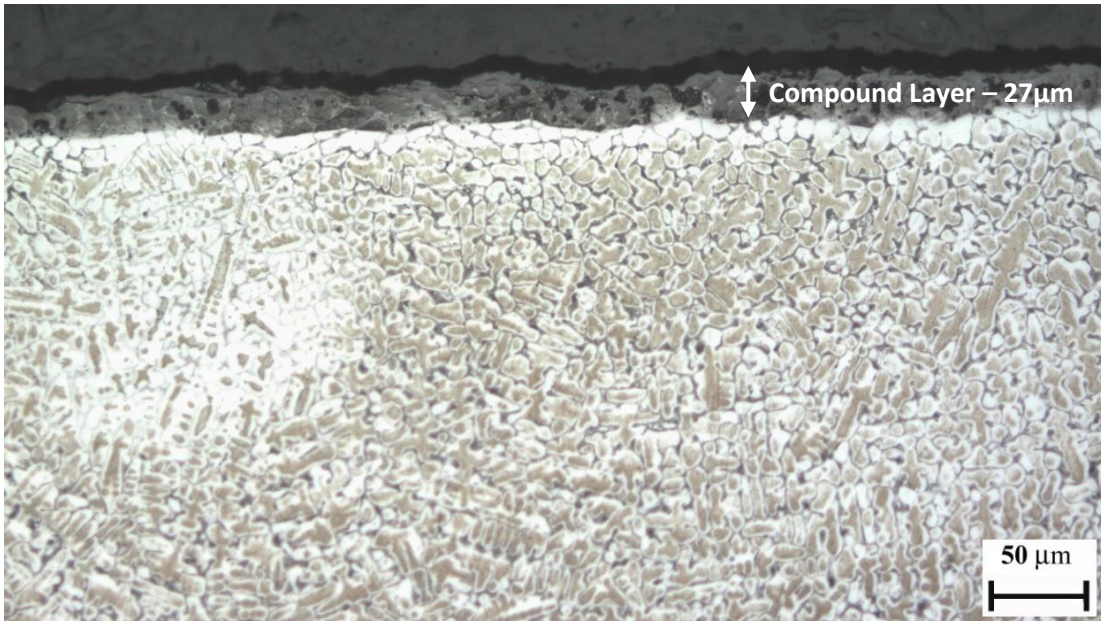

Figure 6.3: *Microstructure of nitrided Stellite 6 single layer weld cladding demonstrating compound layer*

6.5 Results

6.5.1 Material characterisation

6.5.1.2 Microhardness profiles

A microhardness profile was taken on each material to establish how the hardness altered with depth. Figure 6.4 demonstrates that there is a significant hardness increase for both the nitrided samples when compared to their untreated counterparts (80HV increase for single layer and 130HV increase for double layer). However, there is a sharp decrease in hardness with increasing depth. The nitrided Stellite 6 materials reached the core hardness of the untreated Stellite 6 at an approximate depth of 0.75mm. The increased hardness is associated with the nitride compound layer and by the diffusion of nitrides which hardens the material as the solute nitrogen atoms have diffused into the metallic matrix and are located in interstitial sites between metallic solvent atoms (Co).

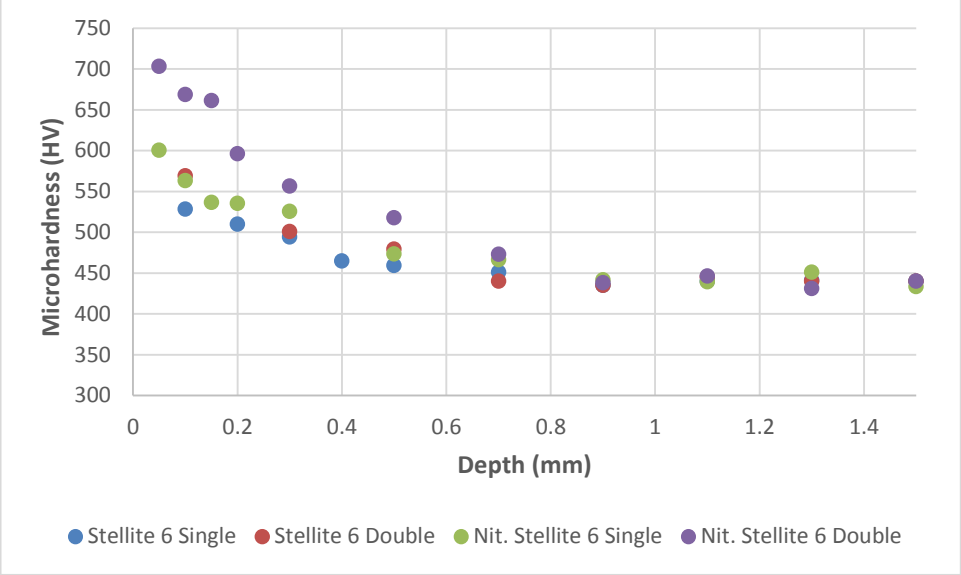

Figure 6.4: *Microhardness profiles of each test material against surface depth*

6.5.1.2 XRD analysis

The XRD analysis was conducted using the set-up described in Chapter 3.2.4.2, to determine the metallic and ceramic phases present in the nitrided and non-nitrided Stellite 6 weld claddings. Figure 6.5 shows the XRD patterns for the Stellite 6 single and double layer weld claddings. Both Stellite 6 weld claddings exhibited the same major peak which represented the main phase of FCC-Co. The Stellite 6 single layer weld cladding also

exhibited two smaller peaks which indicated the presence of a Co-W phase, however, this was not found to be present in the Stellite 6 double layer. A chromium carbide (Cr_7C_3) and a cobalt iron (Co Fe) phase were identified for the Stellite 6 double layer weld cladding. These phases were not observed in the XRD pattern for the Stellite 6 single layer weld cladding. The differences between the phases observed between the single and double layer Stellite 6 weld claddings are most likely to be associated with the welding process, i.e. differences in cooling rates and weld dilution. The presence of a Co-Fe phase instead of a FCC-Co, may result in some differences between the corrosive wear performance of the non-nitrided Stellite 6 weld claddings.

Figure 6.6 demonstrates the XRD patterns for the nitrided Stellite 6 single and double layer weld claddings. Both nitrided weld claddings exhibited similar phases at lower 2θ angles. A chromium nitride phase (β-Cr_2N) and a cobalt nitride phase (Co N) were identified in both nitrided Stellite 6 weld claddings. The main phase for both materials was found to be cobalt iron (Co Fe). At higher 2θ angles, the nitrided Stellite 6 single layer weld cladding exhibited further cobalt iron phases as well as a different chromium nitride phase (γ-Cr N). These were not detected in the XRD pattern for the nitrided Stellite 6 double layer weld cladding. The chromium nitride phases could potentially be detrimental to the corrosion resistance of the nitrided Stellite 6 weld claddings; however, they will increase the hardness of the weld claddings (corresponds to hardness values measured in Table 6.2 and Figure 6.4) which will improve their sliding abrasion resistance.

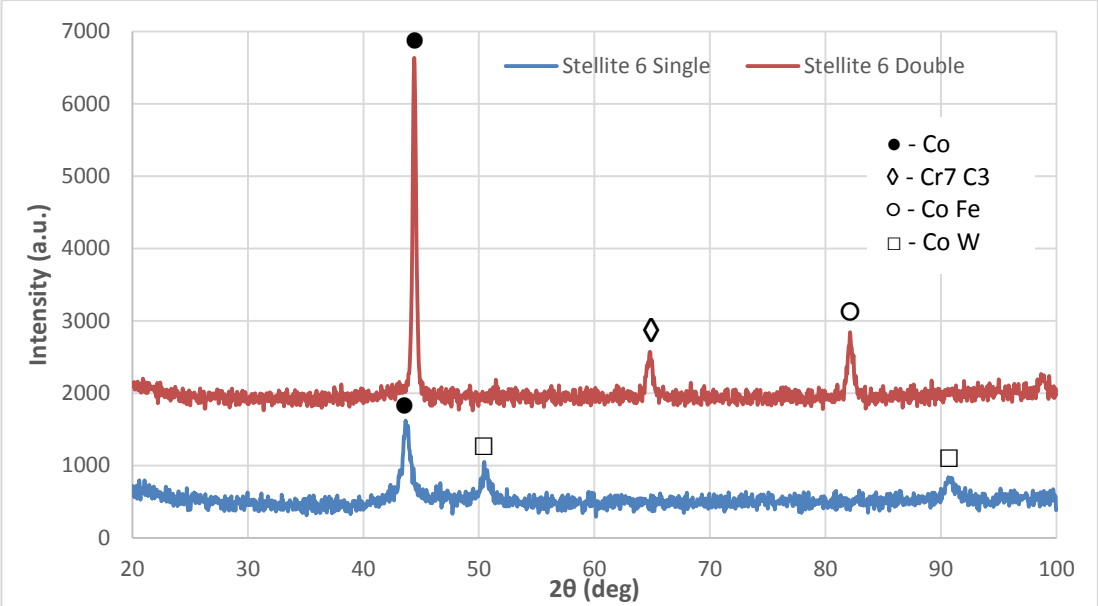

Figure 6.5: *XRD patterns of the Stellite 6 single and double layer weld claddings*

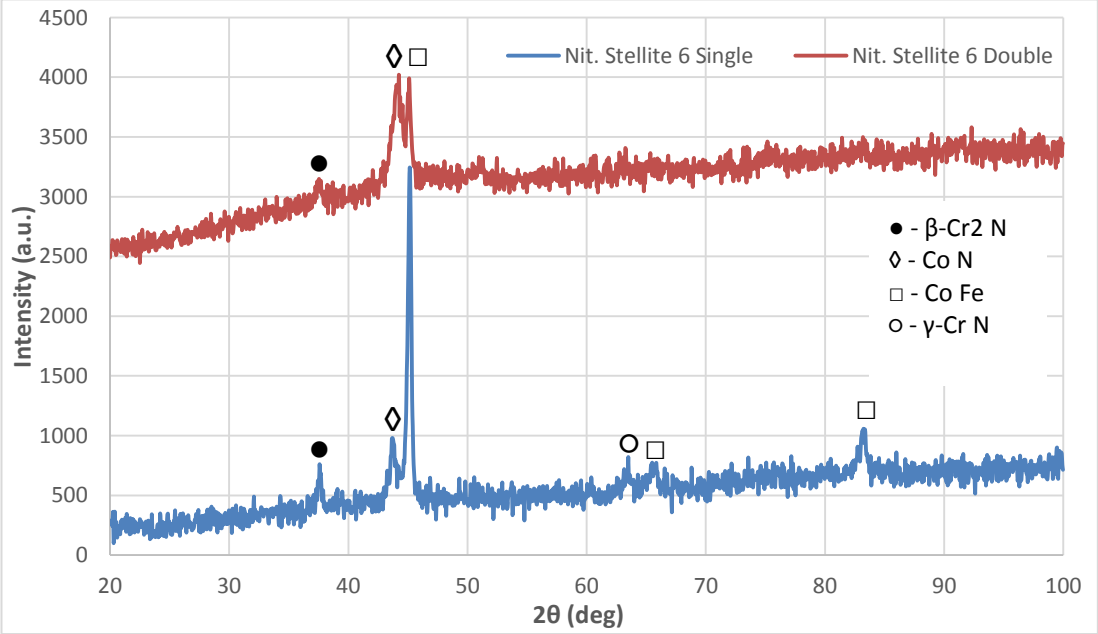

Figure 6.6: *XRD patterns for the Nit. Stellite 6 single and double layer weld claddings*

6.5.2 Total volume loss

Figure 6.7 displays the total volume loss for each test material in FEC and CP test environments. The error bands represent the scatter between at least four replicates. For tests with large scatters, additional tests were conducted. On average the total volume loss

for the nitrided Stellite 6 alloys was reduced (28%-38%) compared to the as-welded Stellite 6 alloys. There was little to no difference between the performance of the single and double layer Stellite 6 weld claddings. Similarly, when CP was applied no considerable reduction in total volume loss was observed.

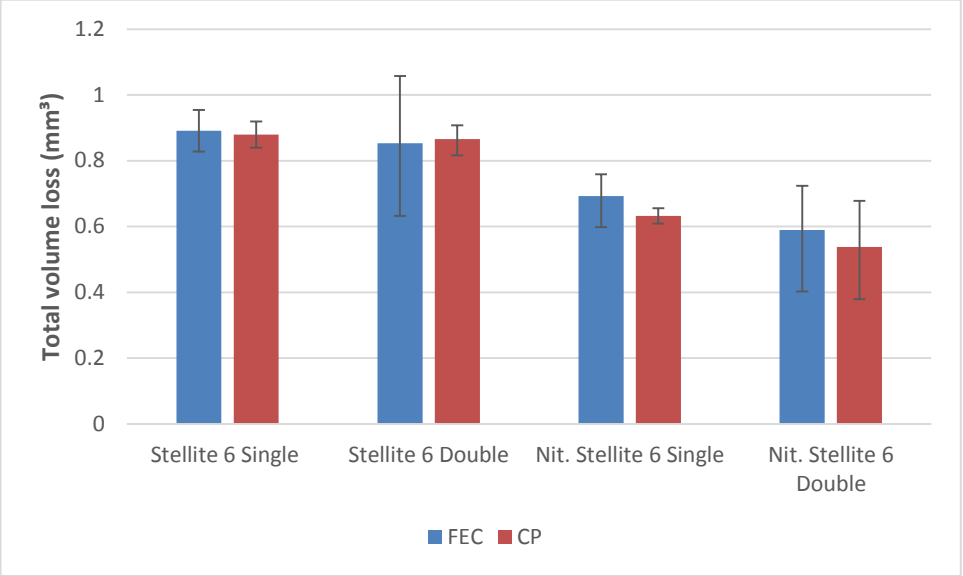

Figure 6.7: *Total volume losses of the tested materials under solid-liquid conditions*

6.5.3 Electrochemical monitoring

Figures 6.8 and 6.9 display the anodic and cathodic polarisation scans for the full size specimens (38mm diameter) of each test material under static and solid-liquid conditions. The electrode potentials are normalised for a simpler comparison between materials. In static conditions, there is a substantial reduction in corrosion rate of the Nit. 905M39 steel when compared to the untreated 905M39 steel. However, the opposite trend was observed for the Stellite 6 weld claddings as the untreated alloys exhibited better corrosion resistance than the nitrided Stellite 6 weld claddings. Concentration polarisation can be observed in the cathodic scans of the poor corrosion resistant materials.

In solid-liquid conditions, the corrosion rate for the nitrided 905M39 steel increased significantly as the impacting solid particles have removed the nitride layer and exposed the low alloy steel substrate. The corrosion rate of the untreated Stellite 6 weld claddings also increase due to the removal of the passive oxide film by the impacting sand particles. This

has resulted in them exhibiting similar corrosion behaviour of the nitrided Stellite 6 weld claddings.

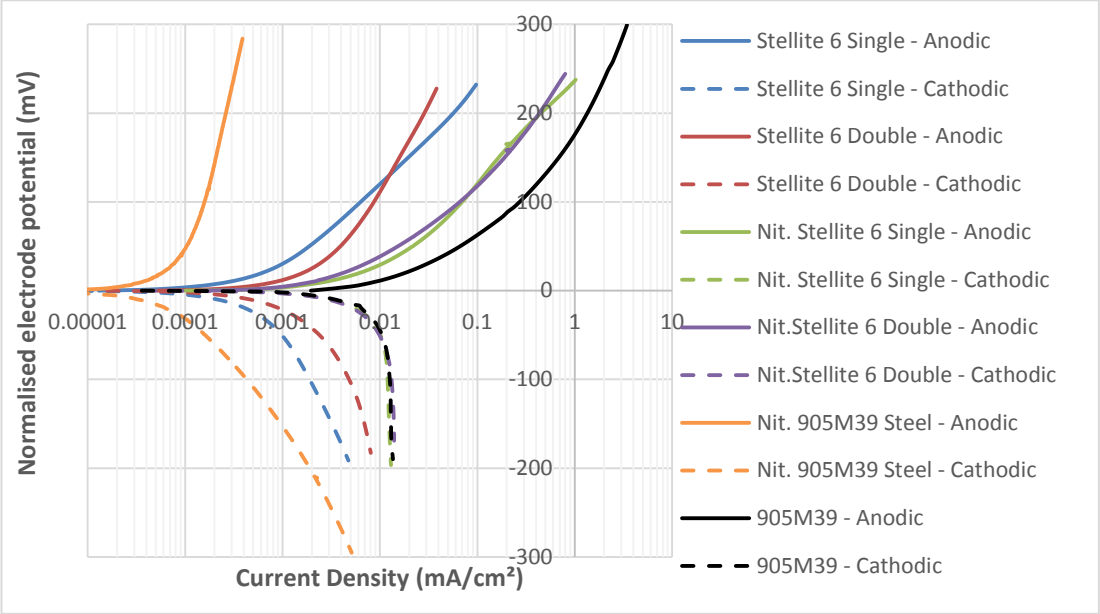

Figure 6.8: *Anodic and cathodic polarisation scans on the full specimen of all tested materials in static conditions*

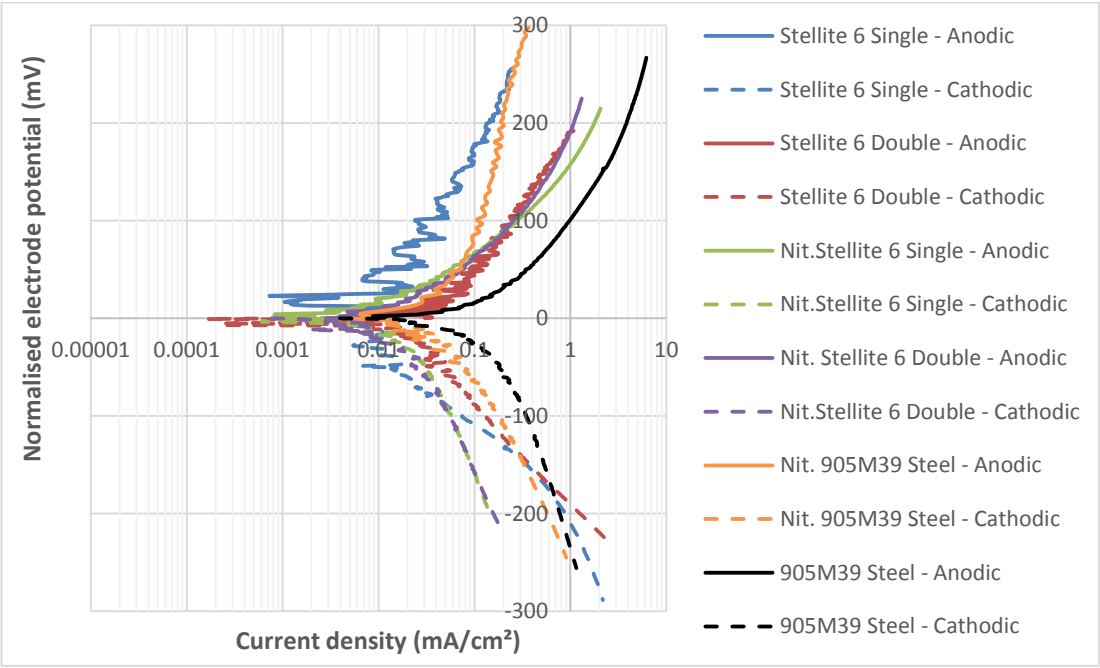

Figure 6.9: *Anodic and cathodic polarisation scans on the full specimen of all tested materials in solid-liquid conditions*

Tables 6.4 and 6.5 display the measured free corrosion potentials, corrosion current densities and calculated volume losses due to corrosion for full specimens of all tested materials under static and solid-liquid conditions. There was a significant increase in corrosion rates for each test material as the environment became more aggressive which would be expected. In static conditions, the untreated Stellite 6 weld claddings demonstrated significantly reduced corrosion rates compared to the nitrided Stellite 6 weld claddings. Conversely, the nitrided 905M39 steel exhibited a substantially smaller corrosion rate compared to the untreated 905M39 steel. In solid-liquid conditions, nitrided and untreated Stellite 6 weld claddings exhibited similar corrosion rates and the nitrided 905M39 steel displayed a significantly increased corrosion rate due to the partial removal of the nitride layer.

Table 6.4: *Measured free corrosion potentials, corrosion current densities and calculated volume losses due to corrosion for full specimens in static conditions*

Material	**E_{corr} (mV)**	**Corrosion current density (mA/cm^2)**	**Volume loss due to corrosion (mm^3)**
Stellite 6 Single	-363	0.0006	0.0011
Stellite 6 Double	-518	0.0010	0.0017
Nit. Stellite 6 Single	-388	0.0105	0.0179
Nit. Stellite 6 Double	-415	0.0120	0.0205
Nit. 905M39 Steel	-234	0.0001	0.0002
905M39 Steel	-623	0.0262	0.0395

Table 6.5: *Measured free corrosion potentials, corrosion current densities and calculated volume losses due to corrosion for full specimens in solid-liquid conditions*

Material	E_{corr} (mV)	Corrosion current density (mA/cm^2)	Volume loss due to corrosion (mm^3)
Stellite 6 Single	-479	0.01	0.017
Stellite 6 Double	-443	0.03	0.051
Nit. Stellite 6 Single	-346	0.02	0.034
Nit. Stellite 6 Double	-396	0.02	0.034
Nit. 905M39 Steel	-433	0.07	0.102
905M39 Steel	-488	0.18	0.271

Figure 6.10 displays the anodic polarisation scans for the Stellite 6 single layer weld cladding in both wear regions (DIZ and OA) under solid-liquid conditions. The anodic polarisation scans for the remaining materials are shown in Appendix B. The anodic polarisation scans were conducted after the stabilisation of the free corrosion potential (E_{corr}) and by using the same methodology as described in Chapter 3.3.4. The electrode potentials have been normalised for better comparison purposes due to the large differences between the two areas. The non-nitrided Stellite 6 weld claddings exhibited fluctuations in current density which is indicative of de-passivation/re-passivation events occurring due to the disturbance of a passive film. The current densities of the OA for the non-nitrided Stellite 6 weld claddings as well as the nitrided Stellite 6 double layer were considerably smaller than that of the current densities of the DIZ. However, for the nitrided Stellite 6 single layer, current densities of the OA were similar to that of the DIZ and the fluctuations in current densities were less pronounced, particularly in the OA.

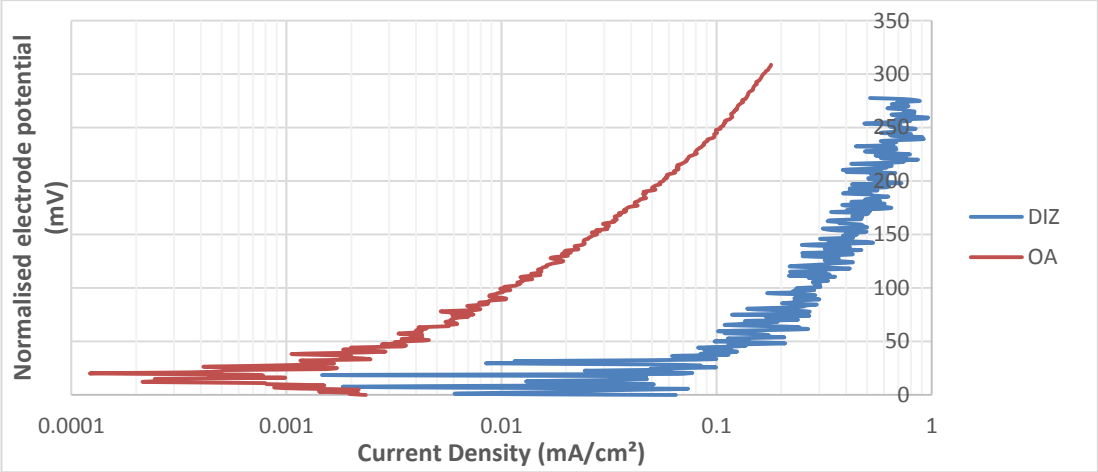

Figure 6.10: *Anodic polarisation scans in both wear regions of Stellite 6 single weld cladding in solid-liquid conditions*

The measured free corrosion potentials and Tafel extrapolated corrosion current densities in both wear regions for the tested materials are given in Table 6.6. Faraday's law (Chapter 2.4.1) was used to calculate the volume loss due to corrosion. The corrosion current densities were found to be greater in the DIZ than the OA for all test materials with the exception of the Nit. Stellite 6 single layer weld cladding. For alloys with passive films, the corrosion rate in the DIZ is significantly greater than the corrosion rate in the OA as the environment is more aggressive; hence, the passive film is less stable which results in a high corrosion rate. Conversely, for alloys with weaker passive films (i.e. Nit. Stellite 6 single layer weld cladding), the corrosion rates in both the DIZ and OA are more likely to be similar as the alloy is likely to exhibit active behaviour even in less aggressive environments. In terms of volume loss due to corrosion, all materials exhibited similar material loss in the DIZ. However, in the OA, the nitrided Stellite 6 alloys displayed significantly greater volume loss compared to their untreated counter parts, hence, indicating their poorer corrosion resistance.

Table 6.6: *Measured free corrosion potential corrosion current density and calculated volume loss due to corrosion on both wear regions for all test materials in solid-liquid conditions*

Material	DIZ (0.2cm^2)			OA (11cm^2)		
	E_{corr} (mV)	Corrosion current density (mA/cm^2)	Volume loss due to corrosion (mm^3)	E_{corr} (mV)	Corrosion current density (mA/cm^2)	Volume loss due to corrosion (mm^3)
Stellite 6 Single	-574	0.17	0.005	-461	0.002	0.003
Stellite 6 Double	-588	0.10	0.003	-480	0.002	0.003
Nit. Stellite 6 Single	-474	0.10	0.003	-425	0.100	0.17
Nit. Stellite 6 Double	-636	0.20	0.006	-441	0.060	0.10

6.5.4 Post-test examination

6.5.4.1 Macroscopic examination

Figure 6.11 displays the post-test surfaces of the materials after solid-liquid conditions. No corrosion product was evident on the test materials. The test materials have the typical surface damage which comprises of a wear scar, a halo around the wear scar (which is a result of the turbulent flow produced in this region) and the outer area (where the flow is less turbulent). The outer edges of the nitrided Stellite 6 weld claddings displayed virtually no damage as the nitride layer was still present (dark outer region).

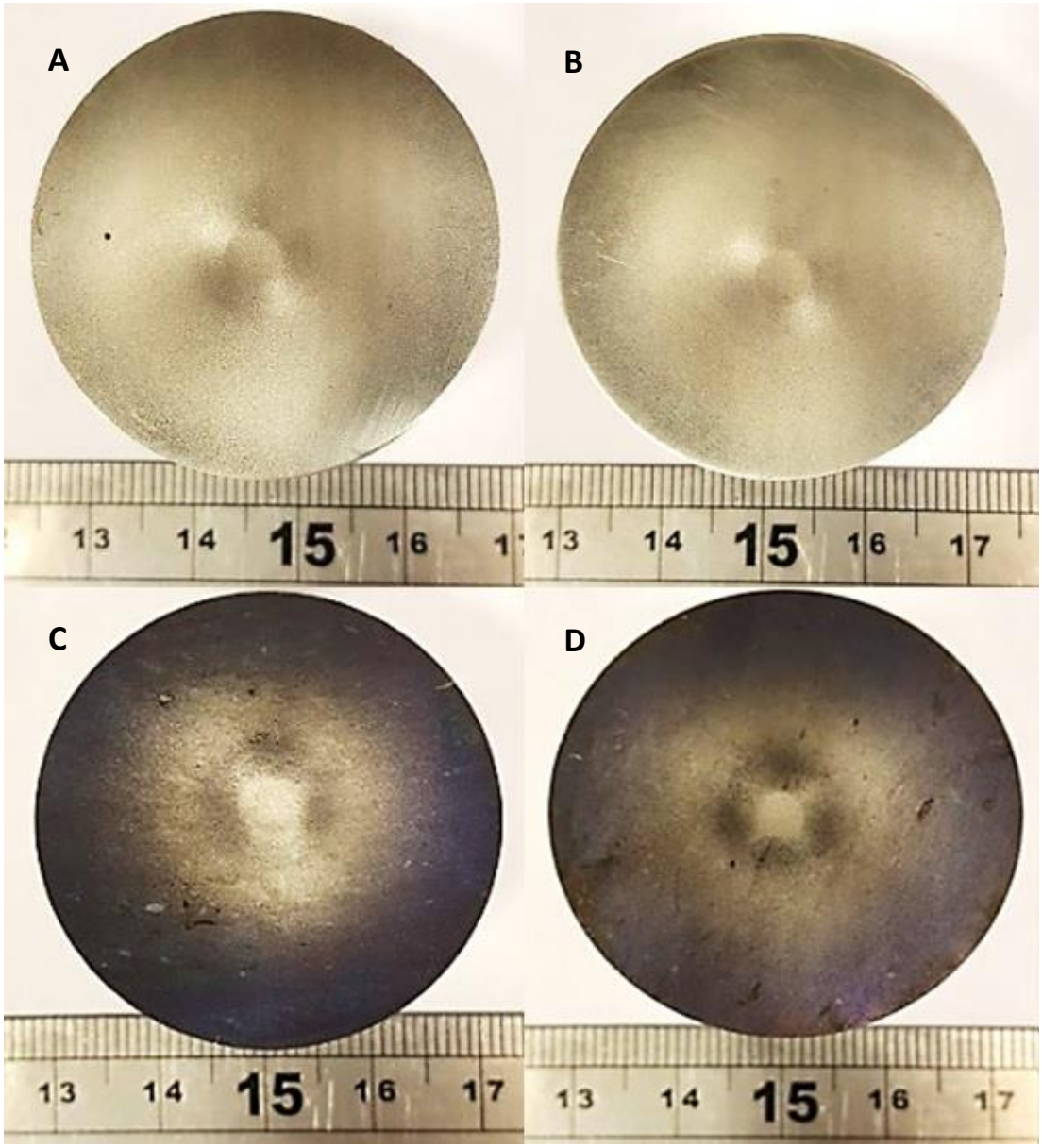

Figure 6.11: *Post-test surfaces of the test materials after solid-liquid conditions: Stellite 6 Single – A; Stellite 6 Double - B; Nitrided Stellite 6 Single – C; Nitrided Stellite 6 Double - D*

6.5.4.2 Microscopic examination

The wear mechanisms occurring beneath the jet were evaluated through cross sections of the tested material and were subsequently assessed through SEM analysis. The untreated Stellite 6 double layer weld cladding (Figure 6.12) exhibited small craters with plastically deformed lips in the softer Co-rich matrix as a result of the impacting sand particles. No cracks were observed on the Cr-carbides. Similar damage was observed in the nitrided

Stellite 6 double layer weld cladding (Figure 6.13) as the Co-matrix was preferentially removed resulting in Cr-carbides being exposed to the impacting sand particles.

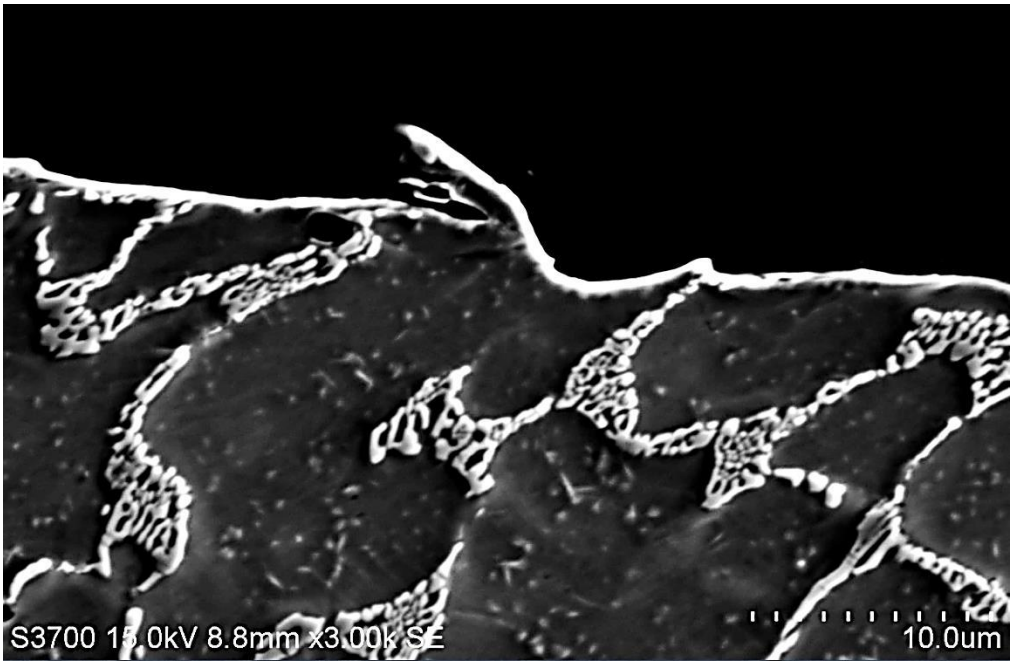

Figure 6.12: *Cross section of the erosion-corrosion wear scar of Stellite 6 Double layer weld cladding exhibiting plastically deformed craters in the Co-matrix*

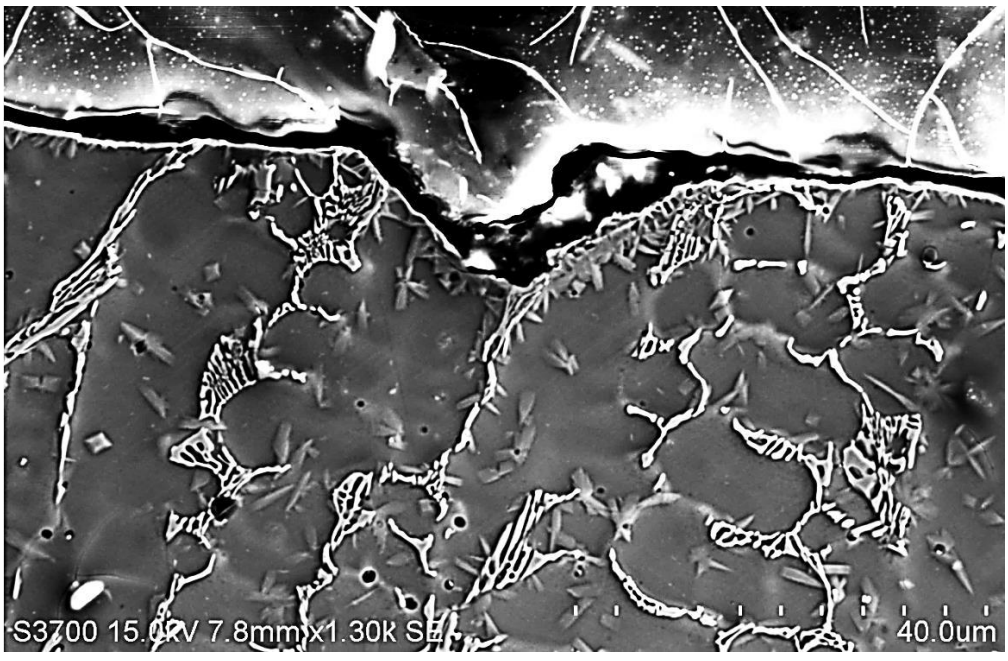

Figure 6.13: *Cross section of the erosion-corrosion wear scar of the Nit. Stellite 6 Double layer weld cladding with plastically deformed craters in the Co-matrix*

6.5.4.3 Wear scar profile scans

Wear scar profile scans were conducted on post-test surfaces using the surface topography technique described in Chapter 3.5.2, to assess the behaviour in the wear scar of the four test materials. The wear scar profile scans were assessed for both FEC and ICCP conditions. Figure 6.14 illustrates the U-shaped wear scar profiles which were observed for the nitrided Stellite 6 single layer weld cladding. The wear scar profiles for the remaining materials are shown in Appendix B. The width of the wear scars were approximately 4.5mm which corresponds to the diameter of the nozzle (4mm) used in this study.

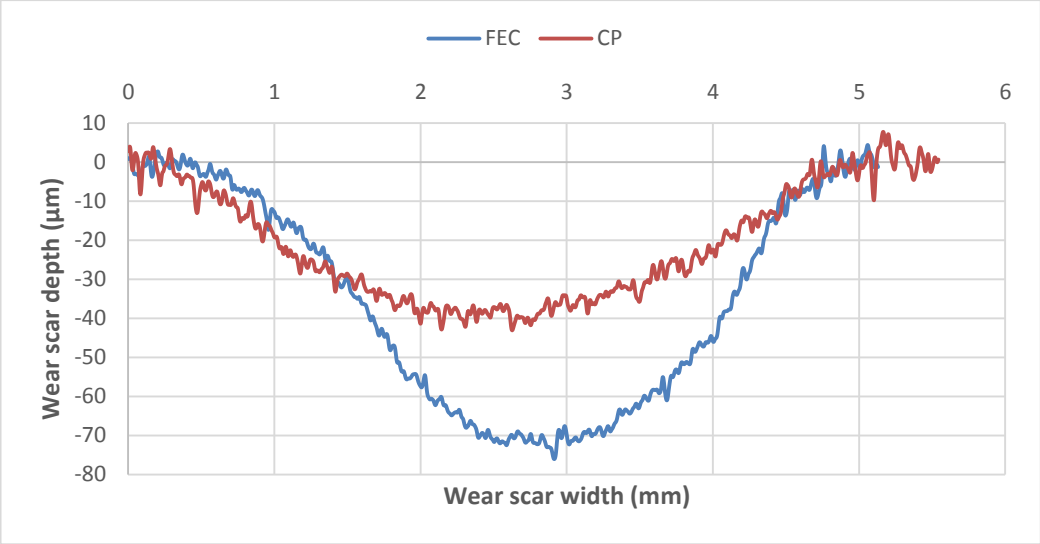

Figure 6.14: *Wear scar profile for Nitride. Stellite 6 Single layer weld cladding in FEC and ICCP conditions*

6.5.4.4 Volumetric analysis

The volume measurement for the Stellite 6 Single layer weld cladding in the direct impinged zone after a solid-liquid experiment is shown in Figure 6.15. The surface topography method described in Chapter 3.5.2 was used to measure the volume loss.

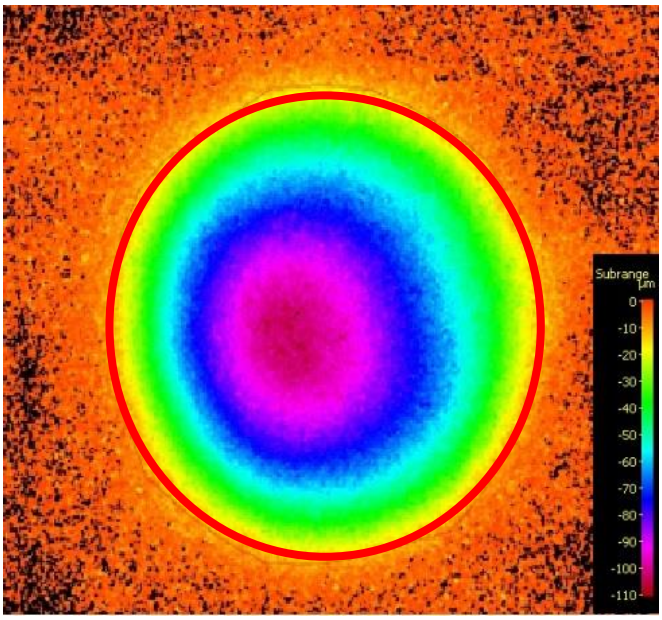

Figure 6.15: *Volumetric analysis on the wear scar of the Stellite 6 single layer weld cladding surface after a solid-liquid experiment*

The average volume losses for the tested materials are given in Figure 6.16. There was no apparent effect of nitriding on the FEC results. It was observed that there was no benefit in applying ICCP to the untreated Stellite 6 weld claddings and in some cases would be detrimental. A reduction in average wear scar volume was observed for the nitrided Stellite 6 weld claddings when ICCP was applied.

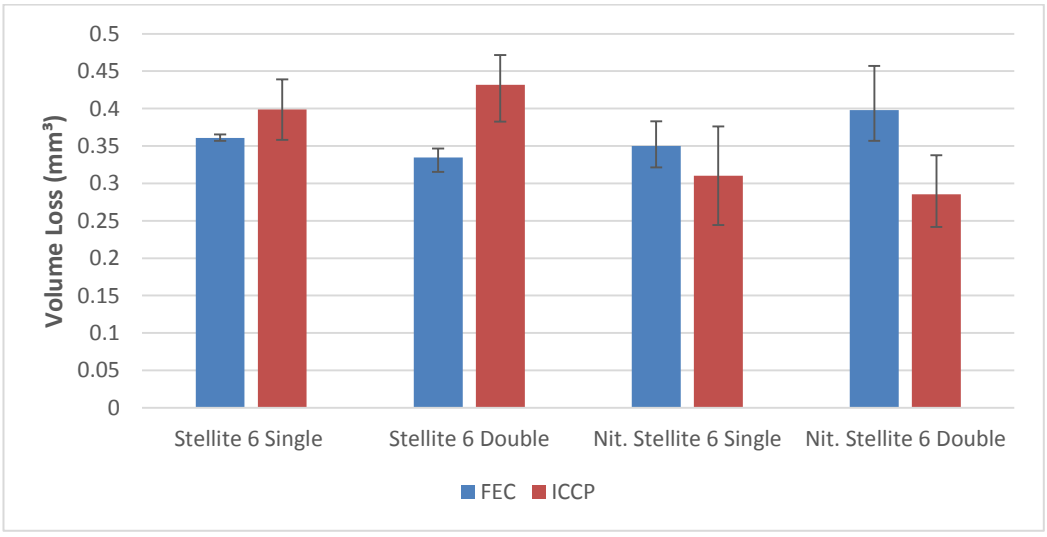

Figure 6.16: *Average wear scar volume loss for the tested materials in FEC and ICCP conditions*

6.6 Repetitive impact testing

The Stellite 6 weld claddings were also assessed under repetitive impact with slurry conditions as described in Chapter 3.4 and 5.4. This was conducted in order to assist with the feasibility of using Stellite 6 weld claddings as an alternative candidate for valve seats. The wear scar depths, volume losses and the circularity of tested sand particles were assessed.

6.6.1 Wear scar depths

The average wear scar depths for the tested materials under repetitive impact conditions are shown in Figure 6.17. The untreated Stellite 6 single weld cladding exhibited the greatest wear scar depth, while the untreated Stellite 6 double weld cladding displayed the lowest wear scar depth. The nitrided Stellite 6 double layer weld cladding exhibited greater wear scar depths than its untreated counterpart.

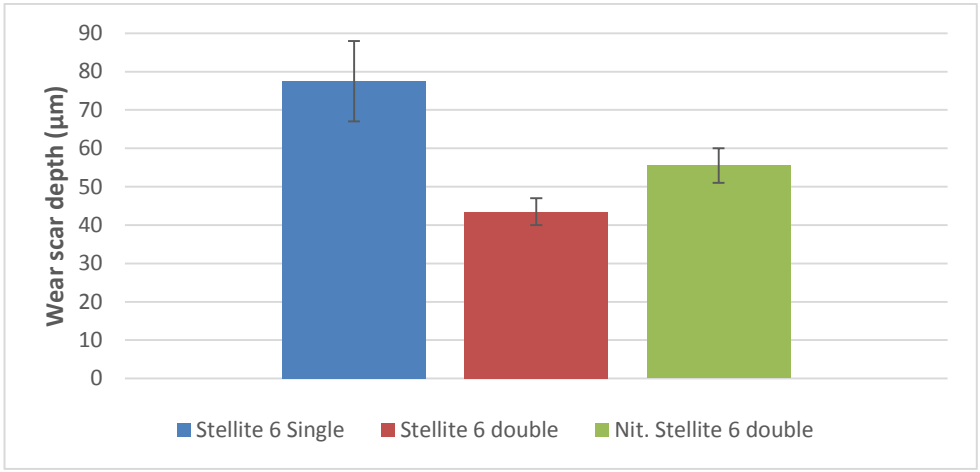

Figure 6.17: *Average wear scar depths for the tested materials under repetitive impact conditions*

6.6.2 Wear scar volume loss

The average wear scar volume losses for the tested materials are shown in Figure 6.18. The Stellite 6 single layer weld cladding exhibited the greatest wear scar volume loss which correlates with the findings with wear scar depth. However, the nitrided Stellite 6 double layer weld cladding displayed a smaller wear scar volume loss compared to the Stellite 6 double layer weld cladding. There was also a lack of correlation between the wear scar depths and volume losses for the nitrided Stellite 6 double layer weld cladding which can be

attributed to the non-uniform wear scar produced during the repetitive impact tests (Figure 6.19).

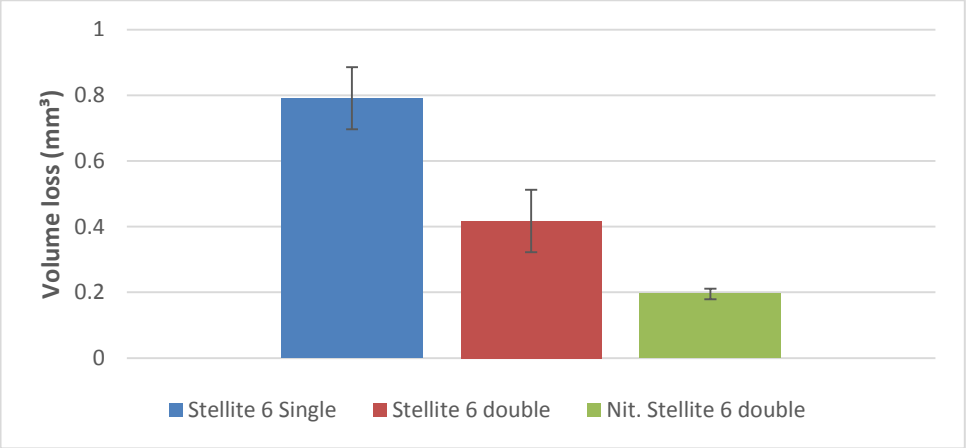

Figure 6.18: *Average wear scar losses for the tested materials under repetitive impact conditions*

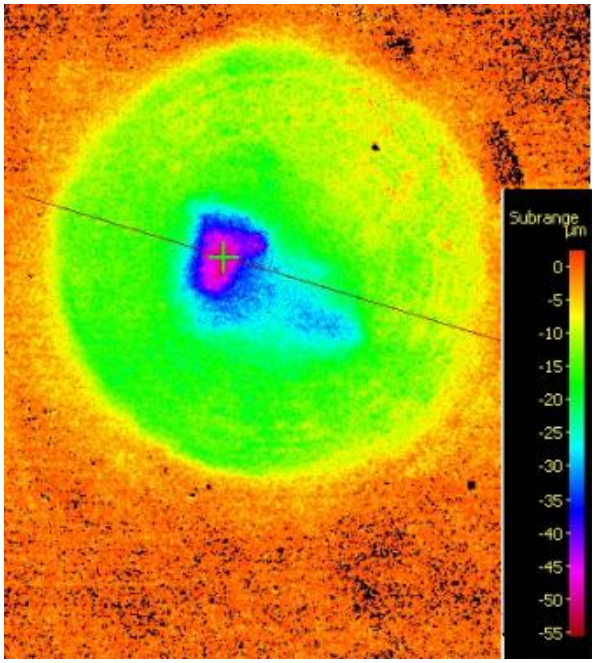

Figure 6.19: *Non-uniform wear scar of Nitrided Stellite 6 double layer weld cladding*

6.6.3 Circularity factor of tested sand particles

Table 6.7 illustrates the range of CF values (<0.8, 0.8-0.9 and >0.9) and the amount of sand post-test sand particles observed in each CF value range. A total of 100 sand particles were measured randomly after each experiment. Also, 100 untested sand particles were

measured as a reference. There was a reduction in CF values of the post-test sand particles as they have become damaged from the repetitive impact tests. However, most of the sand particles had a CF value greater than 0.8 which indicates that they still meet the requirement of the ISO and API standards [6.29, 6.30].

Table 6.7: *Amount of sand particles for each CF range for all test materials in repetitive impact with slurry test conditions*

Material	CF value <0.8	CF value 0.8-0.9	CF value >0.9
Untested sand particles (reference)	1	35	64
Stellite 6 Single	7	50	43
Stellite 6 Double	4	56	40
Nit. Stellite 6 Double	7	55	38

6.6.4 Wear mechanisms in the repetitive impact wear scars

Figures 6.20 - 6.22 display cross sections of repetitive impact wear scars of the tested materials to assess the material degradation mechanisms. A subsurface crack emanating from the edge of the wear scar was observed on the Stellite 6 double layer weld cladding. Small craters caused by material removal of both Co-matrix and Cr-carbides were also observed on the Stellite 6 double layer weld cladding. For the nitrided Stellite 6 double layer weld cladding, a network of subsurface cracks parallel to the surface were observed in the nitride layer. Below the network of subsurface cracking, Cr-carbides were also observed to be cracked. This feature was not present in the untreated Stellite 6 weld cladding.

Figure 6.20: *Cross section of repetitive impact wear scar of Stellite 6 double layer weld cladding demonstrating subsurface crack at edge of wear scar*

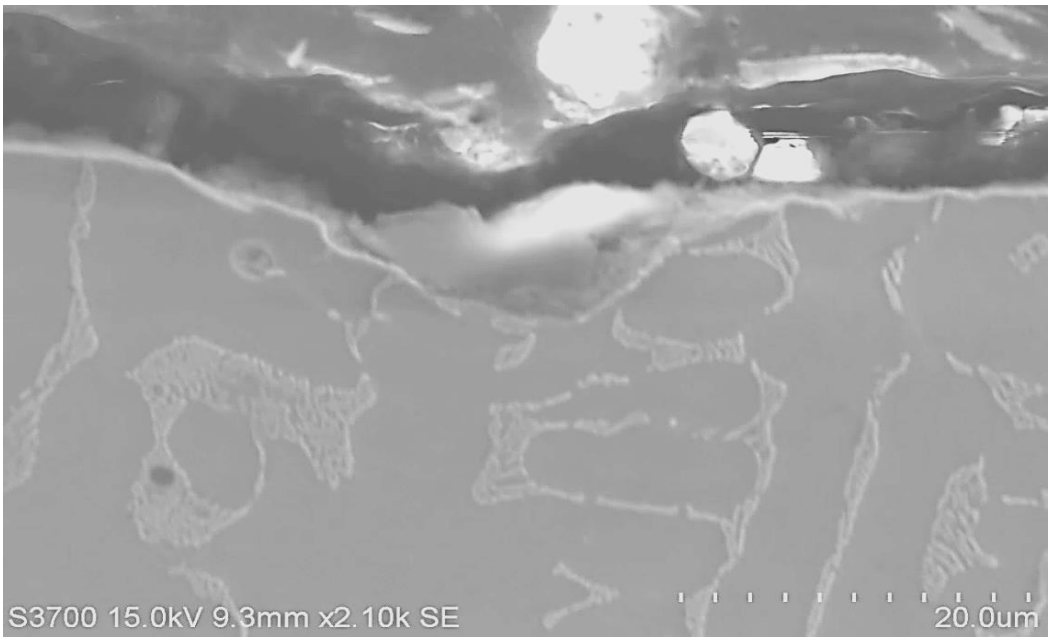

Figure 6.21: *Cross section of repetitive impact wear scar of Stellite 6 double layer weld cladding exhibiting a crater formed from material removal*

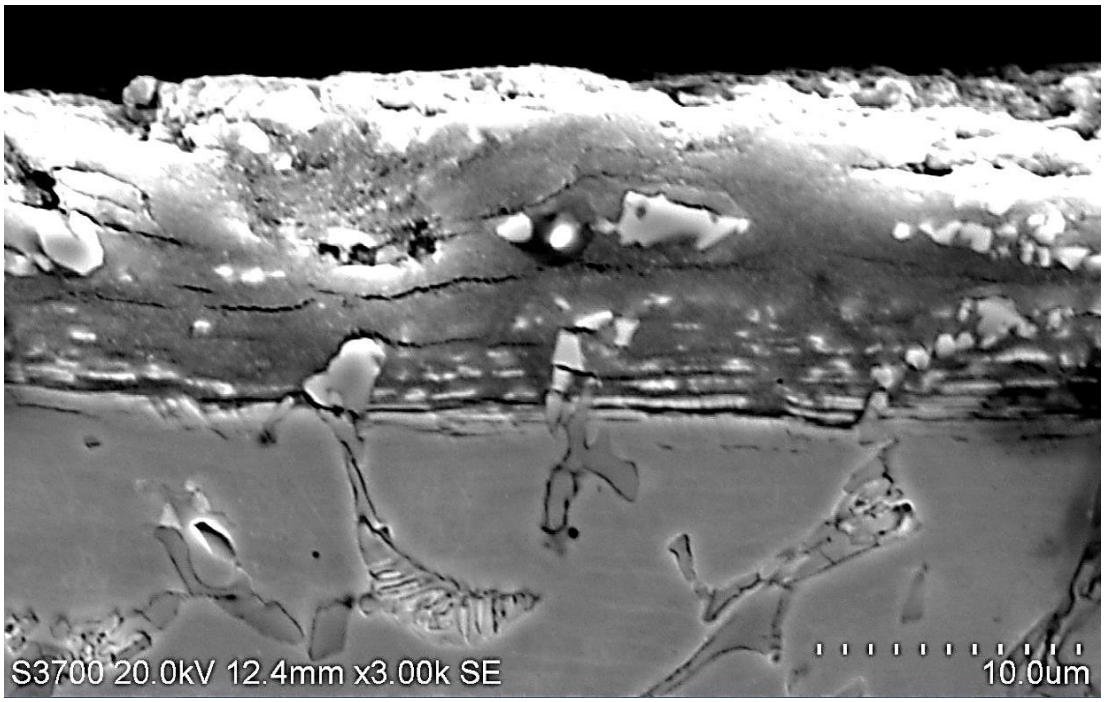

Figure 6.22: *Cross section of repetitive impact wear scar of Nit. Stellite 6 double layer weld cladding exhibiting subsurface cracks of the nitride layer and of Cr-carbides*

6.7 Discussion

This test programme aimed at assessing the potential of Stellite 6 weld claddings in corrosive wear situations in saline environments as well as the possible improvement associated with a nitriding treatment. The following section will discuss the findings of this testing programme in detail.

6.7.1 Total volume loss (TVL) in free erosion-corrosion conditions

From Figure 6.7, it is clear that there is virtually no difference between the single and double layer Stellite 6 weld claddings under solid-liquid conditions. There also appears to be some benefit in nitriding the Stellite 6 weld claddings and the reasons for this will be discussed further in this section.

6.7.2 Breakdown of total volume loss in free erosion-corrosion (FEC) conditions

The volume loss in the outer area (OA) was calculated by subtracting the measured volume loss in the direct impinged zone (DIZ) from the total volume loss (TVL) as described in Chapter 3.5.3. Figure 6.23 shows the breakdown of the total volume loss into the volume losses in both wear regions (DIZ and OA) under solid-liquid conditions. In the DIZ, the tested

materials exhibited similar volume losses. However, in the OA, the volume losses for the nitrided Stellite 6 weld claddings are significantly smaller than that of the untreated Stellite 6 weld claddings. This is most likely to be associated with the increased hardness of the nitrided weld claddings which has increased the resistance to abrasion damage (predominant wear mechanism in the OA) of the Stellite 6 weld claddings.

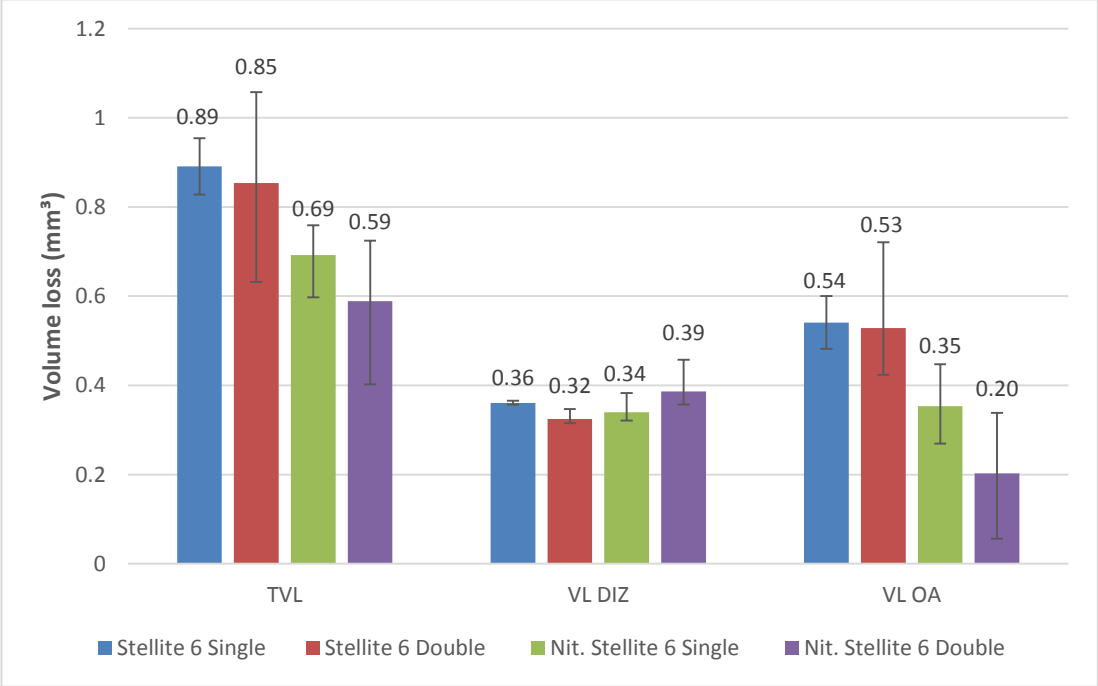

Figure 6.23: *Breakdown of the total volume loss into the two distinct wear regions (DIZ & OA) under FEC solid-liquid conditions*

6.7.3 Breakdown of total volume loss in cathodic protection (CP) conditions

The breakdown of the total volume loss into the two wear regions for the tested materials under cathodic protection (CP) conditions is shown in Figure 6.24. When CP was applied to the test materials, there was virtually no difference for the untreated Stellite 6 weld claddings and a slight reduction for the nitrided weld claddings. Similar trends with FEC conditions were observed in the OA as the nitrided weld claddings exhibited smaller volume losses compared to the untreated weld claddings due to their increased hardness. However, in the DIZ there was a noticeable reduction in volume loss when CP was applied to the nitrided Stellite 6 weld claddings. This was not observed for the untreated weld claddings, the volume loss in the DIZ actually increased when CP was applied.

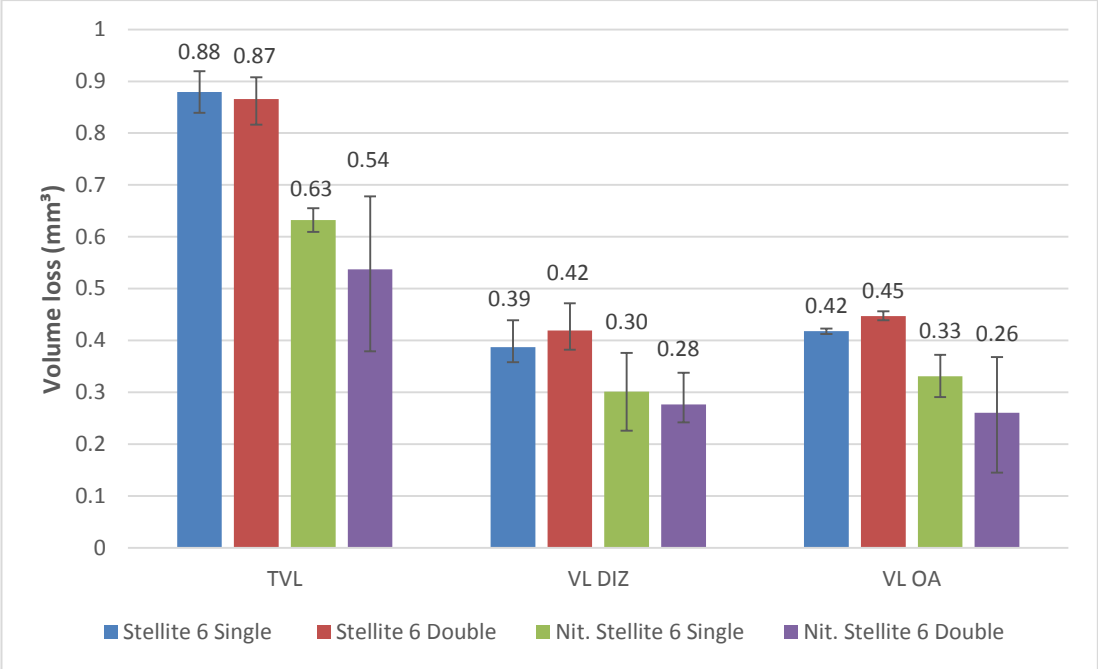

Figure 6.24: *Breakdown of the total volume loss into the two distinct wear regions (DIZ & OA) under CP solid-liquid conditions*

6.7.4 Discrimination of the TVL in the DIZ and OA

Figure 6.25 illustrates the quantitative volume losses of the different degradation processes which were measured using the volumetric analysis technique described in Chapter 3.5.3. Each degradation process will be discussed separately in subsequent subsections.

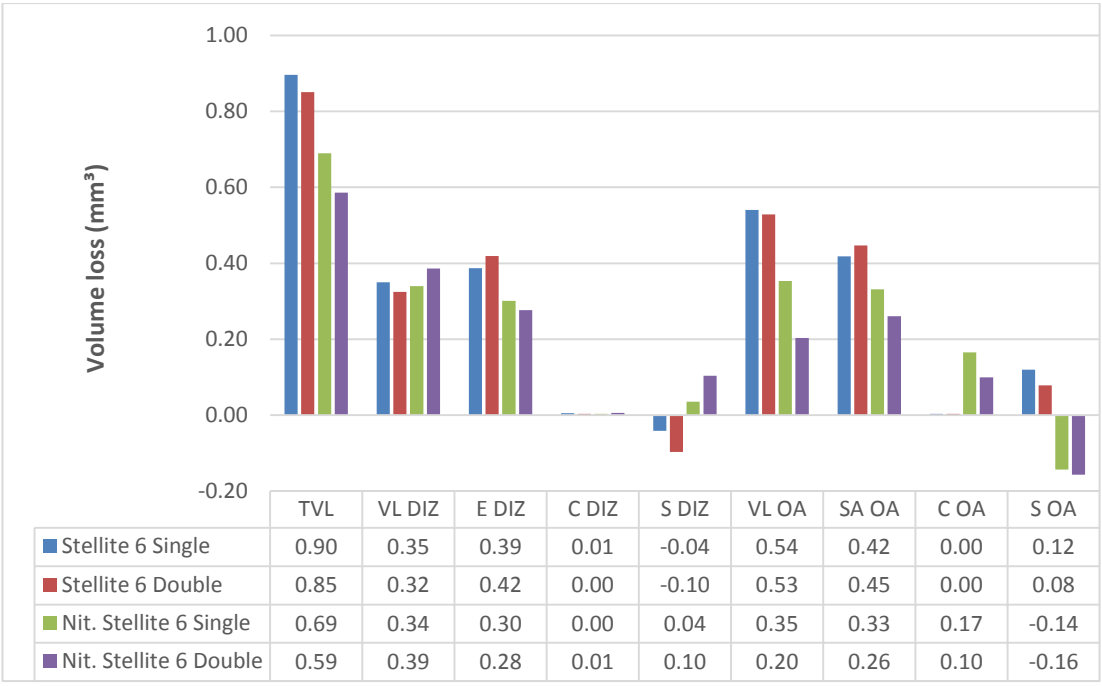

	TVL	VL DIZ	E DIZ	C DIZ	S DIZ	VL OA	SA OA	C OA	S OA
Stellite 6 Single	0.90	0.35	0.39	0.01	-0.04	0.54	0.42	0.00	0.12
Stellite 6 Double	0.85	0.32	0.42	0.00	-0.10	0.53	0.45	0.00	0.08
Nit. Stellite 6 Single	0.69	0.34	0.30	0.00	0.04	0.35	0.33	0.17	-0.14
Nit. Stellite 6 Double	0.59	0.39	0.28	0.01	0.10	0.20	0.26	0.10	-0.16

Figure 6.25: *Discrimination between the different material degradation processes on the tested materials under solid-liquid conditions*

6.7.3 High angle erosion damage in the direct impinged zone (DIZ)

The high angle erosion damage occurring in the DIZ was measured in terms of volume loss from the cathodically protected test samples. These measurements are given in Figures 6.16 and 6.24. The nitrided Stellite 6 weld claddings exhibited marginally lower volume losses compared to the untreated weld claddings. This would suggest that the nitride layer can successfully increase the high angle erosion resistance of the Stellite 6 weld claddings. Although it is tempting to attribute this effect to increased hardness after the nitriding process, it must be recognised that this observation has not been found to universally lead to improved erosion resistance [6.19, 6.31, 6.32].

6.7.4 Corrosion and synergy in the direct impinged zone (DIZ)

Figure 6.25 demonstrates that the majority of the damage in the DIZ for the tested materials was mechanical. The corrosion damage in the DIZ for the materials was observed to be almost negligible (less than 2% of total volume loss). A substantial proportion of the material loss was attributed to synergy for both nitrided weld claddings (12% - Nit. Stellite 6 single and 29% - Nit. Stellite 6 double). This may be attributed to galvanic interactions

between the various phases in the nitride layer which were found to be present in the nitrided Stellite 6 weld claddings.

A possible reason for the negative synergy values could be that localised hydrogen embrittlement mechanisms may occur when cathodic protection was applied. Any involvement of hydrogen embrittlement would be expected to be more pronounced at a more negative electrode potential at which hydrogen production cathodic reactions are accelerated. Nevertheless, to examine this possibility, cathodic protection tests were conducted on the Stellite 6 single layer weld cladding at a range of electrode potentials (-700mV, -800mV and -900mV) each test had two replicates. Table 6.8 demonstrates that the volume losses were similar for each electrode potential and that the average volume loss at all electrode potentials were similar to the average volume loss in FEC conditions. The additional cathodic protection tests demonstrate that hydrogen embrittlement is not an issue. Other possible reasons for negative synergy are discussed subsequently in Chapter 6.7.7.

Table 6.8: *Comparison of volume losses of single layer Stellite 6 weld cladding at different cathodic potentials*

Single Layer Stellite 6 Weld Cladding	CP (-700mV)	CP (-800mV)	CP (-900mV)	FEC
Volume loss 1 (mg)	0.89	0.84	0.85	
Volume loss 2 (mg)	0.86	0.92	0.83	
Average volume loss (mg)	0.87	0.89	0.84	0.90

6.7.5 Sliding abrasion damage in the outer area (OA)

Figures 6.24 and 6.25 show the volume losses (ICCP conditions) in the OA which are associated with sliding abrasion damage. It is clear that the nitrided Stellite 6 weld claddings exhibit significantly reduced volume losses compared to the untreated Stellite 6 weld claddings. Since it is better established that there is a correlation between hardness

and abrasion resistance, this can be attributed to the higher hardness as a result of the nitriding process which has increased the sliding abrasion resistance of the weld claddings.

6.7.6 Corrosion and synergy in the outer area (OA)

Figure 6.25 displays the measured corrosion and calculated synergy volume losses for the tested materials. The volume losses due to corrosion for the untreated weld claddings were observed to be negligible (Table 6.6). However, volume losses due to corrosion for the nitrided Stellite 6 weld claddings were significant (Nit. Stellite 6 single – 25% of total volume loss, Nit. Stellite 6 double – 17% of total volume loss). The poor corrosion resistance of the nitrided Stellite 6 weld claddings can be attributed to the formation of chromium and cobalt nitrides which have formed in the nitride layer. The anodic polarisation curves of the OA for the nitrided Stellite 6 weld claddings are displayed in Appendix B. The curves show high corrosion rates in the OA and virtually no evidence of repassivation/depassivation activity; this would be expected for a material with no passive oxide film. The lack of passivity of the nitride layer has been observed in past studies and is attributed to reduced chromium in solid solution as it has a high affinity with nitrogen [6.26, 6.27].

The untreated Stellite 6 weld claddings exhibited a noticeable amount of synergy in the OA (Stellite 6 single – 13% and Stellite 6 double – 9%). This could be attributed to galvanic interactions between the various microstructural phases (Co, Cr_7C_3, CoFe and CoW) which were observed in the untreated Stellite 6 weld claddings. However, negative synergy was observed for both nitrided Stellite 6 weld claddings, possible reasons for this will be discussed in the subsequent section.

6.7.7 Negative synergy postulations

A variety of negative synergy theories have been observed and discussed in several studies and reviews [6.33–6.39]. Postulations include: impacting sand particles can strain harden the surface of the material which reduces its erosion rate, high concentrations of solid particles block the surface from impacting sand particles, localised (flash) temperatures on the material surface may alter the oxide film composition and microstructure, hence, reducing the erosion rate of the material. These negative synergy theories seem unlikely to be the explanation for the observations in this study.

A plausible explanation for the observed increase in volume loss from FEC to ICCP for the untreated Stellite 6 weld claddings in the DIZ may be as a result of the passive oxide film (produced during FEC conditions) being able to provide some protection to the material surface from impacting sand particles at high angles; such protection being absent when ICCP is applied. This theory has been proposed by other researchers [6.34, 6.39].

A proposed theory for the negative synergy observed for the nitrided Stellite 6 weld claddings in the OA is as follows: as the nitriding process has produced nitride precipitates (CrN, Cr_2N, CoN – Figure 6.6), the solid solution matrix has depleted chromium content. The nitride precipitates are unlikely to corrode as they are a ceramic phase; therefore, the corrosion product formed on the surface is likely to be cobalt-rich, which is harder than the soft non-corroded Co-alloy matrix. The surface region of OA experiences a quite different mechanical deterioration process (abrasion) than the DIZ and comprises a dense array of nitride particles in the surface and immediate subsurface regions. It is possible that this dense array of nitride particles and Co-rich corrosion product can provide additional wear resistance compared to the situation where corrosion is prevented (ICCP). The potential negative synergy mechanism is depicted in the schematic in Figure 6.26.

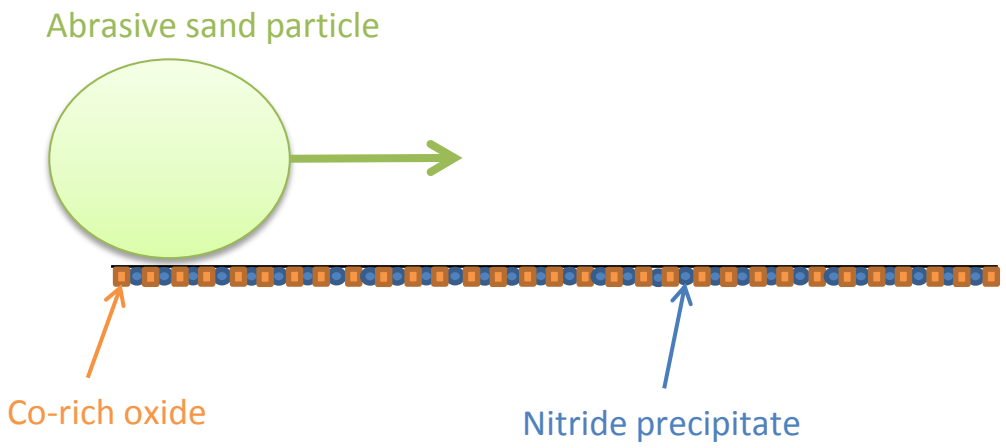

Figure 6.26: *Negative synergy mechanism for Nitrided Stellite6 weld claddings in OA*

6.7.8 Repetitive impact testing

The result from Figure 6.18 (wear scar volume loss) suggests that there may be an advantage in nitriding the Stellite 6 weld cladding as the wear scar volume loss is substantially reduced compared to the untreated weld claddings. Both the untreated and nitrided Stellite 6 weld claddings exhibited subsurface cracking in the wear scar.

6.8 Relevance of work to the design and operation for hydraulic fracturing pump components

This study has demonstrated that Stellite 6 weld claddings have potential in increasing the life of some hydraulic fracturing components which experience corrosion, erosion-corrosion and repetitive impact wear. A further outcome of this study has shown that there is virtually no difference between a single and double layer Stellite 6 weld cladding in terms of corrosion and erosion-corrosion resistance. From an industrial standpoint this is important as it assists in reducing the manufacturing costs of the Stellite 6 weld cladding process. Finally, understanding the environmental conditions which components experience is crucial as it will influence the material selection as in some instances the nitriding process was beneficial to the wear resistance of the Stellite 6 weld claddings. However, in some cases, particularly in terms of corrosion, the nitriding process is detrimental.

6.9 Conclusions

1. Stellite 6 weld claddings demonstrate good corrosion and erosion-corrosion resistance for new components and for repairing components.
2. Not much difference has been observed between single and double layer weld claddings in terms of erosion-corrosion performance – from a business point of view this is beneficial as components could just have a single layer which will reduce the cost of manufacture.
3. Nitriding can be beneficial in certain instances and knowing the environmental conditions of the component will dictate whether it is worthwhile nitriding a component.
4. Although material loss due to pure corrosion for the Stellite 6 weld claddings was very low, the synergy value was significant. This points to the relative vulnerability of some two phase materials to micro-galvanic effects that lead to increased material losses associated with synergy.

5. Negative synergy was observed for the untreated Stellite 6 weld claddings in the DIZ and the nitrided Stellite 6 weld claddings in the OA. Some possible explanations for the observed negative synergy in the nitrided Stellite 6 weld claddings have been presented but this aspect is unresolved without further work.
6. The findings have demonstrated the additional, refined, advantages from the in-house volumetric analysis evaluation method used in this study. For example, the nitriding process was observed to be beneficial against corrosion-abrasion wear, whereas, there was not much benefit in high angle corrosive wear conditions.

6.10 References

[6.1] A. Neville and T. Hodgkiess, "Characterisation of high-grade alloy behaviour in severe erosion-corrosion conditions," *Wear*, vol. 233–235, pp. 596–607, 1999.

[6.2] U. Malayoglu and A. Neville, "Mo and W as alloying elements in Co-based alloys—their effects on erosion–corrosion resistance," *Wear*, vol. 259, no. 1–6, pp. 219–229, 2005.

[6.3] R. Liu, J. Yao, Q. Zhang, M. X. Yao, and R. Collier, "Effects of molybdenum content on the wear/erosion and corrosion performance of low-carbon Stellite alloys," *Mater. Des.*, vol. 78, pp. 95–106, 2015.

[6.4] H. Yu, R. Ahmed, H. de Villiers Lovelock, and H. Davies, "Influence of Manufacturing Process and Alloying Element Content on the Tribomechanical Properties of Cobalt-Bases Alloys," *J. Tribol. (Transactions ASME - F -)*, vol. 131, pp. 11601–11606, 2009.

[6.5] A. Neville, M. Reyes, T. Hodgkiess, and A. Gledhill, "Mechanisms of wear on a Co-base alloy in liquid–solid slurries," *Wear*, vol. 238, pp. 138–150, 2000.

[6.6] M. X. Yao, J. B. C. Wu, and Y. Xie, "Wear, corrosion and cracking resistance of some W- or Mo-containing Stellite hardfacing alloys," *Mater. Sci. Eng. A*, vol. 407, no. 1–2, pp. 234–244, 2005.

[6.7] N. Andrews, L. Giourntas, A. M. Galloway, and A. Pearson, "Effect of impact angle on the slurry erosion-corrosion of Stellite 6 and SS316," *Wear*, vol. 320, no. 1, pp. 143–151, 2014.

[6.8] U. Malayoglu and A. Neville, "Comparing the performance of HIPed and Cast Stellite 6 alloy in liquid–solid slurries," *Wear*, vol. 255, no. 1–6, pp. 181–194, 2003.

[6.9] M. Reyes and A. Neville, "Degradation mechanisms of Co-based alloy and WC metal–matrix composites for drilling tools offshore," *Wear*, vol. 255, no. 7–12, pp. 1143–1156, 2003.

[6.10] A. Neville, H. Xu, and M. Reyes, "Corrosion and erosion-corrosion behavior of a Co-based alloy and a Ni-containing austenitic cast iron," in: *NACE Int. Corros. Conf. Expo*,

2000.

[6.11] G. Nelson, G. Powell, and V. Linton, "Investigation of the wear resistance of high chromium white irons," in: *19th International conference on surface modification technologies*, 2006.

[6.12] S. Hattori and N. Mikami, "Cavitation erosion resistance of stellite alloy weld overlays," *Wear*, vol. 267, no. 11, pp. 1954–1960, 2009.

[6.13] M. Lee, Y. Kim, Y. Oh, Y. Kim, S. Lee, H. Hong, and S. Kim, "Study on the cavitation erosion behavior of hardfacing alloys for nuclear power industry," *Wear*, vol. 255, no. 1–6, pp. 157–161, 2003.

[6.14] L. Benea, P. Ponthiaux, F. Wenger, J. Galland, D. Hertz, and J. Y. Malo, "Tribocorrosion of stellite 6 in sulphuric acid medium: electrochemical behaviour and wear," *Wear*, vol. 256, no. 9–10, pp. 948–953, 2004.

[6.15] H. So, C. T. Chen, and Y. A. Chen, "Wear behaviours of laser-clad stellite alloy 6," *Wear*, vol. 192, pp. 78–84, 1996.

[6.16] R. Singh, D. Kumar, S. K. Mishra, and S. K. Tiwari, "Laser cladding of Stellite 6 on stainless steel to enhance solid particle erosion and cavitation resistance," *Surf. Coatings Technol.*, vol. 251, pp. 87–97, 2014.

[6.17] J. Shin, J. Doh, J.-K. Yoon, D. Lee, and J. Kim, "Effect of Mo on the microstructure and wear resistance of cobalt-base Stellite hardfacing alloys.pdf," *Surf. Coat. Technol.*, vol. 166, pp. 117–126, 2003.

[6.18] S. A. Romo, J. F. Santa, J. E. Giraldo, and A. Toro, "Cavitation and high-velocity slurry erosion resistance of welded Stellite 6 alloy," *Tribol. Int.*, vol. 47, pp. 16–24, 2012.

[6.19] M. Jones and R. J. Llewellyn, "Assessing the Erosion Corrosion Properties of Materials for Slurry transportation and processing in the oil sands industry," in: *NACE Int. Corros. Conf. Expo*, 2007.

[6.20] J. R. Davis, *Surface Hardening of Steels: Understanding the basics,* ASM

International, 2002.

[6.21] B. Podgornik, J. Vižintin, and V. Leskovšek, “Wear properties of induction hardened, conventional plasma nitrided and pulse plasma nitrided AISI 4140 steel in dry sliding conditions,” *Wear*, vol. 232, no. 2, pp. 231–242, 1999.

[6.22] B. Podgornik, F. Majdic, V. Leskovsek, and J. Vizintin, “Improving tribological properties of tool steels through combination of deep-cryogenic treatment and plasma nitriding,” *Wear*, vol. 288, pp. 88–93, 2012.

[6.23] G. Karafyllias, F. Brownlie, L. Giourntas, T. Hodgkiess, A. M. Galloway, and A. Pearson, “Corrosive wear behaviour of various nitriding treatments on a low alloy steel,” in *TurkeyTrib’15*, 2015.

[6.24] B. S. Mann and V. Arya, “Abrasive and erosive wear characteristics of plasma nitriding and HVOF coatings: Their application in hydro turbines,” *Wear*, vol. 249, no. 5–6, pp. 354–360, 2001.

[6.25] B. S. Mann and V. Arya, “An experimental study to corelate water jet impingement erosion resistance and properties of metallic materials and coatings,” *Wear*, vol. 253, pp. 650–661, 2002.

[6.26] J. Chen, X. Y. Li, T. Bell, and H. Dong, “Improving the wear properties of Stellite 21 alloy by plasma surface alloying with carbon and nitrogen,” *Wear*, vol. 264, no. 3–4, pp. 157–165, 2008.

[6.27] J. Lutz and S. Mandl, “Reduced tribocorrosion of CoCr alloys in simulated body fluid after nitrogen insertion,” *Surf. Coatings Technol.*, vol. 204, no. 18–19, pp. 3043–3046, 2010.

[6.28] J. Lutz, C. Díaz, J. A. García, C. Blawert, and S. Mändl, “Corrosion behaviour of medical CoCr alloy after nitrogen plasma immersion ion implantation,” *Surf. Coatings Technol.*, vol. 205, no. 8–9, pp. 3043–3049, 2011.

[6.29] ISO 13503: Petroleum and natural gas industries — Completion fluids and materials Part II: Measurement of properties of proppants used in hydraulic fracturing and

gravel-packing operations, 2006.

[6.30] American Petroleum Institute, "API RP 19C.", 2014.

[6.31] L. Giourntas, T. Hodgkiess, and A. M. Galloway, "Comparative study of erosion–corrosion performance on a range of stainless steels," *Wear*, vol. 332–333, pp. 1051–1058, 2015.

[6.32] W. S. Li, Z. P. Wang, Y. Lu, and L. H. Yuan, "Corrosion Wear Behavior of Al-Bronzes in 3.5% NaCl Solution," *J. Mater. Eng. Perform.*, vol. 15, no. 1, pp. 102–110, 2006.

[6.33] T. J. Harvey, J. A. Wharton, and R. J. K. Wood, "Development of synergy model for erosion–corrosion of carbon steel in a slurry pot," *Tribology*, vol. 1, no. 1, pp. 33–47, 2007.

[6.34] R. J. K. Wood, "Erosion-corrosion interactions and their effect on marine and offshore materials," *Wear*, vol. 261, no. 9, pp. 1012–1023, 2006.

[6.35] K. S. Tan, J. A. Wharton, and R. J. K. Wood, "Solid particle erosion-corrosion behaviour of a novel HVOF nickel aluminium bronze coating for marine applications - Correlation between mass loss and electrochemical measurements," *Wear*, vol. 258, no. 1–4, pp. 629–640, 2005.

[6.36] A. Pasha, H. M. Ghasemi, and J. Neshati, "Synergistic Erosion–Corrosion Behavior of X-65 Carbon Steel at Various Impingement Angles," *J. Tribol.*, vol. 139, no. 1, p. 11105, 2016.

[6.37] J. Basumatary, M. Nie, and R. J. K. Wood, "The Synergistic Effects of Cavitation Erosion–Corrosion in Ship Propeller Materials," *J. Bio- Tribo-Corrosion*, vol. 1, no. 2, pp. 1–12, 2015.

[6.38] R. J. K. Wood and S. P. Hutton, "The synergistic effect of erosion and corrosion: published results," *Wear*, vol. 140, pp. 387–394, 1990.

[6.39] R. J. K. Wood, "Tribo-corrosion of coatings: a review," *J. Phys. D. Appl. Phys.*, vol. 40, no. 18, pp. 5502–5521, 2007.

Chapter 7

Alternative materials and manufacturing options for hydraulic fracturing pump components – additive manufactured alloys

7.1 Introduction

Corrosion and erosion-corrosion damage has a major effect on the life expectancy of hydraulic fracturing pump equipment. One option to increase the life expectancy of pump equipment is to use materials with increased corrosion and wear resistance. Another option is to restore damaged components with repair techniques such as welding and additive manufacturing. Therefore, corrosion and wear resistant alternative materials for both of these options are highly sought after.

Additive manufacturing (AM) is defined as the process of making 3D objects from 3D model data through the addition of layers-upon-layers of material (plastic, metal, etc.). AM is an attractive manufacturing option for pump components due to shorter lead times, parts can be built as a single unit and it could be used as a repair technique for damaged parts. The AM process also offers the possibility in developing functionally graded materials which are optimised for corrosion and wear resistance.

Four additively manufactured alloys (UNS S31600, UNS S15500, UNS R56400 (Ti-based) and UNS N07718 (Ni-based)) were produced by a Powder Bed Fusion (PBF) process. In this study, these materials were compared with conventionally manufactured counterparts of the same material grades. The materials were assessed in terms of microstructure, hardness, corrosion, erosion-corrosion and repetitive impact resistance using techniques described in Chapter 3. This study aims to understand the material properties associated with the AM process and identify the impact of the manufacturing process on performance for the tested materials. The study will also consider the differences in material performance between stainless steels and more corrosion resistance materials such as Inconel and titanium alloys.

7.2 Literature review

7.2.1 Overview of additive manufacturing process

The additive manufacturing process has been developed over several decades in order to produce metal, ceramic and polymer parts via a variety of additive processes [7.1]. The main difference between additive manufacturing techniques and conventional techniques (such as milling, turning, cutting, boring, etc.) is that conventional techniques are a subtractive process, i.e. material is removed in order to make the part, whereas, additive

processes selectively deposits material so that the shape of the final part is produced during the deposition of the material [7.2].

The additive manufacturing technique enables new developments for manufacturing which includes the production of highly complex shapes, rapid production which significantly reduces component lead time and allows for selectively tailoring material composition and properties throughout a component [7.3]. For industrial pump components, metal additive manufacturing (MAM) presents a variety of advantageous features compared to conventional manufacturing processes.

The MAM process begins with a 3D model of the desired component produced in a Computer Aided Design (CAD) package. The 3D model is then sectioned into a series of "2D" layers (20-1000μm in thickness) which are then input into the MAM system [7.4]. Each layer is deposited by melting a powder feedstock by a high power energy source which fuses the deposited layer together and also fuses the deposited layer into previously built layers. The successive addition of layers eventually produces a full 3D component.

The build plane of MAM 3D components is defined as the XY plane in which the layers are being deposited. The build direction is referred to as the Z plane in which layers are being built upon, this plane is perpendicular to the XY plane.

MAM systems contain a build plate on which components are manufactured. The plate is occasionally heated for some additive processes to improve the thermodynamic characteristics of the process. The build plate is positioned within an airtight vacuum chamber which commonly contains small amounts of inert gas which improve the additive process thermodynamics, eliminates material oxidation and reduces build-up of electrical charge [7.1]. Within the build chamber, a power source, either a laser (LAM) or an electron beam (EBAM), melts the material feedstock. Once a layer has been built, the build plate is lowered or the power source is raised to the equivalent thickness of the next layer [7.2].

The feedstock form and the way it is introduced into the MAM process varies significantly between each system. The two common forms of feedstock are powder and wire. The wire is introduced at a controlled rate adjacent to the power source. For the powder feedstock method, there are two predominant processes; powder feed (PF) and powder bed (PB)

[7.4]. For the PF system, the feedstock is introduced directly beneath the power source. For PB systems (Figure 7.1), a layer of powder is "raked" across the entire surface of the build plate before the power source melts the feedstock material.

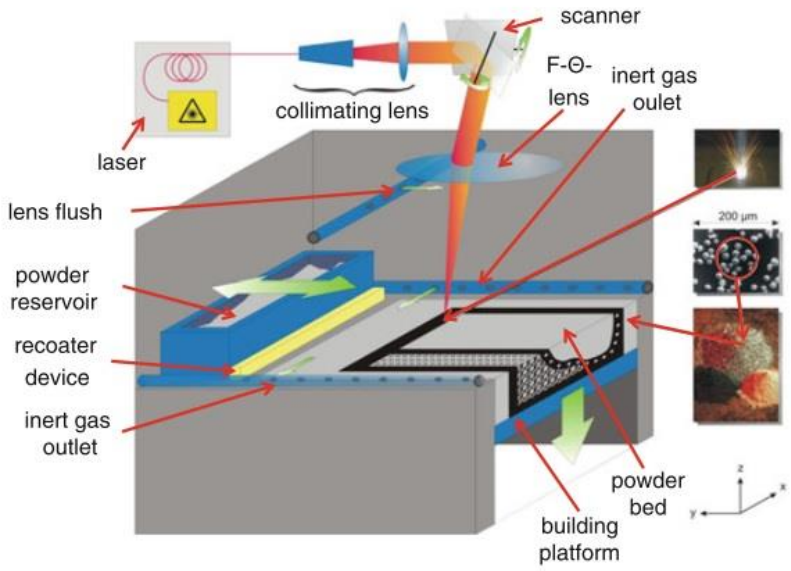

Figure 7.1: *Schematic of powder bed laser additive manufacturing machine [7.1]*

Currently the cost associated with MAM is significantly greater when compared to traditional manufacturing techniques such as casting and wrought processes. The higher costs are mainly associated with high feedstock production costs and slow manufacturing rates [7.2]. The primary objective for additive manufacturing process is to produce parts which, at a minimum, exhibit material properties which are equivalent to conventional manufacturing techniques. The main properties which are required to be achieved are density, strength, Young's modulus, hardness, residual stresses, durability, shape accuracy and surface finish.

Density & Porosity

A vital feature of the additive manufacturing process is to achieve the complete density of the part, which conversely implies that the part will contain no porosity. Porosity can be present in an additively manufactured part through two mechanisms. Pores can form due to gas evolution from the vaporised feedstock during solidification which becomes entrapped within the part. These pores are typically spherical in shape and are smaller than 100µm [7.5]. The second process results in irregular shaped pores which are formed when

molten material does not completely fill a volume which is caused by rapid solidification or the presence of un-melted feedstock [7.4].

Porosity can act as stress concentration and crack initiation sites which severely reduce the mechanical properties of a part [7.2]. Significant progress has been made to ensure the quality of the MAM process and that it can achieve near-dense parts. Porosity is eliminated through the optimisation of process parameters as well as the quality and size of powder feedstock. Hot Isostatic Pressing (HIP) has demonstrated its capability of reducing the size and quantity of pores in MAM parts [7.6]. It has become industry norm to achieve MAM parts with a density of 99.9% which is equivalent to traditionally manufactured parts.

Shape accuracy and surface finish

Surface finish and geometric accuracy of parts are other concerns with the MAM process. Currently, all MAM systems require a 2D approximation of the final product as an input. The main issue arises from developing curved surfaces in the build direction as a single layer cannot incorporate contours at the edges of components. This results in a "staircase effect" (Figure 7.2) which is an engineering concern with current MAM processes [7.1]. Reducing the layer thickness can mitigate this issue slightly, however, this is limited to the availability and size of the powder feedstock. The thickness of the layer is also dictated by the surface roughness which is influenced by the adhesion of un-melted powders to the melted surface.

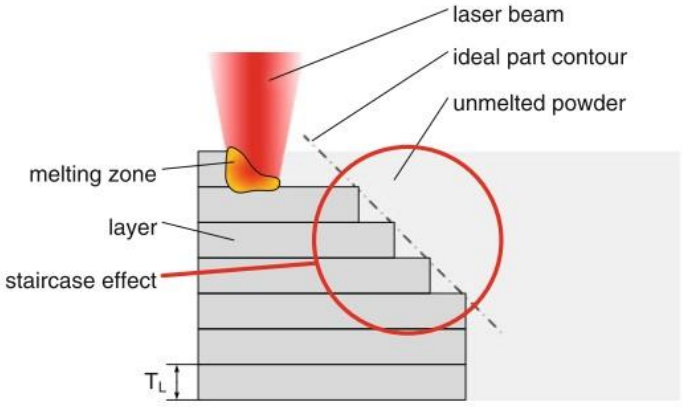

Figure 7.2: *Staircase effect from MAM processes [7.1]*

Inaccuracies in shape geometry of a MAM part can be a result of relaxation of thermally induced residual stresses. These residual stresses are commonly introduced where there are differences in thermal expansion of the MAM material [7.7]. Internal voids, particularly overhangs, are susceptible to sagging which results the melted materials flowing downwards [7.1]. It is also common for a support structure to be designed into the process which minimises component warping. The geometric inaccuracies recur often and so strategies' to compensate for such inaccuracies can be implemented to the MAM process [7.3].

Mechanical properties

The mechanical properties of the MAM processed parts must be consistent and at a minimum equivalent to that of the mechanical properties achieved by traditional manufacturing processes. The two process features which dictate the mechanical properties are the directionality of the build and the complex thermal cycles which the MAM part undergoes during deposition.

During the MAM process, the material experiences a complex series of melting/solidification and heating/cooling stages. The periodic changes in temperature are caused by the concentrated heat input from the energy source. The energy source is concentrated to a diameter of 100-500μm with a power rating of 200-400W [7.1]. The cooling rate of the material can be extremely high, in some cases it can reach 10^3-10^4 K/s [7.2].

The cyclic heating and cooling of the AM material often lead to highly refined microstructures [7.1]. This tends to correspond to an enhanced hardness and mechanical strength, however, this effect also results in a reduction in toughness and ductility compared to conventionally manufactured materials [7.8]. The strategy used for scanning is the crucial variable to the heat flow which a part will undergo when it is being built; therefore, it is one of the main processing parameters.

The thermodynamics of the additive process is also affected by [7.3]:

- The form and absorptivity of the feedstock.
- The thermal conductivity of the feedstock.

- The composition of the feedstock powder.
- The build surroundings such as build chamber, atmosphere and build plate.
- The melt-pool characteristics.

The directionality of the build is another noticeable feature of the MAM process as parts are often orthotropic [7.1]. The direction of the heat flow determines the local microstructure and is predominately in the negative build direction (located away from the heat source). This can lead to specific microstructural features in the build plane and a columnar microstructure in the build direction [7.2]. Another factor which may affect mechanical properties of MAM alloys is residual stress.

7.2.2 Material characteristics of additively manufactured alloys

Currently, research conducted on additively manufactured alloys has primarily focused on their inherent microstructure, mechanical properties and corrosion resistance. No research studies appear to have been conducted assessing the corrosive wear resistance of additively manufactured materials. A literature review of material characteristics of the studied MAM alloys (UNS S31600, UNS S15500, UNS R56400 and UNS N07718) will be discussed in this section.

Austenitic stainless steel - UNS S31600/UNS S31603

Research studies conducted on AM UNS S31603 have reported two main microstructural features as a result of the MAM process. Elongated grains have been observed in the build direction whereas, in the build plane, equiaxed grain cells of 1μm diameter have also been detected [7.9–7.13]. It is postulated that these features develop from the directionality of the heat source and the high cooling rates associated with the MAM process. Mechanical properties (Young's modulus, yield strength and tensile strength) were found to be similar and in some cases greater than that of conventionally manufactured UNS S31603. However, it was also noted that the AM UNS S31603 alloys were anisotropic as the mechanical properties were dependent upon build directionality [7.10, 7.14, 7.15]. Some studies have also observed segregation of elements such as molybdenum and chromium to grain boundaries during the MAM process [7.9–7.12]. This segregation phenomenon may cause a reduction in the corrosion resistance of the MAM material due to localised weakening of the passive film [7.9, 7.10].

Martensitic precipitation hardened stainless steel - UNS S15500

A limited amount of work has been conducted on assessing material properties of AM UNS S15500. The microstructure of the AM UNS S15500 has been reported as martensitic with some retained austenite located between martensitic lathes. Well defined melt pool boundaries have also been observed [7.16]. The tensile properties for horizontally and vertically built test samples were found to be equivalent to or greater than that of conventionally manufactured UNS S15500 [7.16]. The horizontally built samples exhibited better tensile properties than vertically built samples. This was attributed to fabrication defects and their orientation relative to the applied load. In vertically built samples, the applied load is perpendicular to the tensile load axis, whereas, for a horizontally built sample the tensile loads are parallel to the tensile load axis. Therefore, in vertically built samples the defect expands at smaller stress levels. Fatigue testing of the AM UNS S15500 was found to have an endurance limit 20% less than that of conventionally manufactured UNS S15500 [7.16, 7.17]. This was mainly attributed to the surface finish of the samples as the roughness of the conventionally manufactured (0.2μm Ra) was significantly smoother than that of AM samples (3μm Ra).

Alpha-beta phase titanium alloy - UNS R56400

There has been a significant amount of research in characterising AM UNS R56400 due to high cost, issues with conventional forming processes and its wide use in the medical industry for prosthetic implants [7.4]. The microstructure of the AM UNS R56400 has widely been reported as exhibiting acicular α'-martensite with fine β phase dispersed throughout the matrix [7.18–7.20]. The acicular microstructure predominantly occurs due to the high thermal gradients associated with the MAM process which inhibits grain nucleation and growth. The pitting resistance of AM UNS R56400 has been widely reported to be equivalent to or better than wrought alloys which is indicative of a stable passive film [7.18, 7.21, 7.22]. Dai et al. observed a difference in corrosion resistance between different planes of AM UNS R56400 [7.19]. The inferior corrosion resistance of the XZ plane (build direction) was attributed to the presence of more α'-martensite and the smaller presence of β phase in the microstructure of the XZ plane when compared to the XY plane.

Nickel-based alloy - UNS N07718

Studies of AM UNS N07718 have been limited to assessing its microstructure and mechanical properties. The studies have reported columnar grains and directional dendrite growth in as-deposited parts [7.23–7.28]. The rapid cooling rates associated with the MAM process are too great to permit the formation of precipitates [7.25, 7.26]. Therefore, AM UNS N07718 parts are often heat treated to improve its mechanical properties [7.23, 7.24, 7.26]. The ageing heat treatment of the alloy allows precipitation of γ' and γ'' and δ phases at grain boundaries and also throughout the grains [7.23–7.25, 7.27, 7.28]. After the ageing process the hardness and strength of the AM UNS N07718 have been reported to be as comparable and, in some instances, even superior than that of conventionally manufactured UNS N07718 [7.23, 7.25, 7.26, 7.28]. Elemental segregation of niobium (niobium-rich region which has not formed precipitates) has also been observed which will likely be detrimental to the corrosion resistance of the AM UNS N07718 [7.25, 7.27].

7.2.3 Corrosive wear studies of conventionally produced Inconel and titanium alloys

This section will be an overview of corrosive wear studies of Inconel and titanium alloys. A comprehensive literature study of stainless steels under corrosive wear conditions detailing the main observations has been discussed in Chapter 4.2.2. Therefore, corrosive wear studies comparing only stainless steels will not be discussed further in this section to avoid repetition.

There have been limited studies assessing the corrosive wear behaviour of Ni-Cr alloy, UNS N07718. Ramesh et al. assessed a plasma sprayed UNS N07718 coating on a mild steel substrate (grade undefined) in a slurry erosion testing machine with a 3.5%NaCl aqueous solution with silica sand particles [7.29]. The UNS N07718 coated samples exhibited significantly greater corrosive wear resistance than uncoated samples. It was also reported that a thicker coating (250μm) exhibited marginally better corrosive wear resistance than a thinner coating (200μm). The same authors observed similar trends when an aluminium alloy (UNS A96061) was used as the coating substrate [7.30].

Zhou and Bahadur assessed the erosion resistance (dry conditions) of a precipitation hardened Ti-6Al-4V alloy, UNS R56400, using various sizes of silicon carbide particles and impingement velocities [7.31]. The study observed that the maximum wear rate was

obtained with a particle size of 40µm and the erosion rate was proportional to the squared velocity.

Another study by the same authors evaluated the erosion-corrosion behaviour of UNS R56400 under elevated temperature conditions (200°C - 800°C) [7.32]. The erosion rate was observed to increase with increasing temperature due to increased oxidation at elevated temperatures. The main erosion mechanism was observed to be ploughing which lead to a pile-up of material around the deformed groove. This mechanism caused severe plastic deformation and generated microcracks within the heavily deformed material which resulted in material removal.

Yerramareddy and Bahadur studied the erosion behaviour (dry conditions) of UNS R56400 in different heat treated conditions [7.33]. Erosion rates were observed to increase with precipitation due to the aging process, however, overaging of the UNS R56400 was found to improve its erosion resistance due to the agglomeration of precipitates. The erosion mechanisms for the UNS R56400 was observed to be cutting or ploughing (dependent upon impingement angle) which led to flake formation and eventually separation of the flake from the material surface.

Mochizuki et al. evaluated the cavitation erosion resistance of three commercially pure titanium grades (TB270H (130HV), TB340H (156HV) and TB480H (180HV)) and a UNS R56400 alloy [7.34]. The UNS R56400 alloy exhibited significantly greater resistance to cavitation erosion than the commercially pure titanium grades. The erosion mechanism observed from the cavitation erosion tests were transgranular and intergranular cracks which were formed due to plastic deformation of grains. As the UNS R56400 exhibited the smallest grain size this resulted in the greatest resistance to cavitation erosion.

Neville and McDougall studied the erosion-corrosion and cavitation erosion of a grade 2 CP-Ti, UNS R5111, UNS R56400 (ELI – Extra Low Interstitial, with low oxygen content) and UNS R56400 (ELI/Ru – Ru was added for improved corrosion resistance) [7.35]. The CP-Ti performed poorest in both erosion-corrosion and cavitation conditions. In erosion-corrosion conditions, the other titanium alloys performed similarly, however, under cavitation-corrosion conditions the UNS R56400 (ELI/Ru) performed significantly better

than the other alloys as the test duration increased. This was attributed to the improved corrosion resistance of the UNS R56400 (ELI/Ru) and the greater proportion of corrosion damage in cavitation-corrosion conditions compared to erosion-corrosion conditions.

A study by Emiliani and Brown assessed two microstructural forms of UNS R56400 (equiaxed α + β and basketweave α + β) under erosion conditions (dry environment) at normal incidence with silica sand particles at a velocity of 61m/s [7.36]. The basketweave microstructure exhibited significantly greater erosion resistance than the equiaxed microstructure. This was attributed to the higher ductility of the equiaxed microstructure.

Chen et al. assessed the erosion-corrosion resistance of UNS R56400, UNS S31600 and UNS N05500 (Ni-Cu alloy – Monel K500) using a pin-on-disk test machine with an aluminium oxide pin in a 3.5%NaCl aqueous solution [7.37]. The UNS S31600 exhibited the greatest material loss compared to the other alloys. This was attributed to severe plastic deformation occurring on UNS S31600 due to its lower yield strength compared to the other tested alloys.

This literature review has demonstrated that there have been several studies assessing the microstructure and mechanical properties of AM alloys, however, there is limited work assessing their durability under corrosive wear conditions. The reported elemental segregation of elements such as molybdenum and chromium may have a detrimental effect on the corrosion resistance of the AM alloys. It is clear that a significant amount of research into the corrosive wear resistance of AM alloys is required before they can be selected as appropriate materials for hydraulic fracturing pump components, hence, the requirement of the present study.

7.3 Experimental objectives

The detailed literature review described in Chapters 7.2.2 and 7.2.3, identified a lack of studies assessing the corrosive wear resistance of MAM materials and also a limited evaluation of the erosion-corrosion behaviour of Inconel and titanium alloys. The main objective of this experimental work was to compare the erosion-corrosion and repetitive impact wear behaviour of MAM and conventionally manufactured materials (of the same grade as the MAM alloys). A further outcome of the study will be the comparison between

an austenitic stainless steel, a precipitation hardened stainless steel, an Inconel alloy and a titanium alloy under erosion-corrosion and repetitive impact wear conditions. The assessment was conducted using a closed loop submerged jet impingement rig and a repetitive impact testing machine which are both described earlier in Chapter 3. The enhanced volumetric analysis technique (Chapter 3.5.3) was utilised on erosion-corrosion test samples to quantify the impingement erosion, sliding abrasion, corrosion and synergy material degradation mechanisms. The final outcome of this study will assist in identifying whether MAM is a viable manufacturing and/or repair method for hydraulic fracturing pump equipment.

7.4 Materials and methods

Four different alloys manufactured from two different manufacturing methods were assessed in this study. The specified alloys chosen were in line with the interests of the industrial collaborator as they are currently used or are potential material candidates for hydraulic fracturing pump components. The corrosive wear behaviour of a conventionally wrought method (rolled bar) was compared with a MAM process (powder bed fusion process). The following materials were assessed:

- UNS S31600 – austenitic stainless steel
- UNS S15500 – precipitation hardened martensitic stainless steel
- UNS R56400 – alpha-beta grade 5 titanium alloy
- UNS N07718 – precipitation hardened nickel-chromium alloy

Table 7.1 lists the nominal density (obtained from supplier) of the alloys along with the measured macro-hardness values of the test surfaces for both the wrought and additive manufactured materials. The nominal chemical compositions (obtained from supplier) along with a semi-quantitative EDS analysis of the principal alloying elements for both wrought and additive manufactured materials are given in Tables 7.2 – 7.5. The chemical compositions of the wrought and additive manufactured materials were found to be generally similar to the nominal chemical compositions.

Table 7.1: *Nominal densities (obtained from supplier) and measured macro-hardness of the four tested alloys (wrought and additive manufactured)*

Material	Density (g/cm³)	Hardness (HV) - Wrought	Hardness (HV) – AM
UNS S31600	8.0	170	200
UNS S15500	7.8	360	430
UNS R56400	4.5	320	350
UNS N07718	8.3	390	400

Table 7.2: *Nominal chemical composition (obtained from supplier) and EDS analysis for wrought and additive manufactured UNS S31600*

Element	Si	Cr	Mn	Fe	Ni	Mo
Nominal	<0.75	16.0 – 18.0	<2.0	Bal	10.0 -14.0	2.0 – 3.0
Wrought	0.5	16.9	2.1	68.7	9.5	2.3
Additive manufactured	0.9	18.4	1.5	63.9	12.3	3.0

Table 7.3: *Nominal chemical composition (obtained from supplier) and EDS analysis for wrought and additive manufactured UNS S15500*

Element	Si	Cr	Mn	Fe	Ni	Mo
Nominal	<1.0	14.0 -15.5	<1.0	Bal	3.5 - 5.5	2.5 - 4.5
Wrought	0.5	14.6	1.2	71.6	5.5	6.7
Additive manufactured	0.8	14.9	0.0	74.6	3.8	5.8

Table 7.4: *Nominal chemical composition (obtained from supplier) and EDS analysis for wrought and additive manufactured UNS R56400*

Element	Al	Ti	V	Fe
Nominal	5.5 - 6.8	Bal	3.5 - 4.5	<0.25
Wrought	6.5	90.2	3.3	0
Additive manufactured	6.4	89.8	3.8	0

Table 7.5: *Nominal chemical composition (obtained from supplier) and EDS analysis for wrought and additive manufactured UNS N07718*

Element	Al	Ti	Cr	Fe	Ni
Nominal	0.2 – 0.8	0.7-1.2	17.0 – 21.0	Bal	50.0 – 55.0
Wrought	0.8	1.2	19.8	18.7	59.4
Additive manufactured	0.3	0.7	17.0	18.5	56.3

Figures 7.3 – 7.10 show the microstructures of the tested wrought and additive manufactured materials. The wrought UNS S31600 in Figure 7.3 shows an austenitic microstructure with equiaxed grains and δ-ferrite located at the grain boundaries. Bands of δ-ferrite are also present throughout the microstructure caused by the rolling process during the manufacture of the wrought bar. The AM UNS S31600 also exhibited an austenitic microstructure with delta ferrite grain boundaries, however, the grains were observed to be irregular in shape due to the MAM process as given in Figure 7.4. The laser tracks from the MAM process were also present, however, they were less defined due to the subsequent heat treatment process (given in Chapter 3.2.1). The AM UNS S31600 also exhibited a small amount of porosity.

The wrought and AM UNS S15500 (Figures 7.5 and 7.6 respectively) exhibited a martensitic microstructure with retained austenite. The AM UNS S15500 exhibited a refined microstructure due to the MAM process whereas, the wrought alloy demonstrated larger acicular grains.

A fully equiaxed α+β microstructure is observed in Figure 7.7 for the wrought UNS R56400. The microstructure is predominately α phase (light) with retained β phase (dark) at the grain boundaries. A significant amount of lamellar α phase was also evident in the β phase. The AM UNS R56400 (Figure 7.8) demonstrates acicular α' phase (martensitic structure) with intergranular β phase which was a result of the high cooling rates associated with the MAM process.

The microstructure of wrought UNS N07718 (Figure 7.9) displays a γ-austenite structure with white precipitates in relief (light particles). The AM UNS N07718 in Figure 7.10 exhibits

a γ-austenite microstructure and short needle-shaped precipitates caused by rapid solidification during the MAM process.

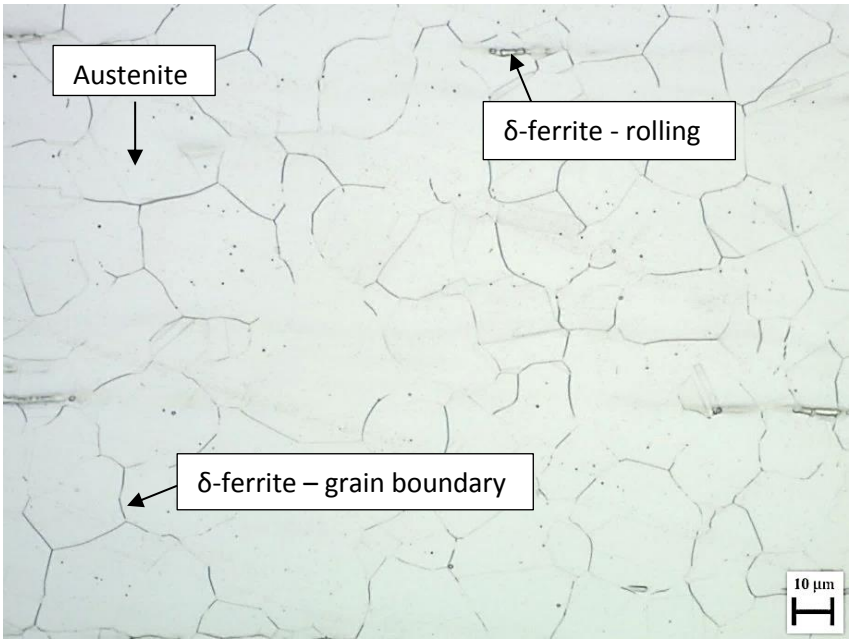

Figure 7.3: *UNS S31600 wrought microstructure*

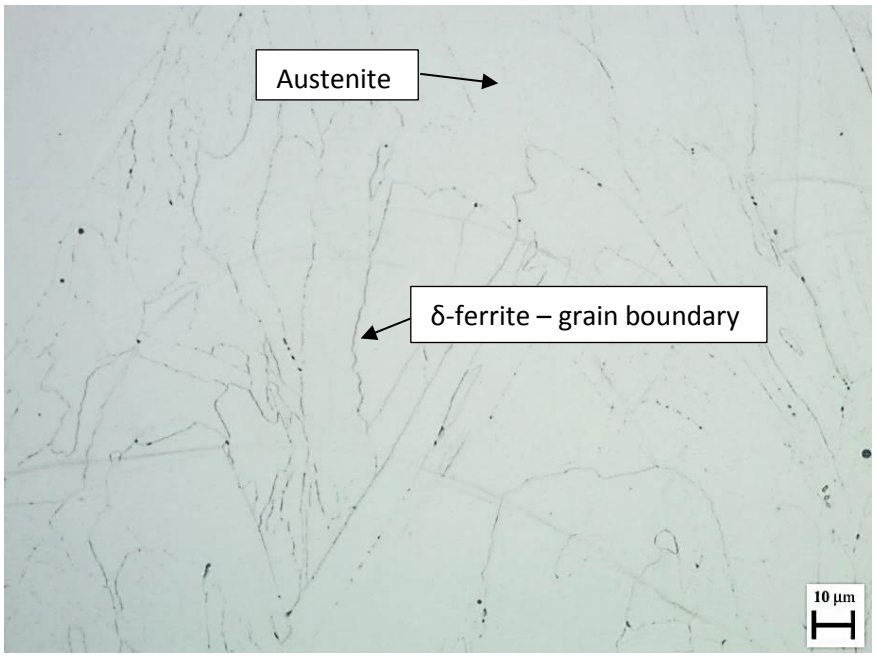

Figure 7.4: *UNS S31600 AM microstructure*

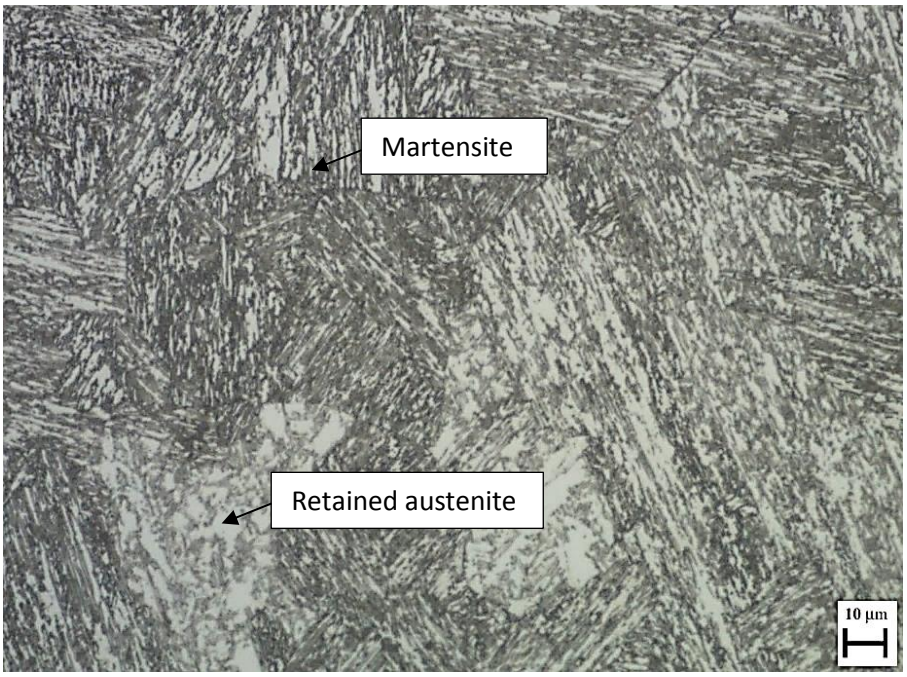

Figure 7.5: *UNS S15500 wrought microstructure*

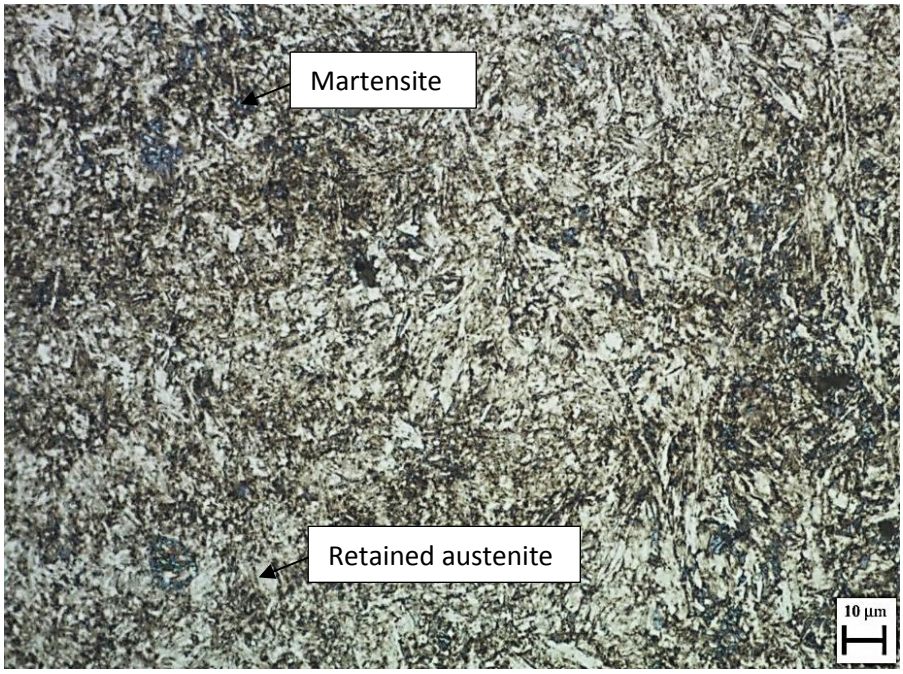

Figure 7.6: *UNS S15500 AM microstructure*

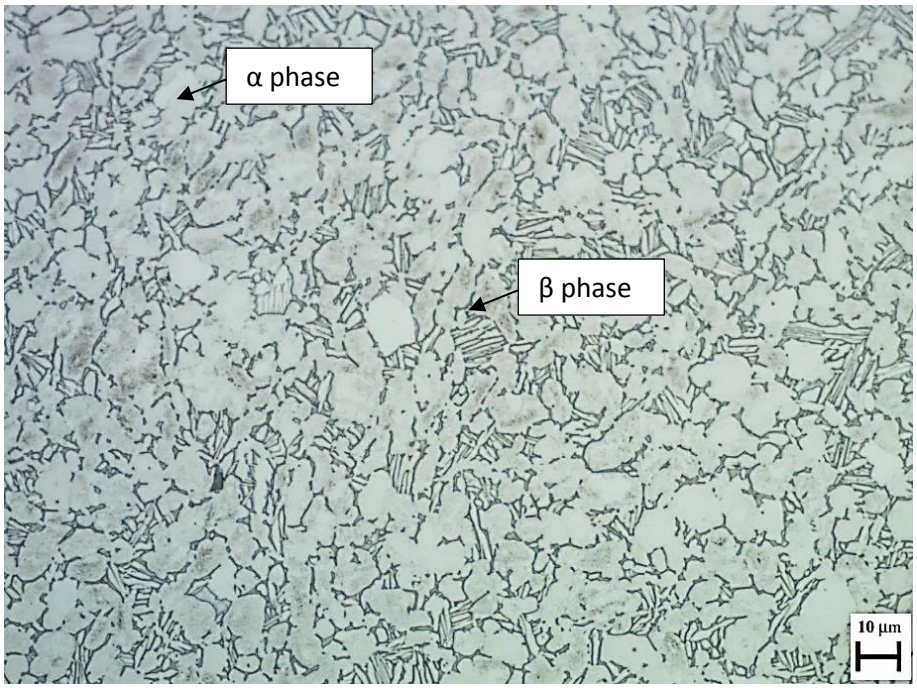

Figure 7.7: *UNS R56400 wrought microstructure*

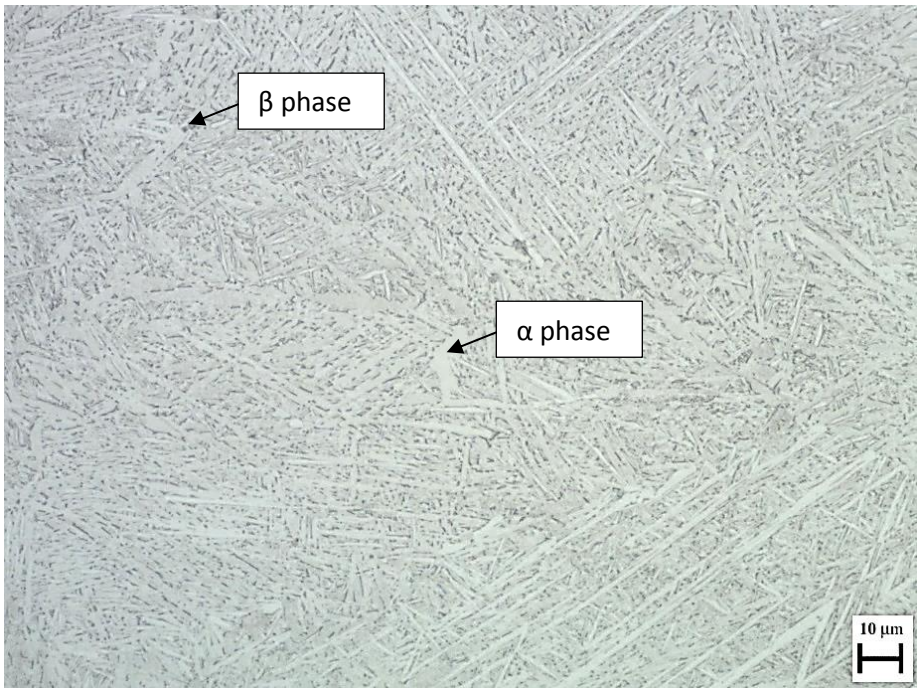

Figure 7.8: *UNS R56400 AM microstructure*

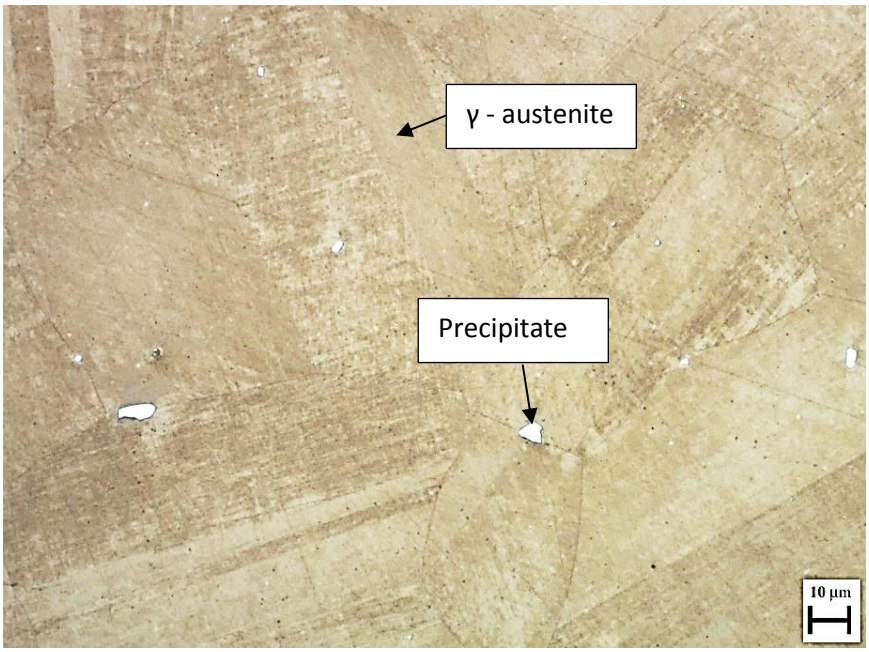

Figure 7.9: *UNS N07718 wrought microstructure*

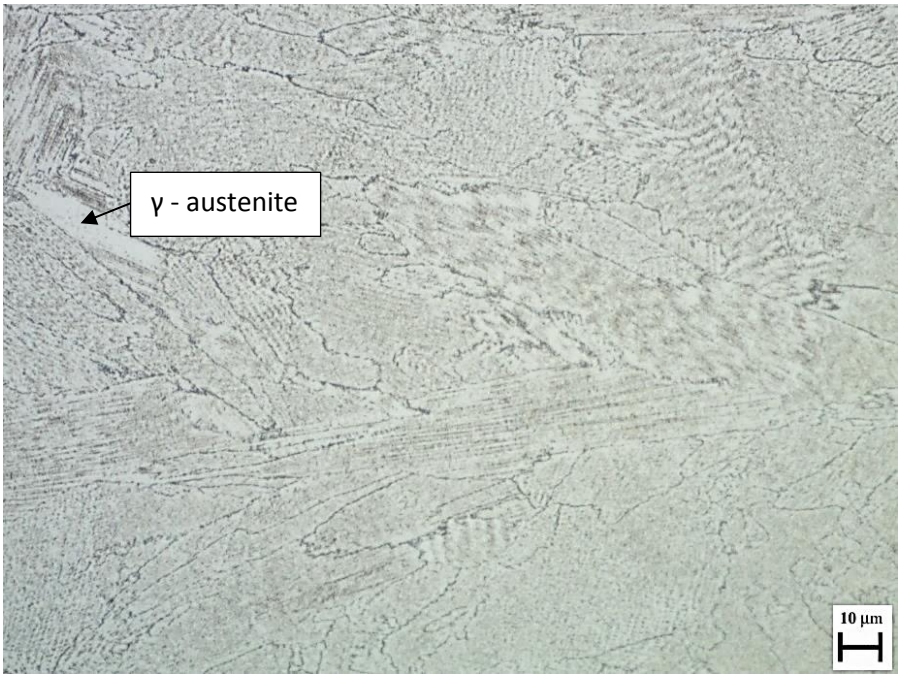

Figure 7.10: *UNS N07718 AM microstructure*

The erosion-corrosion testing was conducted in a closed loop submerged jet impingement rig described in Chapter 3.3.1. The test duration was one hour and the nozzle diameter was 4mm. The erosion-corrosion tests were conducted with a 3.5%NaCl aqueous solution with a

sand concentration of 0.5g/l. The temperature of the aqueous solution was 40±2°C and the velocity of the impinging jet was 18m/s. Cathodic protection was applied through the ICCP method described in Chapter 3.3.5 and potentiodynamic polarisation scans were conducted using the methodology described in Chapter 3.3.4.

7.5 Results

7.5.1 XRD analysis

The metallic phases present in the additive manufactured and wrought alloys were assessed by XRD analysis, set-up described in Chapter 3.2.4.2. Figures 7.11–7.14 show the XRD patterns for the additive manufactured and wrought alloys. Overall, the additive manufactured materials exhibited similar phases to the wrought alloys. The only observable difference occurred with the UNS S15500 AM alloy (Figure 7.12), which exhibits two austenite peaks (retained austenite) which are not identified with wrought UNS S15500. The XRD analysis suggests that the corrosive wear behaviour should be similar for both wrought and additive manufactured alloys.

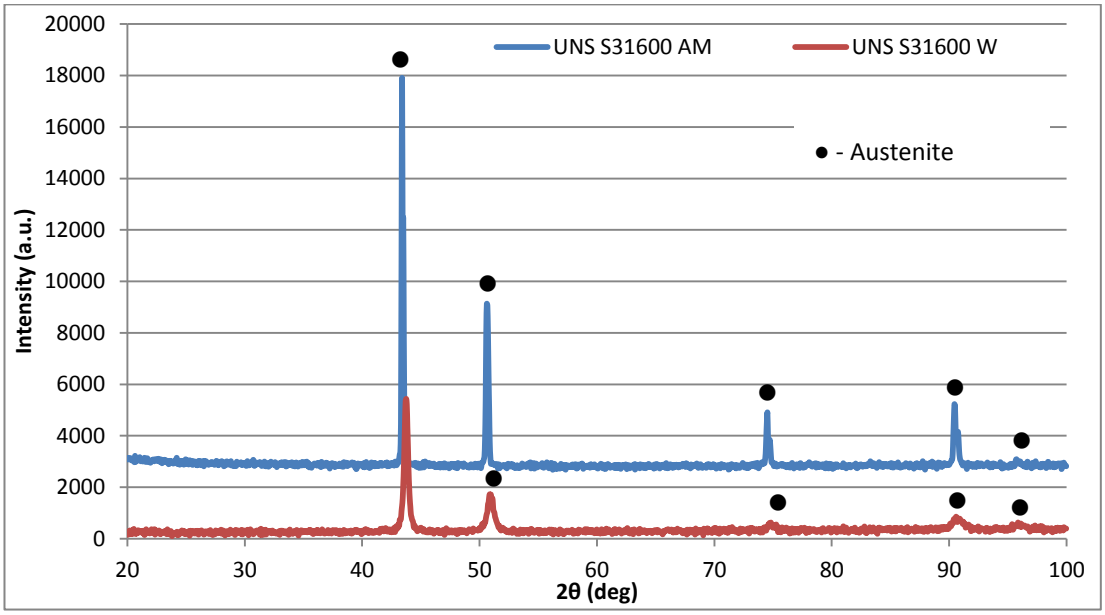

Figure 7.11: *XRD patterns for UNS S31600 AM and W*

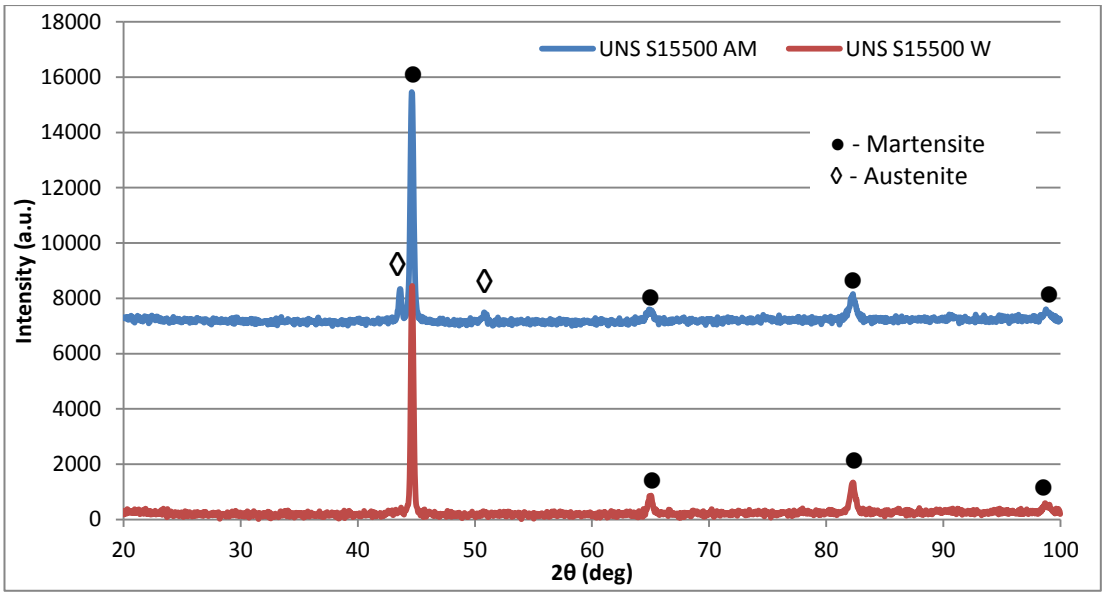

Figure 7.12: *XRD patterns for UNS S15500 AM and W*

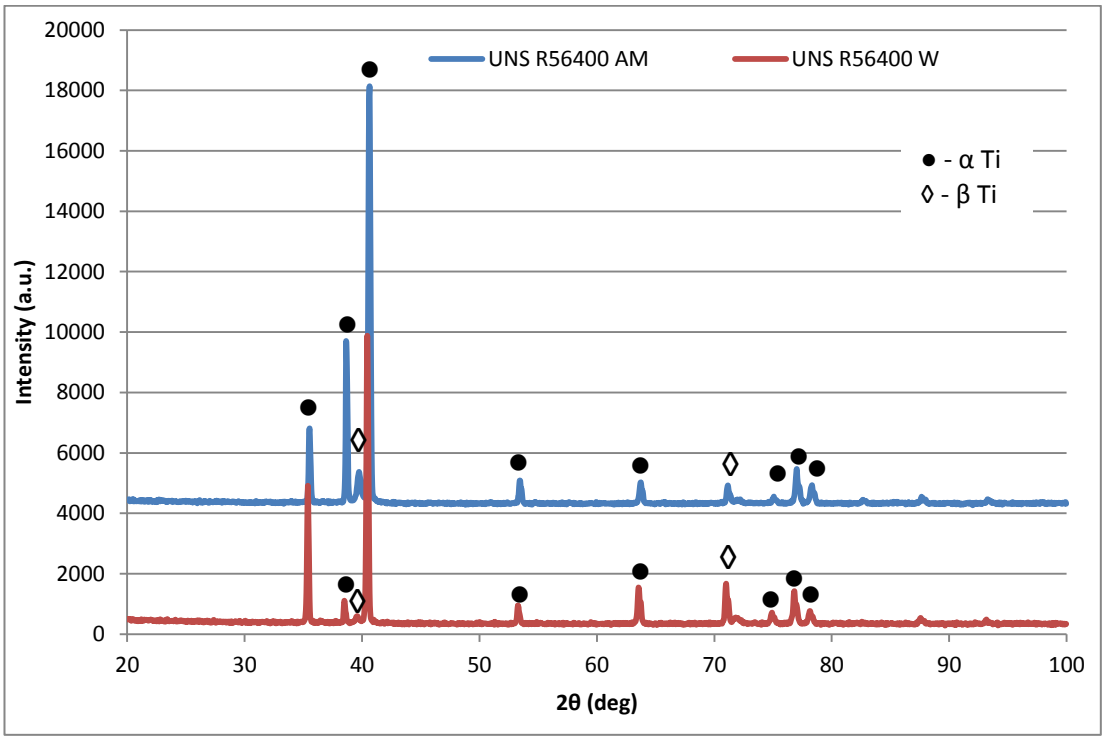

Figure 7.13: *XRD patterns for UNS R56400 AM and W*

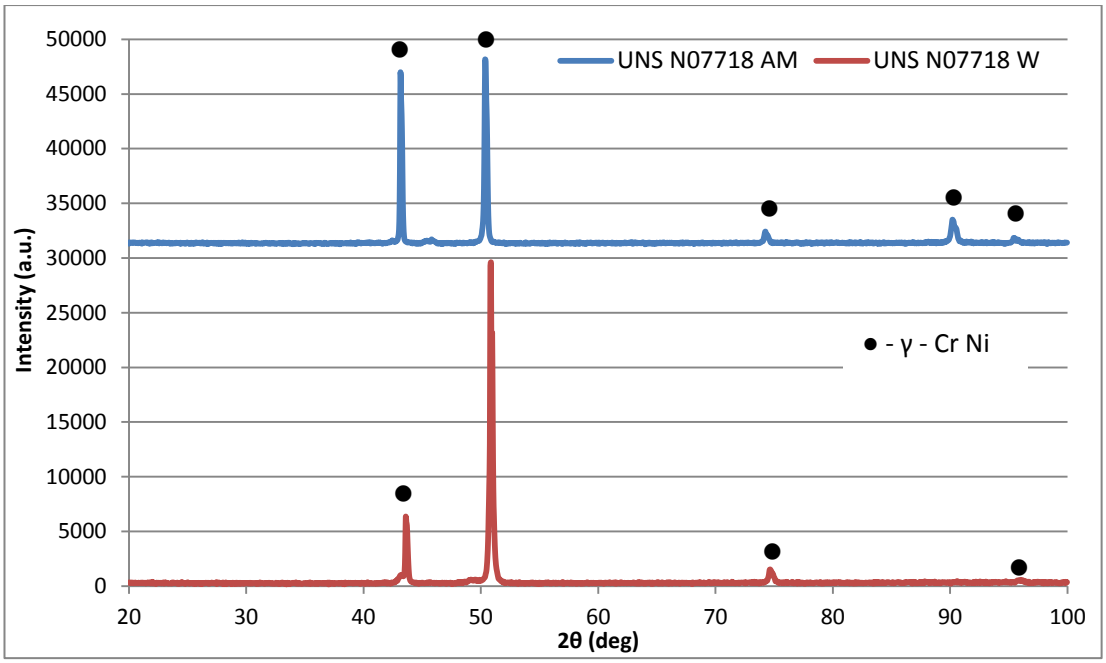

Figure 7.14: *XRD patterns for UNS N07718 AM and W*

7.5.2 Volume loss measurements

The average mass loss values were converted to total volume losses by using the nominal density values stated in Table 7.1. This allowed for a more accurate comparison between the test materials due to the significant differences in material densities. The total average volume losses for the test materials are given in Figure 7.15. A total of 4 replicates for each material was tested which is represented by the scatter band for each test material.

The results demonstrate that the AM materials exhibit similar performance to their wrought (W) counterparts under solid-liquid conditions. In terms of material performance, the UNS N07718 alloys (W and AM) demonstrate the greatest erosion-corrosion resistance under the test conditions. The application of ICCP resulted in a reduction in average volume loss for all test materials. Although, for some materials, the differences between FEC and ICCP conditions were of such small magnitude to be within the scatter bands (Figure 7.15).

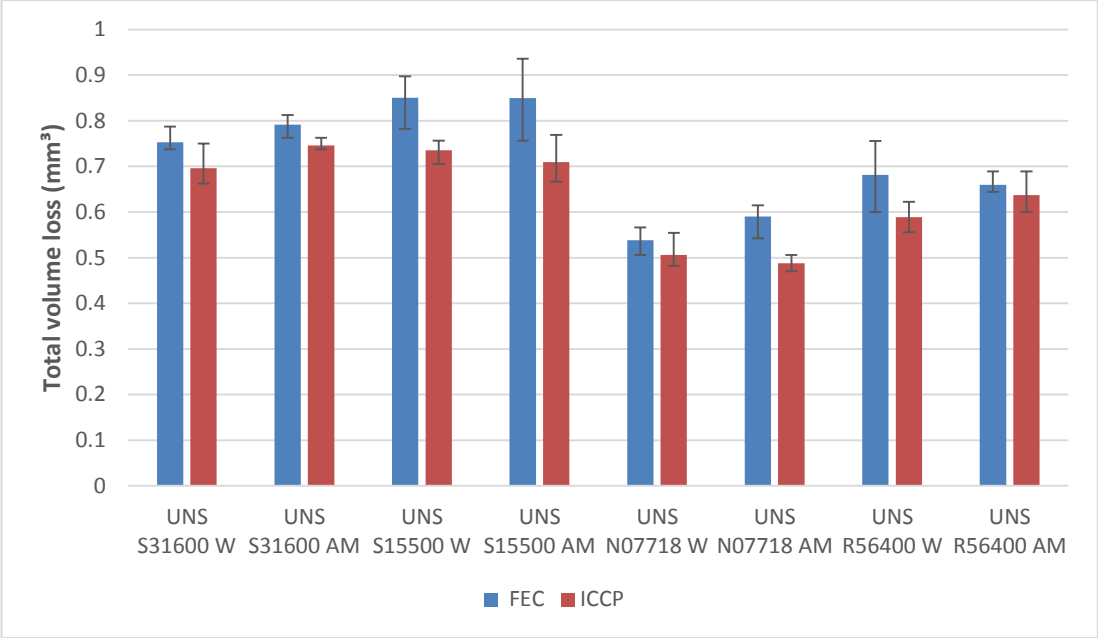

Figure 7.15: *Total volume losses for the test materials under solid-liquid impingement conditions*

7.5.3 Electrochemical monitoring

Figures 7.16 – 7.18 show the anodic and cathodic polarisations scans for the full specimens (38mm diameter) of each test material under static, flowing and solid-liquid conditions respectively. The electrode potentials are normalised for a simpler comparison between materials. In static and flowing conditions, the additively manufactured materials exhibit more passive behaviour than their wrought counterparts. However in static conditions, for the UNS S15500 AM, once above 150mV from E_{corr}, the alloy exhibits active behaviour as the passive film has broken down. In static and flowing conditions, most materials exhibit concentration polarisation caused by the reduction of oxygen available at the surface for cathodic reactions. Under solid-liquid conditions, all test materials exhibit higher corrosion current densities and associated de-passivation/re-passivation due to the breakdown and recovery of the passive film caused by impacting solid particles.

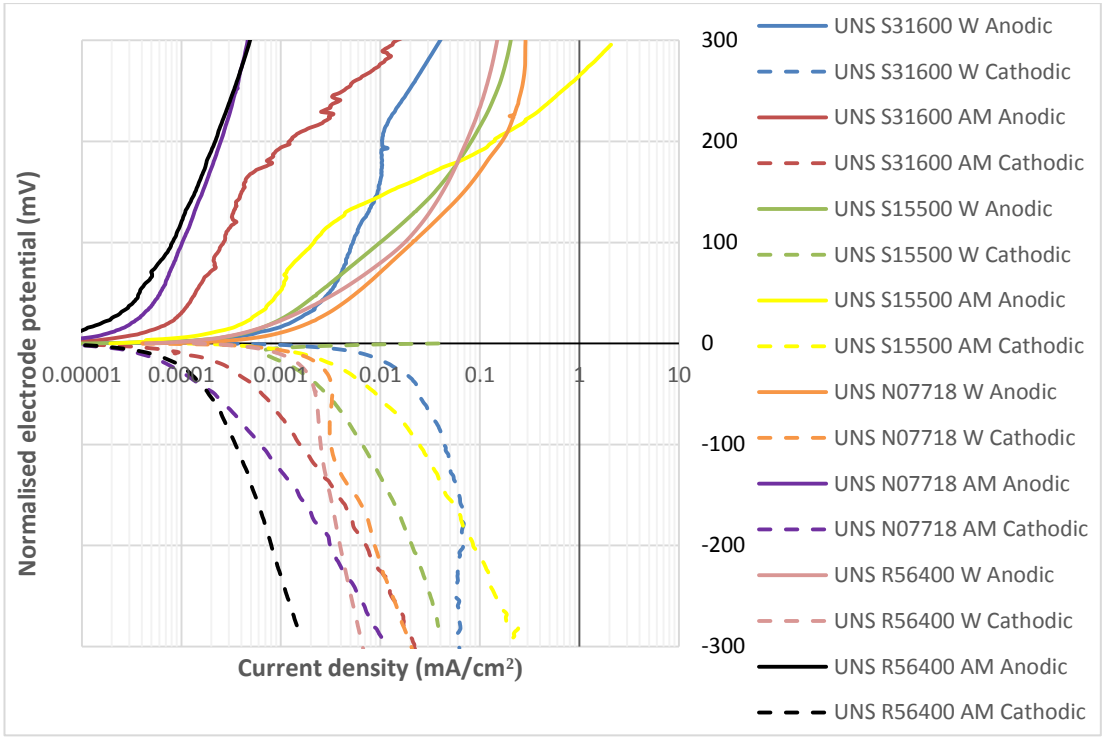

Figure 7.16: *Anodic and cathodic polarisation scans on the full specimen of all tested materials in static conditions*

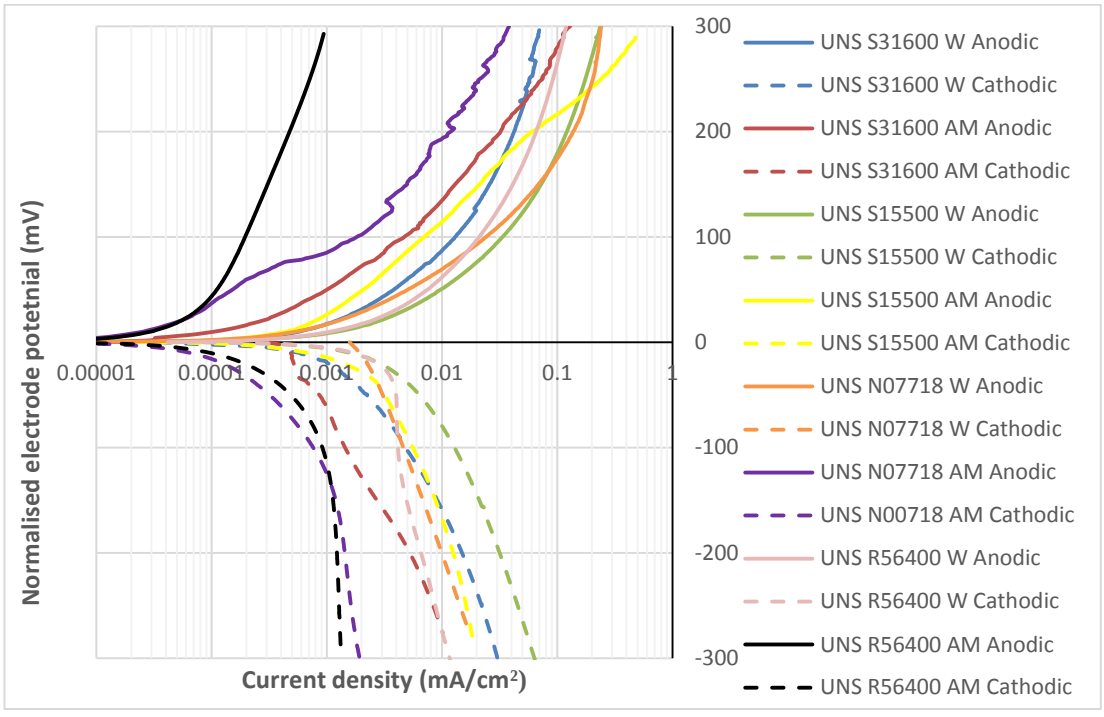

Figure 7.17: *Anodic and cathodic polarisation scans on the full specimen of all tested materials in flowing conditions*

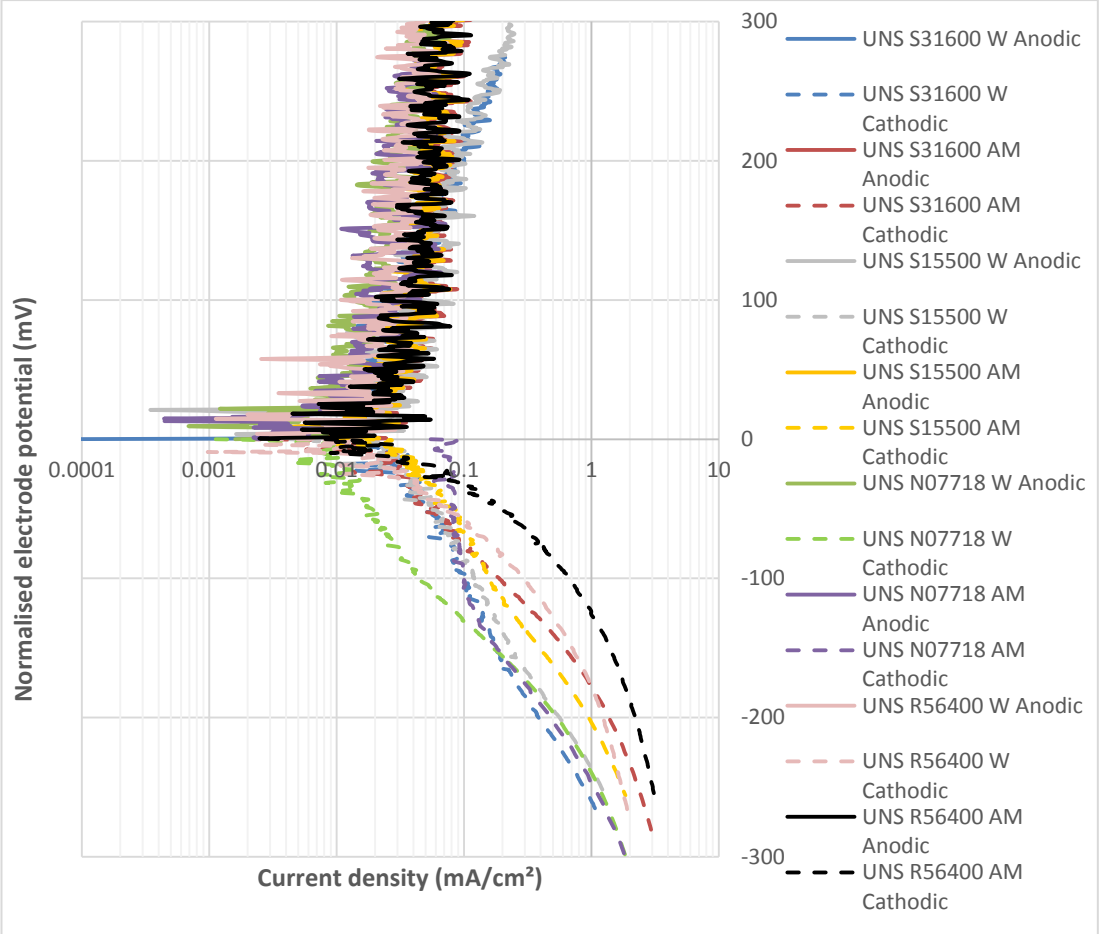

Figure 7.18: *Anodic and cathodic polarisation scans on the full specimen of all test materials in solid-liquid conditions*

The measured free corrosion potentials, corrosion current densities and calculated volume losses due to corrosion for all materials in each test environment are given in Tables 7.6–7.8. In general, there was an increase in corrosion current densities and, hence, volume loss due to corrosion as the test conditions became more aggressive (i.e. static to solid-liquid conditions). In static and flowing conditions, the AM materials exhibited significantly lower corrosion rates than that of their wrought counterparts (with the exception of UNS S15500 in flowing conditions). This suggests that the AM materials were able to establish more stable passive oxide films. However, in solid-liquid conditions, the corrosion rates of the AM materials were similar to that of the wrought materials. This is due to the breakdown of the passive film caused by the repeated impacts of solid particles.

Table 7.6: *Measured free corrosion potentials, corrosion current densities and calculated volume losses due to corrosion for full specimens in static conditions*

Material	E_{corr} (mV)	Corrosion current density (mA/cm^2)	Volume loss due to corrosion (mm^3/hr)
UNS S31600 W	-350	0.01500	0.00205
UNS S31600 AM	-181	0.00005	0.00007
UNS S15500 W	-269	0.00200	0.00297
UNS S15500 AM	-247	0.00060	0.00089
UNS N07718 W	-263	0.00200	0.00245
UNS N07718 AM	-174	0.00002	0.00002
UNS R56400 W	-217	0.00200	0.00222
UNS R56400 AM	-471	0.00002	0.00002

Table 7.7: *Measured free corrosion potentials, corrosion current densities and calculated volume losses due to corrosion for full specimens in flowing conditions*

Material	E_{corr} (mV)	Corrosion current density (mA/cm^2)	Volume loss due to corrosion (mm^3/hr)
UNS S31600 W	-237	0.00300	0.00411
UNS S31600 AM	-87	0.00010	0.00014
UNS S15500 W	-287	0.00500	0.00742
UNS S15500 AM	-245	0.00600	0.00891
UNS N07718 W	-243	0.00200	0.00245
UNS N07718 AM	+102	0.00002	0.00002
UNS R56400 W	-222	0.00400	0.00445
UNS R56400 AM	+31	0.00006	0.00007

Table 7.8: *Measured free corrosion potentials, corrosion current densities and volume losses due to corrosion for full specimens in solid-liquid conditions*

Material	E_{corr} (mV)	Corrosion current density (mA/cm^2)	Volume loss due to corrosion (mm^3/hr)
UNS S31600 W	-375	0.022	0.030
UNS S31600 AM	-421	0.025	0.034
UNS S15500 W	-399	0.023	0.034
UNS S15500 AM	-418	0.031	0.046
UNS N07718 W	-389	0.010	0.012
UNS N07718 AM	-423	0.013	0.016
UNS R56400 W	-477	0.016	0.018
UNS R56400 AM	-505	0.019	0.021

Anodic polarisation scans were undertaken for each test material in both wear regions (DIZ and OA) under solid-liquid conditions. The anodic polarisations scans were conducted after the stabilisation of the free corrosion potential (E_{corr}) and by using the same methodology as described in Chapter 3.3.4. The electrode potentials have been normalised for better comparison purposes due to the large differences between the two areas and represents the electrode potential at a minimum of 25mV more negative than E_{corr}. As illustrated in Figure 7.19 for UNS S31600 W and in Appendix C for the remaining materials, the current densities were observed to be greater in the DIZ than the OA for all test materials. The fluctuations in current density are indicative of de-passivation/re-passivation events occurring on the passive film.

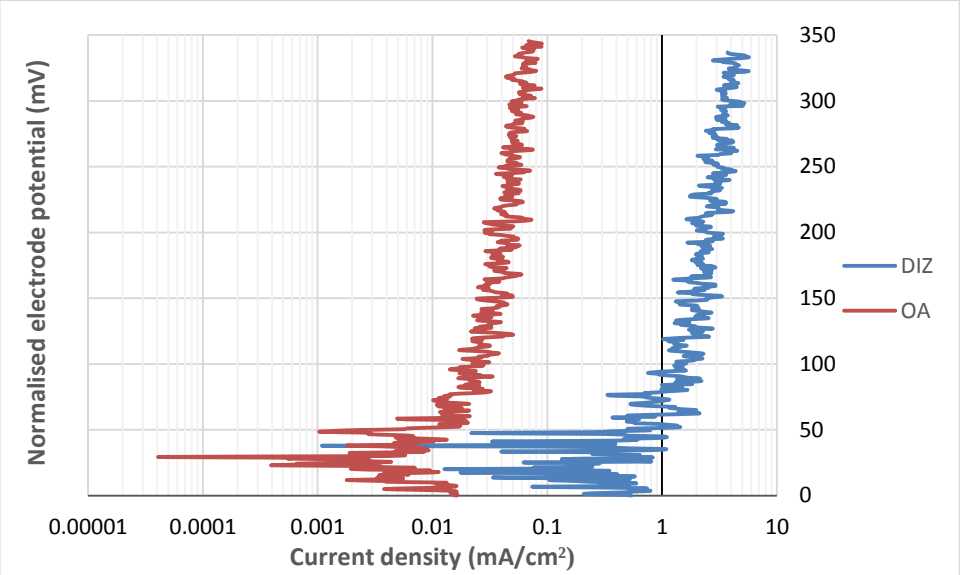

Figure 7.19: *Anodic polarisation scans on both wear regions of UNS S31600 W in solid-liquid conditions*

The E_{corr} values of both segmented regions as well as the Tafel extrapolated current densities for each test material are given in Table 7.9. Faraday's law (Chapter 2.4.1) was used to calculate the volume loss due to corrosion. The corrosion current densities were observed to be significantly greater in the DIZ compared to the OA for all of the test materials. This would be expected as the erosion-corrosion conditions are significantly more aggressive directly underneath the nozzle. For the W and AM stainless steel alloys (UNS S31600 and UNS S15500), the volume loss due to corrosion was lower in the outer region than in the DIZ. For the Inconel and titanium alloys, the volume loss was observed to be similar in both regions due to their excellent resistance to corrosion. An interesting observation is the difference between the E_{corr} values between the DIZ and OA of the test materials (with exception of the wrought UNS S31600 and UNS S15500). This is likely to lead to galvanic interactions between the DIZ and OA during the solid-liquid impingement conditions.

Table 7.9: *Measured free corrosion potential, corrosion current densities and calculated volume losses on both segmented wear regions for all materials in solid-liquid conditions*

Material	DIZ (0.2cm^2)			OA (11cm^2)		
	E_{corr} (mV)	Corrosion current density (mA/cm^2)	Volume loss due to corrosion (mm^3)	E_{corr} (mV)	Corrosion current density (mA/cm^2)	Volume loss due to corrosion (mm^3)
UNS S31600 W	-432	0.70	0.010	-434	0.013	0.017
UNS S31600 AM	-523	0.40	0.016	-358	0.006	0.007
UNS S15500 W	-429	0.80	0.021	-430	0.030	0.043
UNS S15500 AM	-505	0.60	0.026	-356	0.006	0.009
UNS N07718 W	-525	0.10	0.002	-379	0.003	0.004
UNS N07718 AM	-504	0.15	0.003	-368	0.004	0.005
UNS R56400 W	-621	0.10	0.002	-476	0.008	0.008
UNS R56400 AM	-601	0.10	0.002	-451	0.006	0.006

Breakdown polarisation tests were conducted to assess the passive film behaviour of the test materials. Figure 7.20 illustrates the breakdown potential (E_b) anodic polarisation scans for all of the test materials in static conditions. The measured electrode potential was not normalised for this comparison. The measured breakdown potentials are given in Table 7.10. The AM and W UNS S15500 both exhibited active behaviour, therefore, did not exhibit any breakdown potential. The AM and W UNS S31600 exhibited similar breakdown potentials, however, AM UNS S31600 broke down at a smaller current density than that of the W UNS S31600. A similar trend was observed for the AM UNS N07718 and UNS R56400 when compared with their wrought counterparts.

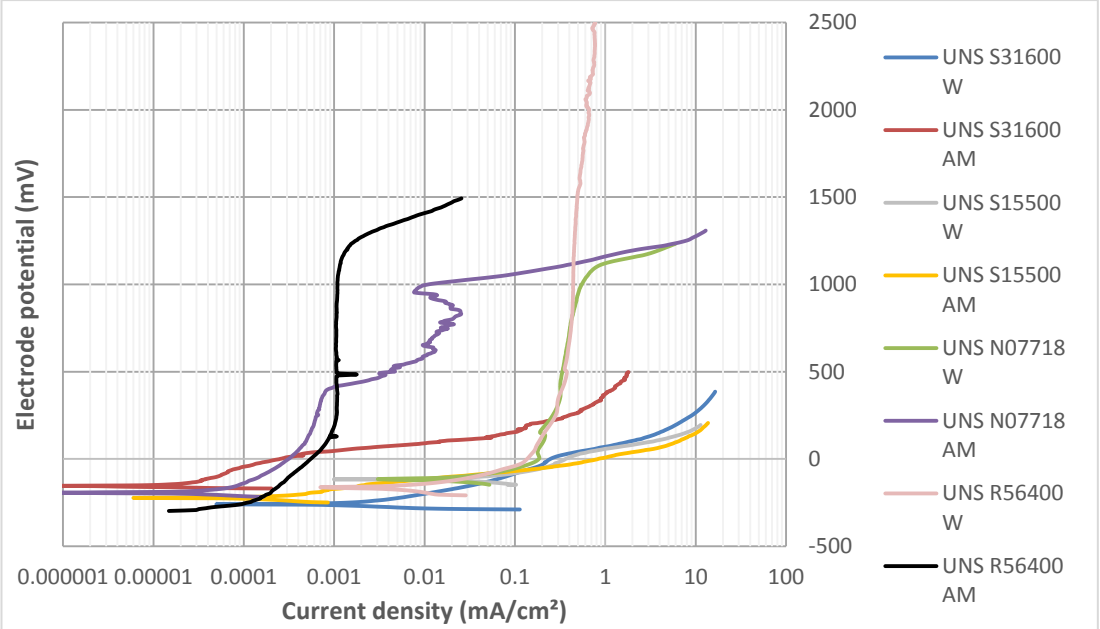

Figure 7.20: *Breakdown potential anodic polarisation scans for all test materials in static conditions*

Table 7.10: *Breakdown potentials for all test materials*

Material	Breakdown potential, E_b (mV)
UNS S31600 W	+25
UNS S31600 AM	+50
UNS S15500 W	Active
UNS S15500 AM	Active
UNS N07718 W	+1100
UNS N07718 AM	+1000
UNS R56400 W	No breakdown
UNS R56400 AM	+1200

7.5.4 Post-test examination

7.5.3.1 Surface topography

7.5.3.1.1 Wear mechanisms under the jet

The material degradation mechanisms occurring underneath the jet were determined through cross sections of the tested material which were subsequently assessed through

SEM. Figure 7.21 demonstrates the post-tested cross section of the UNS 15500 W wear scar, the remaining cross sections are shown in Appendix C. The tested materials exhibited similar wear mechanisms underneath the impinging jet. Both wrought and additively manufactured materials exhibited ploughing-type wear mechanisms where impacting sand particles have caused material to plastically deform and lips which contain highly strained material. A plastically deformed subsurface was also observed for some of the test materials (UNS S31600 W, UNS S15500 W, UNS S15500 AM, UNS R56400 W).

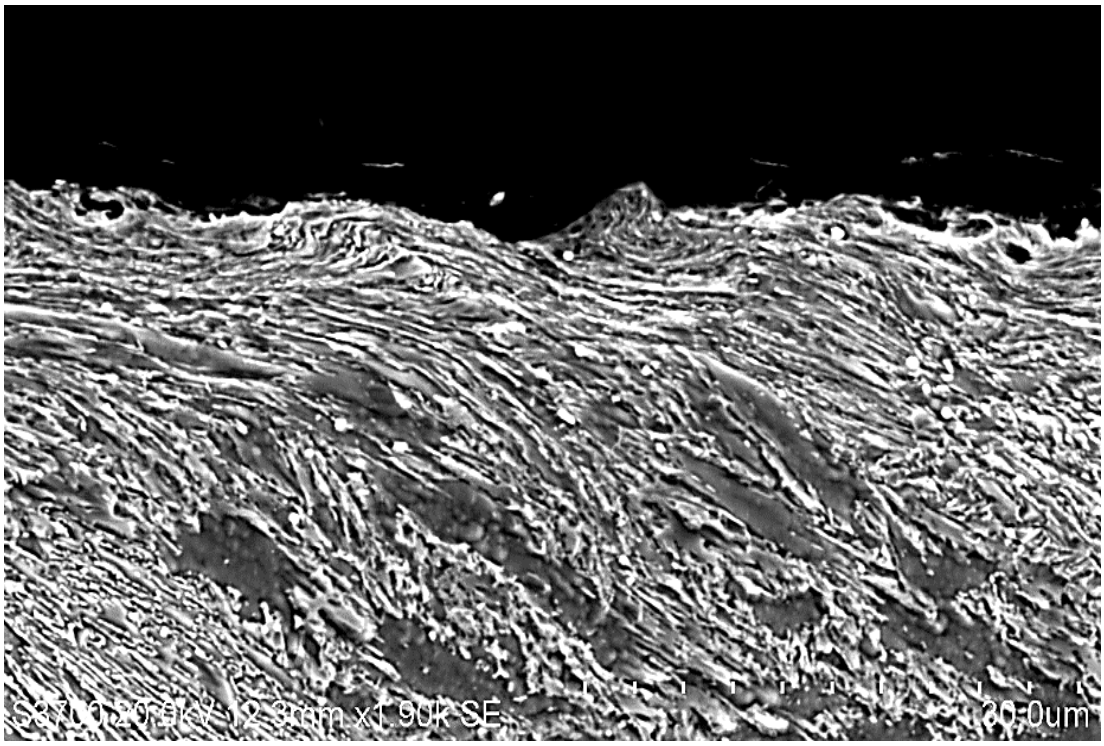

Figure 7.21: *Cross section of erosion-corrosion wear scar of UNS S15500 W with plastically deformed material*

7.5.3.1.2 Wear scar profile scans

Wear scar profile scans were conducted on post-test surfaces using the surface topography technique described in Chapter 3.5.2, to assess the behaviour in the wear scar of the eight test materials. The wear scar profile scans were conducted for both FEC and ICCP conditions. Figure 7.22 illustrates the U-shaped profiles which were observed for the UNS S31600 W and AM materials, the remaining wear scar profiles are given in Appendix C. The width of the wear scars were observed to be approximately 4.5mm which corresponds to the nozzle diameter (4mm) which was used in this study.

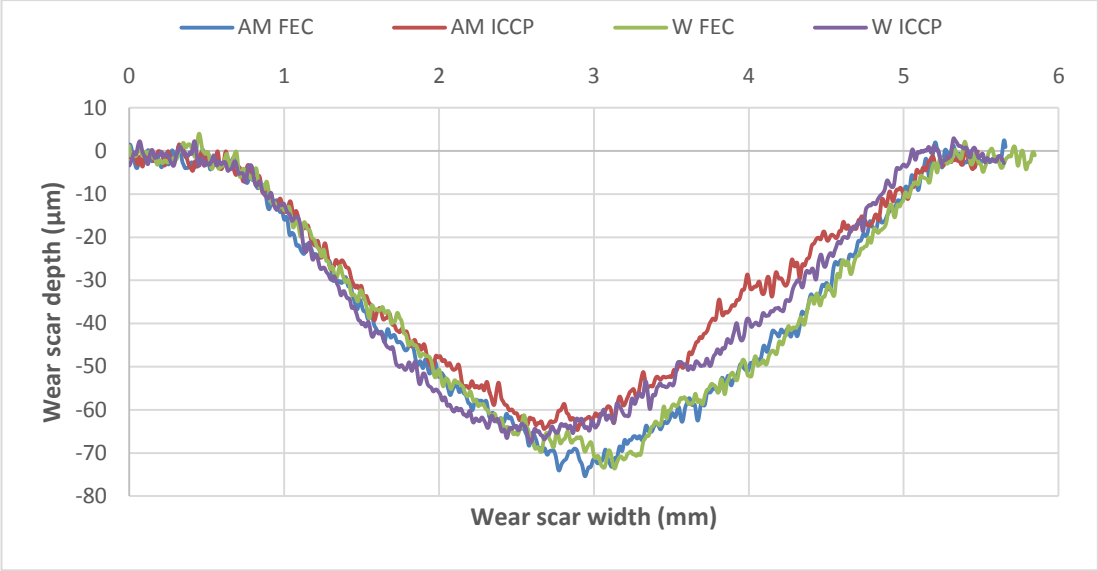

Figure 7.22: *Wear scar profiles for UNS S31600 W and AM in FEC and ICCP conditions*

7.5.3.2 Volumetric analysis

The volume measurement for the UNS S31600 AM in the direct impinged zone after a solid-liquid experiment is shown in Figure 7.23. The surface topography method described in Chapter 3.5.2 was used to measure the volume loss.

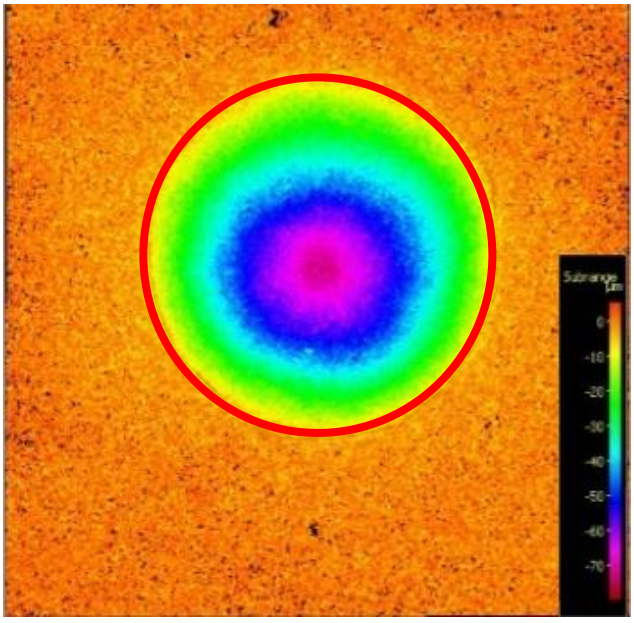

Figure 7.23: *Volumetric analysis on the wear scar of the UNS S31600 AM surface after a solid-liquid experiment*

The volume losses in the wear scars for the test materials are given in Figure 7.24. The wear scar volume losses for the additively manufactured materials were observed to be similar to that of their wrought counterparts. In general, the application of cathodic protection did not reduce the wear scar volume losses for the tested materials. The stainless steels exhibited similar wear scar volume losses which indicate that there is little difference between them in terms of mechanical damage at high impingement angles. The Inconel and titanium alloys exhibited lower wear scar volume losses compared to the stainless steels.

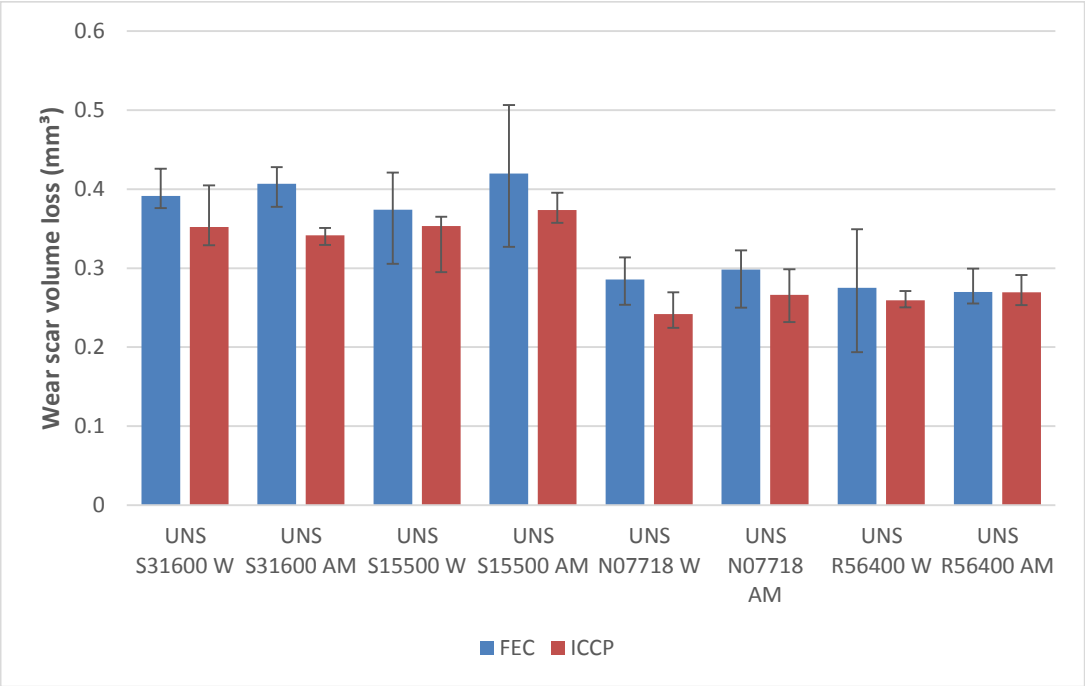

Figure 7.24: *Wear scar volume loss of the test materials in FEC and ICCP conditions*

7.6 Repetitive impact results

The additively manufactured materials were also assessed in repetitive impact with slurry conditions as described in Chapters 3.4 and 5.4. This was conducted in order to assist with the feasibility of using additively manufactured materials as an alternative candidate for valve seats. The wear depths, volume losses and the circularity of tested sand particles were assessed.

7.6.1 Wear scar depths

The average wear scar depths for the test materials in repetitive impact with slurry conditions are shown in Figure 7.25. There was a reduction in average wear scar depth when comparing the additively manufactured materials with their wrought counterparts but, in some cases, the differences were within the experimental scatter. The UNS S15500 AM exhibited the smallest wear scar depth of all the tested materials. The UNS S31600 W performed the poorest.

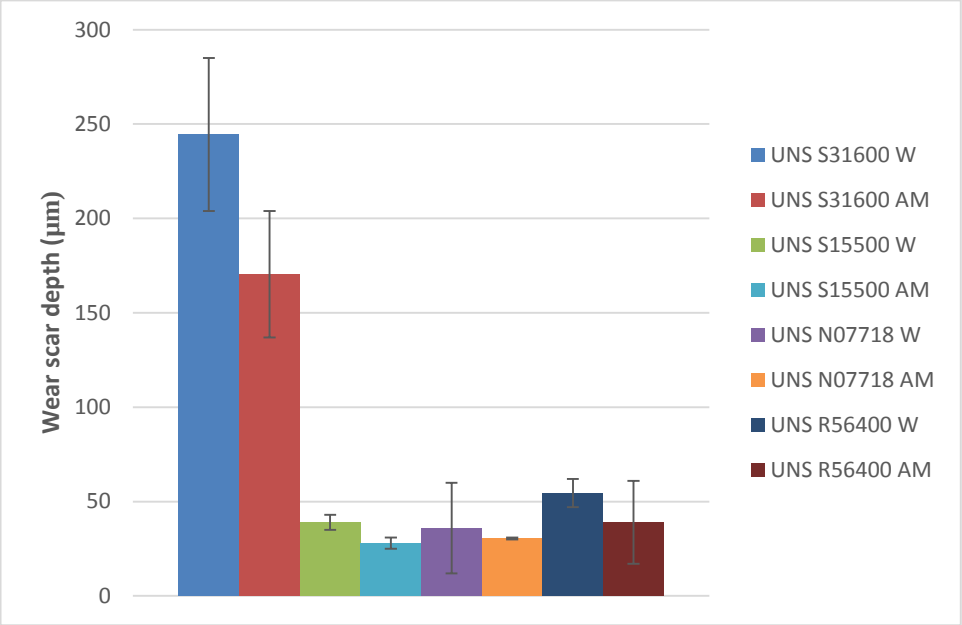

Figure 7.25: *Wear scar depths of the tested materials in repetitive impact with slurry conditions*

7.6.2 Wear scar volume loss

The wear scar volume losses of the tested materials in repetitive impact with slurry conditions are given in Figure 7.26. Materials with a wear scar volume loss are given in Figure 7.27 for a better comparison. There was a significant reduction in wear scar volume loss for the additively manufactured UNS S31600 and UNS S15500 when compared to their wrought counterparts. Similarly with the wear scar depths, the UNS S15500 AM exhibited the lowest wear scar volume loss, whereas, the UNS S31600 W performed the poorest.

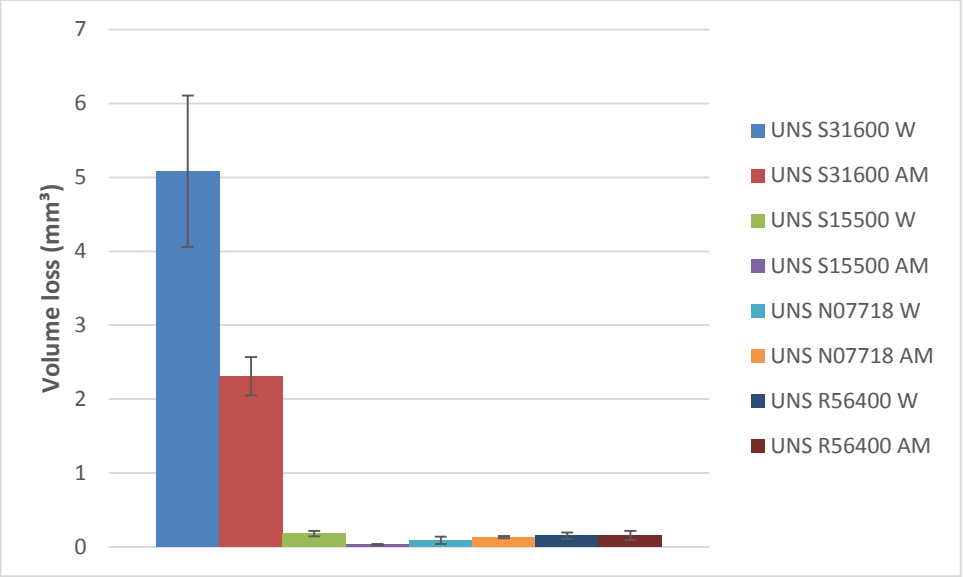

Figure 7.26: *Wear scar volume losses of the tested materials in repetitive impact with slurry conditions*

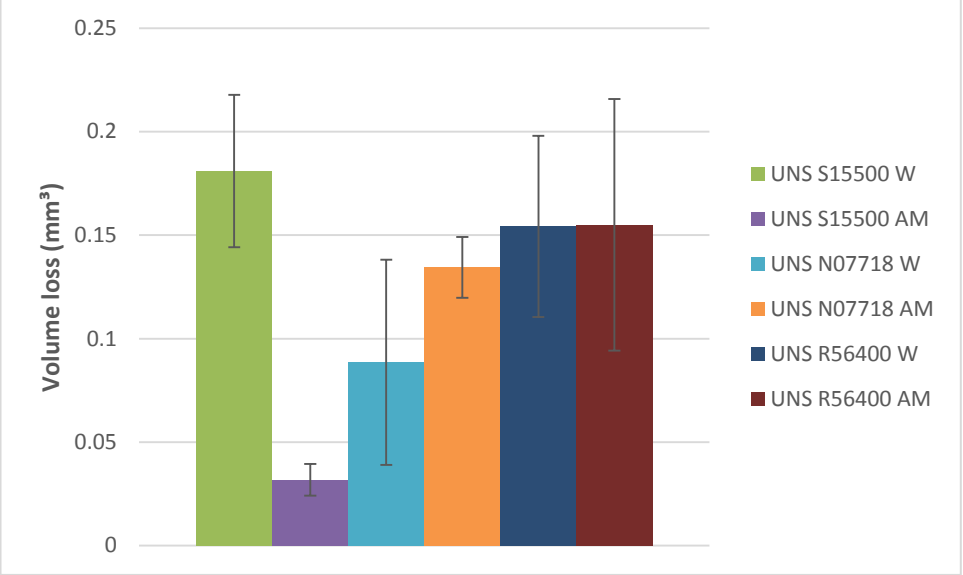

Figure 7.27: *Wear scar volume losses for tested materials (with a volume loss less than 0.25mm³) in repetitive impact with slurry conditions*

7.6.3 Circularity factor of tested sand particles

In line with the CF values measured after the repetitive impact tests on Stellite 6 weld claddings (Chapter 6.6.3) and the other test materials in Chapter 5.4.3, some of the sand particles experienced a reduction in CF due to damage in the repetitive impact tests but most had a CF value greater than 0.8, which indicates that they still meet the requirement

of the ISO and API standards [7.38, 7.39]. The detailed measurements are shown in Appendix C.

7.7 Discussion

7.7.1 Total volume loss (TVL) in free erosion-corrosion (FEC) conditions

From Figure 7.15, it is clear that the additively manufactured materials have similar erosion-corrosion resistance to their wrought counterparts. The wrought stainless steel alloys (UNS S31600 and UNS S15500) exhibited similar erosion-corrosion resistance under the solid-liquid testing conditions. These findings have been observed in previous studies [7.40, 7.41]. The titanium and Inconel alloys (UNS R56400 and UNS N07718) both exhibited significantly improved erosion-corrosion resistance when compared to the stainless steel alloys. The UNS N07718 performed the best under solid-liquid erosion-corrosion conditions. The reasons for this observation will be discussed further in this section.

7.7.2 Breakdown of total volume loss in free erosion-corrosion (FEC) conditions

Figure 7.28 shows the breakdown of the total volume loss into the volume losses in both wear regions (DIZ and OA) under solid-liquid conditions. The additive manufactured materials exhibited similar volume losses in both wear regions compared to their wrought counterparts. The stainless steel alloys exhibited similar volume losses in the DIZ and the UNS S31600 alloys performed slightly better in the OA compared to the UNS S15500 alloys despite their difference in microstructure and hardness. A possible explanation for this observation could be due to the work hardening effect of UNS S31600 [7.42–7.44]. It has been postulated (Wood et al. [7.42] and Singh et al. [7.43]) that impacting sand particles result in localised phase transformations of austenite to martensite. Therefore, this could be a possible explanation why the austenitic stainless steel performed similarly with the precipitation hardened martensitic stainless steel in the DIZ.

The titanium alloy (UNS R56400) and the Inconel alloy (UNS N07718) both performed similarly in the DIZ. However, in the OA, where sliding abrasion damage is prevalent, the Inconel alloy performs the best compared to the other test materials. This can be attributed to its higher hardness which will improve its sliding abrasion resistance. In the OA, the volume loss of the titanium alloy performs similarly to that of the stainless steels which suggests that it has less resistance to sliding abrasion resistance due to its lower hardness.

However, the link with hardness is not universal as the UNS S15500 stainless steel which has similar hardness with the Inconel alloy performs poorest in the OA. Another feature demonstrated in Figure 7.28 is how an apparent difference in overall material loss (TVL) between two materials (UNS N07718 and UNS R56400 alloys) can be identified as an effect under low-angle (sliding abrasion) conditions rather than in high angle erosion conditions.

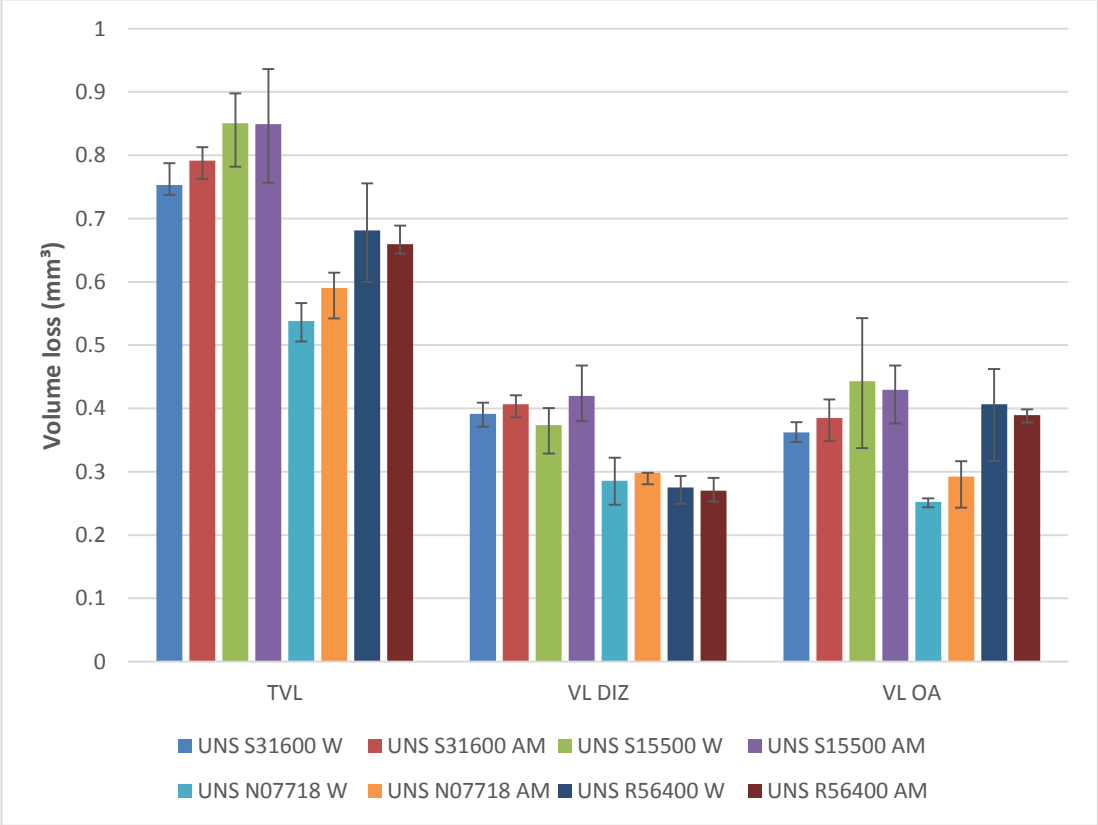

Figure 7.28: *Breakdown of the total volume loss into the two distinct wear regions (DIZ & OA) under FEC solid-liquid conditions*

7.7.3 Breakdown of total volume loss in cathodic protection (CP) conditions

The breakdown of the total volume loss into the two wear regions for the tested materials under cathodic protection (CP) conditions is shown in Figure 7.29. Similar trends were observed in both FEC and CP conditions, for instance the stainless steels performed poorer in the DIZ compared to the Inconel and titanium alloys. The additively manufactured materials performed similarly in both wear regions compared to their wrought counterparts. The titanium and Inconel alloys exhibited similar volume losses in the DIZ which were substantially lower than the stainless steel alloys. The titanium alloy performed

similarly to that of the stainless steel alloys in the OA. The Inconel alloy performed the best in the OA.

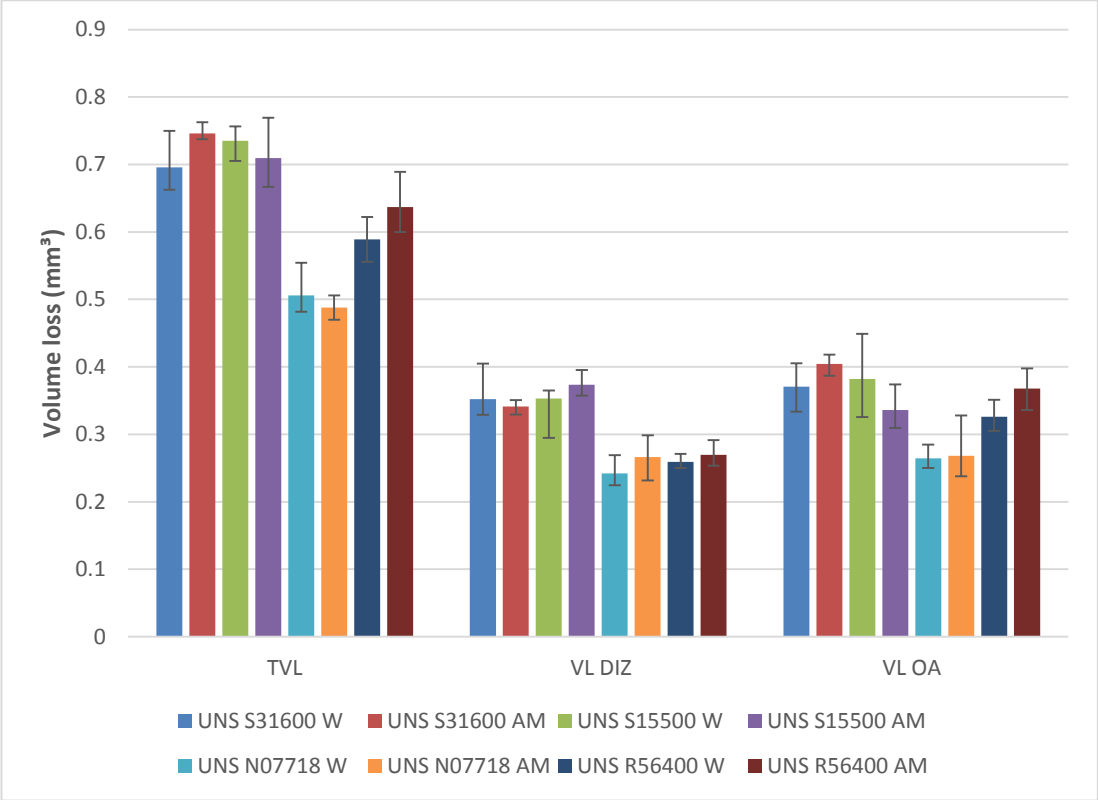

Figure 7.29: *Breakdown of the total volume loss into the two distinct wear regions (DIZ & OA) under CP solid-liquid conditions*

7.7.4 Discrimination of the TVL in the DIZ and OA

Figure 7.30 illustrates the quantitative volume losses of the different degradation processes which were measured using the volumetric analysis technique described in Chapter 3.5.3. Each degradation process will be discussed separately in subsequent subsections.

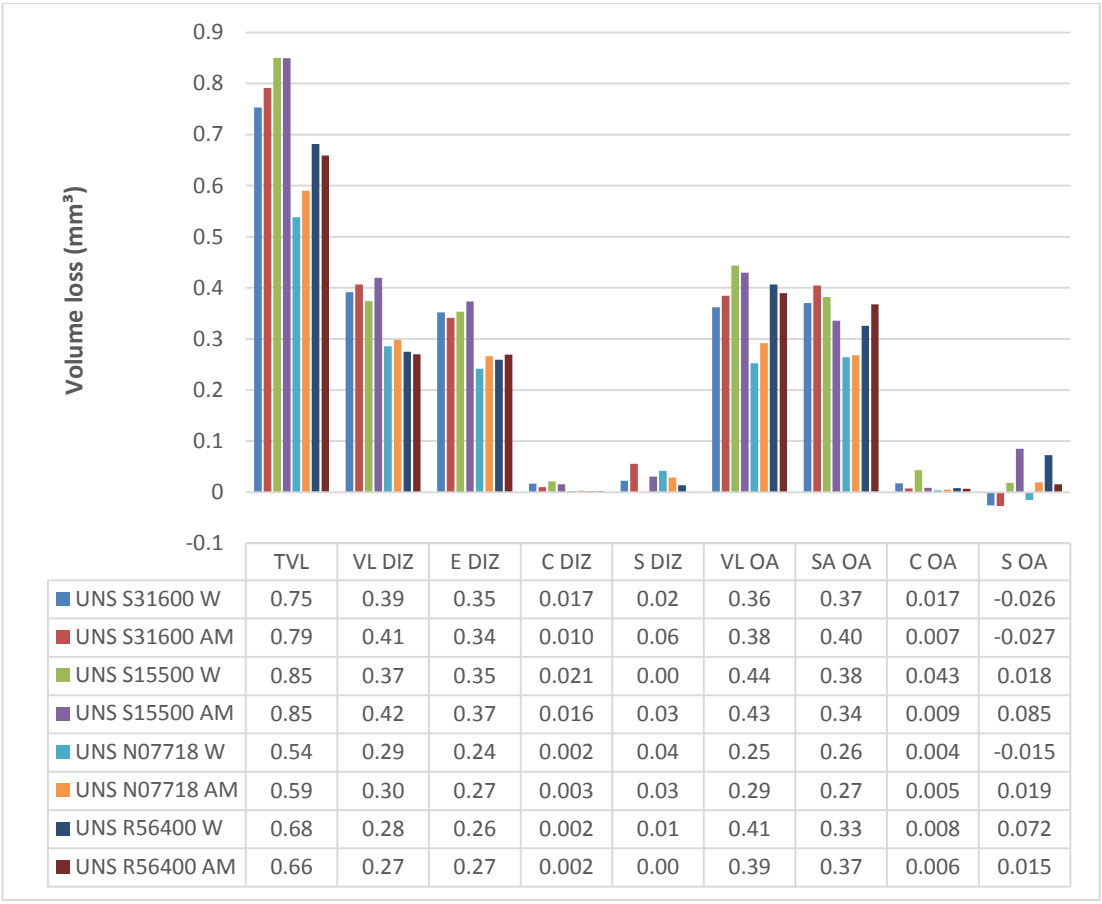

	TVL	VL DIZ	E DIZ	C DIZ	S DIZ	VL OA	SA OA	C OA	S OA
UNS S31600 W	0.75	0.39	0.35	0.017	0.02	0.36	0.37	0.017	-0.026
UNS S31600 AM	0.79	0.41	0.34	0.010	0.06	0.38	0.40	0.007	-0.027
UNS S15500 W	0.85	0.37	0.35	0.021	0.00	0.44	0.38	0.043	0.018
UNS S15500 AM	0.85	0.42	0.37	0.016	0.03	0.43	0.34	0.009	0.085
UNS N07718 W	0.54	0.29	0.24	0.002	0.04	0.25	0.26	0.004	-0.015
UNS N07718 AM	0.59	0.30	0.27	0.003	0.03	0.29	0.27	0.005	0.019
UNS R56400 W	0.68	0.28	0.26	0.002	0.01	0.41	0.33	0.008	0.072
UNS R56400 AM	0.66	0.27	0.27	0.002	0.00	0.39	0.37	0.006	0.015

Figure 7.30: *Discrimination between the different material degradation processes on the tested materials under solid-liquid conditions*

7.7.5 High angle erosion damage in the direct impinged zone (DIZ)

The damage caused by high angle erosion in the direct impinged zone was measured in terms of volume loss from the cathodically protected test samples. These measurements were given in Figures 7.24 and 7.29. The stainless steel alloys exhibited greater volume loss due to high angle erosion compared to the titanium and Inconel alloys. Both stainless steels exhibited similar volume losses under the high angle erosion conditions. As mentioned in Chapter 7.7.1, this may be attributed to the work hardening effect (UNS S31600) of the impacting solid particles which cause localised phase transformation of austenite to martensite [7.42–7.46]. The AM alloys exhibited similar volume loss in the DIZ when compared to their W counterpart. Hence, indicating that even a refined microstructure does not improve the resistance to high angle erosion damage.

Similarly with previous results in this study, there has been a lack of correlation with high angle erosion resistance and material hardness. Table 7.11 shows the hardness and H/E ratio values for the tested materials along with their measured volume losses due to high angle erosion. There is no obvious linkage with the H/E ratio values and a material's resistance to high angle erosion.

Table 7.11: *H/E values and measured volume losses due to high angle erosion for the tested materials*

Material	Hardness (HV)	H/E	Volume loss due to high angle erosion (mm^3)
UNS S31600 W	170	0.012	0.35
UNS S31600 AM	200	0.011	0.34
UNS S15500 W	360	0.018	0.35
UNS S15500 AM	430	0.022	0.37
UNS N07718 W	390	0.022	0.24
UNS N07718 AM	400	0.022	0.27
UNS R56400 W	320	0.028	0.26
UNS R56400 AM	350	0.031	0.27

7.7.6 Corrosion and synergy in the direct impinged zone (DIZ)

Figure 7.30 demonstrates that the majority of the damage for the tested materials was mechanical (83% - 99% of the volume loss in the DIZ). The wrought UNS S15500 was most susceptible to corrosion in the DIZ (13% of the volume loss in the DIZ). The additively manufactured UNS S31600 exhibited the greatest amount of synergy in the DIZ (12% of the volume loss in the DIZ). The stainless steels exhibited higher corrosion rates compared to the Inconel and titanium alloys; hence, indicating the superior corrosion resistance of the Inconel and titanium alloys as would be expected.

The small amount of corrosion damage, shown in Table 7.9, was calculated from the anodic polarisation scans of the segmented samples. Erosion is the predominant material degradation mechanism in this wear region due to the velocity, size, shape and concentration of the sand particles.

7.7.7 Sliding abrasion in the outer area (OA)

The volume loss due to sliding abrasion was calculated by subtracting the volume loss due to high angle erosion from the total volume loss under cathodic protection conditions. As mentioned previously, there is often a good linkage with material hardness and sliding abrasion resistance. In this study this has been found to be true for the tested materials with the exception of the UNS S15500 wrought and additively manufactured, which exhibited high hardness but poor sliding abrasion resistance.

In general, the additively manufactured and wrought alloys displayed similar sliding abrasion resistance. The Inconel alloys exhibited the greatest resistance to sliding abrasion damage. This may be associated with its slightly higher hardness compared to the other test materials.

7.7.8 Corrosion and synergy in the outer area (OA)

Anodic polarisation scans of the segmented samples (Figures 7.19 and Appendix 7.1-7.7) gave an indication of the corrosion damage occurring in the outer area (OA) of the tested materials. The wrought UNS S15500 exhibited the largest amount of corrosion damage in the OA (approximately 10% of volume loss in the OA). The UNS N07718 alloys (W and AM) exhibited the lowest corrosion damage in the OA (approximately 2% of volume loss in the OA). As the conditions are less turbulent in the OA compared to the DIZ, the passive film of the corrosion resistant materials is more stable; hence, the corrosion damage tends to be smaller. Moreover, the superior performance of the wrought UNS N07718 and UNS R56400 alloys is indicative of a more resistant passive film on these alloys. The AM process appears, however, to have produced a passive film on the stainless steels that are similar in corrosion resistance to those on the Ni-base and Ti-base alloys.

A significant amount of synergy damage was observed in the UNS S15500 AM and UNS R56400 W (approximately 20% and 18% of the volume loss in the OA, respectively). For the UNS S15500 AM, the greater synergy may be attributed to its complex microstructure (tempered martensite with retained austenite) which led to micro-galvanic corrosion interactions between the two phases. The synergy occurring in the titanium alloy may be attributed to the complex galvanic interactions occurring between the alpha and beta

phase which weakens the bond between the two phases leading to higher material loss by sliding abrasion.

Negative synergy in the OA was also observed for three of the tested materials (UNS S31600 W and AM as well as UNS N07718 W). Table 7.12 displays the experimental error (from the scatter bands) for the three materials in the volume loss OA measurements along with the calculated percentage of negative synergy from Figure 7.31. For the additively manufactured and wrought UNS S31600, the experimental error accounts for the calculated negative synergy values and the negative synergy value for the wrought UNS N07718 material is extremely low; therefore, it can be considered that the actual synergy values for the three test materials have a negligible effect on the overall abrasion-corrosion behaviour.

Table 7.12: *Experimental error and percentage of negative synergy in OA volume loss and for the three test materials*

Material	Experimental error (%)	Calculated % of negative synergy
UNS S31600 W	9	7
UNS S31600 AM	19	7
UNS N07718 W	4	6

7.7.9 Repetitive impact testing

As observed from Figures 7.25, 7.26 and 7.27, the additive manufactured materials performed similarly, and in some instances better, than their wrought counterparts. When comparing the average wear scar depths and volume losses, the UNS S15500 AM performed the best of the tested materials.

Figure 7.31 shows the relationship between material hardness and repetitive impact resistance. In this particular case, an increase in hardness has led to a reduction in wear scar depth under repetitive impact conditions. This was not observed in a previous chapter

(Figure 5.41). Figure 7.32 illustrates the relationship between the H/E ratio of the test materials with their resistance to repetitive impact wear. In this instance, there is no clear linkage, which is a similar observation from a previous chapter (Figure 5.43). This further illustrates the complexity of predicting material wear performance with material properties.

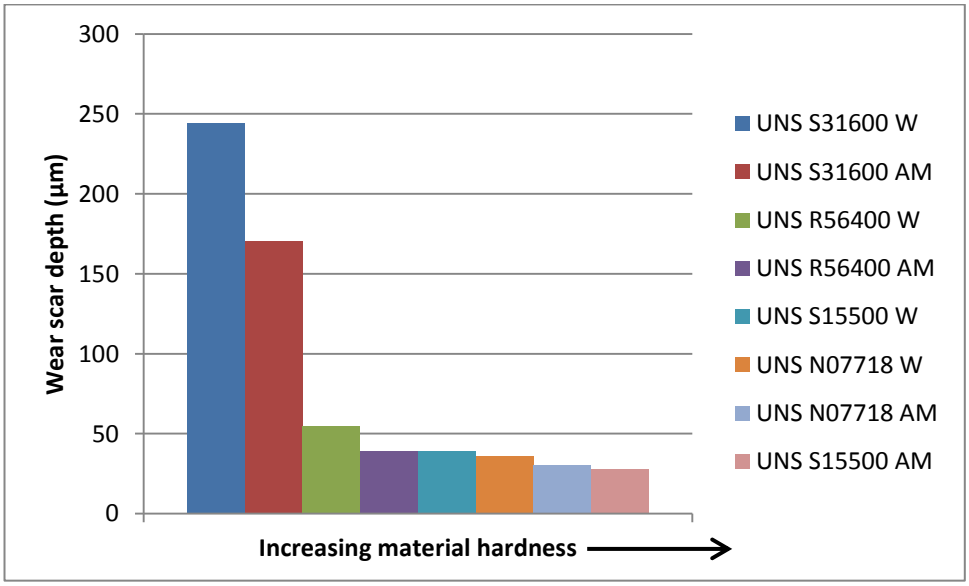

Figure 7.31: *Relationship between material hardness and repetitive impact resistance of the tested materials*

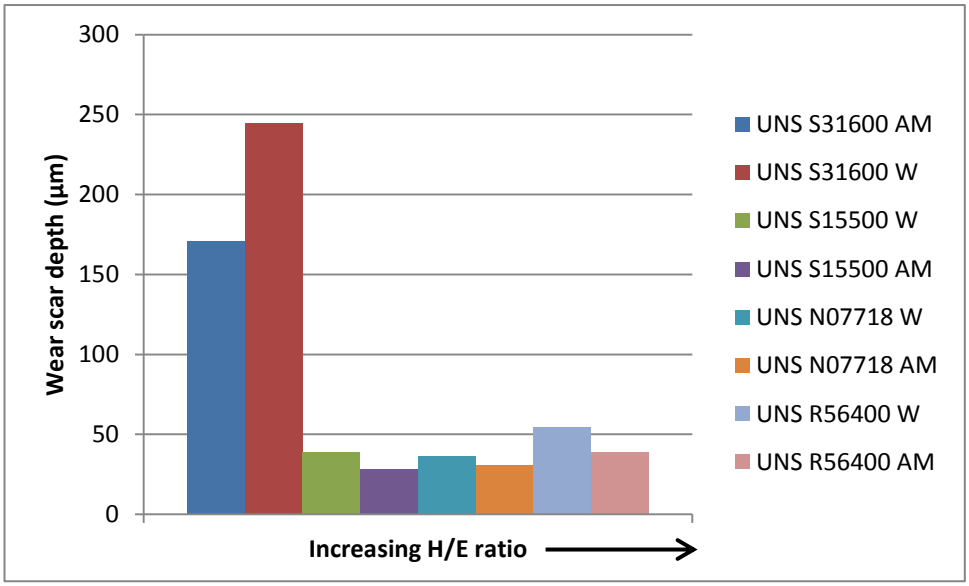

Figure 7.32: *Relationship between H/E ratio and repetitive impact resistance of the tested materials*

Table 7.13 shows the ranking of the tested materials with respect to their wear scar volume loss under repetitive impact conditions, measured material properties (yield strength, Ultimate Tensile Strength (UTS) and hardness) as well as the applied pressure during repetitive impact testing. As the UNS S31600 AM and wrought alloys exhibited yield strengths similar or less than that of the applied pressure (414MPa) during testing, then these materials exhibited the largest wear scar volume loss under repetitive impact conditions. The other test materials demonstrated yield strengths significantly greater than the applied impact pressure, therefore, their wear scar volume loss is drastically smaller than the UNS S31600 alloys. When comparing the better performing materials with their UTS, there is a general trend that a greater UTS yields a smaller wear scar volume loss. In terms of hardness and H/E, there is no relationship with wear scar volume loss. This contradicts the relationship observed in Figure 7.31 with wear scar depths and material hardness. Once again, this indicates the complexity of relating material properties with repetitive impact wear resistance.

Table 7.13: *Ranking of tested materials under repetitive impact conditions with measured material properties and applied repetitive impact pressure*

Rank	Material	Wear scar volume loss (mm^3)	Applied repetitive impact Pressure (MPa)	Yield strength (MPa)	UTS (MPa)	Hardness (HV)	H/E
1	UNS S15500 (AM)	0.032	414	1028	1348	430	0.0217
2	UNS N07718 (W)	0.089	414	1081	1348	390	0.0219
3	UNS N07718 (AM)	0.134	414	740	1131	400	0.0224
4	UNS R56400 (W)	0.154	414	910	1000	320	0.0273
5	UNS R56400 (AM)	0.155	414	900	1014	350	0.0315
6	UNS	0.181	414	998	1098	360	0.0177

	S15500 (W)						
7	UNS S31600 (AM)	2.310	414	428	640	200	0.0112
8	UNS S31600 (W)	5.080	414	284	436	170	0.0124

7.8 Relevance of work to the design and operation for hydraulic fracturing pump components

This study has shown that additively manufactured materials perform similarly, and in some instances better, than wrought materials under corrosion, erosion-corrosion and repetitive impact test conditions. Therefore, additive manufacturing can be an attractive manufacturing option for the production of hydraulic fracturing pump components. This has to be set against the high associated costs of the additive manufacturing process but the findings from this study provides a sound basis to drive further advances in AM technology to yield reduced costs and even better component durability. It is clear that the AM components would be required to significantly outperform components manufactured from conventional techniques. However, a possible more immediate advantage of the AM process is the prospect of using AM to repair damaged components. This could potentially increase the life of components in service and thereby provide a competitive advantage.

7.9 Conclusions

1. The literature review revealed that, although some physical characterisation studies have been undertaken on the alloys under consideration herein, very little effort has been invested in the corrosion behaviour and no previous work appears to have been conducted on the corrosive wear performance of these alloys.
2. The AM materials exhibited different microstructures to their wrought counterparts; however, the microstructural phases were the same. The UNS S15500 and UNS R56400 demonstrated a finer microstructure compared to the wrought alloys. This can be attributed to the AM process as both wrought and AM materials exhibited similar heat treatments. The refined microstructures of the AM materials resulted in greater hardness compared to the wrought alloys. The EDS

analysis also indicated that both AM and wrought materials had similar chemical compositions.

3. The polarisation scans of the materials demonstrated that the AM materials had better corrosion resistance than the wrought materials in static and flowing conditions. This is likely to be attributed to the AM materials producing a thicker and more stable passive film. Although it has been out with the scope of this study to characterise the passive oxide films, it would be possible to characterise and compare AM and wrought passive films through Auger electron spectroscopy and/or transmission electron microscopy. In solid-liquid conditions, where the passive films are periodically removed by impacting sand particles, both AM and wrought materials exhibited similar behaviour.
4. The AM and equivalent wrought alloys exhibited similar performance under erosion-corrosion conditions. The Inconel alloy demonstrated the best erosion-corrosion resistance. This was attributed to its excellent corrosion resistance and good resistance to both high angle erosion and sliding abrasion damage.
5. The benefits of using the enhanced volumetric analysis technique was again shown as it demonstrated that the better performance of the Inconel alloys compared to the titanium-bases alloys was a result of its better resistance to abrasion-corrosion damage as both performed similarly under direct impingement corrosive wear conditions.
6. In repetitive impact conditions, the AM and equivalent wrought materials performed similarly and in some cases demonstrated better repetitive impact resistance. The UNS S15500 AM alloy exhibited the greatest resistance to repetitive impact. In terms of wear scar depths, a relationship with hardness was observed. However, this relationship was not observed with wear scar volume loss. The yield strength and UTS were observed to have better linkage with wear scar volume loss. This again illustrates the complexity of comparing material properties with wear resistance.

7.10 References

[7.1] C. Emmelmann, J. Kranz, D. Herzog, and E. Wycisk, "Laser Additive Manufacturing of Metals," in *Laser technology in biomimetics*, 2013, pp. 143–162.

[7.2] W. E. Frazier, "Metal additive manufacturing: A review," *J. Mater. Eng. Perform.*, vol. 23, no. 6, pp. 1917–1928, 2014.

[7.3] X. Gong, T. Anderson, and K. Chou, "Review on powder-based electron beam additive manufacturing technology," in *ASME/ISCIE 2012 International symposium on flexible automation*, 2017.

[7.4] D. Herzog, V. Seyda, E. Wycisk, and C. Emmelmann, "Additive manufacturing of metals," *Acta Mater.*, vol. 117, pp. 371–392, 2016.

[7.5] N. T. Aboulkhair, N. M. Everitt, I. Ashcroft, and C. Tuck, "Reducing porosity in AlSi10Mg parts processed by selective laser melting," *Addit. Manuf.*, vol. 1, pp. 77–86, 2014.

[7.6] C. Qiu, N. J. E. Adkins, and M. M. Attallah, "Microstructure and tensile properties of selectively laser-melted and of HIPed laser-melted Ti-6Al-4V," *Mater. Sci. Eng. A*, vol. 578, pp. 230–239, 2013.

[7.7] A. L. Cooke and J. A. Soons, "Variability in the Geometric Accuracy of Additively Manufactured Test Parts," in *21st Annual International Solid Freeform Fabrication Symposium*, 2010.

[7.8] J. J. Lewandowski and M. Seifi, "Metal Additive Manufacturing: A Review of Mechanical Properties," *Annu. Rev. Mater. Res.*, vol. 46, no. 1, pp. 151–186, 2016.

[7.9] J. R. Trelewicz, G. P. Halada, O. K. Donaldson, and G. Manogharan, "Microstructure and Corrosion Resistance of Laser Additively Manufactured 316L Stainless Steel," *JOM*, vol. 68, no. 3, pp. 850–859, 2016.

[7.10] M. Ziętala, T. Durejko, M. Polański, I. Kunce, T. Płociński, W. Zieliński, M. Łazińska, W. Stępniowski, T. Czujko, K. J. Kurzydłowski, and Z. Bojar, "The microstructure, mechanical properties and corrosion resistance of 316L stainless steel fabricated

using laser engineered net shaping," *Mater. Sci. Eng. A*, vol. 677, pp. 1–10, 2016.

[7.11] Y. Zhong, L.-E. Rännar, L. Liu, A. Koptyug, S. Wikman, J. Olsen, D. Cui, and Z. Shen, "Additive manufacturing of 316L stainless steel by electron beam melting for nuclear fusion applications," *J. Nucl. Mater.*, vol. 486, pp. 234–245, 2017.

[7.12] Y. Zhong, L. Liu, S. Wikman, D. Cui, and Z. Shen, "Intragranular cellular segregation network structure strengthening 316L stainless steel prepared by selective laser melting," *J. Nucl. Mater.*, vol. 470, pp. 170–178, 2016.

[7.13] E. Yasa and J. P. Kruth, "Microstructural investigation of selective laser melting 316L stainless steel parts exposed to laser re-melting," *Procedia Eng.*, vol. 19, pp. 389–395, 2011.

[7.14] P. Guo, B. Zou, C. Huang, and H. Gao, "Study on microstructure, mechanical properties and machinability of efficiently additive manufactured AISI 316L stainless steel by high-power direct laser deposition," *J. Mater. Process. Technol.*, vol. 240, pp. 12–22, 2017.

[7.15] B. Zhang, L. Dembinski, and C. Coddet, "The study of the laser parameters and environment variables effect on mechanical properties of high compact parts elaborated by selective laser melting 316L powder," *Mater. Sci. Eng. A*, vol. 584, pp. 21–31, 2013.

[7.16] H. K. Rafi, T. L. Starr, and B. E. Stucker, "A comparison of the tensile, fatigue, and fracture behavior of Ti-6Al-4V and 15-5 PH stainless steel parts made by selective laser melting," *Int. J. Adv. Manuf. Technol.*, vol. 69, no. 5–8, pp. 1299–1309, 2013.

[7.17] A. B. Spierings, T. L. Starr, and K. Wegener, "Fatigue performance of additive manufactured metallic parts," *Rapid Prototyp. J.*, vol. 19, no. 2, pp. 88–94, 2013.

[7.18] J. J. de Damborenea, M. A. Arenas, M. A. Larosa, A. L. Jardini, C. A. de Carvalho Zavaglia, and A. Conde, "Corrosion of Ti6Al4V pins produced by direct metal laser sintering," *Appl. Surf. Sci.*, vol. 393, pp. 340–347, 2017.

[7.19] N. Dai, L. C. Zhang, J. Zhang, X. Zhang, Q. Ni, Y. Chen, M. Wu, and C. Yang,

"Distinction in corrosion resistance of selective laser melted Ti-6Al-4V alloy on different planes," *Corros. Sci.*, vol. 111, pp. 703–710, 2016.

[7.20] N. Dai, L.-C. Zhang, J. Zhang, Q. Chen, and M. Wu, "Corrosion behavior of selective laser melted Ti-6Al-4V alloy in NaCl solution," *Corros. Sci.*, vol. 102, pp. 484–489, 2016.

[7.21] D. H. Abdeen and B. R. Palmer, "Corrosion evaluation of Ti-6Al-4V parts produced with electron beam melting machine," *Rapid Prototyp. J.*, vol. 22, no. 2, pp. 322–329, 2016.

[7.22] B. Zhao, H. Wang, N. Qiao, C. Wang, and M. Hu, "Corrosion resistance characteristics of a Ti-6Al-4V alloy scaffold that is fabricated by electron beam melting and selective laser melting for implantation in vivo," *Mater. Sci. Eng. C*, vol. 70, pp. 832–841, 2017.

[7.23] Z. Wang, K. Guan, M. Gao, X. Li, X. Chen, and X. Zeng, "The microstructure and mechanical properties of deposited-IN718 by selective laser melting," *J. Alloys Compd.*, vol. 513, pp. 518–523, 2012.

[7.24] Q. Jia and D. Gu, "Selective laser melting additive manufacturing of Inconel 718 superalloy parts: Densification, microstructure and properties," *J. Alloys Compd.*, vol. 585, pp. 713–721, 2014.

[7.25] D. Zhang, W. Niu, X. Cao, and Z. Liu, "Effect of standard heat treatment on the microstructure and mechanical properties of selective laser melting manufactureed Inconel 718 superalloy," *Mater. Sci. Eng. A*, vol. 644, pp. 32–40, 2015.

[7.26] P. L. Blackwell, "The mechanical and microstructural characteristics of laser-deposited IN718," *J. Mater. Process. Technol.*, vol. 170, no. 1–2, pp. 240–246, 2005.

[7.27] L. L. Parimi, G. A. Ravi, D. Clark, and M. M. Attallah, "Microstructural and texture development in direct laser fabricated IN718," *Mater. Charact.*, vol. 89, pp. 102–111, 2014.

[7.28] K. N. Amato, S. M. Gaytan, L. E. Murr, E. Martinez, P. W. Shindo, J. Hernandez, S. Collins, and F. Medina, "Microstructures and mechanical behavior of Inconel 718

fabricated by selective laser melting," *Acta Mater.*, vol. 60, no. 5, pp. 2229–2239, 2012.

[7.29] C. S. Ramesh, D. S. Devaraj, R. Keshavamurthy, and B. R. Sridhar, "Slurry erosive wear behaviour of thermally sprayed Inconel-718 coatings by APS process," *Wear*, vol. 271, no. 9–10, pp. 1365–1371, 2011.

[7.30] C. S. Ramesh, S. Kumar, D. S. Devaraj, and R. Keshavamurthy, "Slurry Erosive Wear Behavior of Plasma Sprayed Inconel-718 Coatings on Al6061 Alloy," *J. Miner. Mater. Charact. Eng.*, vol. 10, no. 5, pp. 445–453, 2011.

[7.31] J. R. Zhou and S. Bahadur, "Effect of blending of silicon carbide particles in varying sizes on the erosion of Ti-6Al-4V," *Wear*, vol. 132, no. 2, pp. 235–246, 1989.

[7.32] J. Zhou and S. Bahadur, "Erosion-corrosion of Ti-6Al-4V in elevated temperature air environment," *Wear*, vol. 187, pp. 332–339, 1995.

[7.33] S. Yerramareddy and S. Bahadur, "Effect of operational variables, microstructure and mechanical properties on the erosion of Ti-6Al-4V," *Wear*, vol. 142, no. 2, pp. 253–263, 1991.

[7.34] H. Mochizuki, M. Yokota, and S. Hattori, "Effects of materials and solution temperatures on cavitation erosion of pure titanium and titanium alloy in seawater," *Wear*, vol. 262, no. 5–6, pp. 522–528, 2007.

[7.35] A. Neville and B. A. B. McDougall, "Erosion – and cavitation – corrosion of titanium and its alloys," *Wear*, vol. 250, pp. 726–735, 2001.

[7.36] M. Emiliani and R. Brown, "The effect of microstructure on the erosion of Ti-6Al-4V by spherical particles at 90° impact angles," *Wear*, vol. 94, no. 3, pp. 323–338, 1984.

[7.37] J. Chen, F. Y. Yan, B. B. Chen, and J. Z. Wang, "Assessing the tribocorrosion performance of Ti-6Al-4V, 316 stainless steel and Monel K500 alloys in artificial seawater," *Mater. Corros.*, vol. 64, no. 5, pp. 394–401, 2013.

[7.38] ISO 13503: Petroleum and natural gas industries — Completion fluids and materials

Part II: Measurement of properties of proppants used in hydraulic fracturing and gravel-packing operations, 2006.

[7.39] American Petroleum Institute, "API RP 19C.", 2014.

[7.40] L. Giourntas, T. Hodgkiess, and A. M. Galloway, "Comparative study of erosion–corrosion performance on a range of stainless steels," *Wear*, vol. 332–333, pp. 1051–1058, 2015.

[7.41] H. Meng, X. Hu, and A. Neville, "A systematic erosion-corrosion study of two stainless steels in marine conditions via experimental design," *Wear*, vol. 263, pp. 355–362, 2007.

[7.42] R. J. K. Wood, J. C. Walker, T. J. Harvey, S. Wang, and S. S. Rajahram, "Influence of microstructure on the erosion and erosion-corrosion characteristics of 316 stainless steel," *Wear*, vol. 306, no. 1–2, pp. 254–262, 2013.

[7.43] T. Singh, S. N. Tiwari, and G. Sundararajan, "Room temperature erosion behaviour of 304, 316 and 410 stainless steels," *Wear*, vol. 145, no. 1, pp. 77–100, 1991.

[7.44] L. Giourntas, "Investigation of erosion-corrosion behaviour of pump materials," Ph.D. Thesis, University of Strathclyde, 2016.

[7.45] M. Qian and W. Chaochang, "Impact-abrasion behavior of low alloy white cast irons," *Wear*, vol. 209, pp. 308–315, 1997.

[7.46] I. M. Hutchings, "Mechanisms of the Erosion of Metals by Solid Particles," *Eros. Prev. Useful Appl. ASTM STP 664*, W. F. Adler, Ed., American Society for Testing Materials, pp. 59-76, 1979.

Chapter 8

General discussion, conclusions and recommendations for future work

Chapter 8: General discussion, concluding remarks and recommendations for future work

Summary of findings

As a prelude to the general discussion and concluding remarks, a brief review of the main findings with respect to the objectives of the study (given in Chapter 1.1) is presented below.

1. Objective - Understand the degradation processes which are occurring in the Weir Group PLC hydraulic fracturing pumping equipment.
    - Finding - Assessment of post-service valve seats demonstrated significant corrosive wear damage along with repetitive impact wear.
    - Finding - Novel repetitive impact-with-slurry test rig developed to simulate the repetitive impact wear observed on valve seats – reproduced subsurface cracking of the carburised steel observed in both post-service valve seats and samples tested in the novel test rig.
    - Finding - Enhanced analysis of corrosive wear on the slurry impinging jet rig test samples demonstrated different degrees of relative damage in the different hydrodynamic zones; thus enhancing the assessment capabilities of the submerged jet impingement testing technique.
2. Objective - Assess the effect of altering the water source (freshwater to brine) on the corrosive wear behaviour of the materials.
    - Finding - For low alloy steel, as the salinity increased from 0.05%NaCl to 3.5%NaCl, the corrosive wear damage substantially increased, however, above 3.5%NaCl the material loss was observed to be similar.
    - Finding - For stainless steels, as the salinity increased, there was a marginal increase in corrosive wear damage at all salinity levels. The material damage for the stainless steels was significantly smaller compared to the low alloy steel.
3. Objective - Assess the potential benefit of applying cathodic protection (impressed current and sacrificial anode/coating) to extend the life of the hydraulic fracturing pumping equipment.
    - Finding - Both the impressed current and sacrificial anode cathodic protection methods were observed to be extremely beneficial for the low alloy steel. The positive result from this laboratory study has resulted in a

follow-up project assessing SACP in full scale hydraulic fracturing pump equipment.

4. Objective - Assess alternative materials, surface engineering treatments and alternative manufacturing methods to develop a material selection solution to assist with improving the life span of components.
    - Finding - Stellite 6 weld claddings exhibited generally good corrosive and repetitive impact wear resistance and would be worthy of further assessment. Nitriding was found to be effective in improving the mechanical wear resistance of the Stellite 6 weld claddings, but was observed to be detrimental to their corrosion resistance. Therefore, the nitrided Stellite 6 weld claddings may be a more attractive material candidate in freshwater environments.
    - Finding - The additive manufactured alloys were observed to exhibit better corrosion resistance in static and flowing conditions compared to conventionally manufactured alloys. Both additive manufactured and equivalent wrought alloys were found to have similar corrosive wear resistance. This indicates that the potential of additive manufacturing should now be assessed in terms of detailed manufacturing factors and cost as it is unlikely that there will be any impairment to the durability of additively manufactured components in corrosive wear applications.

8.1 General discussion

This section presents a general discussion regarding the main findings of the thesis and the potential impact that could have on hydraulic fracturing pumping equipment. The results from the slurry impinging jet experiments from each chapter are combined and presented as a material database for ranking purposes. Similarly, a ranking table for the test materials under repetitive impact with slurry is also presented.

8.1.1 Effect of salinity on erosion-corrosion

Hydraulic fracturing utilises a range of water supplies from low-salinity freshwater through to high salt burdens. Thus, the first part of this study was to assess the effect of salinity on the erosion-corrosion resistance of a low alloy steel and a variety of stainless steels. A

recently in-house developed volumetric analysis technique was used to characterise the various material degradation mechanisms that occur during a slurry impinging jet experiment. The aqueous solution used for testing contained suspended sand particles and the salinity varied from low salinity freshwater through to high salt burdens. Table 8.1 shows the volume losses (also as a percentage increase in volume loss) in the DIZ and OA of the tested materials for each salinity concentration. An increase in volume loss was observed for all of the tested materials in both wear regions as the salinity level was increased. The following comments are general outcomes observed for the effect of salinity on the test materials;

- In the DIZ, there were increases in volume losses from 3% to 29% with increased salinity level as the majority of damage in this region is mechanical (high angle erosion).
- Similarly, in the OA, the stainless steel alloys exhibited increases in volume loss from 3-30% with increased salinity as sliding abrasion wear was the predominant material degradation mechanism.
- However, in the OA, there was a substantial increase in volume loss for the low alloy steel (UNS G43400) as the salinity was increased from freshwater to greater salinities. This was attributed the poor corrosion resistance of the low alloy steel which was vulnerable to corrosion-related material degradation processes.

Table 8.1: *Volume losses (with percentage increase in volume loss – red text) in the DIZ and OA of the tested materials for each salinity concentration*

Material	VL DIZ (mm^3)			VL OA (mm^3)		
	0.05%NaCl	3.5%NaCl	10%NaCl	0.05%NaCl	3.5%NaCl	10%NaCl
UNS G43400	0.45	0.49 (8%)	0.53 (15%)	0.86	2.94 (71%)	2.42 (64%)
UNS S15500	0.36	0.37 (3%)	0.48 (25%)	0.38	0.44 (6%)	0.54 (30%)
UNS S32760	0.25	0.31 (19%)	0.34 (26%)	0.35	0.41 (15%)	0.45 (22%)
UNS S31600	0.34	0.39 (13%)	0.48 (29%)	0.36	0.37 (3%)	0.47 (23%)

In summary, therefore, it is evident that increases in salinity are likely to be significant in terms of material durability for all ferrous materials over a range of impingement angles but by far the most vulnerable grade of steel, in low angle corrosion abrasion conditions, is the low-alloy type that sees substantial application in the hydraulic fracturing industry. The limited studies which have been previously conducted to assess the effect of salinity have observed an initial increase in corrosion rate of the test materials before a reduction above salinity levels of 3-4%NaCl [8.1–8.3]. However, it should be noted that these previous studies were not conducted under slurry impingement test conditions.

8.1.2 Effect of cathodic protection on erosion-corrosion

Cathodic protection was utilised in this study for two purposes – to assist with the understanding of the fundamental wear mechanisms which occur during slurry impingement jet experiments and to assess the potential of using cathodic protection to reduce the corrosive wear of engineering alloys assessed in this study. Table 8.2 displays

the volume losses for all of the tested materials with the application of cathodic protection. The percentage highlighted in green indicates a lower volume loss, whereas, a percentage highlighted in red indicates a higher volume loss. As expected there was a substantial benefit in applying cathodic protection to the low alloy steel to reduce material loss in the corrosive wear environment. However, it should be noted that the majority of the reduction was observed in the OA, as mechanical damage is the predominant mechanism that occurs in the DIZ. Another interesting observation was that SACP, with both a zinc anode and Zinga paint, were just as effective in reducing the volume loss of the low alloy steel. For the other test materials, the application of cathodic protection generally provided a 1%-28% reduction in volume loss.

In summary, these findings have demonstrated that, from a fundamental corrosive wear mechanisms viewpoint, the test conditions in this project have represented circumstances in which, for materials with relatively good corrosion resistance, mechanical damage (high angle erosion and sliding abrasion) was the predominant wear mechanism. For lower grade materials (such as UNS G43400), however, the predominant deterioration mechanism depends crucially upon the impingement angle in that, at high angle, mechanical erosion mechanisms again dominate but, at lower (abrasion-like) angles, the corrosive wear is dominated by corrosion processes.

Table 8.2 provides another example of the benefits of discriminating the total mass loss (TML) from impingement tests on reasonably-sized specimens into damage in the DIZ and OA in which the TML registers a substantial benefit of the application of CP but the extended analysis reveals that this improvement is virtually entirely confined to the low-angle, (sand particles abrading the surface at low angles) region (OA). Moreover, the findings from this research have led to an investigation by the industrial sponsor to assess the potential of sacrificial anode cathodic protection in hydraulic fracturing pumping equipment.

Table 8.2: *Volume losses for all tested materials with the application of cathodic protection (green – lower, red – higher)*

Material	Full specimen (mm³)			DIZ (mm³)			OA (mm³)		
	FEC	CP	%	FEC	CP	%	FEC	CP	%
UNS G43400 ICCP	3.43	1.03	70	0.49	0.49	0	2.94	0.54	82
UNS G43400 SACP – zinc anode	3.43	0.91	73	0.49	0.43	12	2.94	0.49	83
UNS G43400 SACP – Zinga paint	3.43	0.98	71	0.49	0.55	12	2.94	0.43	85
UNS S15500	0.82	0.72	12	0.37	0.34	8	0.44	0.39	11
UNS S32760	0.71	0.59	17	0.31	0.28	10	0.41	0.31	24
UNS S31600	0.76	0.67	12	0.39	0.33	15	0.37	0.34	8
Stellite 6 single	0.89	0.88	1	0.36	0.39	8	0.54	0.42	22
Stellite 6 double	0.85	0.87	2	0.32	0.42	31	0.53	0.45	15
Nit. Stellite 6 single	0.69	0.63	9	0.34	0.30	12	0.35	0.33	6
Nit. Stellite 6 double	0.59	0.54	9	0.39	0.28	28	0.20	0.26	30
UNS S31600 W	0.75	0.70	7	0.39	0.35	10	0.36	0.37	3
UNS S31600 AM	0.79	0.75	5	0.41	0.34	17	0.38	0.40	5
UNS S15500 W	0.85	0.74	13	0.37	0.35	5	0.44	0.38	14
UNS S15500 AM	0.85	0.71	16	0.42	0.37	12	0.43	0.34	21
UNS R65400 W	0.68	0.59	13	0.28	0.26	7	0.41	0.33	20
UNS R56400 AM	0.66	0.64	3	0.27	0.27	0	0.39	0.37	5
UNS N07718 W	0.54	0.51	6	0.29	0.24	17	0.25	0.26	4
UNS N07718 AM	0.59	0.49	17	0.30	0.27	10	0.29	0.27	7

8.1.3 Comparison of materials in erosion-corrosion conditions

Table 8.3 demonstrates the material database which has been developed from the findings of this study under slurry impingement conditions. The vulnerability of the tested materials for each material degradation process was evaluated via a comparison with the austenitic stainless steel. The performance ratio (Eq. 8.1) between the austenitic stainless steel and the test material was utilised to evaluate the behaviour of each material and for each degradation process.

$$Performance\ ratio = \frac{Vol\ loss_{UNS\ S31600} - Vol\ loss_{test\ material}}{|Vol\ loss_{UNS\ S316100}|} \qquad \text{Eq. 8.1}$$

The green values highlighted in Table 8.3 indicate a lower volume loss compared to the austenitic stainless steel, whereas, a red value indicates a higher volume loss compared to the austenitic stainless steel.

The extended analysis enhances the material selection process by assisting with the prediction of service life for currently used and alternative materials for hydraulic fracturing pump components. From Table 8.3, the UNS G43400 low alloy steel is the worst performing material in nearly all aspects of resistance to erosion-corrosion in saline conditions. It is particularly poor at low angle – even in terms of resistance to pure mechanical abrasion damage but especially so in regards to corrosion-related attack. The low alloy steel was also the least resistant to pure erosion damage at 90° impingement angle. All-in-all, these comparative findings demonstrate that appropriate alternative material selection for hydraulic fracturing pumping equipment, should deliver improvements in component durability over a range of erosion-corrosion conditions.

The Cr-alloyed stainless steels and Ni-base alloys present potential improvements over most of the wear mechanisms (high angle erosion, sliding abrasion and corrosion) in Table 8.3. In this respect field experience has shown that the UNS S15500 stainless steel for fluid ends supports this feature but Table 8.3 indicates that increased life expectancy is likely to accrue from the adoption of a high-alloyed duplex stainless steel (UNS S32760) or of the Ni-Cr based alloys – but these strategies would entail increased cost.

In terms of obtaining an initial indication of the potential of AM materials, the data in Table 8.3 provides the first reported evidence that the AM process performs similarly and in some cases better, compared to conventionally manufactured alloys under corrosive wear conditions. Hence, the material database can help to build confidence in existing and new manufacturing technologies before the testing of full scale prototype hydraulic fracturing pump components.

Table 8.3: *Material database developed from study findings (3.5%NaCl with suspended sand particles)*

Material	TVL	TVL CP	E (DIZ)	C (DIZ)	S (DIZ)	SA (OA)	C(OA)	S (OA)
UNS G43400	3.5	0.5	0.5	0.2	1.9	0.5	59.1	89.9
UNS S15500	0.1	0.1	0.0	0.1	1.0	0.1	1.0	2.3
UNS S32760	0.1	0.1	0.1	0.7	0.7	0.1	0.6	6.9
Stellite 6 single	0.2	0.3	0.2	0.8	2.2	0.2	0.8	11.0
Stellite 6 double	0.1	0.3	0.3	0.9	3.9	0.2	0.8	7.5
Nit. Stellite 6 single	0.1	0.1	0.1	0.9	0.0	0.1	6.5	10.9
Nit. Stellite 6 double	0.2	0.2	0.2	0.8	2.0	0.3	3.5	12.1
UNS S31600 AM	0.1	0.1	0.0	0.5	15.7	0.1	0.8	0.3

UNS S15500 W	0.1	0.1	0.0	0.3	11.0	0.0	0.5	1.5
UNS S15500 AM	0.1	0.0	0.1	0.3	5.7	0.1	0.7	3.2
UNS R65400 W	0.1	0.2	0.3	0.8	2.3	0.1	0.7	2.9
UNS R56400 AM	0.1	0.1	0.2	0.8	4.3	0.0	0.8	1.4
UNS N07718 W	0.3	0.3	0.3	0.8	12.3	0.3	0.8	0.6
UNS N07718 AM	0.2	0.3	0.2	0.8	9.0	0.3	0.8	1.5
Green – Lower volume loss compared to UNS S31600W Red – Higher volume loss compared to UNS S31600W								

8.1.4 Repetitive impact testing

Table 8.4 shows the ranking of the tested materials under repetitive impact test conditions with respect to their wear scar depth. Surprisingly, the 27%Cr cast iron with the presence of chromium carbides (hard and brittle and would be expected to suffer from severe cracking and lead to significant material loss), performed the best under repetitive impact conditions and the currently used material for the valve seat (carburised UNS G86200) was only slightly more damaged than the 27%Cr cast iron. The results from the repetitive impact tests indicate that there is a trade-off between hardness and toughness which stops the

material from plastically deforming or from failing in a brittle manner (cracking). The best performing materials were hardened (through heat treatments or alloying) and exhibited a martensitic microstructure.

Table 8.4: *Ranking of the tested materials under repetitive impact conditions with respect to wear scar depth (where ranking number 1 is most resistant and 24 is least resistant)*

Material	Wear scar depth (µm)	Ranking
27% Cr cast iron	8	1
Carburised UNS G86200	11	2
UNS S42000 (480HV)	17	3
Induction hardened UNS G52986	19	4
Quenched & tempered UNS G52986	26	5
UNS S15500 AM	28	6
Induction hardened UNS G41400	29	7
UNS N07718 AM	30	8
UNS N07718 W	36	9
UNS R56400 AM	39	10
UNS S15500 W	39	11
Nitrided 905M39 steel	39	12
Stellite 6 double	43	13
UNS S32760	52	14
UNS R56400 W	55	15
Nit. Stellite 6 double	56	16

37%Cr cast iron	58	17
Stellite 6 single	78	18
UNS S42000 (280HV)	81	19
UNS S44003	98	20
UNS S44004	103	21
UNS S31600 AM	170	22
HVOF WC-10Ni	175	23
UNS S31600 W	245	24

8.2 Concluding remarks

This research project has involved an experimental study of the factors that are considered to contribute to serious material degradation of key components in the pumping systems used in the hydraulic fracturing industry. The main objectives have been to identify the major material degradation mechanisms and to assess the potential of alternative materials, manufacturing processes and surface engineering strategies that could deliver more durable components compared to the currently used materials.

Evidence from the field indicated that the pump components were suffering from corrosive attack and erosion-corrosion over a range of impingement angles in aqueous slurries. In addition, the valve and seats were subjected to periodic metal on metal impact. To investigate this latter phenomenon, repetitive impact testing equipment was developed and used to assess the comparative performance of a range of materials. The conclusions from the experimental conditions (erosion-corrosion and repetitive impact wear) conducted in this study are outlined below.

8.2.1 Currently used materials -Low alloy steel (UNS G43400) and carburised low alloy steel (UNS G86200)

The carburised steel proved to be one of the most resistant to repetitive impact but suffered serious damage, from both mechanical and corrosion-related attack, in erosion-corrosion situations from field experience. The low alloy steel was also observed to be more vulnerable in high salinity aqueous solutions. This observation provides an indication that the durability issue in service mainly involves corrosive wear rather than direct impact processes. The findings illustrate how the choice of optimum material represents a formidable challenge. There was, however, clear evidence that the application of CP, even in the presence of suspended solid particles, was capable of reducing the severity of degradation and this feature has led to the initiation of a follow-up project, the objective of which is to assess the potential application of CP in near-operational and service conditions.

8.2.2 Alternative conventional materials and surface engineering treatments

The investigation has demonstrated that corrosion-resistant alloys provide superior resistance to erosion-corrosion and this has led to application of UNS S15500 precipitation hardened stainless steel for some components in the hydraulic fracturing pumping equipment. Higher-alloy stainless steels appear to be additionally durable but there are obvious cost considerations associated with their adoption. The repetitive impact testing also demonstrated that there are potential material candidates (such as the 27%Cr cast iron) other than the carburised steel which could provide increased component life of the valve and valve seats.

8.2.3 Additive manufactured materials

These alloys are receiving attention over a wide spectrum of engineering industries. This research appears to represent the first reported assessment of the behaviour of such materials in erosion-corrosion conditions and has provided evidence that such materials are able to match their wrought counterparts. In terms of pure corrosion; this work has indicated that the AM materials possess even greater resistance to attack in quiescent and rapidly flowing (no solids) saline solutions. Thus, the main issues with employing AM materials in hydraulic fracturing pumping equipment is likely to be associated with cost and manufacturing detail rather than issues of durability.

8.2.4 Mechanisms

Erosion-corrosion

- The in-house volumetric analysis technique enabled the discrimination of the two different wear regions which occur during slurry impingement testing:
    - High angle corrosive wear where solid particles result in impact craters forming within the wear scar (direct impinged zone)
    - Low angle corrosive wear where solid particles cause abrasion-like ploughing damage and pitting due to corrosive attack is commonly observed in poor corrosion resistant materials.
- The best performing materials were observed to be 2-phase materials that exhibited good resistance to pure corrosion and pure mechanical damage. However, they tended to suffer from synergy due to micro-galvanic attack at the boundary between the two phases.

Pure electrochemical attack

- An increase in corrosion rates was generally observed from static to flowing (no solids) conditions. This occurred due to the turbulence in the aqueous solution as well as increased oxygen transport to the test surface which resulted in an increase in the rate of the oxygen reduction reaction.
- Corrosion rates generally increased when solid particles were suspended in the aqueous solution. This was due to de-passivation/re-passivation events occurring to the passive oxide films present in the corrosion resistant materials.

Pure mechanical damage

- Any relationship between mechanical properties and resistance to mechanical erosion damage is not straightforward. The commonly observed correlation between abrasion resistance and high hardness is problematical as it was not always observed to be the case in this research study as other material characteristics such as grain size, grain morphology, etc. are also likely to influence the abrasion resistance of a material.

Repetitive impact

- Repetitive impact wear mechanisms were dependent upon material types
    - Soft/ductile materials were observed to suffer from severe plastic deformation (as demonstrated in Figures 5.25, 5.27, 5.34)
    - Hard/brittle materials were observed to suffer from a network of cracks. (as demonstrated in Figures 5.35, 5.36, 5.37 and 5.38)
- The optimum material properties required for repetitive impact resistance is hardness to resist plastic deformation and toughness to resist cracking and brittle failures. However, it is well known that there is a trade-off between hardness and toughness, hence, material selection is not trivial.

8.3 Recommendations for future work

The following list of topics are suggestions for continuation of this work;

- Erosion-corrosion testing: engineering components within the hydraulic fracturing pump and associated equipment are exposed to various angles of impingement, therefore, experiments conducted at various impingement angles (20°, 45°, 60°) will broaden the knowledge in material behaviour.
- Erosion-corrosion testing: more environmental parameters should also be considered such as pH (acid hydraulic fracturing stage), velocity, sand concentration, proppant material (resin silica sand, ceramic). This will assist in determining their effect of erosion, corrosion and synergy in the hydraulic fracturing pump equipment.
- The clear benefits of applying cathodic protection to the low alloy steel (which is used widely in the hydraulic fracturing pump equipment) was observed in this work. The next stage would be to design and implement sacrificial anodes into the equipment to help extend the life of the hydraulic fracturing pump equipment.
- Auger electron spectroscopy to characterise the passive oxide films of the tested AM and wrought alloys
- Further work could also be conducted in assessing other AM processes (Wire Arc AM, EBM, etc.) as well as materials (functionally graded composite coatings).

- Full scale components (new and repaired) with weld cladding and AM techniques to assess their microstructure and corrosive wear properties in controlled full scale testing conditions.
- Repetitive impact testing – Effect of load, proppant (resin coated sand, ceramic), impact angle, salinity.
- Assessment of corrosive and repetitive impact wear resistance of elastomer materials for the valve.

8.4 References

[8.1] D. Brondel, R. Edwards, A. Hayman, D. Hill, and T. Semerad, “Corrosion in the Oil Industry,” *Oilf. Rev.*, pp. 4–18, 1994.

[8.2] H. H. Uhlig and M. C. Morrill, “Corrosion of 18-8 Stainless Steel in Sodium Chloride Solutions,” *Ind. Eng. Chem.*, vol. 33, no. 7, pp. 875–880, 1941.

[8.3] J. Chen, J. Wang, B. Chen, and F. Yan, “Tribocorrosion Behaviors of Inconel 625 Alloy Sliding against 316 Steel in Seawater,” *Tribol. Trans.*, vol. 54, pp. 514–522, 2011.

Appendix A: Chapter 4 additional figures

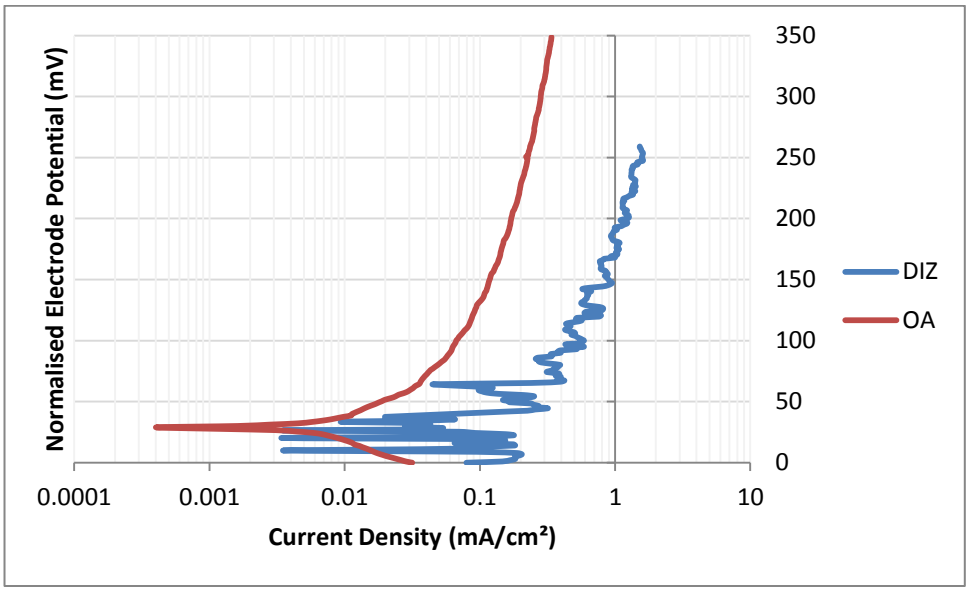

Figure A-1: *Anodic polarisation scans on both wear regions of UNS G43400 in 0.05%NaCl solid-liquid conditions*

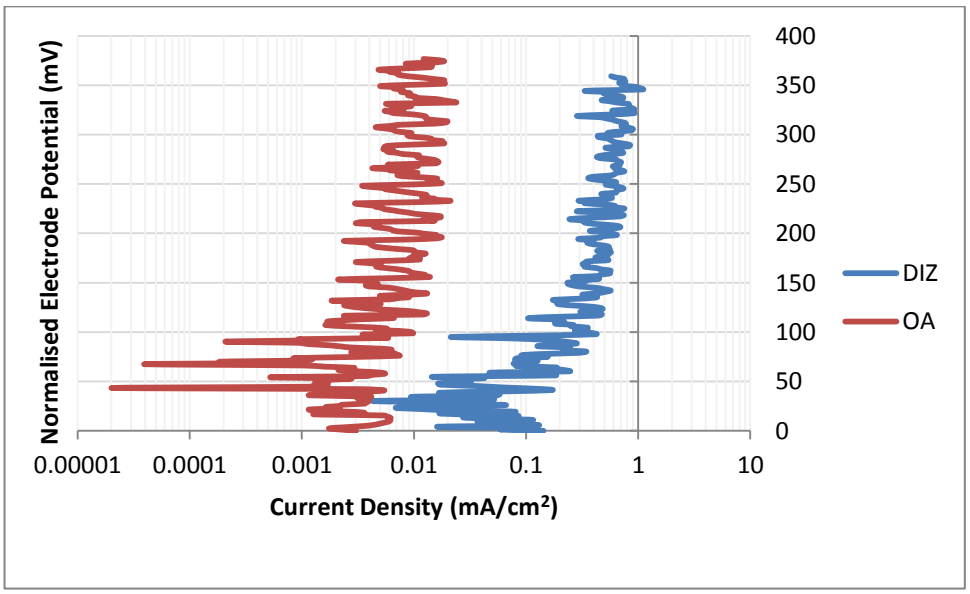

Figure A-2: *Anodic polarisation scans on both wear regions of UNS S32760 in 0.05%NaCl solid-liquid conditions*

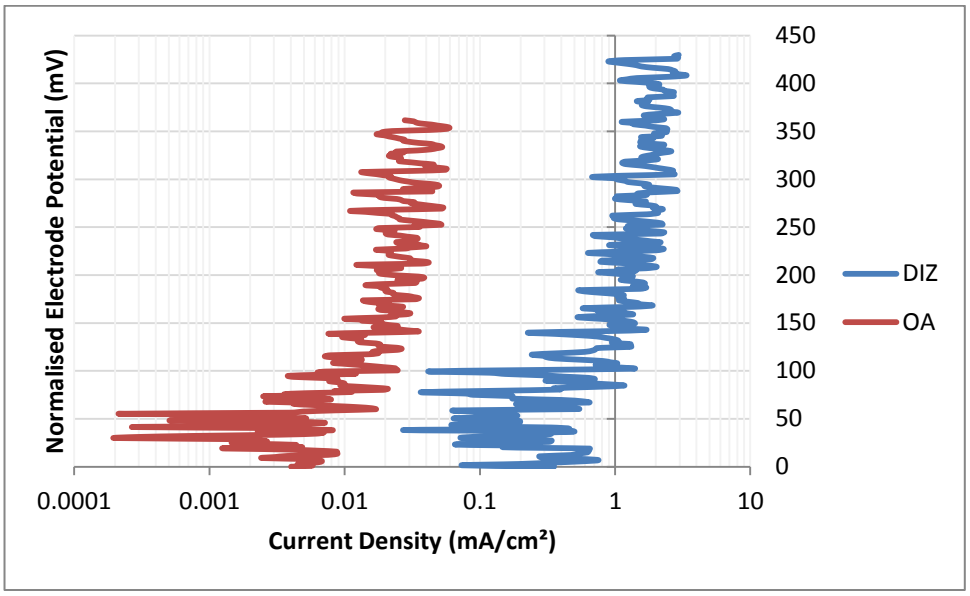

Figure A-3: *Anodic polarisation scans on both wear regions of UNS S31600 in 0.05%NaCl solid-liquid conditions*

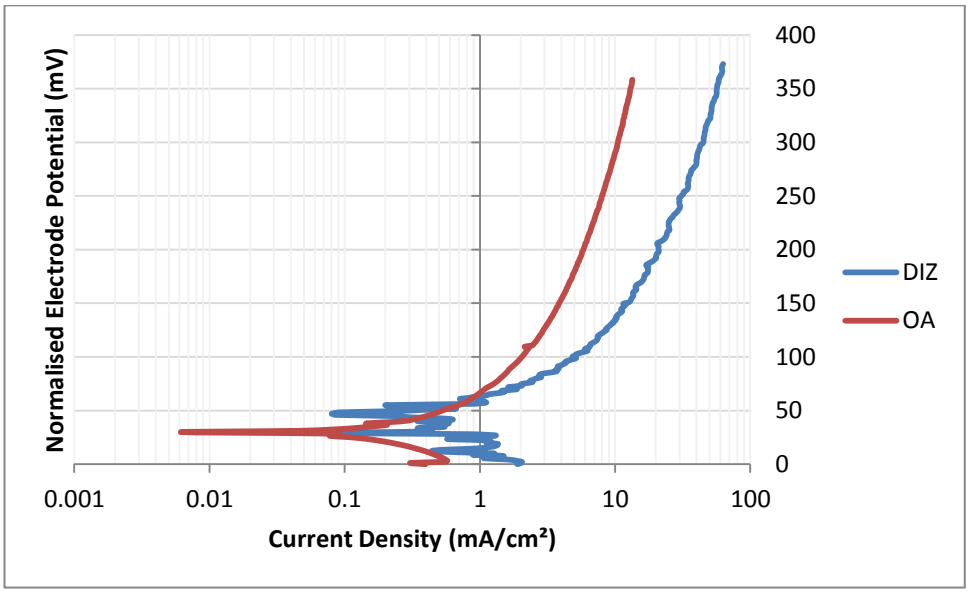

Figure A-4: *Anodic polarisation scans on both wear regions of UNS G43400 in 3.5%NaCl solid-liquid conditions*

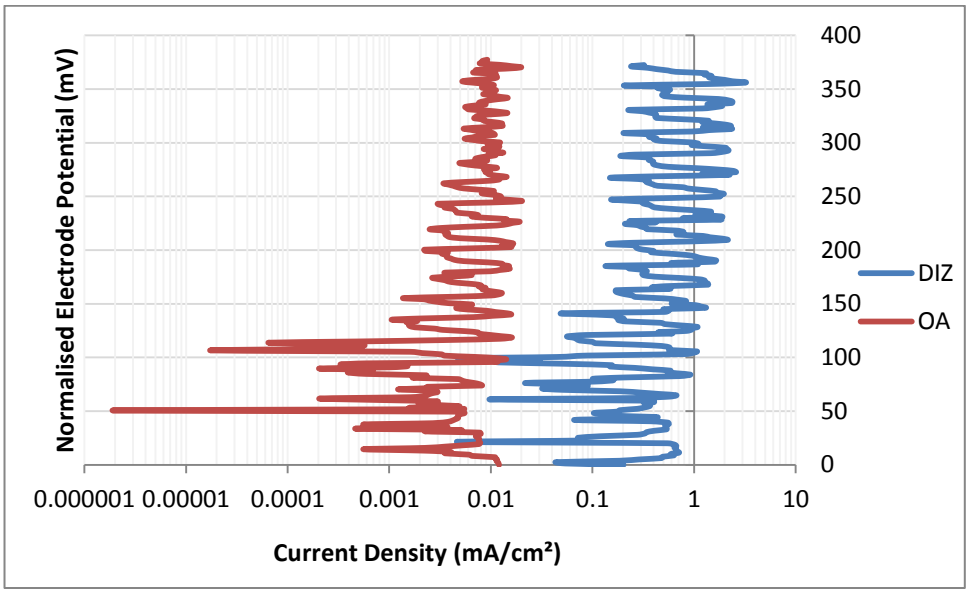

Figure A-5: *Anodic polarisations on both wear regions of UNS S32760 in 3.5%NaCl solid-liquid conditions*

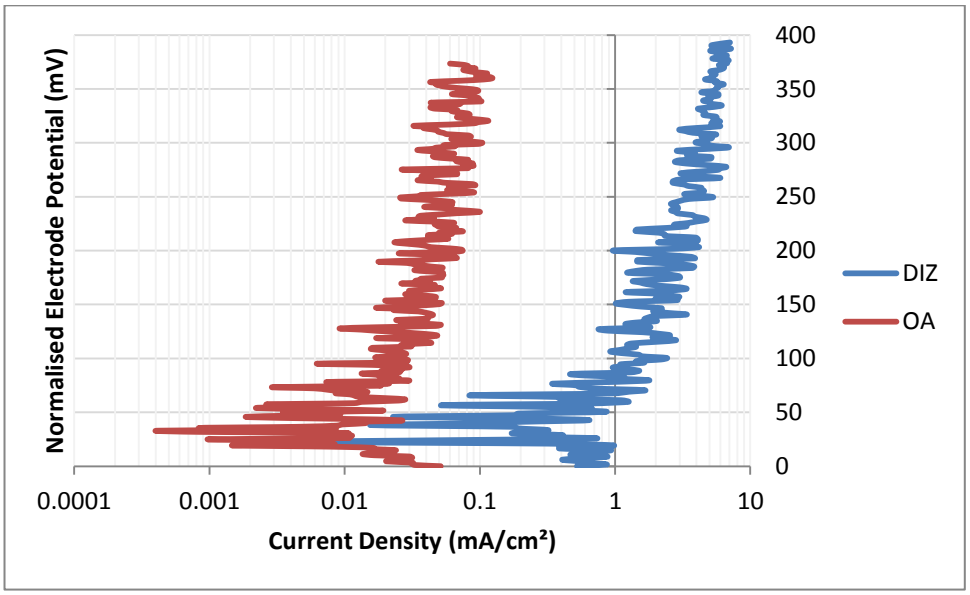

Figure A-6: *Anodic polarisations on both wear regions of UNS S31600 in 3.5%NaCl solid-liquid conditions*

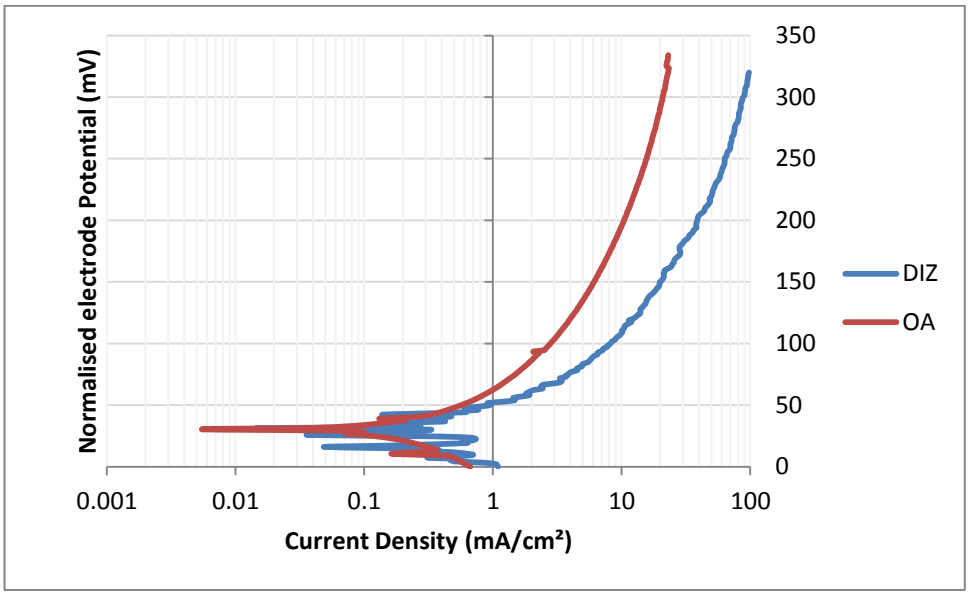

Figure A-7: *Anodic polarisations on both wear regions of UNS G43400 in 10%NaCl solid-liquid conditions*

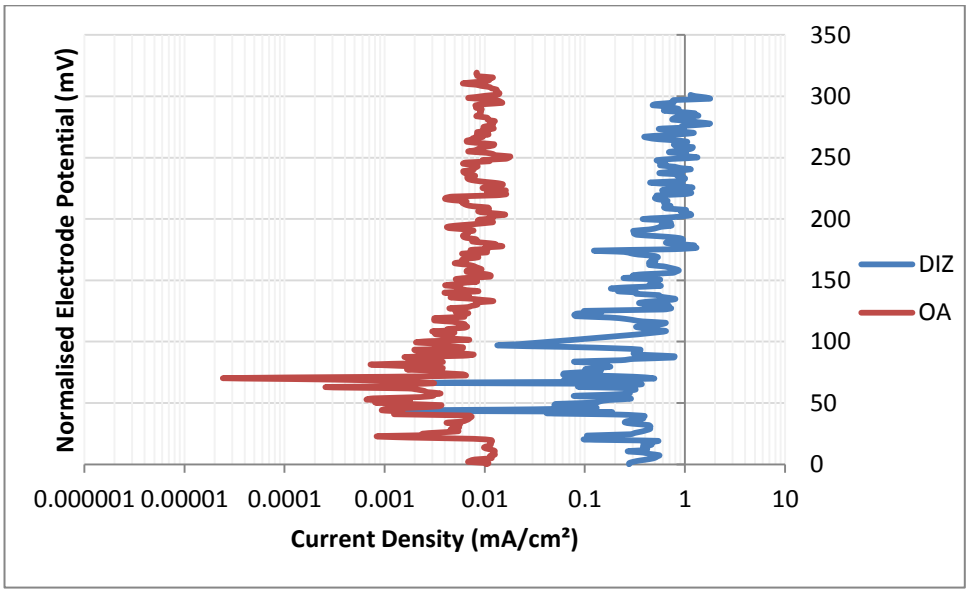

Figure A-8: *Anodic polarisations on both wear regions of UNS S32760 in 10%NaCl solid-liquid conditions*

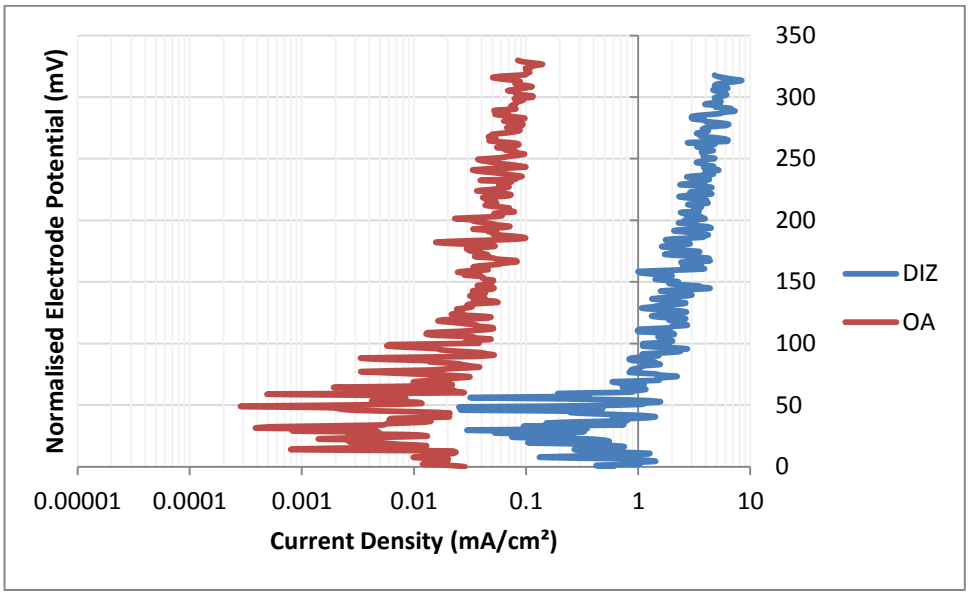

Figure A-9: *Anodic polarisations on both wear regions of UNS S31600 in 10%NaCl solid-liquid conditions*

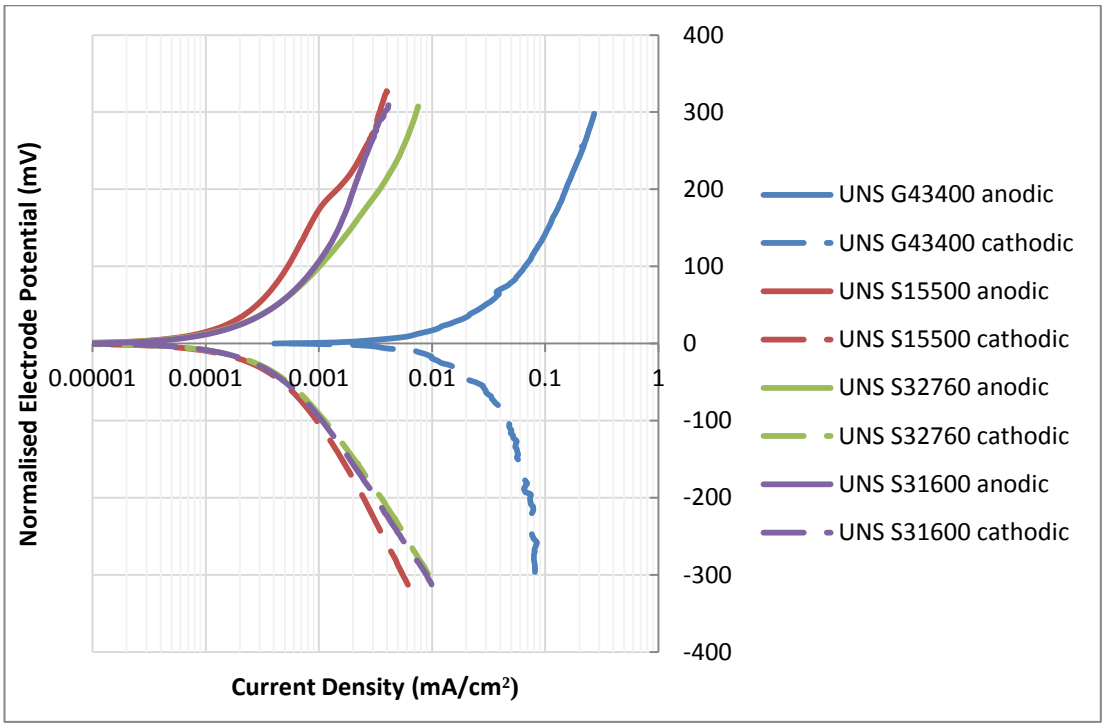

Figure A-10: *Anodic and cathodic polarisation scans on the full specimen of the tested materials in 0.05%NaCl static conditions*

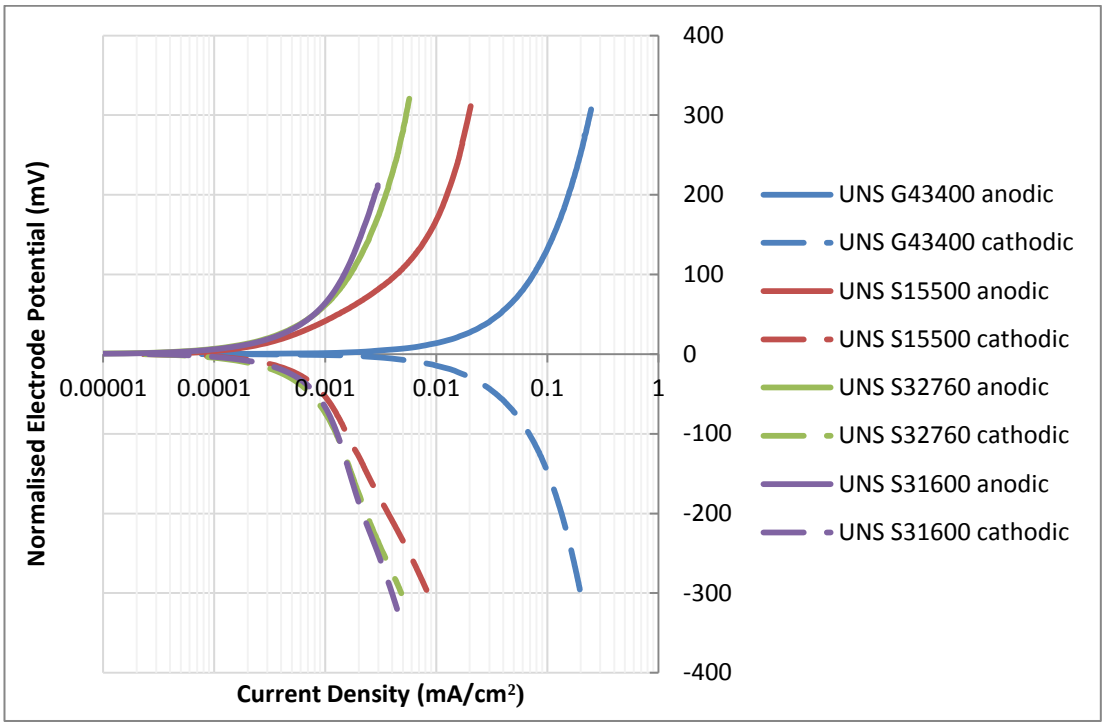

Figure A-11: *Anodic and cathodic polarisations scans on the full specimen of the tested materials in 0.05%NaCl flowing conditions*

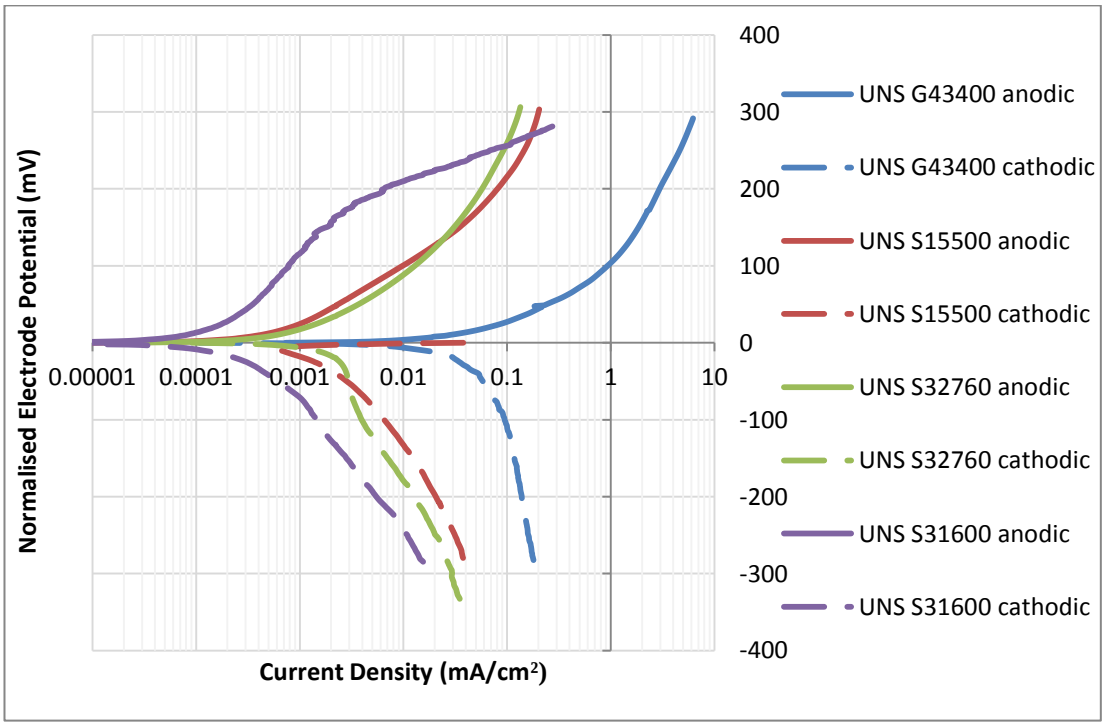

Figure A-12: *Anodic and cathodic polarisation scans on the full specimen of the tested materials in 3.5%NaCl static conditions*

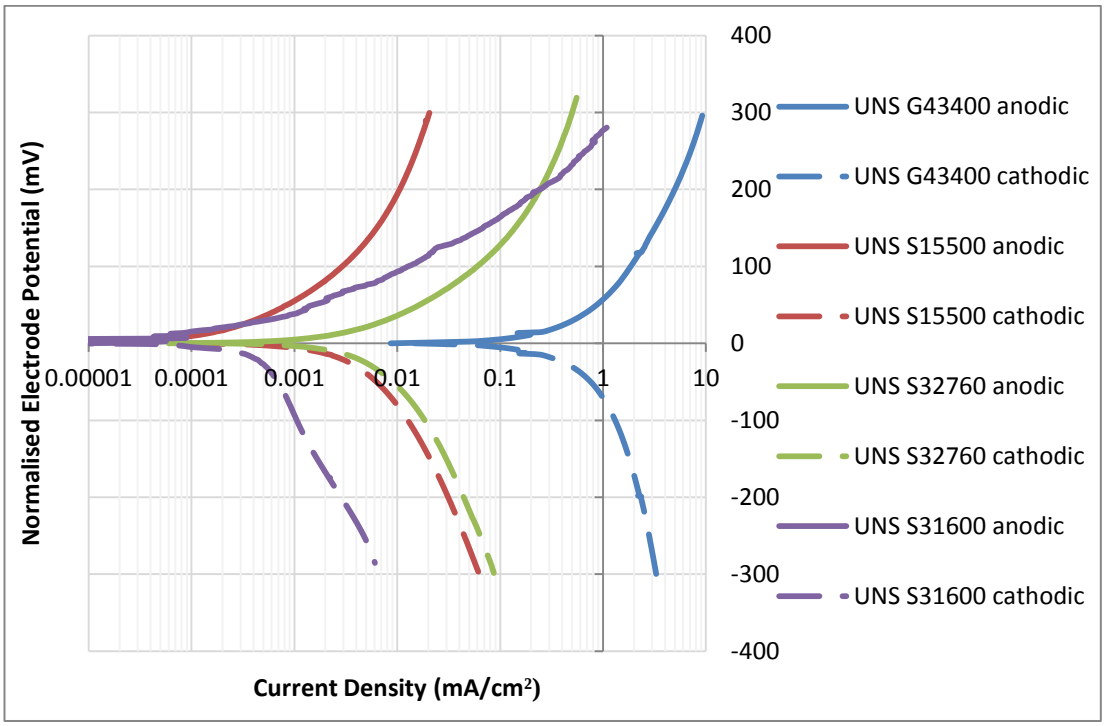

Figure A-13: *Anodic and cathodic polarisation scans on the full specimen of the tested materials in 3.5%NaCl flowing conditions*

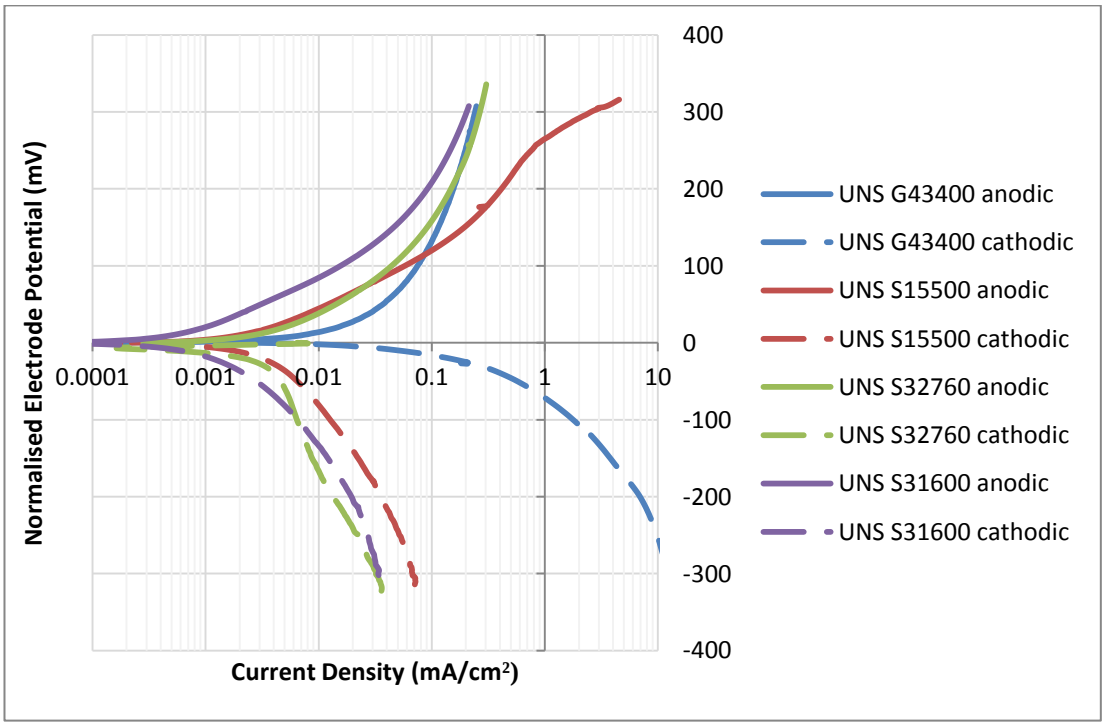

Figure A-14: *Anodic and cathodic polarisation scans on the full specimen of the tested materials in 10%NaCl static conditions*

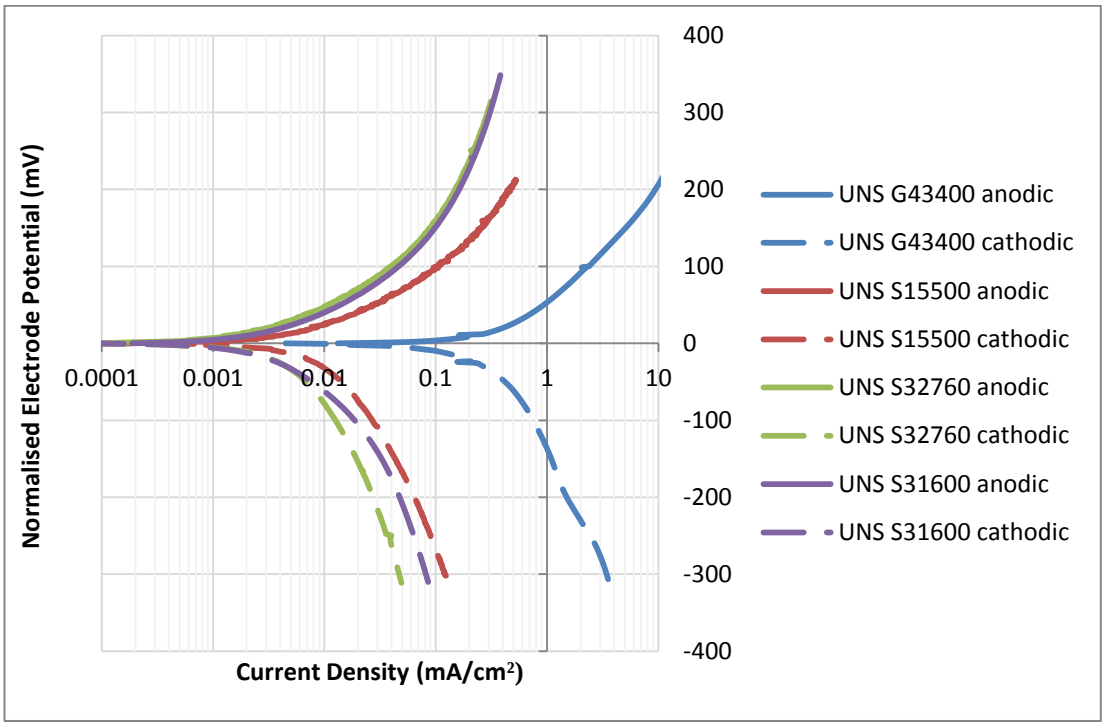

Figure A-15: *Anodic and cathodic polarisation scans on the full specimen of the tested materials in 10%NaCl flowing conditions*

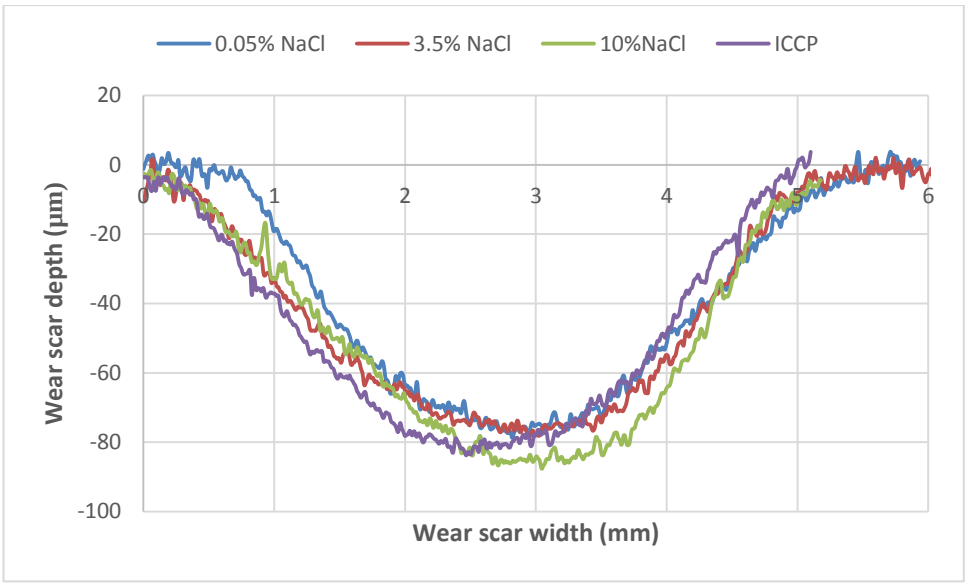

Figure A-16: *Wear scar profile for UNS G43400 in each testing environment in solid-liquid conditions*

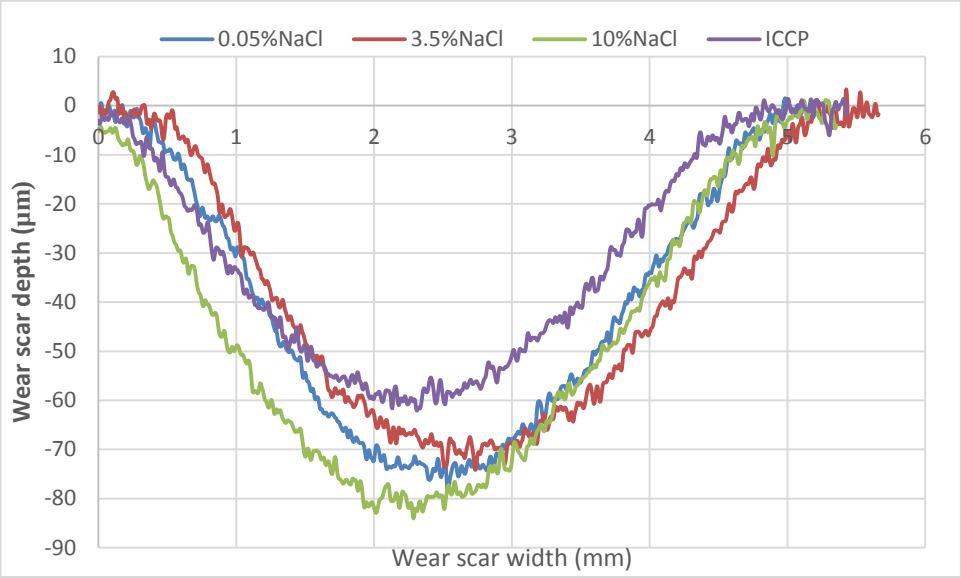

Figure A-17: *Wear scar profile for UNS S15500 in each testing environment in solid-liquid conditions*

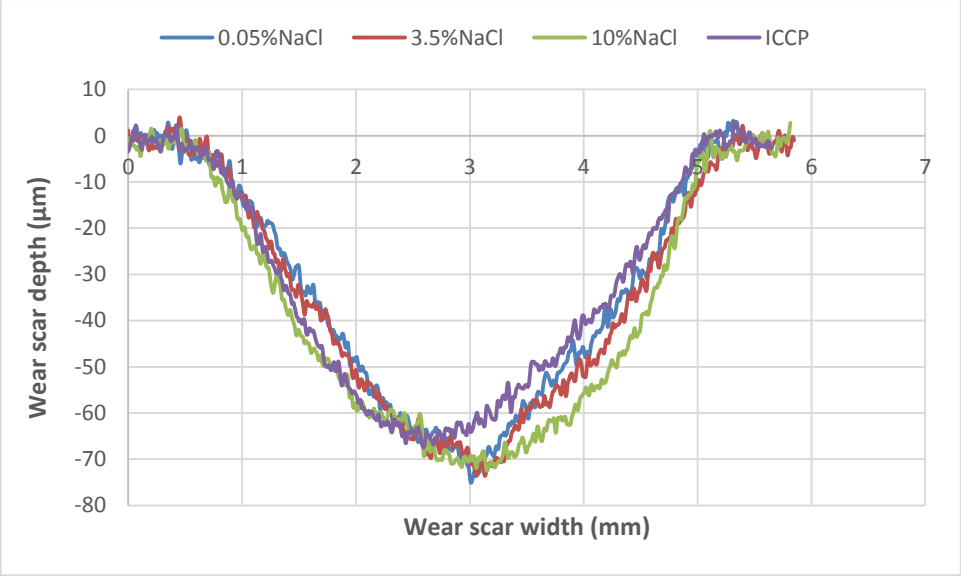

Figure A-18: *Wear scar profiles for UNS S31600 in each testing environment in solid-liquid conditions*

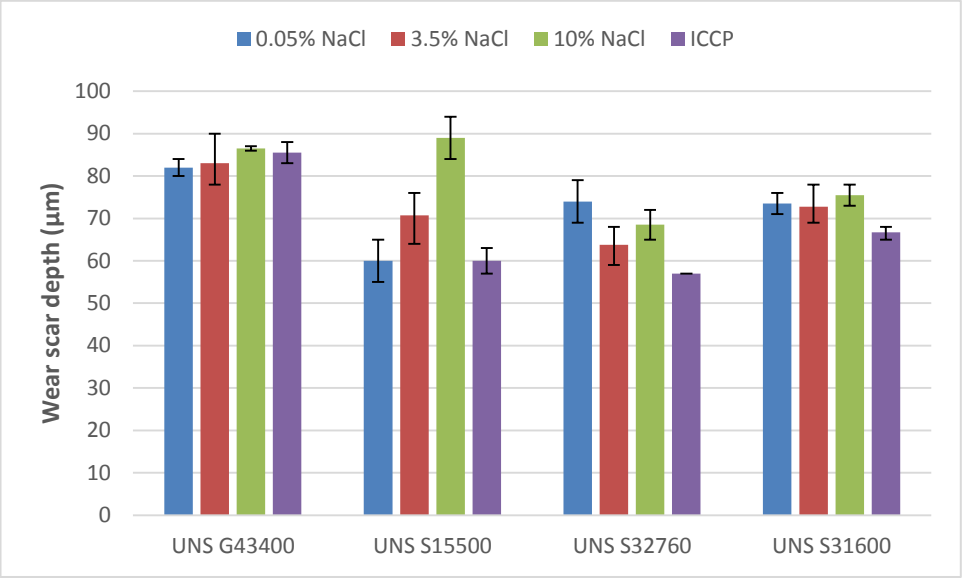

Figure A-19: *Wear scar depths for each test material in the three different salinities and in ICCP conditions*

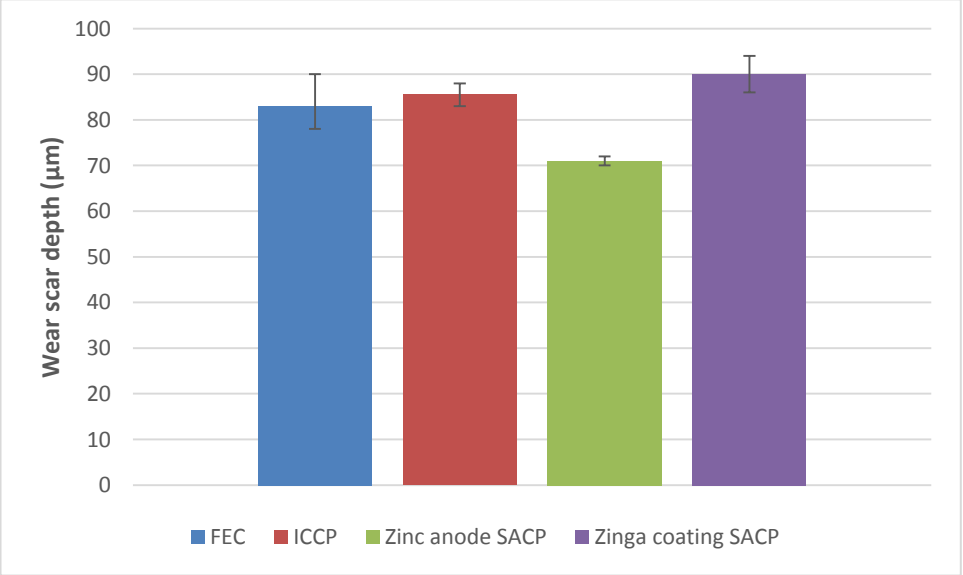

Figure A-20: *Wear scar depths for UNS G43400 in FEC, ICCP and both SACP conditions*

Appendix B: Chapter 6 additional figures

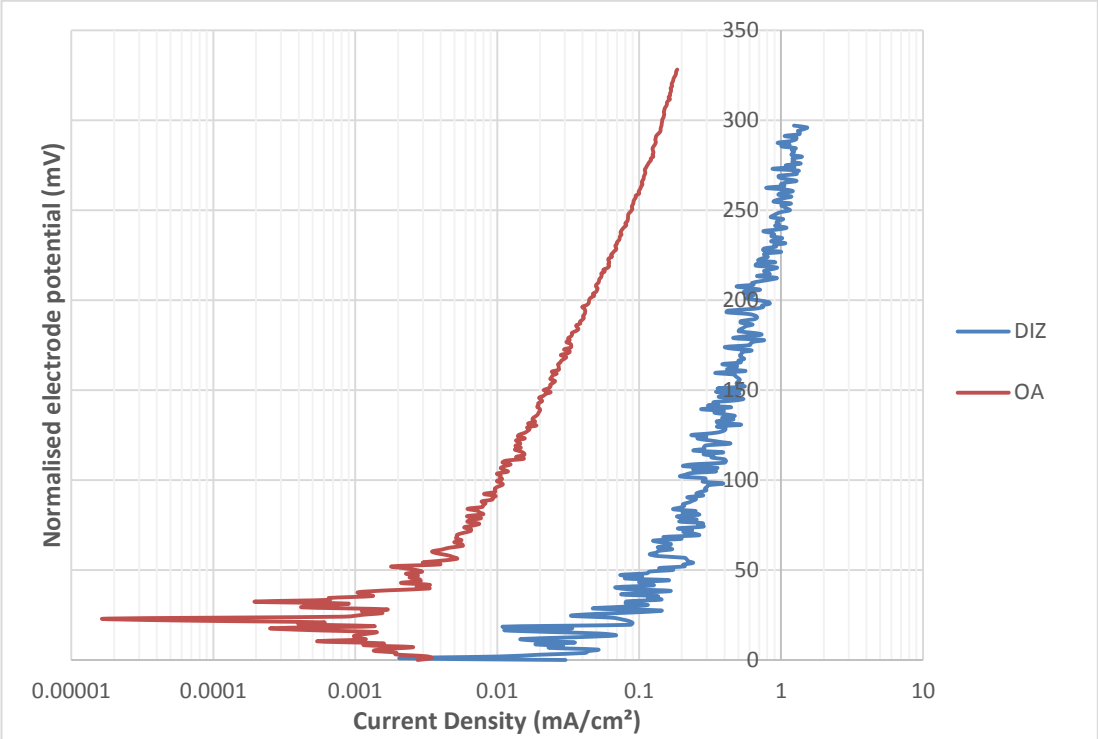

Figure B-1: *Anodic polarisation scans in both wear regions of Stellite 6 double layer weld cladding in solid-liquid conditions*

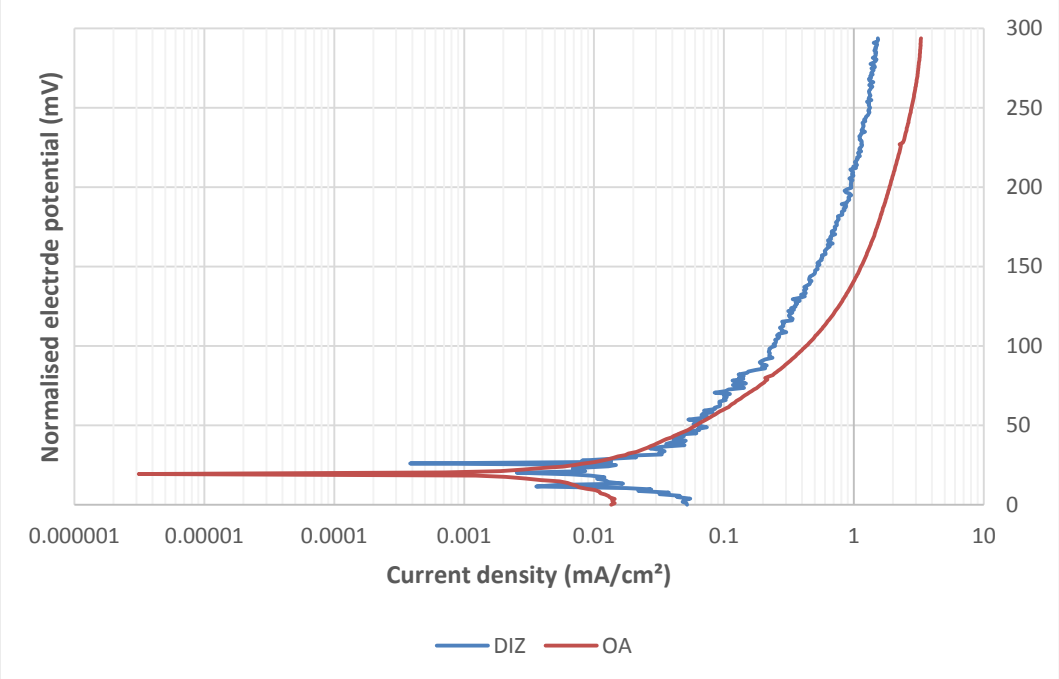

Figure B-2: *Anodic polarisation scans in both wear regions of Nitrided Stellite 6 single layer weld cladding in solid-liquid conditions*

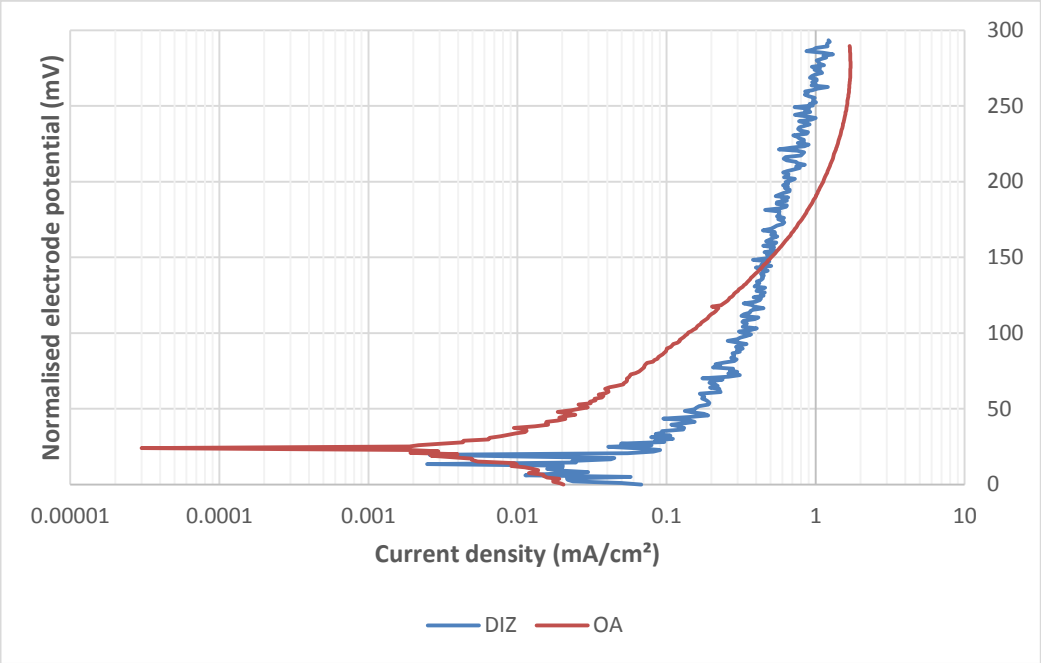

Figure B-3: *Anodic polarisation scans in both wear regions of Nitrided Stellite 6 double layer weld cladding in solid-liquid conditions*

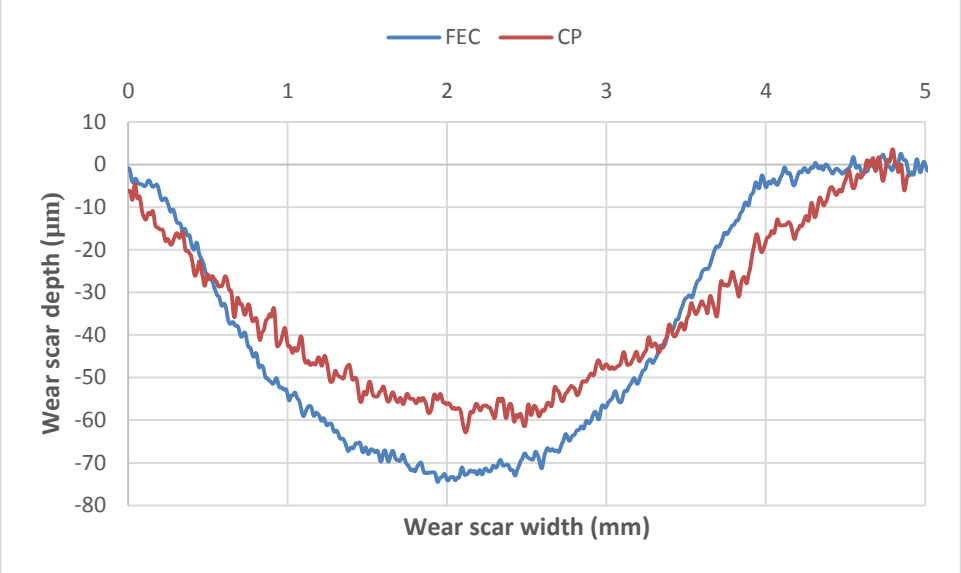

Figure B-4: *Wear scar profiles for Stellite 6 Single layer weld cladding in FEC and ICCP conditions*

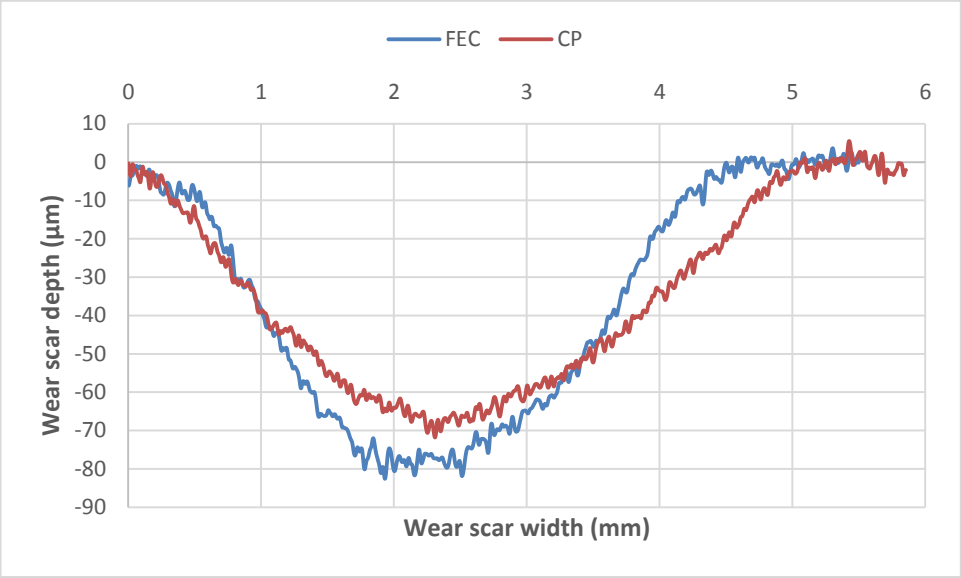

Figure B-5: *Wear scar profile for Stellite 6 Double layer weld cladding in FEC and ICCP conditions*

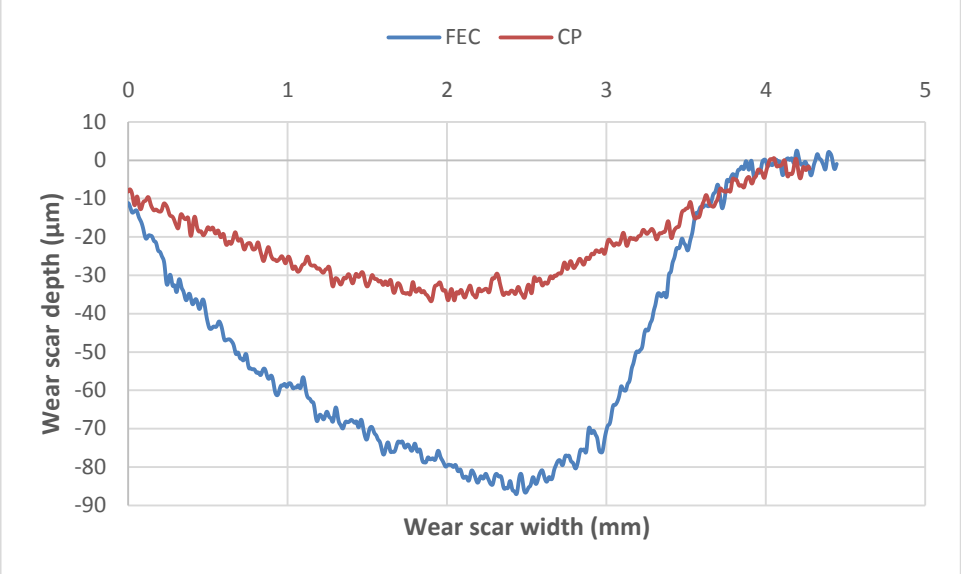

Figure B-6: *Wear scar profiles for Nit. Stellite 6 Double layer weld cladding in FEC and ICCP conditions*

Appendix C: Chapter 7 additional figures

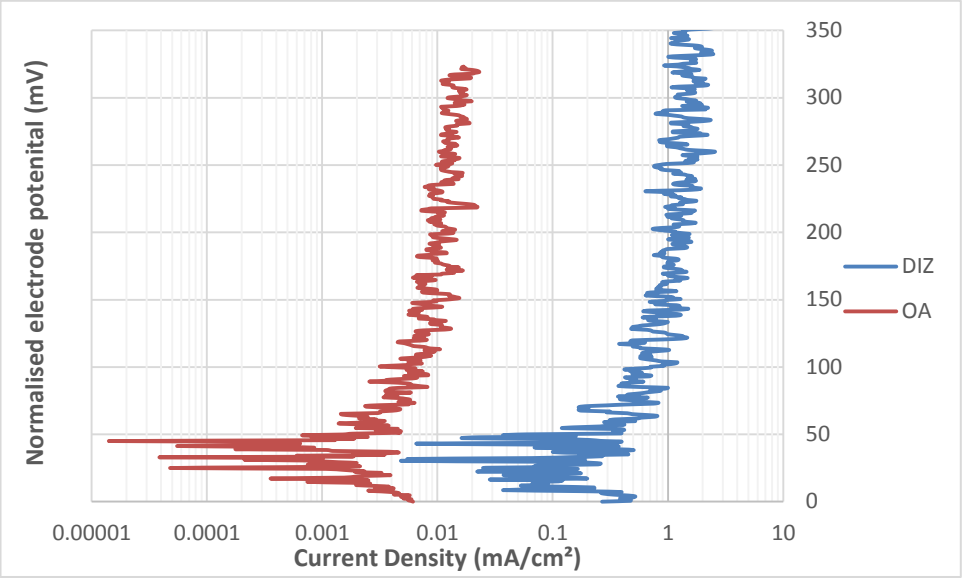

Figure C-1: *Anodic polarisation scans on both wear regions of UNS S31600 AM in solid-liquid conditions*

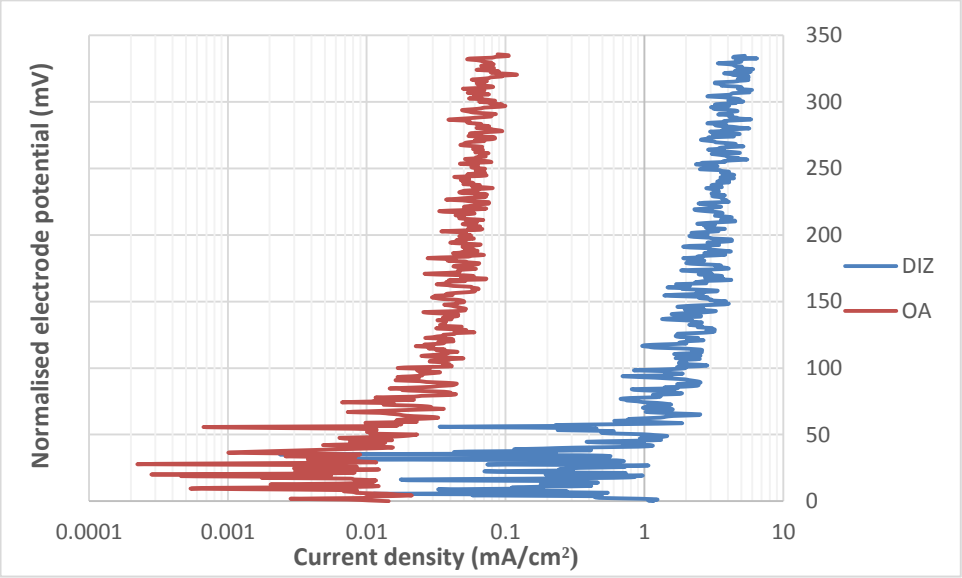

Figure C-2: *Anodic polarisation scans on both wear regions of UNS S15500 W in solid-liquid conditions*

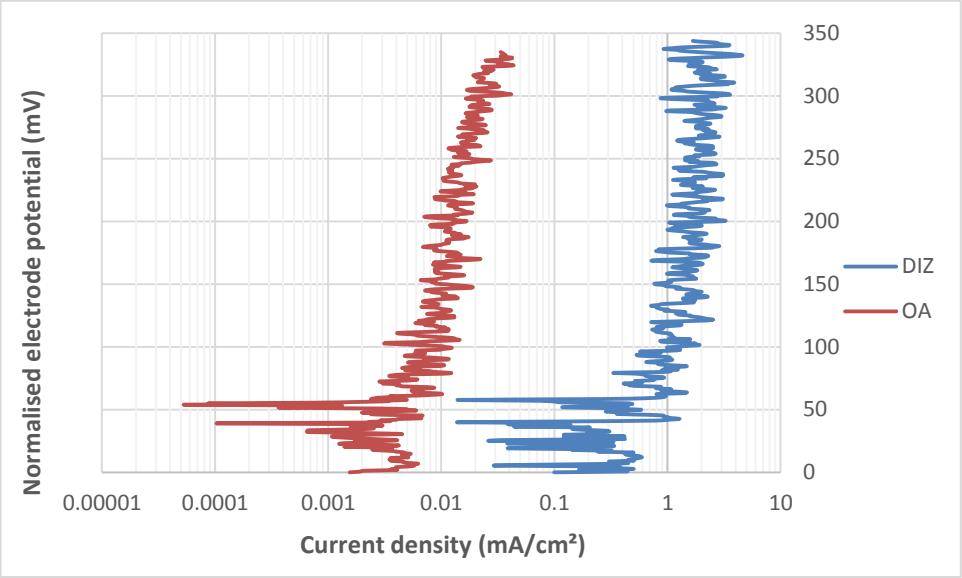

Figure C-3: *Anodic polarisation scans on wear regions of UNS S15500 AM in solid-liquid conditions*

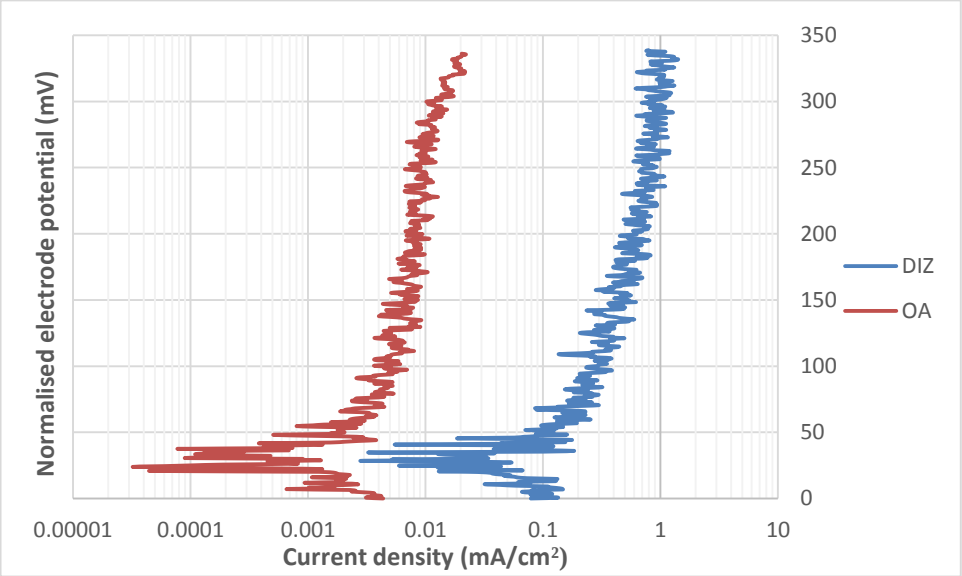

Figure C-4: *Anodic polarisation scans on wear regions of UNS N07718 W in solid-liquid conditions*

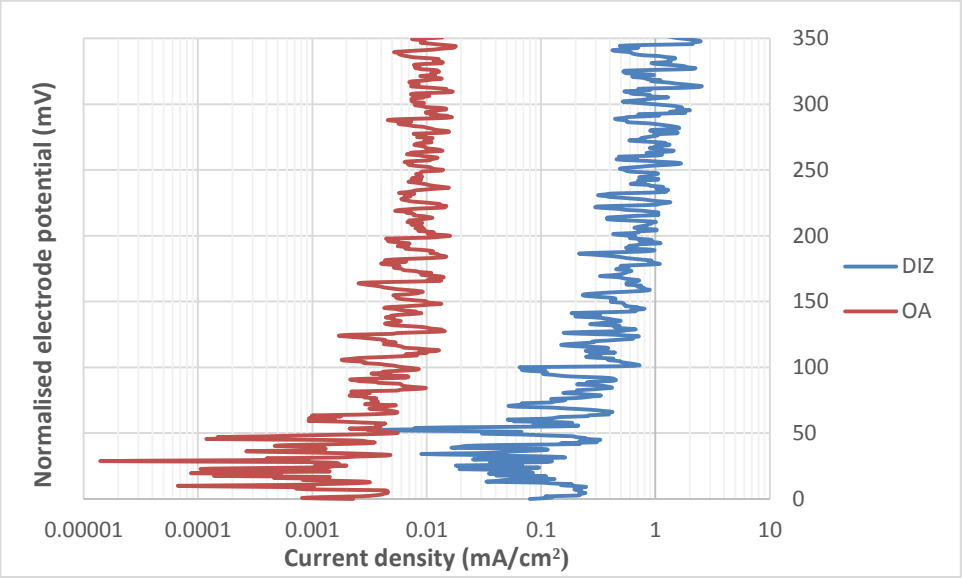

Figure C-5: *Anodic polarisation scans on both wear regions of UNS N07718 AM in solid-liquid conditions*

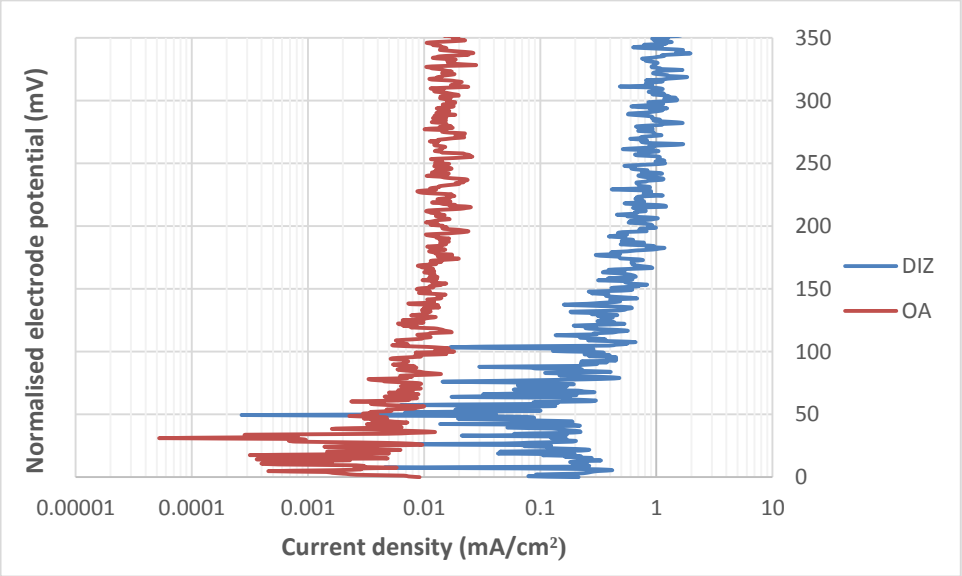

Figure C-6: *Anodic polarisation scans on both wear regions of UNS R56400 W in solid-liquid conditions*

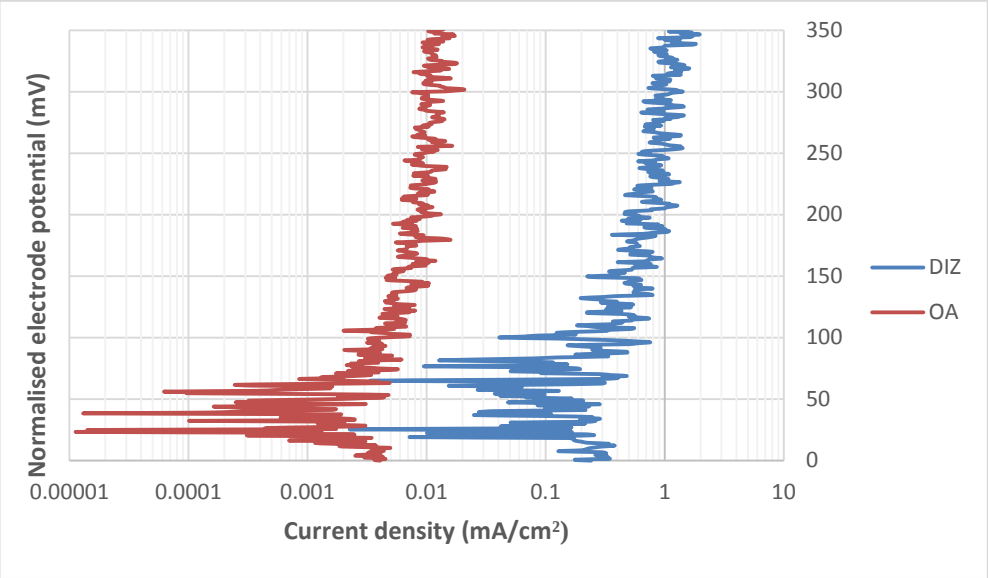

Figure C-7: *Anodic polarisation scans on both wear regions of UNS R56400 AM in solid-liquid conditions*

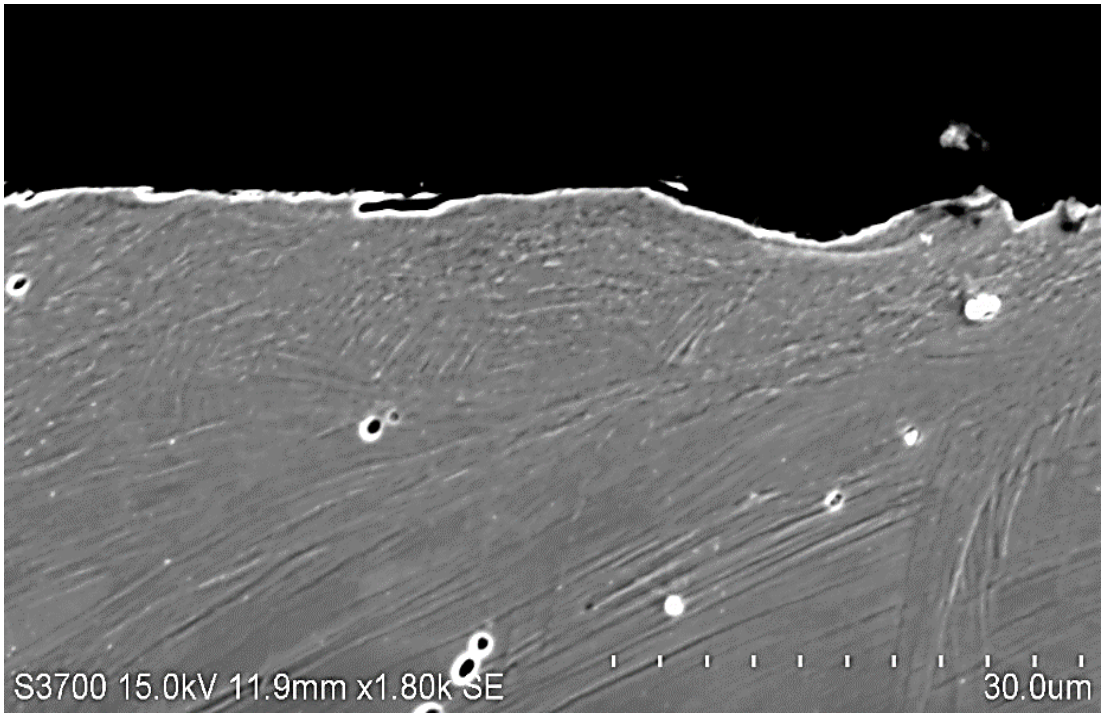

Figure C-8: *Cross section of erosion-corrosion wear scar of UNS S31600 W with plastically deformed material and craters caused by impacting solid particles*

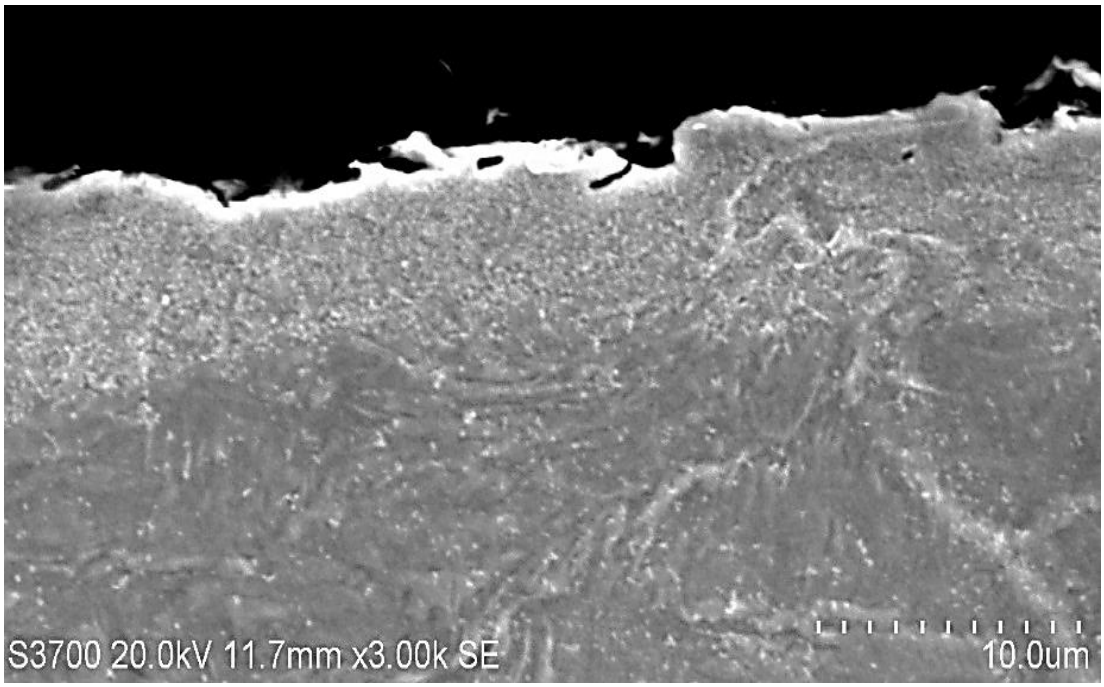

Figure C-9: *Cross section of erosion-corrosion wear scar of UNS S31600 AM with plastically deformed material*

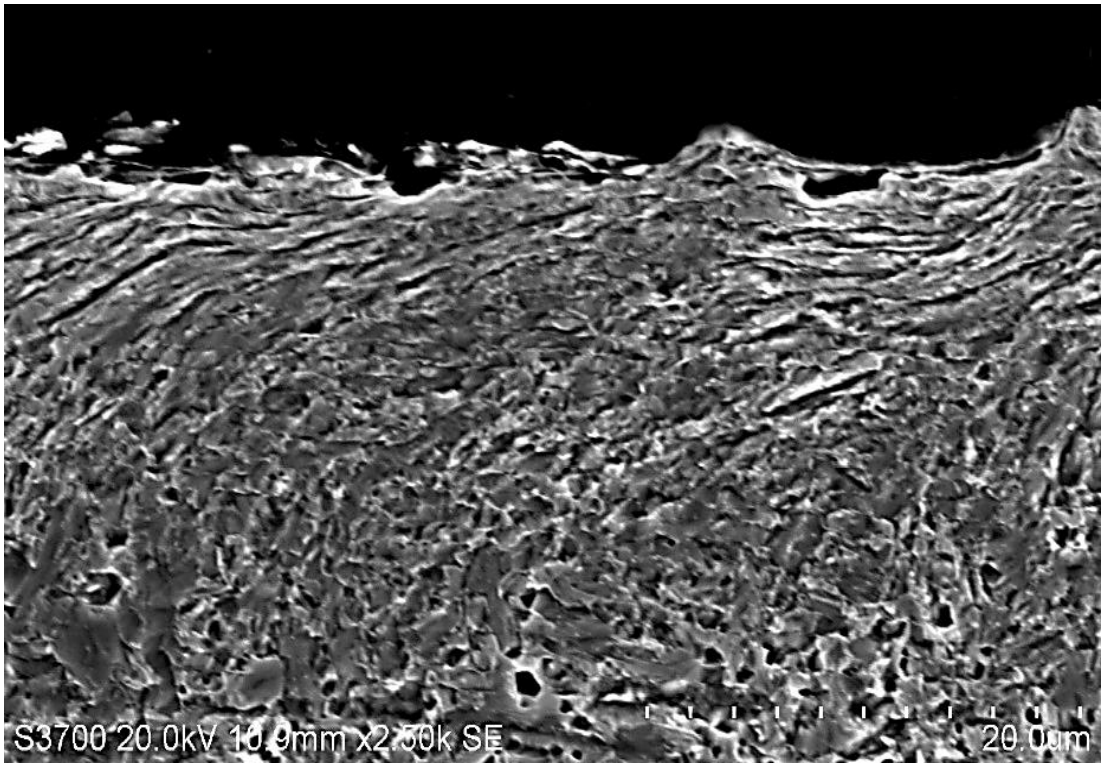

Figure C-10: *Cross section of erosion-corrosion wear scar of UNS S15500 AM with plastically deformed material*

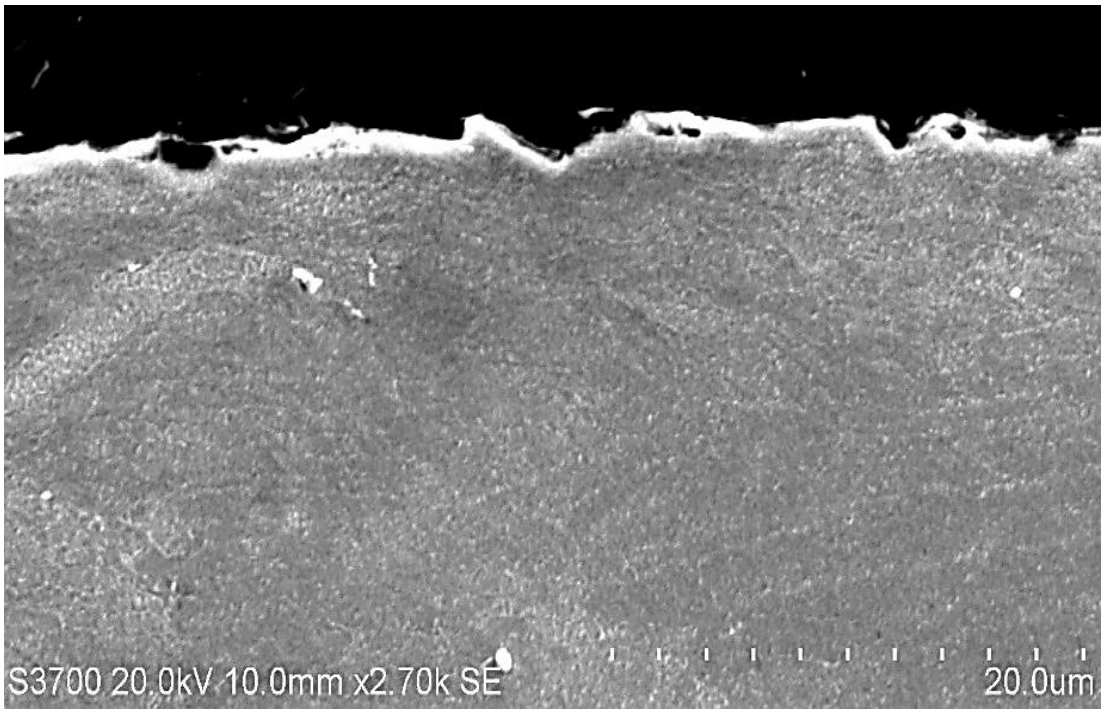

Figure C-11: *Cross section of erosion-corrosion wear scar of UNS N07718 W with plastically deformed material*

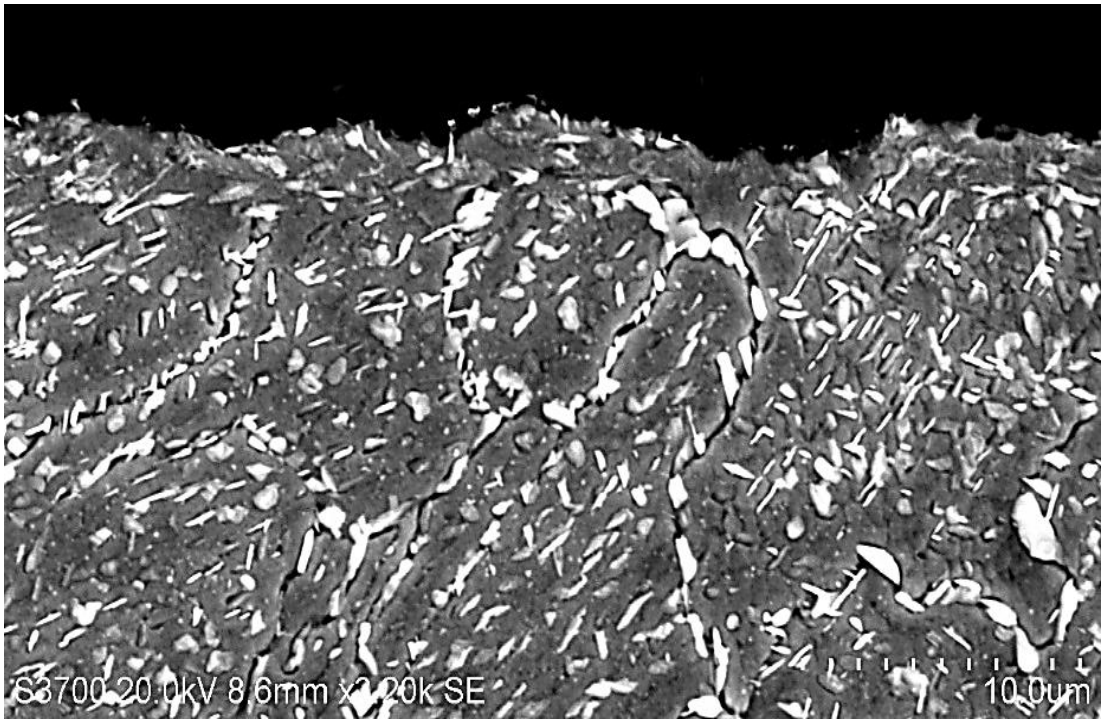

Figure C-12: *Cross section of erosion-corrosion wear scar of UNS N07718 AM with plastically deformed material*

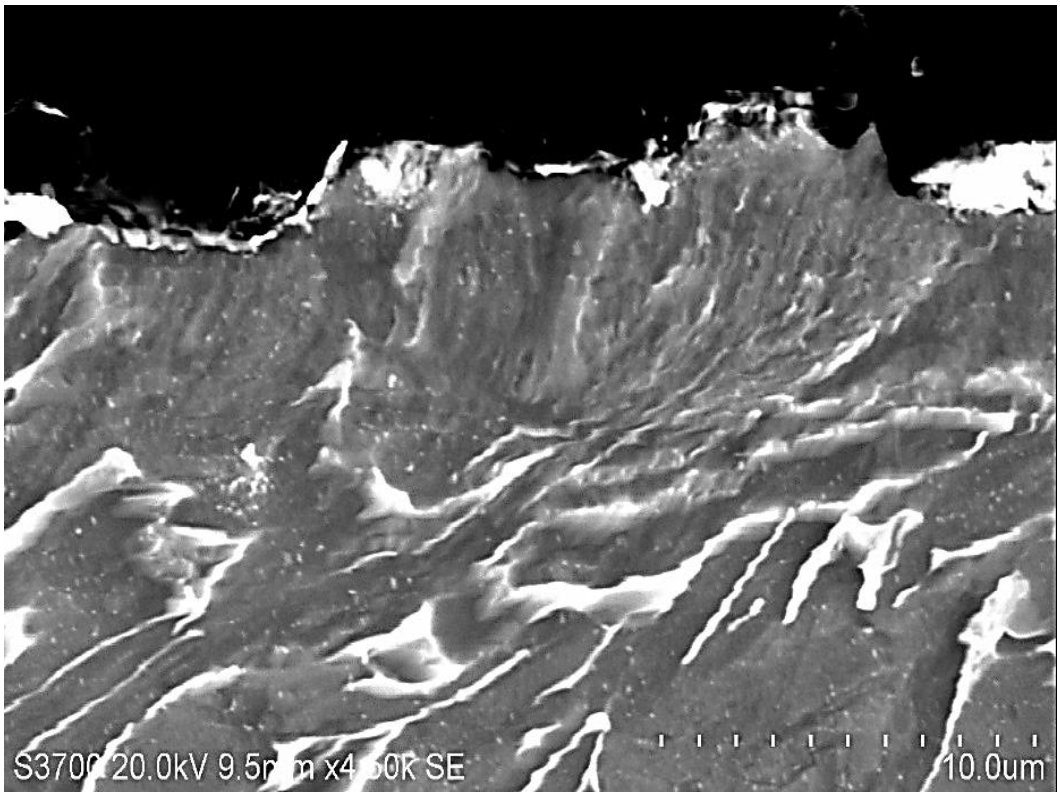

Figure C-13: *Cross section of erosion-corrosion wear scar of UNS R56400 W with plastically deformed material*

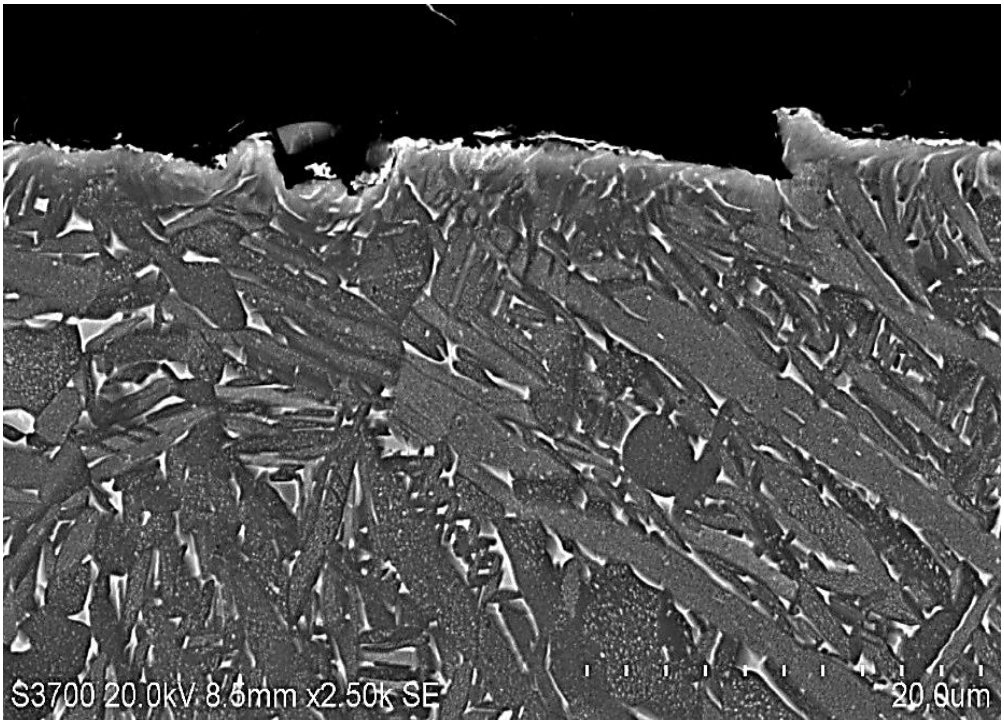

Figure C-14: *Cross section of erosion-corrosion wear scar of UNS R56400 AM with plastically deformed material*

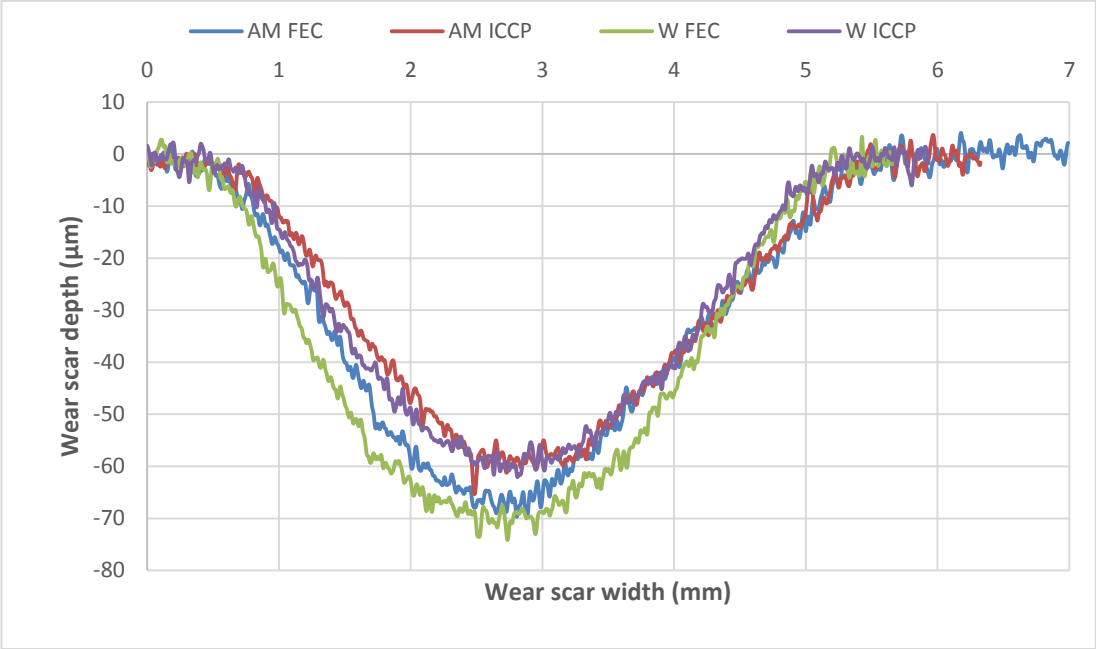

Figure C-15: *Wear scar profiles for UNS S15500 W and AM in FEC and ICCP conditions*

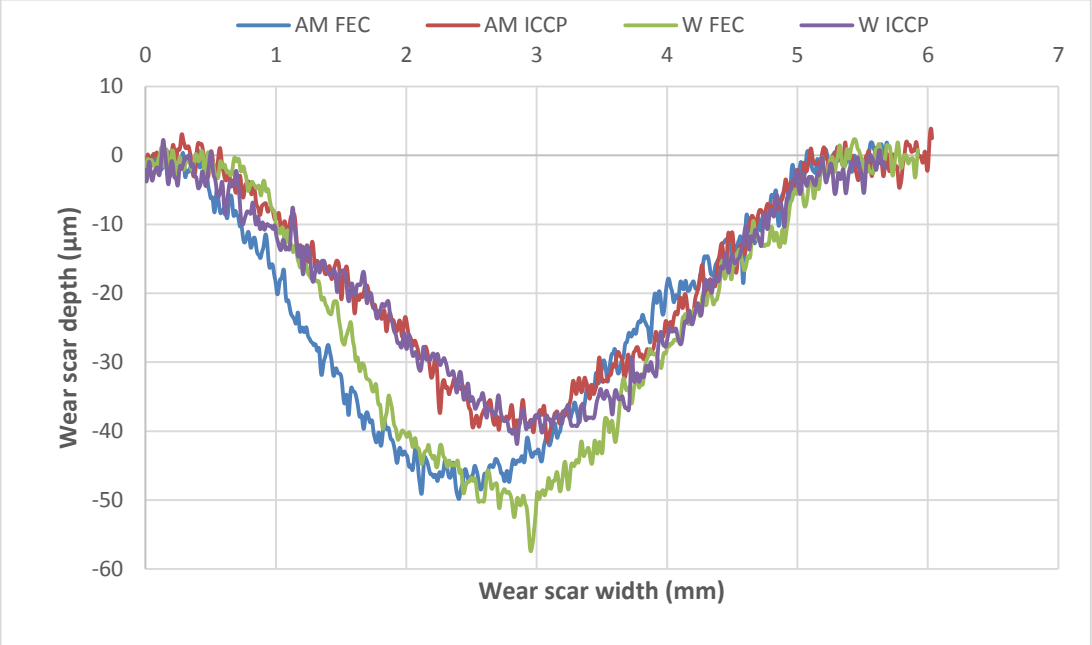

Figure C-16: *Wear scar profiles for UNS N07718 W and AM in FEC and ICCP conditions*

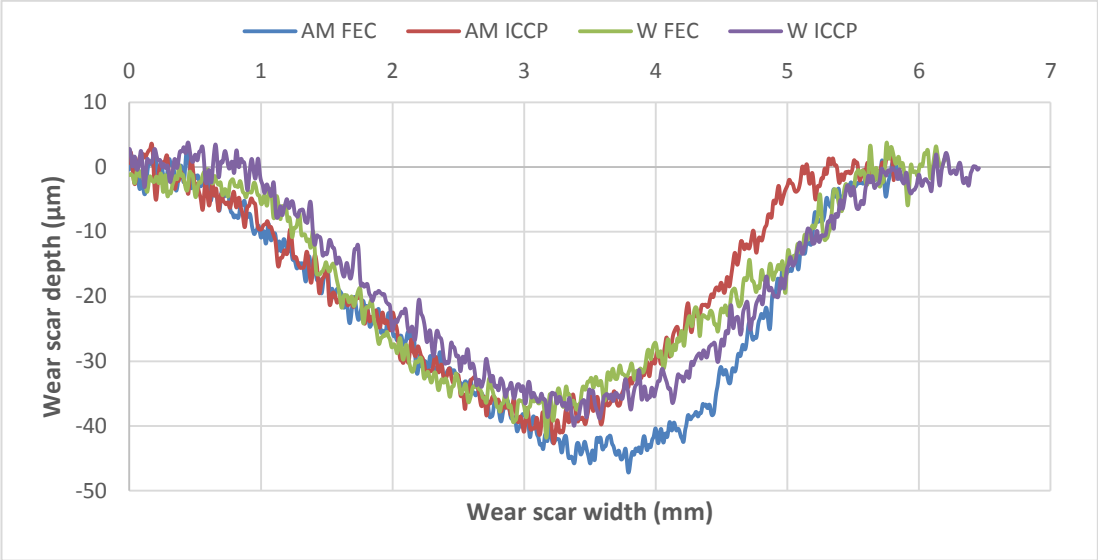

Figure C-17: *Wear scar profiles for UNS R56400 W and AM in FEC and ICCP conditions*

Table C-1: *Amount of sand particles for each CF range for all test materials in repetitive impact with slurry test conditions*

Material	CF value <0.8	CF value 0.8-0.9	CF value >0.9
Untested sand particles (reference)	1	35	64
UNS S31600 W	5	58	37
UNS S31600 AM	0	55	45
UNS S15500 W	20	62	18
UNS S15500 AM	1	52	47
UNS N07718 W	6	53	41
UNS N07718 AM	4	45	51
UNS R56400 W	12	54	34
UNS R56400 AM	9	47	44